



THE UNIVERSITY OF QUEENSLAND  
AUSTRALIA

# Non-classical States of Light

Agata Maria Brańczyk

A thesis submitted for the degree of  
Doctor of Philosophy at  
The University of Queensland

School of Mathematics and Physics

August, 2010



---

# Declaration

---

## Declaration by author

This thesis is composed of my original work, and contains no material previously published or written by another person except where due reference has been made in the text. I have clearly stated the contribution by others to jointly-authored works that I have included in my thesis.

I have clearly stated the contribution of others to my thesis as a whole, including statistical assistance, survey design, data analysis, significant technical procedures, professional editorial advice, and any other original research work used or reported in my thesis. The content of my thesis is the result of work I have carried out since the commencement of my research higher degree candidature and does not include a substantial part of work that has been submitted to qualify for the award of any other degree or diploma in any university or other tertiary institution. I have clearly stated which parts of my thesis, if any, have been submitted to qualify for another award.

I acknowledge that an electronic copy of my thesis must be lodged with the University Library and, subject to the General Award Rules of The University of Queensland, immediately made available for research and study in accordance with the Copyright Act 1968.

I acknowledge that copyright of all material contained in my thesis resides with the copyright holder(s) of that material.

## Statement of Contributions to Jointly Authored Works Contained in the Thesis

Agata M. Brańczyk and T. C. Ralph, *Teleportation using squeezed single photons*, Phys. Rev. A **78**, 052304 (2008) – Incorporated as Chapter 3.

T. C. Ralph was responsible for the initial proposal and partially responsible for development of the idea and drafting the article. Agata M. Brańczyk was responsible for the remainder of the work.

Agata M. Brańczyk, T. C. Ralph, Wolfram Helwig, Christine Silberhorn, *Optimised generation of heralded Fock states using parametric down conversion*, New J. Phys. **12** 063001 (2010) – Incorporated as Chapter 4.

Christine Silberhorn was responsible for the initial proposal and partially responsible for development of the idea and drafting the article. Wolfram Helwig was responsible for development of the formalism. T. C. Ralph was partially responsible for the drafting of the article. Agata M. Brańczyk was responsible for the remainder of the work.

Agata M. Brańczyk, Alessandro Fedrizzi, Timothy C. Ralph, Andrew G. White, *Engineered optical nonlinearity for a quantum light source*, arXiv:1005.3086 [quant-ph] (2010) – Incorporated as Chapter 5.

Timothy C. Ralph and Andrew G. White were partially responsible for developing the proposal and drafting the article. Alessandro Fedrizzi was responsible for performing the experiment. Agata M. Brańczyk and Alessandro Fedrizzi were equally responsible for the remainder of the work.

### **Statement of Parts of the Thesis Submitted to Qualify for the Award of Another Degree**

Some parts of Chapter 2 were submitted for BSc Honours, The University of Queensland, 2005, degree awarded 22 July 2005.

### **Published Works by the Author Incorporated into the Thesis**

Agata M. Brańczyk and T. C. Ralph, *Teleportation using squeezed single photons*, Phys. Rev. A **78**, 052304 (2008) – Incorporated as Chapter 3.

Agata M. Brańczyk, T. C. Ralph, Wolfram Helwig, Christine Silberhorn, *Optimised generation of heralded Fock states using parametric down conversion*, New J. Phys. **12** 063001 (2010) – Incorporated as Chapter 4.

Agata M. Brańczyk, Alessandro Fedrizzi, Timothy C. Ralph, Andrew G. White, *Engineered optical nonlinearity for a quantum light source*, arXiv:1005.3086 [quant-ph] (2010) – Incorporated as Chapter 5.

---

Agata M. Brańczyk

August, 2010

---

# Acknowledgements

---

First and foremost, I would like to thank my principal supervisor, Tim Ralph for his guidance, patience and support; for providing me with really interesting research and making my PhD fun. I also want to thank my associate supervisor, Alexei Gilchrist, for all his help, especially during the earlier parts of my PhD.

Thanks to Christine Silberhorn, who kindly hosted me in Erlangen for 3 months in 2008. My visit to Erlangen was an exceedingly rewarding experience for me. Thanks must also go out to Christine's wonderful group, which at the time consisted of Malte Avenhaus, Benjamin Brecht, Katuscia Cassemiro, Andreas Christ, Andreas Eckstein, Wolfram Helwig, Felix Just, Kaisa Laiho, Wolfgang Maurer, Peter Mosley, Andreas Schreiber and Christoph Söller, with whom I thoroughly enjoyed working and, of course, drinking fine Bavarian beer.

Thanks to my collaborators, Alessandro Fedrizzi and Tom Stace. It was a pleasure working with you and I look forward to continuing to do so in the future. Thanks to all the people who helped me throughout this PhD. Peter Rohde, and later, Charles Meaney, who were my default go-to people when I was stuck on pretty much anything. Thanks to Sean Barrett, Carl Caves, Andrew Doherty, Nick Menicucci, Gerard Milburn, Michael Nielsen, Tobias Osborne and Andrew White, for useful and engaging conversations over the years.

Thanks to my office mates—past and present—Tony Downes, Henry Haselgrove, Alex Hayes, Austin Lund, Charles Meaney, Jacques Pienaar, Peter Rohde and Christian Weedbrook, for providing music, laughter and eclectic conversation. Also, thanks to Danielle Facer and Ruth Forrest, for organising my travel, scholarships and in general looking after me.

Thanks to Eric Cavalcanti, for not only being a great person to bounce ideas of, but a true friend.

Thanks to my family, who compassionately stopped asking a long time ago how the thesis was going, and for their continual love and support.

Finally I would like to thank my parter, Simon O'Connell, for being there every step of the way—for cheering me up during setbacks and helping me celebrate accomplishments. Whether you want it or not, this thesis is as much yours as it is mine.



---

# Abstract

---

Optical quantum computing, quantum information and quantum communication protocols rely on the generation of qubits encoded in optical systems, many of which can be generate via the process of spontaneous parametric down-conversion. In this thesis, we investigate down-converted states, in the context of quantum computing and quantum information. In the high gain regime, a type I down-converted state can be described as a single-mode squeezed vacuum state. We present an analysis of photon-subtracted squeezed vacuum states as a resource for teleportation of coherent state qubits and propose proof-of-principle experiments for the demonstration of coherent-state teleportation and entanglement swapping. In the low gain regime, the output state of a type II parametric down-converter can be approximated as containing pairs of single photons, which can be used to herald the presence of one- or two- photon Fock states in one mode, conditional on the detection of the same number of photons in the other mode. We explore the effects of spectral filtering and inefficient detection, of the heralding mode, on the count rate,  $g^{(2)}$  and purity of the heralded state, as well as the fidelity between the resulting state and an ideal Fock state. We also develop a technique for controlling the joint spectral profile of the down-converted photons. By exploiting the dependence of the effective nonlinearity of a periodically poled crystal on its poling order, we tailor the nonlinearity profile and therefore the phase matching function of the down-converted photons. Finally, we consider the validity of the Taylor series expansion of the unitary operator which governs the evolution of the fields within the crystal, in comparison to the strictly correct time-ordered Dyson series expansion.

**Keywords**

Quantum Optics, Quantum Computing, Quantum Information, Nonlinear Optics, Spontaneous Parametric Down-conversion, Schrödinger Cat States, Teleportation

**Australian and New Zealand Standard Research Classifications  
(ANZSRC)**

020604 75%, 020603 25%

---

# Contents

---

<b>Declaration</b>	<b>i</b>
<b>Acknowledgements</b>	<b>iii</b>
<b>Abstract</b>	<b>v</b>
<b>1 Introduction</b>	<b>1</b>
1.1 A Brief History of Quantum Optics . . . . .	1
1.2 Quantum Information . . . . .	2
1.3 Optical Qubits . . . . .	4
<b>2 Basic Concepts and Formalisms</b>	<b>7</b>
2.1 Quantum Mechanics . . . . .	7
2.1.1 Pure and Mixed States . . . . .	7
2.1.2 Quantum Dynamics . . . . .	7
2.1.3 Simple Harmonic Oscillator . . . . .	8
2.1.4 Fock States . . . . .	9
2.1.5 Coherent States . . . . .	9
2.1.6 Squeezed States . . . . .	10
2.1.7 Projective Measurements . . . . .	10
2.1.8 Normalised Second-order Correlation Function . . . . .	11
2.1.9 Wigner Function . . . . .	11
2.2 Qubit Formalism and Quantum Information . . . . .	12
2.2.1 The Pauli Matrices . . . . .	13
2.2.2 Quantum Fidelity . . . . .	14
2.2.3 Quantum Entanglement . . . . .	14
2.2.4 Bell States . . . . .	15

---

2.2.5	Quantum Teleportation . . . . .	15
2.3	Quantum Optics . . . . .	16
2.3.1	Coherent State Encoding for Optical Quantum Computing . . . . .	16
2.3.2	Schrödinger Cat States . . . . .	16
2.3.3	Photons as Fock States . . . . .	16
2.3.4	Beamsplitters . . . . .	17
2.4	Spontaneous Parametric Down-conversion . . . . .	17
2.4.1	Single Mode . . . . .	18
2.4.2	Multi Mode . . . . .	18
2.4.3	Quasi Phase Matching . . . . .	20
<b>3</b>	<b>Teleportation Using Squeezed Single Photons</b>	<b>23</b>
3.1	Coherent-state Teleportation . . . . .	24
3.2	Approximating Cat States . . . . .	27
3.3	Squeezed Single-photon State as a Resource . . . . .	29
3.4	Proposed Experiments . . . . .	31
3.4.1	Teleportation . . . . .	31
3.4.2	Entanglement Swapping . . . . .	32
3.5	Error Analysis . . . . .	34
3.5.1	Teleportation . . . . .	34
3.5.2	Entanglement Swapping . . . . .	37
3.6	Discussion . . . . .	38
<b>4</b>	<b>Optimised Generation of Heralded Fock States Using SPDC</b>	<b>39</b>
4.1	Single-photon Sources . . . . .	40
4.2	Spontaneous Parametric Down Conversion . . . . .	41
4.3	Spectral Filtering . . . . .	43
4.4	Generating Single-photon Fock States . . . . .	45
4.4.1	Case 1: Perfect Detection in the Triggering Idler Mode . . . . .	45
4.4.2	Case 2: Inefficient Detection in the Triggering Idler Mode . . . . .	47
4.4.3	Case 3: Filtering the Idler State . . . . .	48
4.5	Generating 2-photon Fock States . . . . .	51
4.5.1	Case 1: Perfect Detection in the Triggering Idler Mode . . . . .	51

---

4.5.2	Case 2: Inefficient Detection in the Triggering Idler Mode . . .	52
4.5.3	Case 3: Filtering of the Idler State . . . . .	52
4.6	Physical Example I - Correlated JSA . . . . .	54
4.7	Physical Example II - Group Velocity Matching . . . . .	58
4.7.1	Symmetric JSA . . . . .	59
4.7.2	Asymmetric JSA . . . . .	62
4.7.3	Generating Two-photon Fock States . . . . .	66
4.8	Discussion . . . . .	66
<b>5</b>	<b>Tailoring the Nonlinearity of a Nonlinear Crystal</b>	<b>69</b>
5.1	Spectral Amplitude of Down-converted Photons . . . . .	70
5.2	Tailoring the Nonlinearity . . . . .	71
5.3	The Custom-poled Crystal . . . . .	73
5.4	Two-photon Interference . . . . .	74
5.5	Quantum Beating . . . . .	77
5.6	Separable Joint Spectral Amplitude . . . . .	78
5.7	Arbitrary Phasematching Functions . . . . .	79
5.8	Discussion . . . . .	82
<b>6</b>	<b>Time Ordering in Spontaneous Parametric Down-conversion</b>	<b>83</b>
6.1	Type II SPDC Hamiltonian . . . . .	84
6.2	Evaluating the Dyson series expansion . . . . .	87
6.2.1	First Order Term . . . . .	87
6.2.2	Second Order Term . . . . .	89
6.2.3	Third Order Term . . . . .	91
6.3	Comparing With the Taylor Series . . . . .	96
6.4	Discussion . . . . .	98
<b>7</b>	<b>Conclusion</b>	<b>99</b>
<b>A</b>	<b>Appendix to <i>Tailoring the Nonlinearity of a Nonlinear Crystal</i></b>	<b>103</b>
A.1	Gaussian Approximation to Sinc Function . . . . .	103
A.2	Detailed Model . . . . .	103

---

<b>B Appendix to <i>Time-ordering in Spontaneous Parametric Down-conversion</i></b>	<b>105</b>
B.1 Commutativity of the SPDC Hamiltonian . . . . .	105
B.2 Sanity Check . . . . .	108
B.3 Evaluating the Taylor series expansion . . . . .	112
B.3.1 First Order Term . . . . .	112
B.3.2 Second Order Term . . . . .	113
B.3.3 Third Order Term . . . . .	115
B.4 Correction to the vacuum state amplitude using the Dyson series . .	119
B.5 Correction to the two-photon state amplitude using the Dyson series	120
B.6 Permutations . . . . .	127
B.7 Change of Time Integration Variables . . . . .	128
B.7.1 Two Dimensional . . . . .	128
B.7.2 Three Dimensional . . . . .	128
B.8 Evaluate $\int_0^\infty ds \exp(ixs)$ . . . . .	130

---

# List of Figures

---

2.1	Intensity growth as a function of crystal length in a QPM crystal. . . . .	20
3.1	Coherent-state teleportation scheme. . . . .	25
3.2	Success probabilities of teleportation scheme. . . . .	26
3.3	Fidelities and required squeezing parameters for teleportation scheme. . . . .	28
3.4	Wigner functions. . . . .	29
3.5	Fidelities for teleportation scheme. . . . .	30
3.6	Fidelities for teleportation scheme. . . . .	32
3.7	Coherent state entanglement swapping scheme . . . . .	33
3.8	Fidelities for entanglement swapping scheme . . . . .	34
3.9	Lossy teleportation and entanglement swapping scheme. . . . .	35
3.10	Fidelities for lossy teleportation scheme. . . . .	35
3.11	Fidelities for lossy teleportation scheme. . . . .	36
3.12	Fidelities for lossy entanglement swapping scheme. . . . .	37
4.1	Schematic diagrams of SPDC setup . . . . .	46
4.2	Spectral functions for highly correlated JSA . . . . .	55
4.3	Probability (single-photon detection), fidelity, $g^{(2)}$ and purity for highly correlated JSA . . . . .	56
4.4	Probability and nonlinearity for achieving a fidelity of $F = 0.95$ . . . . .	57
4.5	Probability (two-photon detection), fidelity and purity for highly correlated JSA . . . . .	58
4.6	Spectral functions for separable symmetric JSA . . . . .	60
4.7	Probability (single-photon detection), fidelity, $g^{(2)}$ and purity for separable symmetric JSA . . . . .	61
4.8	Probability (two-photon detection), fidelity and purity for separable symmetric JSA . . . . .	62
4.9	Spectral functions for separable asymmetric JSA . . . . .	63

---

4.10	Probability (single-photon detection), fidelity, $g^{(2)}$ and purity for separable asymmetric JSA . . . . .	65
4.11	Probability (two-photon detection), fidelity and purity for separable asymmetric JSA . . . . .	66
5.1	Nonlinearity profile and phase-matching function for cpKTP and ppKTP crystals . . . . .	72
5.2	Magnified image of part of the custom-poled KTP crystal . . . . .	73
5.3	Two-photon interference experimental setup . . . . .	74
5.4	Two-photon interference patterns for cpKTP and ppKTP crystals . . . . .	76
5.5	Spatial quantum beating for cpKTP and ppKTP crystals . . . . .	77
5.6	Nonlinearity profiles and corresponding PMFs for $m_{\min} = 1$ and $m_{\min} = 2$ tailored crystals . . . . .	78
5.7	Nonlinearity profile for triangular PMF . . . . .	80
5.8	Nonlinearity profile for top-hat PMF . . . . .	80
6.1	Integration regions for second and third order term . . . . .	85
6.2	Cartoon depicting the different permutations of the order in which two pairs of photons are created . . . . .	85
6.3	Cartoon depicting the different permutations of the order in which three pairs of photons are created . . . . .	86
6.4	Schematic diagrams demonstrating the energy conservation relationships between the pump, idler and signal photons . . . . .	88
A.1	Comparison between basic and domain-by-domain models . . . . .	104
B.1	Time integration region for second-order term . . . . .	128
B.2	Time integration region for third-order term . . . . .	129

---

# List of Tables

---

3.1	Teleportation scheme corrections . . . . .	26
4.1	Summary of multi-mode creation operators, spectral modes and states	43
5.1	Values for poling order $m$ , domain number $n$ and Duty cycle $D$ used to generate a discrete approximation to a Gaussian nonlinearity profile.	71
5.2	Values for poling order $m$ , domain number $n$ used to generate a discrete approximation to a Gaussian nonlinearity profile . . . . .	79
5.3	Numerical comparison of the purity $p$ of heralded single-photons of a standard crystal and two cpKTP crystals of length $L$ . . . . .	79
5.4	Values for poling order $m$ and domain number $n$ used to generate discrete approximations to triangular and top-hat nonlinearity profiles	81



# Introduction

---

## 1.1 A Brief History of Quantum Optics

In the mid-to-late seventeenth century, a debate was being waged over the nature of light. On one side, were René Descartes and Isaac Newton, positing that light was a beam of particles. Newton argued that only particles could be reflected and travel in straight lines, the way in which light was observed to do [1]. While Newton's theory of optics explained reflection and refraction, it could not explain certain other observed properties of light, like diffraction, interference and polarisation.

On the other side of the debate were Robert Hooke, Christiaan Huygens and Augustin-Jean Fresnel, who proposed that light was a wave, naturally explaining diffraction and interference, in addition to reflection and refraction [2]. Although Newton's particle theory was favoured over Huygens' wave theory for over a century—reputedly, a result of Newton's high regard—the tables eventually began to turn. In the early 1800s, Thomas Young's double slit experiment and the development of James Clerk Maxwell's famous equations in the later part of the century—which were subsequently verified by experiments by Heinrich Hertz—finally brought about wide acceptance of the wave theory. However, this long-awaited victory would not last long.

In 1901, Max Planck successfully predicted the electromagnetic spectrum emitted by a black body by assuming that light is emitted in discrete packets, i.e. *quanta*, introducing the uncomfortable notion of wave-particle duality. This signified the first *quantum theory* of light and the birth of quantum mechanics. Although Planck believed that this assumption was only a convenient fudge, rather than a reflection of the nature of reality, Einstein would later use the same assumption to explain the photoelectric effect, for which he was awarded the Nobel Prize in 1921.

This was followed by a collection of *ad hoc* approaches, which, later became known as the *old quantum theory*. In 1913, Niels Bohr explained the spectral lines of the hydrogen atom by discretising the distances at which electrons could orbit the nucleus, and soon after, Arnold Sommerfeld quantized the z-component of angular

momentum. A decade later, Louis-Victor de Broglie proposed that *all* matter has a wave-like nature. He later shared the 1937 Nobel prize with George Paget Thomson and Clinton Joseph Davisson, who experimentally confirmed de Broglie's hypothesis for electrons. In 1924, the *photon* was shown to exist as a distinct entity, via the Compton effect [3].

Around the time following de Broglie's proposal, quantum mechanics went through an upheaval. Niels Bohr and Werner Heisenberg attempted to reconcile the strange predictions of quantum mechanics with the everyday, seemingly classical world, via what is now known as the *Copenhagen interpretation* of quantum mechanics. Heisenberg derived his uncertainty principle, which states that position and momentum can not be known simultaneously with arbitrary precision. Along with Max Born, he also developed the first complete and correct formulation of quantum mechanics known as *matrix mechanics*. Erwin Schrödinger developed wave mechanics, and Paul Dirac showed that it was equivalent to Heisenberg's approach. Dirac formulated the relativistic Schrödinger equation and developed bra-ket notation and John von Neumann recast quantum mechanics in terms of linear Hermitian operators on Hilbert spaces. Out of the initial turmoil, rose a robust mathematical framework for the construction of physical theories: quantum mechanics as we know it today [4, 5].

While quantum mechanics was being used to make predictions about the behaviour of matter, it was still possible to explain most of the observed optical phenomena—diffraction, interference, image formation, frequency doubling and wave mixing—using the classical theory of electromagnetic radiation based on Maxwell's equations [6, 7]. Subsequent experiments with low numbers of photons could also be explained equally well with classical or quantum theories, namely, Geoffrey Taylor's single-photon version of Young's double slit experiment and Robert Hanbury Brown and Richard Twiss' photon bunching experiments. Even the newly-developed laser could be described as a classical coherent state of light.

However, in 1963, Roy Glauber formulated a quantum theory of optical coherence which predicted photon *antibunching*—a uniquely quantum phenomenon. In 1975, Howard Carmichael and Daniel Walls predicted that light generated by fluorescence from a two-level atom would exhibit antibunching; and the first non-classical effect in optics was observed by H. Jeff Kimble, Mario Dagenais and Leonard Mandel in 1976, when they confirmed Carmichael and Walls' predictions. Nine years later, R.E. Slusher observed another prediction of quantum theory—squeezed light.

## 1.2 Quantum Information

As quantum mechanics was reaching maturity, another—seemingly unrelated—discipline was evolving. In the 1930s, Alan Turing had developed the abstract notion

---

of what we now call a programable computer: the *Turing machine* [8]. Soon after, the first computers constructed from vacuum tubes as their electronic components, were developed [4]. In 1947, John Bardeen, Walter Brattain and Will Shockley developed the transistor—a semiconductor device used to amplify and switch electronic signals—which would replace vacuum tubes as the active component, allowing computers which were smaller, faster, cheaper to produce, required less power, and were more reliable. They received the 1956 Nobel prize for their achievements. From the development of computers, emerged the discipline of computer science and the closely-related discipline of information theory, founded in 1948 by Claude Shannon [9].

In the early 1980s, Richard Feynman and David Deutsch introduced the notion of a computational device based upon the principles of quantum mechanics: a *quantum computer* [4, 10]. Such a device addressed the difficulties of simulating quantum mechanical systems on classical computers. A decade later, Peter Shor demonstrated that the prime factors of an integer could be efficiently solved on a quantum computer<sup>1</sup> [11, 12] and Lov Grover showed that the problem of conducting a search through an unstructured space<sup>2</sup> could also be sped up on a quantum computer [13].

Along with the notion of a quantum computer, arose the concepts of *quantum information* and *quantum cryptography*. A quantum bit, or *qubit* was introduced as an analogue to the classical mechanism for storing information—the bit. In contrast to a classical bit, the qubit can take on a *superposition* of the logical states **0** and **1**. A qubit has the potential to be realised in a wide variety of physical systems, for example, photon number or polarisation, electron number or electron spin, or the spin of the nucleus of an atom.

With the advent of heralded single-photon sources, quantum optics became an ideal testbed for some of the key concepts in quantum information. John Bell’s 1964 introduction of a test for the EPR paradox—a thought experiment contrived thirty years earlier by Einstein, Boris Podolski and Nathan Rosen [14]—which relied on the quantum concept of *entanglement*, was experimentally realised by Alain Aspect, Phillipe Grangier and Gerard Roger in 1982 [15]. Quantum teleportation, proposed by Charles Bennett *et al.* in 1993 [16]—which also relied on the concept of entanglement—was experimentally demonstrated by Dirk Bouwmeester *et al.* in 1997 with the teleportation of a polarisation encoded qubit [17].

In 2001, Emanuel Knill, Raymond Laflamme, and Gerard Milburn launched the field of linear optical quantum computing, by showing that scalable quantum computing is possible with single-photon sources, linear optical elements, and single-photon

---

<sup>1</sup>This would have implications for bank security, which presently relies on the assumption that it takes a long time for a classical computer to factor a large number.

<sup>2</sup>For example, finding a particular phone number in a phone book without knowing the corresponding name.

detectors [18]. Two years later, Jeremy O’Brien *et al.* [19], and independently Pittman *et al.* [20], demonstrated a controlled-not gate—an entangling gate crucial for quantum computation—using only linear optical elements.

### 1.3 Optical Qubits

Optical quantum computing, quantum information and quantum communication protocols rely on the generation of qubits encoded in optical systems. Some typical examples include single- or multi-photon qubits, coherent-state qubits or qubits encoded in the position and momentum eigenstates of the electromagnetic field—all of which can be generated by the process of *spontaneous parametric down-conversion*—a nonlinear optical process in which a photon from a pump laser, incident on a nonlinear birefringent crystal, converts into two single photons under conservation of energy and momentum.

In the low-gain regime, the output state of a parametric down-converter can be approximated as a pair of two single photons. The experiments by Bouwmeester *et al.*, O’Brien *et al.* and Pittman *et al.*, as well as many others, have made use of single photons generated using this process. However, using higher pump powers, the output state can also be described as a squeezed state, allowing the heralding of higher-order photon-number states. Superpositions of coherent states, known as *kitten states*, can be approximated by subtracting photons from the output squeezed state, as was shown in references [21, 22]. Position and momentum eigenstates can also be approximated by strongly squeezed states.

This thesis represents my contribution to the understanding and characterisation of states generated by this presently indispensable process, in the context of quantum computing and quantum information. The basic concepts and formalisms used throughout this thesis are presented in Chapter 2. The rest of the thesis can be roughly separated into two parts.

The first part, consisting of Chapter 3, is devoted to the analysis of Schrödinger kitten states, generated by the photon-subtraction process mentioned above, as a resource for the teleportation of coherent state qubits. Teleportation can be used as a building block for a number of single- and multi-qubit gates—and is itself the identity gate. A single-photon-subtracted squeezed vacuum state is only an approximation to a kitten state—albeit an extremely good one at low amplitudes—and it is important to determine the parameters under which this approximate state serves as an adequate resource state for performing quantum gates.

The larger, second part of this thesis, encompassing Chapters 4, 5 and 6, deals with the spectral properties of the states generated by parametric down-conversion. The down-converted photons are typically entangled in the frequency degree of freedom,

---

a characteristic which is not considered when treating the output in a simplified single-frequency-mode picture, as was done in Chapter 3.

Chapter 4 models the creation of one- and two-photon states. The detection of  $n$  photons in one output mode<sup>3</sup> of a type II down-converter heralds the presence of  $n$  photons in the other mode. However, spectral entanglement, combined with the low spectral resolution of the heralding detector, renders the heralded state mixed in frequency—an undesirable consequence. The effects of spectral filtering of the heralding state are analysed to determine an optimal method for generating pure photon-number states. In particular, higher-order down-conversion events in the form of four photons are considered, as they may have adverse effects on the success of spectral filtering. In addition, by considering four-photon states, the heralding of two-photon number states can be analysed.

Chapter 5 deals with controlling the joint spectral profile of the down-converted photons. The profile depends on a number of parameters, namely, the spectral profile of the input pump laser; the group velocity conditions which themselves depend on the composition of the down-conversion crystal; and the profile of the phase matching function, which is related, via the Fourier transform, to the nonlinearity profile of the down-conversion crystal. The first two aspects have been studied extensively—see for example [23, 24, 25, 26, 27, 28, 29, 30, 31, 32]. The third is the focus of Chapter 5. By exploiting the dependence of the effective nonlinearity of a periodically poled crystal on its poling order, it is possible to tailor a nonlinearity profile and therefore the phase matching function of the down-converted photons. The most immediate application of this technique may be the generation of pure photon-number states. The design of a custom poled crystal with a Gaussian profile was performed in collaboration with Alessandro Fedrizzi, an experimental physicist, who verified the profile of the down-converted photons from the custom poled crystal using a two-photon interference experiment. These experimental results are also presented.

Chapter 6 considers the multi-mode Hamiltonian that governs the evolution of the fields inside the crystal. If the Hamiltonian does not commute with itself at all times—as is the case for the multimode down-conversion Hamiltonian—then the expansion of the evolution operator must take the form of the time-ordered Dyson series, as opposed to the much simpler Taylor series. By expanding the evolution operator to third order, the conditions under which the Taylor series is a valid approximation are revealed. In addition, some new and interesting behaviour is predicted.

---

<sup>3</sup>The photons are typically down-converted into two orthogonal polarisation modes and then distributed into different spatial modes using a polarising beamsplitter.



---

# Basic Concepts and Formalisms

---

## 2.1 Quantum Mechanics

### 2.1.1 Pure and Mixed States

In quantum mechanics, a physical state can be represented by a state vector in a complex vector space [5]. Using Dirac, or *ket*, notation, we write such a state as  $|\psi\rangle$ . A quantum system whose state  $|\psi\rangle$  is known exactly is said to be in a *pure* state.

We can also represent a quantum state as a density operator, which for a pure state, is denoted as  $\rho = |\psi\rangle\langle\psi|$ . If  $\rho$  is not in a pure state, then it is said to be in a *mixed* state. A mixed state can be written as  $\rho = \sum_i p_i |\psi_i\rangle\langle\psi_i|$  where  $\rho$  is a *mixture* of the states  $|\psi_i\rangle$  with probabilities  $p_i$ . A mixed state can be thought of as a classical probability distribution of pure states. Related to this is a property of quantum states known as the *purity*, defined as

$$P = \text{Tr}[\rho^2]. \quad (2.1)$$

If  $P = 1$ , then  $\rho$  is in a pure state while if  $P < 1$ ,  $\rho$  is in a mixed state [4].

### 2.1.2 Quantum Dynamics

#### Solutions to the Schrödinger Equation for the State Ket

To study the evolution of a state, we want to know how it changes under a time displacement  $t_0 \rightarrow t$ . This can be defined in terms of the *time-evolution operator*  $\hat{U}(t, t_0)$

$$|\psi_{t_0}; t\rangle = \hat{U}(t, t_0)|\psi_{t_0}\rangle \quad (2.2)$$

The Schrödinger equation is the fundamental equation for the time-evolution oper-

ator. Everything that has to do with time development follows from this equation.

$$i\hbar \frac{\partial}{\partial t} \hat{U}(t, t_0) = \hat{H} \hat{U}(t, t_0), \quad (2.3)$$

where  $\hat{H}$  is the operator that corresponds to the total energy of the system, known as the *Hamiltonian*. Equation 2.3 is equivalent to

$$i\hbar \frac{\partial}{\partial t} |\psi_{t_0}; t\rangle = \hat{H} |\psi_{t_0}; t\rangle, \quad (2.4)$$

when applied to a ket. If we are given  $\hat{U}(t, t_0)$  and we know how it acts on  $|\psi_{t_0}\rangle$ , we can circumvent equation 2.4 and simply apply  $\hat{U}(t, t_0)$  to  $|\psi_{t_0}\rangle$ . There are three cases for formal solutions to the Schrödinger equation.

**Case 1:** If the Hamiltonian is independent of time, the solution to the Schrödinger equation is

$$\hat{U}(t, t_0) = e^{-\frac{i}{\hbar} \hat{H} t}. \quad (2.5)$$

**Case 2:** If the Hamiltonian is time-dependant and it commutes with itself at all times, i.e.  $[\hat{H}(t_1), \hat{H}(t_2)] = 0$ , the solution to the Schrödinger equation is

$$\hat{U}(t, t_0) = e^{-\frac{i}{\hbar} \int_{t_0}^t dt' \hat{H}(t')}. \quad (2.6)$$

**Case 3:** If the Hamiltonian is time-dependant and does *not* commute with itself at all times, i.e.  $[\hat{H}(t_1), \hat{H}(t_2)] \neq 0$ , the solution to the Schrödinger equation is

$$\hat{U}(t, t_0) = \mathcal{T} e^{-\frac{i}{\hbar} \int_{t_0}^t dt' \hat{H}(t')}. \quad (2.7)$$

where  $\mathcal{T}$  is the time ordering operator. Equation 2.7 can be expanded into what is sometimes known as the Dyson series.

$$\hat{U}(t, t_0) = 1 + \sum_{n=1}^{\infty} \left(-\frac{i}{\hbar}\right)^n \int_{t_0}^{t_1} dt_1 \int_{t_0}^{t_2} dt_2 \dots \int_{t_0}^{t_{n-1}} dt_n \hat{H}(t_1) \hat{H}(t_2) \dots \hat{H}(t_n). \quad (2.8)$$

The difference between Cases 2 and 3 in spontaneous parametric down-conversion (see Section 2.4) will be the subject of Chapter 6.

### 2.1.3 Simple Harmonic Oscillator

The basic Hamiltonian for the simple harmonic oscillator is [5]

$$\hat{H} = \frac{\hat{p}^2}{2m} + \frac{m\omega^2 \hat{x}^2}{2} \quad (2.9)$$

where  $\omega$  is the angular frequency of the classical oscillator. The Hermitian operators  $\hat{x}$  and  $\hat{p}$  are the position and momentum operator respectively. We now define two non-Hermitian operators,

$$\hat{a} = \sqrt{\frac{m\omega}{2\hbar}} \left( \hat{x} + \frac{i\hat{p}}{m\omega} \right), \quad \hat{a}^\dagger = \sqrt{\frac{m\omega}{2\hbar}} \left( \hat{x} - \frac{i\hat{p}}{m\omega} \right), \quad (2.10)$$

known as the *annihilation* and *creation operators* respectively. These operators satisfy the commutation relation  $[\hat{a}, \hat{a}^\dagger] = 1$ . We also define the number operator  $\hat{N} = \hat{a}^\dagger \hat{a}$  and can now write the Hamiltonian in equation 2.9 as

$$\hat{H} = \hbar\omega \left( \hat{N} + \frac{1}{2} \right) \quad (2.11)$$

### 2.1.4 Fock States

A Fock state, also known as a number state, is a state with a well defined number of particles. We denote a Fock state as  $|n\rangle$  where  $n$  is the number of particles in the state.  $|n\rangle$  is an eigenstate of the Hamiltonian for the simple harmonic oscillator [33], i.e.

$$\hat{H}|n\rangle = \hbar\omega \left( n + \frac{1}{2} \right) |n\rangle \quad (2.12)$$

Fock states have the following properties

$$\hat{N}|n\rangle = n|n\rangle, \quad \hat{H}|0\rangle = \frac{\hbar\omega}{2}|0\rangle \quad (2.13)$$

and can be generated by repeated application of the creation operator  $\hat{a}^\dagger$  on the vacuum state

$$|n\rangle = \frac{(\hat{a}^\dagger)^n}{\sqrt{n!}} |0\rangle. \quad (2.14)$$

As their names suggest, annihilation and creation operators have the following effect on number states

$$\hat{a}|n\rangle = \sqrt{n}|n-1\rangle, \quad \hat{a}^\dagger|n\rangle = \sqrt{n+1}|n+1\rangle. \quad (2.15)$$

### 2.1.5 Coherent States

The coherent state is an eigenstate of the annihilation operator [6].

$$\hat{a}|\alpha\rangle = \alpha|\alpha\rangle, \quad (2.16)$$

and can be generated by operating  $D(\alpha)$  on the vacuum state

$$|\alpha\rangle = \hat{D}(\alpha)|0\rangle, \quad (2.17)$$

where  $\hat{D}(\alpha) = e^{-|\alpha|^2/2} e^{\alpha \hat{a}^\dagger} e^{-\alpha^* \hat{a}}$  is the displacement operator. Coherent states contain an indefinite number of particles and can be expanded in terms of the number states

$$|\alpha\rangle = e^{-|\alpha|^2/2} \sum_{n=0}^{\infty} \frac{\alpha^n}{\sqrt{n!}} |n\rangle. \quad (2.18)$$

Coherent states are minimum-uncertainty states and have equal noise in both  $\hat{x}$  and  $\hat{p}$  quadratures. They can be approximated by the field of a laser, as will be discussed in section 2.3.1.

### 2.1.6 Squeezed States

Squeezed states are a general class of minimum-uncertainty states, for which the noise in one quadrature is reduced compared with a coherent state. In order to satisfy the requirements of minimum-uncertainty, the noise in the other quadrature must be greater than that of a coherent state. Squeezed states may be generated using the unitary squeezing operator [6]

$$\hat{S}(\varepsilon) = e^{\frac{1}{2}(\varepsilon^* \hat{a}^2 - \varepsilon \hat{a}^{\dagger 2})}, \quad (2.19)$$

where  $\varepsilon = r e^{2i\phi}$ . The squeezing operator attenuates one component of the complex amplitude and it amplifies the other component. The degree of attenuation and amplification is determined by the *squeezing factor*, or *squeezing parameter*,  $r = |\varepsilon|$ . The angle  $\phi$  determines the axis along which squeezing occurs. The squeezed state  $|\alpha, \varepsilon\rangle$  is obtained by first squeezing the vacuum and then displacing it

$$|\alpha, \varepsilon\rangle = \hat{D}(\alpha) \hat{S}(\varepsilon) |0\rangle. \quad (2.20)$$

The squeezing operator can also be applied to number states to give *squeezed number states*

$$|n, \varepsilon\rangle = \hat{S}(\varepsilon) |n\rangle. \quad (2.21)$$

### 2.1.7 Projective Measurements

A projective measurement is a measurement which projects a system onto an eigenspace of an *observable*  $\hat{M}$ . The observable has the following spectral decompo-

sition:

$$\hat{M} = \sum_m \hat{P}_m \quad (2.22)$$

where  $\hat{P}_m$  is the projector onto the eigenspace of  $\hat{M}$  with eigenvalue  $m$  [4].

If we were to measure the state  $|\psi\rangle$ , the probability of getting the result  $m$  would be given by

$$p_m = \langle \psi | \hat{P}_m | \psi \rangle \quad (2.23)$$

and given that the outcome  $m$  occurred, the state of the system immediately after measurement is

$$\frac{\hat{P}_m |\psi\rangle}{\sqrt{p_m}}. \quad (2.24)$$

We will sometimes use the phrase, ‘to measure in a basis  $\{|m\rangle\}$ ’. This means to perform a projective measurement with projectors  $\hat{P}_m = |m\rangle\langle m|$ .

### 2.1.8 Normalised Second-order Correlation Function

For a single-mode quantum mechanical field, the normalised second order correlation function, sometimes called the “*g two*”, is defined as [6]

$$g^{(2)} = \frac{\langle \hat{a}^\dagger \hat{a}^\dagger \hat{a} \hat{a} \rangle}{\langle \hat{a}^\dagger \hat{a} \rangle^2} = 1 + \frac{V(n) - \bar{n}}{\bar{n}^2} \quad (2.25)$$

where  $V(n)$  is the variance in the photon number and  $\bar{n}$  is the mean. For a coherent state,  $g^{(2)} = 0$ . For a single-photon state  $g^{(2)} = 1$  while for a number state with  $n > 2$ ,  $g^{(2)} = 1 - 1/n$ .

### 2.1.9 Wigner Function

The Wigner function is a quasi-probability distribution [6], and can be defined as

$$W(x) = \frac{1}{\pi^2} \int \exp(\eta^* \alpha - \eta \alpha^*) \chi(\eta) d\eta \quad (2.26)$$

where

$$\chi(\eta) = \text{Tr}[\rho e^{\eta \hat{a}^\dagger - \eta^* \hat{a}}] \quad (2.27)$$

is the symmetrically ordered characteristic function. It is analogous to the phase space probability distribution for a classical particle, however, due to the uncertainty principle, the Wigner function does not satisfy the properties of a conventional probability distribution. For example, the Wigner function can be negative, which is often seen as a signature of a quantum state.

### Coherent State

For a coherent state  $|\alpha\rangle$ , the Wigner function is

$$W(x, p) = \frac{2}{\pi} \exp\left(\frac{1}{2}|\alpha - \alpha_0|^2\right) \quad (2.28)$$

$$= \frac{2}{\pi} \exp\left(-\frac{1}{2}((x - x_0)^2 + (p - p_0)^2)\right), \quad (2.29)$$

where  $x = \text{Re}[\alpha]$  and  $p = \text{Im}[\alpha]$ .

### Squeezed State

For a squeezed state, the Wigner function is

$$W(x, p) = \frac{2}{\pi} \exp\left(-\frac{1}{2}((x - x_0)^2 e^{-2r} + (p - p_0)^2 e^{2r})\right), \quad (2.30)$$

where  $r$  is the squeezing parameter.

### Fock State

The Wigner function for a Fock state  $|n\rangle$  is

$$W(x, p) = \frac{2}{\pi} (-1)^n L_n(4(x^2 + p^2)) e^{-2(x^2 + p^2)}, \quad (2.31)$$

where  $L_n(y)$  is the Laguerre polynomial.

## 2.2 Qubit Formalism and Quantum Information

Classical computation and classical information revolve around the fundamental concept of a mathematical object called a *bit*<sup>1</sup>. A bit can be realised as a physical

---

<sup>1</sup>A *bit* is a binary digit.

system with two distinct states, 0 or 1. In quantum computation and quantum information, we make use of the analogous *quantum bit* or the *qubit*. A two-level system can be assigned the state  $|0\rangle$  or  $|1\rangle$ , where  $\{|0\rangle, |1\rangle\}$  is an orthonormal basis, which correspond to the classical states 0 and 1 [4]. An unusual property of the qubit is that it can also take on states which are in a *superposition* of  $|0\rangle$  and  $|1\rangle$ , a phenomenon that is a characteristic of quantum physics. Such a state can be written as a *linear combination* of states

$$|\psi\rangle = \alpha|0\rangle + \beta|1\rangle \quad (2.32)$$

where  $\alpha$  and  $\beta$  are complex numbers. The state  $|\psi\rangle$  is required to be a unit vector,  $\langle\psi|\psi\rangle = 1$ , therefore it is a requirement that  $|\alpha|^2 + |\beta|^2 = 1$ . This is often known as the *normalisation condition* for state vectors. We can also represent  $|\psi\rangle$  in vector form as

$$|\psi\rangle = \begin{bmatrix} \alpha \\ \beta \end{bmatrix} \quad \text{or} \quad \langle\psi| = [\alpha^* \ \beta^*]. \quad (2.33)$$

Alternatively, we can represent a state  $|\psi\rangle$  as a *density operator*

$$\rho = |\psi\rangle\langle\psi| \quad (2.34)$$

$$= (\alpha|0\rangle + \beta|1\rangle)(\alpha^*\langle 0| + \beta^*\langle 1|) \quad (2.35)$$

$$= |\alpha|^2|0\rangle\langle 0| + |\beta|^2|1\rangle\langle 1| + \alpha\beta^*|0\rangle\langle 1| + \alpha^*\beta|1\rangle\langle 0| \quad (2.36)$$

or as a *density matrix*

$$\rho = \begin{bmatrix} |\alpha|^2 & \alpha\beta^* \\ \alpha^*\beta & |\beta|^2 \end{bmatrix}. \quad (2.37)$$

The presence of off-diagonal elements in  $\rho$  is the defining feature of coherence. In a completely mixed state, there are no off-diagonal elements.

### 2.2.1 The Pauli Matrices

The *Pauli matrices* are  $2 \times 2$  matrices that are often used in quantum information and quantum computation. They can be used to make transformations on states and to represent observables. The Pauli matrices are

$$\begin{aligned} I &= \begin{bmatrix} 1 & 0 \\ 0 & 1 \end{bmatrix} & X &= \begin{bmatrix} 0 & 1 \\ 1 & 0 \end{bmatrix} \\ Y &= \begin{bmatrix} 0 & -i \\ i & 0 \end{bmatrix} & Z &= \begin{bmatrix} 1 & 0 \\ 0 & -1 \end{bmatrix}. \end{aligned} \quad (2.38)$$

$I$  is known as the *identity matrix* while  $X$  and  $Z$  are sometimes referred to as a *bit flip* and a *phase flip*, respectively.  $Y$  is equal to  $XZ$ , up to an overall, irrelevant phase, and can be thought of as both a *bit flip* and a *phase flip*. The Pauli matrices are Hermitian ( $H^\dagger = H$ ) and unitary ( $U^\dagger U = I$ ), which makes them useful in operator expansions.

### 2.2.2 Quantum Fidelity

In quantum information theory, the fidelity is a measure of the distance between two quantum states. The fidelity between two states  $\rho$  and  $\sigma$  is defined to be

$$F(\rho, \sigma) = \left( \text{Tr}[\sqrt{\rho^{1/2} \sigma \rho^{1/2}}] \right)^2. \quad (2.39)$$

If  $\sigma = |\psi\rangle\langle\psi|$  is a pure state, we can reduce equation 2.39 to a much simpler form

$$F(|\psi\rangle, \sigma) = \text{Tr}[\langle\psi|\sigma|\psi\rangle|\psi\rangle\langle\psi|] = \langle\psi|\sigma|\psi\rangle. \quad (2.40)$$

The fidelity ranges between 0 for orthogonal states and 1 for identical states. The fidelity will be used extensively throughout this thesis as a measure of success for various schemes. In such cases, the fidelity is usually taken between the desired ideal output state and the actual output state.

### 2.2.3 Quantum Entanglement

Entanglement is a property of a quantum mechanical state of two (or more) systems where the entangled state can not be written as a product state of its component systems. The Bell states, introduced in Section 2.2.4, are examples of maximally entangled states. Entanglement plays a crucial role in quantum information and computation, for example, in teleportation and superdense coding [4]. A number of methods exist to quantify entanglement of an entangled state. In this thesis, we use the entropy of entanglement, defined as

$$E(\rho) = -\text{Tr}[\rho \log_2 \rho]. \quad (2.41)$$

The entropy of entanglement is valid only for pure bipartite states. It ranges from 0 for a product state to  $\log_2 N$  for a maximally entangled state of two  $N$ -state particles.

### 2.2.4 Bell States

The Bell states are maximally entangled two-qubit states and are used extensively in quantum information and quantum computation. The four Bell states are

$$|\Phi^+\rangle_{AB} = \frac{1}{\sqrt{2}}(|0\rangle_A|0\rangle_B + |1\rangle_A|1\rangle_B), \quad (2.42)$$

$$|\Phi^-\rangle_{AB} = \frac{1}{\sqrt{2}}(|0\rangle_A|0\rangle_B - |1\rangle_A|1\rangle_B), \quad (2.43)$$

$$|\Psi^+\rangle_{AB} = \frac{1}{\sqrt{2}}(|0\rangle_A|1\rangle_B + |1\rangle_A|0\rangle_B), \quad (2.44)$$

$$|\Psi^-\rangle_{AB} = \frac{1}{\sqrt{2}}(|0\rangle_A|1\rangle_B - |1\rangle_A|0\rangle_B). \quad (2.45)$$

### 2.2.5 Quantum Teleportation

Quantum teleportation allows the transfer of an unknown quantum state from one party to another without the direct transfer of any quantum information between the two parties. The required resources are: a shared bipartite entangled state; an apparatus to distinguish the four Bell states and; a classical channel over which classical information can be sent.

Consider two parties, Alice and Bob. They both have one half of the Bell state  $|\Phi^+\rangle_{AB} = \frac{1}{\sqrt{2}}(|0\rangle_A|0\rangle_B + |1\rangle_A|1\rangle_B)$ , which will serve as their entangled resource state. Alice possesses an unknown qubit state  $|\phi\rangle_C = \alpha|0\rangle_C + \beta|1\rangle_C$  which she wants to transfer to Bob. The combined state of the system can be written as

$$|\psi\rangle = |\Phi^+\rangle_{AB}|\phi\rangle_C \quad (2.46)$$

$$= \frac{1}{\sqrt{2}} \left( \alpha|0\rangle_A|0\rangle_B|0\rangle_C + \alpha|1\rangle_A|1\rangle_B|0\rangle_C + \beta|0\rangle_A|0\rangle_B|1\rangle_C + \beta|1\rangle_A|1\rangle_B|1\rangle_C \right) \quad (2.47)$$

$$= \frac{1}{2} \left( |\Psi^+\rangle_{AC}(\alpha|0\rangle_B + \beta|1\rangle_B) + |\Psi^-\rangle_{AC}(\alpha|0\rangle_B - \beta|1\rangle_B) \right. \\ \left. + |\Phi^+\rangle_{AC}(\alpha|1\rangle_B + \beta|0\rangle_B) + |\Phi^-\rangle_{AC}(\alpha|1\rangle_B - \beta|0\rangle_B) \right) \quad (2.48)$$

Writing the combined state in the form shown in equation 2.48, we can see that if Alice were to measure the two qubits in her possession,  $A$  and  $C$ , in the Bell basis, she would project Bob's state into the original state  $\alpha|0\rangle_B + \beta|1\rangle_B$ , up to local single-qubit operation. The final step for Alice is to send a classical message to Bob advising him of which measurement result she obtained. With this knowledge, Bob knows which operations to apply to his state to recover the exact quantum state that Alice began with. These operations are  $I$ ,  $Z$ ,  $X$  and  $XZ$  (see Section 2.2.1), given the measurement results  $|\Psi^+\rangle_{AC}$ ,  $|\Psi^-\rangle_{AC}$ ,  $|\Phi^+\rangle_{AC}$  and  $|\Phi^-\rangle_{AC}$  respectively.

## 2.3 Quantum Optics

### 2.3.1 Coherent State Encoding for Optical Quantum Computing

In optics, the field of a laser is a good approximation to a classical sinusoidal wave and therefore, a coherent state of the simple harmonic oscillator, which describes an oscillating field. Consider two coherent states  $|\alpha\rangle$  and  $|\alpha\rangle$ . These states are not orthogonal, but their overlap  $\langle\alpha|\alpha\rangle = e^{-2|\alpha|^2}$  decreases exponentially with  $|\alpha|$  and for  $|\alpha| = 2$  is practically zero. We can encode our logical basis in these two states such that  $|0\rangle \equiv |\alpha\rangle$  and  $|1\rangle \equiv |\alpha\rangle$ , so that a general qubit state is represented by [34]

$$|\psi\rangle = \mu|0\rangle + \nu|1\rangle \equiv \mu|\alpha\rangle + \nu|\alpha\rangle. \quad (2.49)$$

### 2.3.2 Schrödinger Cat States

Schrödinger's cat paradox is a *gedankenexperiment* which emphasises the unusual consequences of extending the concept of superposition to macroscopically distinguishable objects [34]. A coherent state is the most "classical" of all quantum states, and a superposition of two macroscopically distinguishable, i.e. well-separated, coherent states is referred to as a *cat state*. Consider the states

$$|\text{even}\rangle = \mathcal{N}_+(|\alpha\rangle + |\alpha\rangle), \quad (2.50)$$

$$|\text{odd}\rangle = \mathcal{N}_-(|\alpha\rangle - |\alpha\rangle), \quad (2.51)$$

where  $\mathcal{N}_\pm = 1/\sqrt{2(1 \pm \exp(-2|\alpha|^2))}$ . These states are known as *even* and *odd cat states* because they contain only an even or odd number of photons

$$|\text{even}\rangle = 2\mathcal{N}_+ e^{-|\alpha|^2/2} \sum_{n=0}^{\infty} \frac{\alpha^{2n}}{\sqrt{2n!}} |2n\rangle, \quad (2.52)$$

$$|\text{odd}\rangle = 2\mathcal{N}_- e^{-|\alpha|^2/2} \sum_{n=0}^{\infty} \frac{\alpha^{2n+1}}{\sqrt{(2n+1)!}} |2n+1\rangle. \quad (2.53)$$

### 2.3.3 Photons as Fock States

We define the creation operator for a photon with a spectral distribution  $\psi(\omega)$  as [35, 36]:

$$\hat{A}_\psi^\dagger = \int d\omega \psi(\omega) \hat{a}^\dagger(\omega). \quad (2.54)$$

$\hat{A}_\psi^\dagger$  satisfies all the standard bosonic commutation relations, such as  $[\hat{A}_{\psi_k}, \hat{A}_{\psi_{k'}}^\dagger] = \delta_{k,k'}$ , where  $\psi_k(\omega)$  and  $\psi_{k'}(\omega)$  are orthogonal spectral functions, i.e.  $\int \psi_k(\omega)\psi_{k'}(\omega)d\omega = \delta_{k,k'}$ . An  $n$ -photon state can be written as a Fock state.

$$|n; \psi\rangle = \frac{1}{\sqrt{n!}}(\hat{A}_\psi^\dagger)^n|0\rangle. \quad (2.55)$$

We emphasise the distinction between the states  $\hat{A}_{\psi_k}^\dagger \hat{A}_{\psi_k}^\dagger|0\rangle = \sqrt{2}|2; \psi_k\rangle$  and  $\hat{A}_{\psi_k}^\dagger \hat{A}_{\psi_{k'}}^\dagger|0\rangle = |1; \psi_k\rangle|1; \psi_{k'}\rangle$  for  $k \neq k'$ , where the former is a two-photon Fock state and the latter consists of two single-photon Fock states.

### 2.3.4 Beamsplitters

A *beamsplitter* is a partially reflective optical element which reflects some of the incident light and transmits the rest (assuming no absorption). The amount of light reflected is represented by the intensity reflection coefficient  $\epsilon$ .

A beamsplitter can be modeled by the transformation

$$\hat{a}^\dagger \rightarrow \sqrt{\eta} \hat{c}^\dagger + \sqrt{1-\eta} \hat{d}^\dagger \quad (2.56)$$

$$\hat{b}^\dagger \rightarrow -\sqrt{1-\eta} \hat{c}^\dagger + \sqrt{\eta} \hat{d}^\dagger \quad (2.57)$$

where  $\hat{a}^\dagger$  and  $\hat{b}^\dagger$  represent the beamsplitter input modes,  $\hat{c}^\dagger$  and  $\hat{d}^\dagger$  represent the output modes, and  $\eta$  is the transmission probability.

The ‘ $-$ ’ sign comes from the choice of beamsplitter convention. The usual choice is to set three relative phases to zero and the fourth to  $\pi$ . The normal explanation is that one of the reflected waves has a phase shift of  $180^\circ$  with respect to all other waves [7], which is one choice of phase convention that satisfies conservation of energy.

## 2.4 Spontaneous Parametric Down-conversion

Spontaneous parametric down-conversion is a nonlinear optical process in which a photon from a pump laser, incident on a nonlinear birefringent crystal, converts into two single photons under conservation of energy and momentum. Typically, the down-converted photons are devised to be in orthogonal polarisation or spatially orthogonal modes.

### 2.4.1 Single Mode

Ignoring spectral properties, type-II up-<sup>2</sup> or down-conversion can be modeled in the interaction picture, where the evolution of the state vector is given by [6]

$$|\psi(t)\rangle = \exp(\kappa t(\hat{a}_i^\dagger \hat{a}_s^\dagger - \hat{a}_i \hat{a}_s)) |\psi(t_0)\rangle. \quad (2.58)$$

This gives the output of a SPDC<sup>3</sup>, in the number basis, as

$$|\psi_{\text{out}}\rangle = \frac{1}{\cosh(\kappa t)} \sum_{n=0}^{\infty} \tanh(\kappa t)^n |n\rangle_i |n\rangle_s, \quad (2.59)$$

where  $\kappa$  is the effective nonlinearity and is a function of the pump power and the properties of the nonlinear crystal and  $t$  is the interaction time. The output state is correlated in photon number.

### 2.4.2 Multi Mode

Assuming an undepleted pump which can be treated classically, we can take the multimode Hamiltonian to be [37]

$$\hat{H}(t) = \int_V d^3r \chi^{(2)} E_p^{(+)}(\mathbf{r}, t) \hat{E}_i^{(-)}(\mathbf{r}, t) \hat{E}_s^{(-)}(\mathbf{r}, t) + \text{H.c.}, \quad (2.60)$$

where  $V$  is the spatial mode volume in the waveguide and  $\hat{E}_j(\mathbf{r}, t) = \hat{E}_j^{(+)}(\mathbf{r}, t) + \hat{E}_j^{(-)}(\mathbf{r}, t)$  are the three interacting fields with  $j = p, i, s$  denoting the pump, idler and signal modes respectively.

$$E_p^{(+)}(z, t) = A_p \int d\omega_p \alpha(\omega_p) e^{i(k_p(\omega_p)z + \omega_p t)}, \quad (2.61)$$

$$\hat{E}_j^{(-)}(z, t) = \int d\omega_j A(\omega_j) \hat{a}^\dagger(\omega_j) e^{-i(k_j(\omega_j)z + \omega_j t)} \quad (2.62)$$

are the positive and negative frequency parts of the fields  $E_p(z, t)$  and  $\hat{E}_j(z, t)$  respectively, where  $\alpha(\omega_p) = \exp(-(\omega_p - \mu_p)^2 / 2\sigma_p)$  is the pump envelope function and we have restricted the spatial integral to be over only one dimension, i.e.  $z$ , and  $j = i, s$ . This Hamiltonian does not commute with itself at different times and therefore the evolution of the state vector should consider time ordering, giving the

<sup>2</sup>Upconversion is the reverse process of down-conversion.

<sup>3</sup>Note that an SPDC state of one spatio-spectral mode is exactly equivalent to a two-mode squeezed beam.

output state

$$|\psi(t)\rangle = \hat{\mathcal{U}}(t, t_0)|\psi(t_0)\rangle = \mathcal{T}e^{-\frac{i}{\hbar} \int_{t_0}^t dt' \hat{H}(t')} |\psi(t_0)\rangle, \quad (2.63)$$

where  $\mathcal{T}$  is the time-ordering operator. Recall from Section 2.1.2 that  $\hat{\mathcal{U}}(t, t_0)$  can be expanded into what is known as the Dyson series. We will assume that  $A(\omega_j)$  is slowly varying over the frequencies of interest and therefore we can bring it outside of the integral. We can now write

$$\hat{H}(t) = A \int_{-L/2}^{L/2} dz \int d\omega_i d\omega_s d\omega_p e^{-i\Delta k(\omega_i, \omega_s, \omega_p)z} e^{i\Delta\omega t} \alpha(\omega_p) \hat{a}_i^\dagger(\omega_i) \hat{a}_s^\dagger(\omega_s) + \text{H.c.}, \quad (2.64)$$

where  $L$  is the length of the crystal,  $A = \chi^{(2)} A_p A(\omega_i) A(\omega_s)$ ,  $\Delta k = k_i(\omega_i) + k_s(\omega_s) - k_p(\omega_p)$  is the phase mismatch and  $\Delta\omega = \omega_i + \omega_s - \omega_p$ . Evaluating the integral over  $z$  yields

$$\hat{H}(t) = AL \int d\omega_i d\omega_s d\omega_p \alpha(\omega_p) \Phi(\Delta k(\omega_i, \omega_s, \omega_p)) e^{i\Delta\omega t} \hat{a}_i^\dagger(\omega_i) \hat{a}_s^\dagger(\omega_s) + \text{H.c.}, \quad (2.65)$$

where

$$\Phi(\Delta k(\omega_i, \omega_s, \omega_p)) = \text{sinc}\left(\frac{1}{2}\Delta k(\omega_i, \omega_s, \omega_p)L\right) \quad (2.66)$$

is the phase-matching function and  $\text{sinc}(x) = \sin(x)/x$ . For a periodically poled waveguide (see the next section) of periodicity  $\Lambda$  and poling order  $m$ ,  $\Delta k(\omega_i, \omega_s, \omega_p) = k_i(\omega_i) + k_s(\omega_s) - k_p(\omega_p) + 2\pi/m\Lambda$  [38]. Note that by picking the spatial integration to be centered around  $z = 0$ , it is possible to eliminate a phase term which would normally be present in equation (2.65). The global phase can be disregarded if the subsequent measurements are insensitive to such a phase, e.g. photon-number measurements.

For a pulsed laser, we can assume that the pump field, and therefore the interaction Hamiltonian, is zero before  $t_0$  and after  $t$ . Therefore we can extend the limits of the integration over time to  $-\infty$  and  $\infty$  [39] such that

$$|\psi_{\text{PDC}}\rangle = \mathcal{T}e^{-\frac{i}{\hbar} \int_{-\infty}^{\infty} dt \hat{H}(t)} |\psi(t_0)\rangle. \quad (2.67)$$

Performing the time integral inside the exponent yields  $2\pi\delta(\omega_i + \omega_s - \omega_p)$  which then allows the  $\omega_p$  integral to be evaluated, giving

$$\int_{-\infty}^{\infty} dt \hat{H}(t) = 2\pi AL \int d\omega_i d\omega_s \alpha(\omega_i + \omega_s) \Phi(\omega_i, \omega_s) \times \hat{a}_i^\dagger(\omega_i) \hat{a}_s^\dagger(\omega_s) + \text{H.c.} . \quad (2.68)$$

where  $\Phi(\omega_i, \omega_s) = \Phi(\Delta k(\omega_i, \omega_s, \omega_i + \omega_s))$ .

Taking the first order term of the Taylor series<sup>4</sup> expansion of  $\hat{U}(t, t_0)|0\rangle$  and evaluating the time and pump frequency integrals yields the two-photon state

$$|\psi\rangle = \int \int d\omega_i d\omega_s \alpha(\omega_i + \omega_s) \Phi(\omega_i, \omega_s) \hat{a}_i^\dagger(\omega_i) \hat{a}_s^\dagger(\omega_s) |0\rangle . \quad (2.69)$$

### 2.4.3 Quasi Phase Matching

Consider a perfectly phase-matched crystal with a nonlinearity  $\chi$ . In such a crystal, the down-conversion intensity increases quadratically with the length of the crystal (solid black in Figure 2.1). If, however, the crystal happens to not be phase-matched, as is typically the case, the three interacting fields propagate through the crystal at different velocities, and therefore acquire a relative phase shift. This leads to a down-conversion intensity which oscillates—between zero and some greatly reduced maximum intensity—along the length of the crystal (red line in Figure 2.1).

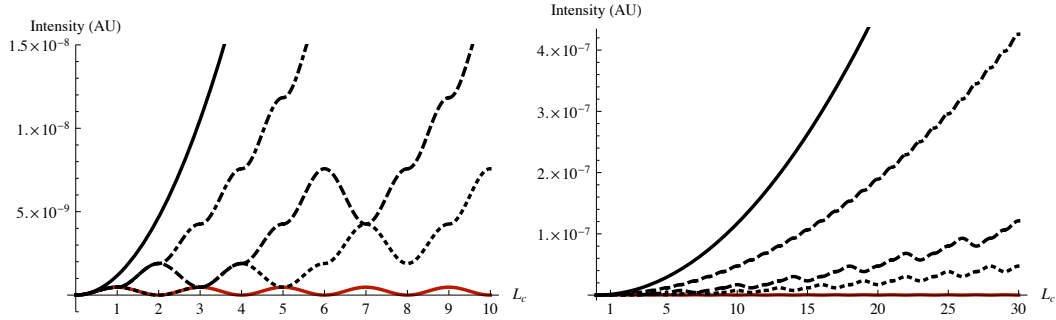


**Figure 2.1:** Intensity growth as a function of crystal length for a crystal with: critical phase matching (solid); first order QPM (dot-dashed); second order QPM (dashed); third order QPM (dotted); and no phase matching (red).

In quasi-phases matching (QPM), the nonlinear medium is inverted whenever the pump and down-converted fields acquire a phase mismatch  $\Delta k = 2\pi m/\Lambda$ —where  $m$  is

<sup>4</sup>Note that to first order, the Taylor and Dyson series are identical.

---

an odd integer—allowing phase-matching of a wide range of wavelengths in different nonlinear materials. In a quasi-phasematched crystal with a poling period  $\Lambda$  [38] the *effective* nonlinearity scales with the poling order as  $\chi_{\text{eff}} = \frac{2\chi}{\pi m}$ , as is shown in Figure 2.1. For odd  $m$ ,  $m$ th order QPM can be achieved by reversing the sign every  $m$  coherence lengths. Even order QPM can be achieved with the combination of two odd orders.



---

# Teleportation Using Squeezed Single Photons

---

Coherent state quantum computing (CSQC) [40, 41] is an optical approach to quantum computing which relies solely on linear optics, state preparation and measurement, rather than in-line optical nonlinearities. Unlike in single-photon linear optical quantum computing (LOQC) [18, 42]—where qubits are encoded in the polarisation, path, frequency etc. of single photons—in CSQC, qubits are encoded in the phase and amplitude of coherent states.

In both coherent-state and linear optical quantum computing, teleportation is used to implement gates using the concept of gate teleportation [43]. A key practical difference between the two schemes is that a simple teleportation scheme, with a high probability of success, exists for CSQC [44, 45], whilst simple LOQC teleportation only works with a 50% success rate [17]. More generally, in the KLM scheme [18] the probability of teleportation scales as  $n/(n + 1)$ , where  $n$  is the number of photons in the entangled state used as a resource and the complexity of the circuit increases with  $n$ . In CSQC the probability increases by simply increasing the amplitude of the inputs. This leads to a significant saving in the overheads for computation.

Due to the non-orthogonality of coherent state qubits, it was first believed that an amplitude of  $\alpha \geq 2$  was required to implement gates for quantum computing [46]. More recently, however, Lund *et al.* [41] presented a universal set of gates for quantum computing which work even for small amplitudes. In this scheme, the size of the coherent state has no effect on the fidelity of the gate—only on the probability with which the gate succeeds. Indeed, below a certain amplitude ( $\alpha \approx 1.2$ ), these gates could not be used for scalable quantum computing, as the probability of success would be too low, nevertheless the probability of success can still be significantly greater than the LOQC bound of 50%. Such heralded gates open the door to a range of exciting possibilities for proof-of-principle experimental implementation of coherent state quantum computing.

In performing these gates, the challenge does not lie in our ability to create large-

amplitude coherent states—these are very well approximated by the output of a laser. The difficulty arises from our inability to create *superpositions* of large-amplitude coherent states. Such coherent state superpositions, introduced in Section 2.3.2 as *cat states*, have not yet been experimentally realised.

However, small amplitude cat states (so-called *kitten states*) can be approximated—in some cases, very well—using photon-subtracted squeezed vacuum states [47]. Such states have already been experimentally demonstrated [21, 22].

In this chapter, we present an analysis of squeezed single-photon states as a resource for teleportation of coherent state qubits and propose proof-of-principle experiments for the demonstration of coherent-state teleportation and entanglement swapping. We include an analysis of the squeezed vacuum state as a simpler approximation to small-amplitude cat states. We also investigate the effects of imperfect sources and inefficient detection on the proposed experiments. We do not discuss approximations to kitten states via homodyne post-selection [48].

A photon-subtracted squeezed vacuum state is mathematically equivalent to a squeezed single-photon state. These terms will be used interchangeably, depending on context, throughout this chapter.

This chapter is organised as follows. In Section 3.1 we revisit the coherent-state teleportation protocol introduced in [44, 45]. In Section 3.2 we discuss approximations to cat states, in particular, the squeezed single-photon state. We then analyse how well these squeezed single-photon states perform, as resource states for the teleportation of arbitrary coherent state qubits, in Section 3.3. In Section 3.4, we propose experimentally realisable demonstrations of coherent-state teleportation using squeezed single photons. In Section 3.5, we analyse the effect of imperfect state preparation and inefficient detection on the teleportation scheme before we conclude and discuss our results in Section 3.6.

### 3.1 Coherent-state Teleportation

The quantum gates presented by Lund *et al.* [41] are all variations of the quantum teleportation scheme [44, 45, 16] shown in Figure 3.1. A general introduction to quantum teleportation can be found in Section 2.2.5. We will use this teleportation scheme as the basis for our proof-of-principle experiments. We define the qubit basis  $|0\rangle = |\alpha\rangle$  and  $|1\rangle = |-\alpha\rangle$  where

$$|\alpha\rangle = e^{-|\alpha|^2/2} \sum_{n=0}^{\infty} \frac{\alpha^n}{\sqrt{n!}} |n\rangle \quad (3.1)$$

is a coherent state of amplitude  $\alpha$ . This basis is only approximately orthogonal where  $\langle\alpha|-\alpha\rangle = e^{-2|\alpha|^2}$ , however, for  $|\alpha| > 2$ , the overlap is practically zero ( $< 4 \times 10^{-4}$ ).

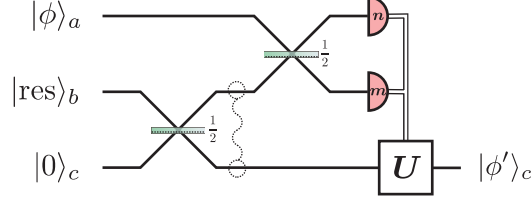


**Figure 3.1:** Teleportation scheme for teleporting the state  $|\phi\rangle_a = \mu|\alpha\rangle_a + \nu|-\alpha\rangle_a$ . A resource state,  $|\text{res}\rangle_b = |\beta\rangle_b \pm |-\beta\rangle_b$ , incident on a 50 : 50 beamsplitter, creates a coherent-state Bell pair in modes  $b$  and  $c$ . After the second beamsplitter, photon-number measurements of modes  $a$  and  $b$  project the state in mode  $c$  into  $|\phi'\rangle_c = |\phi\rangle_a$  (up to local unitaries). Depending on the measurement results, the remaining qubit may need to be corrected, as shown in Table 3.1. For experimental realisation of this scheme,  $|\text{res}\rangle_b = \hat{S}_r|1\rangle_b$  and  $|\phi\rangle_a = |\alpha\rangle_a$ ,  $\hat{S}_{r'}|1\rangle_a$  or  $\hat{S}_{r''}|0\rangle_a$ , where  $r = r_{\text{opt}}(\beta)$ ,  $r' = r_{\text{opt}}(\alpha)$ ,  $r'' = r_{\text{opt-v}}(\alpha)$  and  $\beta = \sqrt{2}\alpha$  (refer to Section 3.4). The squiggly line emphasizes entanglement between qubits.

In this chapter, we will use the convention that  $\alpha$  refers to the initial amplitude of the input states in mode  $a$  while  $\beta$  refers to the initial amplitude of the resource states in mode  $b$  and  $\beta = \sqrt{2}\alpha$ . To teleport an arbitrary coherent-state qubit of amplitude  $\alpha$ , we use an odd cat state of amplitude  $\beta$  as a resource state. The combined input state can therefore be written as

$$|\psi_{\text{in}}\rangle_{a,b,c} = |\phi\rangle_a |\text{res}\rangle_b |0\rangle_c \quad (3.2)$$

$$= (\mu|\alpha\rangle_a + \nu|-\alpha\rangle_a) (|\beta\rangle_b - |-\beta\rangle_b) |0\rangle_c. \quad (3.3)$$

The first beamsplitter, turns the resource state in mode  $b$  into a coherent-state Bell pair in modes  $b$  and  $c$ .

$$|\psi_{\text{BS}}\rangle_{a,b,c} = (\mu|\alpha\rangle_a + \nu|-\alpha\rangle_a) (|\alpha\rangle_b |\alpha\rangle_c - |-\alpha\rangle_b |-\alpha\rangle_c). \quad (3.4)$$

After the second beamsplitter, just before the photon number measurement, the three-mode state is

$$|\psi\rangle_{a,b,c} = \mu|\beta\rangle_a |0\rangle_b |\alpha\rangle_c - \mu|0\rangle_a |\beta\rangle_b |-\alpha\rangle_c + \nu|0\rangle_a |-\beta\rangle_b |\alpha\rangle_c - \nu|-\beta\rangle_a |0\rangle_b |-\alpha\rangle_c. \quad (3.5)$$

From equation (3.5), it can be seen that photon-number measurements of modes  $a$  and  $b$  will project the state in mode  $c$  into  $\mu|\alpha\rangle_c + \nu|-\alpha\rangle_c$ , or some known variation, which can be corrected with single-qubit Pauli operations (refer to Section 2.2.1), as shown in Table 3.1. In practice, only the  $X$  correction (which is simply implemented using a phase shifter) needs to be performed for gate applications [34]. Here we assume corrections are done after detection of the output state. This is called

$m$	$n$	$U$
0	odd	$I$
odd	0	$X$
0	even	$Z$
even	0	$XZ$

**Table 3.1:** An example of corrections for the teleportation scheme shown in Figure 3.1, having used an odd cat state as a resource.

“working in the *Pauli frame*” [49].

Looking back at equation 3.1, we can see that a coherent state contains a  $|0\rangle$  component. This can lead to the detection of zero photons in both modes  $a$  and  $b$  of the state in equation 3.5, in which case, the teleportation fails. Increasing the amplitude of the coherent state increases the probability of successful teleportation, as the probability of a  $|0\rangle$  component in a coherent state decreases. Figure 3.2 (solid lines) shows the success probabilities for a selection of input states which range between two extremities. Notice that in the unique case where  $|\phi\rangle_a = |\alpha\rangle_a - |-\alpha\rangle_a$ , the protocol never fails. This is because the odd cat state is a superposition of only odd photon-number components, and therefore does not contain a  $|0\rangle$ , as we will see in the next section. While the probability of success varies for different input states, when the gate succeeds, it does so with unity fidelity.

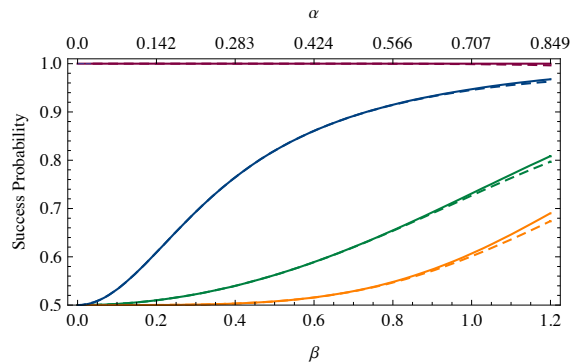


**Figure 3.2:** Success probabilities of the teleportation scheme shown in Figure 3.1 using  $|\text{res}\rangle = |\beta\rangle - |-\beta\rangle$  (solid) and  $|\text{res}\rangle = \hat{S}_r|1\rangle$  (dashed), as discussed in Section 3.3. The unnormalised input states are (from top to bottom):  $|\alpha\rangle - |-\alpha\rangle$  (red);  $\frac{1}{2}|\alpha\rangle - \frac{\sqrt{3}}{2}|-\alpha\rangle$  (blue);  $|\alpha\rangle$  or  $|-\alpha\rangle$  (green); and  $|\alpha\rangle + |-\alpha\rangle$  (yellow). Notice that the success probability is always larger than that of the LOQC scheme which can not succeed more than half of the time.

## 3.2 Approximating Cat States

While simple and elegant in theory, cat states are notoriously difficult to generate experimentally. In this section, we discuss experimentally realisable methods for generating good approximations to cat states. We use the fidelity,  $F(\rho, |\phi\rangle) = \langle \phi | \rho | \phi \rangle$  (see Section 2.2.2), as a measure of similarity between two states, and therefore a measure of how well these generated states approximate the desired cat states. The fidelity ranges between 0, where the states are orthogonal, and 1, where the states are equal.

Consider even and odd cat states of amplitude  $\beta$  [6]

$$|\text{even cat}\rangle = N_+(|\beta\rangle + |-\beta\rangle) \quad (3.6)$$

$$= N_+ e^{-\frac{1}{2}|\beta|^2} \sum_{n=0}^{\infty} \frac{2\beta^{2n}}{\sqrt{2n!}} |2n\rangle, \quad (3.7)$$

$$|\text{odd cat}\rangle = N_-(|\beta\rangle - |-\beta\rangle) \quad (3.8)$$

$$= N_- e^{-\frac{1}{2}|\beta|^2} \sum_{n=0}^{\infty} \frac{2\beta^{2n+1}}{\sqrt{(2n+1)!}} |2n+1\rangle, \quad (3.9)$$

where  $N_{\pm} = 1/\sqrt{2(1 \pm e^{-2|\beta|^2})}$ . By writing the cat states in the Fock basis, we see that the even and odd cat state contain only even and odd photon-number terms respectively.

Now consider the squeezed vacuum state

$$\hat{S}_r|0\rangle = \sum_{n=0}^{\infty} \frac{(\tanh r)^n}{\sqrt{\cosh r}} \frac{\sqrt{2n!}}{2^n n!} |2n\rangle, \quad (3.10)$$

where  $r$  is the squeezing parameter, which also contains only even photon-number terms. The squeezed vacuum state is a Gaussian state, but nevertheless it is a high-fidelity ( $F > 0.99$ ) approximation to the small-amplitude ( $\beta < 0.75$ ) even cat state. Optimising over  $r$ , we find that the fidelity between  $|\beta\rangle + |-\beta\rangle$  and  $\hat{S}_r|0\rangle$  is at a maximum when  $r_{\text{opt-v}}(\beta) = \log\left(\sqrt{2\beta^2 + \sqrt{1 + 4\beta^4}}\right)$ . Figure 3.3 (a) shows how this fidelity and the optimum amount of squeezing  $r$  vary as a function of  $\beta$ .

If one photon is subtracted from the squeezed vacuum state, the resulting state—also known as a squeezed single-photon state—contains only odd photon number terms and is a high-fidelity ( $F > 0.99$ ) approximation to the small-amplitude ( $\beta < 1.2$ ) odd cat state [50].

$$\hat{a}\hat{S}_r|0\rangle = \hat{S}_r|1\rangle = \sum_{n=0}^{\infty} \frac{(\tanh r)^n}{(\cosh r)^{3/2}} \frac{\sqrt{(2n+1)!}}{2^n n!} |2n+1\rangle. \quad (3.11)$$

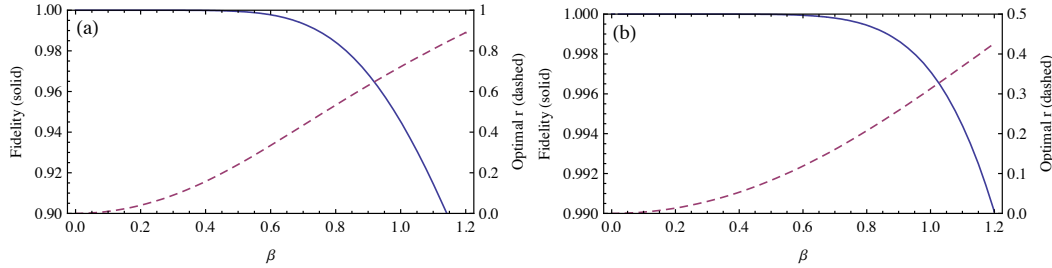


**Figure 3.3:** (a) The fidelity between an even cat state and a squeezed vacuum state (solid) and the optimal squeezing parameter,  $r$  (dashed), as a function of  $\beta$ . (b) The fidelity between an odd cat state and a squeezed single photon (solid) and the optimal squeezing parameter,  $r$  (dashed), as a function of  $\beta$ . Note different scales for the fidelity and the optimum squeezing parameter.

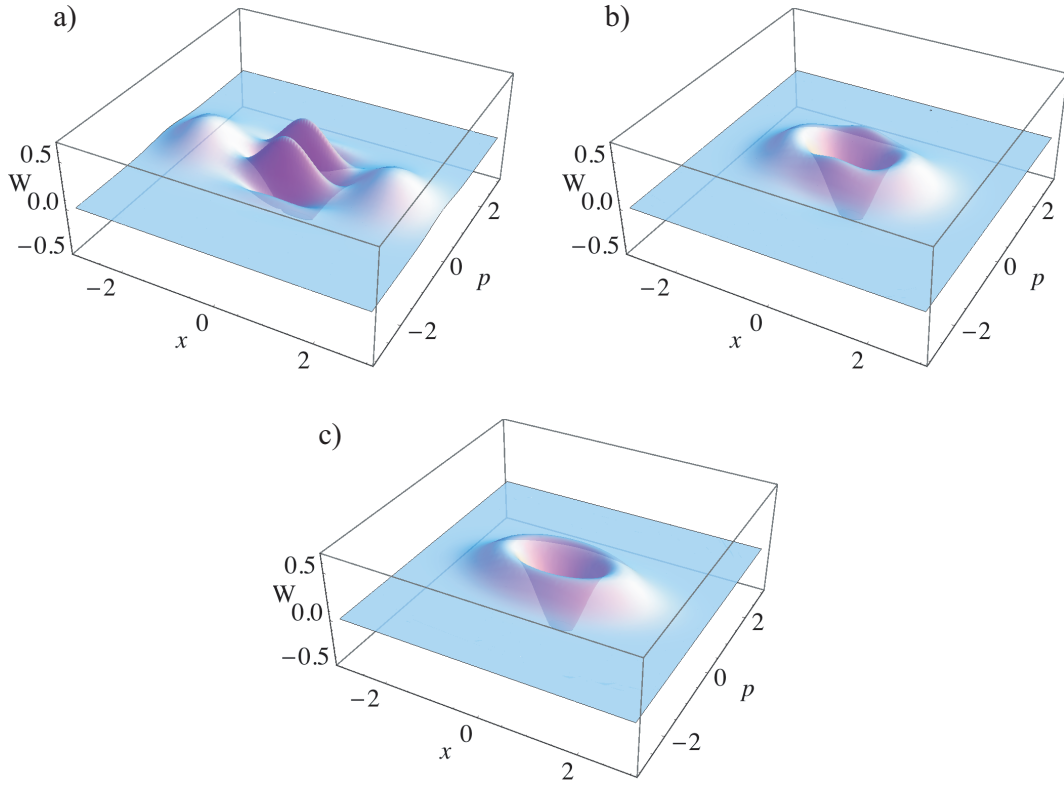
Optimising over  $r$ , we find that the fidelity between  $|\beta\rangle - |-\beta\rangle$  and  $\hat{S}_r|1\rangle$  is at a maximum when  $r_{\text{opt}}(\beta) = \log\left(\sqrt{\frac{2\beta^2}{3} + \frac{1}{3}\sqrt{9 + 4\beta^4}}\right)$ .

Figure 3.3 (b) shows how this fidelity and the optimum amount of squeezing  $r$  vary as a function of  $\beta$ . Figure 3.4 shows the Wigner functions (defined in Section 2.1.9) for odd cat states of amplitudes  $\beta = 2$  and  $\beta = 1$ , as well as for a squeezed single photon.

One can continue to subtract more photons, each time creating a better approximation to either an even or an odd cat state, however this very quickly becomes extraordinarily challenging to implement experimentally. A theoretical analysis of this method was performed in references [50, 51].

In this chapter, we focus on the squeezed single photon, as it is a better cat-state approximation than the squeezed vacuum state, and has already been experimentally demonstrated [21, 22]. However, we include results for the squeezed vacuum state for comparison and to see just how well one can do with a Gaussian state. In the next section, we investigate the eligibility of the squeezed single-photon state as an approximation to an odd cat state, for the purposes of proof-of-principle implementation of the quantum teleportation described in [41].

We emphasize that it should not be taken for granted that a high-fidelity approximation to a cat state will necessarily perform well in CSQC protocols. Take the example of the cat breeding protocol introduced by Lund *et al.* and Jeong *et al.* [47, 52]. Using this scheme, it is possible to create larger cat states by interfering two smaller cat states on a beam splitter, then performing a measurement on one of the output modes. When a squeezed vacuum state is used as an approximation to an even cat state in this protocol, the resultant state is not the expected approx-



**Figure 3.4:** The Wigner function,  $W$ , where  $x$  and  $p$  are the in-phase and out-of-phase quadratures respectively, for a) an odd cat state  $|\beta\rangle - |-\beta\rangle$  where  $\beta = 2$ , b) an odd cat state where  $\beta = 1$  and c) a squeezed single photon  $\hat{S}_r|1\rangle$  where  $r = r_{\text{opt}}(1) \approx 0.31$ . Notice that at  $\beta = 1$ , the Wigner functions for the cat state looks very much like for the squeezed single photon. This becomes more pronounced at even lower  $\beta$ . In the limit of  $\beta \rightarrow 0$ , the odd cat state becomes an unsqueezed single photon.

imation to a larger cat state, but rather the same sized squeezed vacuum state that was input into the scheme. This is in spite of the high fidelity between the squeezed vacuum and the even cat state at small  $\alpha$ .

### 3.3 Squeezed Single-photon State as a Resource

In this section, we will examine how well coherent-state teleportation can be implemented using a squeezed single photon as a resource. In the previous section, we showed that the squeezed single photon is a very good approximation to a small-amplitude odd cat state (and that the squeezed vacuum is also a good approximation to an even cat state, but at smaller amplitudes). To characterise how well the  $\hat{S}_r|1\rangle$

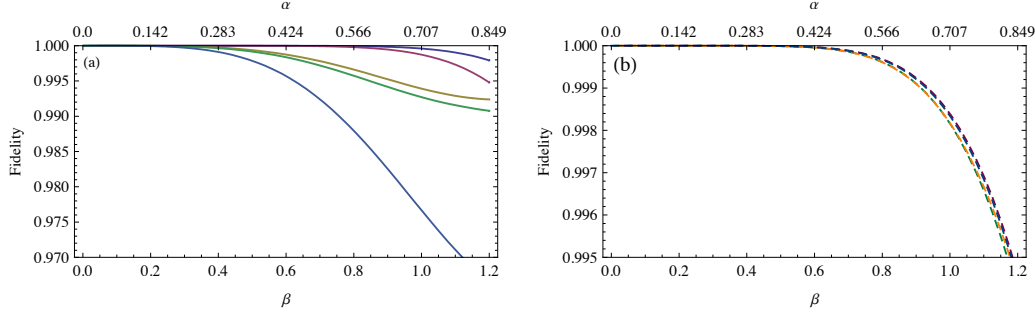


**Figure 3.5:** (a) Fidelities for the teleportation of  $|\phi\rangle_a = |\alpha\rangle - |-\alpha\rangle$  using  $|\text{res}\rangle_b = \hat{S}_r|1\rangle$  given different photon-number measurement results, (from top to bottom)  $m = 1, 2, 3, 4$  and 5. (b) Fidelities for the teleportation scheme using  $|\text{res}\rangle_b = \hat{S}_r|1\rangle$  and a variety of unnormalised input states (from top to bottom):  $|\alpha\rangle - |-\alpha\rangle$  (red);  $\frac{1}{2}|\alpha\rangle + \frac{\sqrt{3}}{2}|-\alpha\rangle$  (blue);  $|\alpha\rangle + |-\alpha\rangle$  (yellow); and  $|\alpha\rangle$  or  $|-\alpha\rangle$  (green). The input state has only a minor effect on the fidelity.

theoretically performs as a resource for teleportation, we will calculate the fidelity  $F(|\phi\rangle_a, |\phi'\rangle_c)$  between the input state  $|\phi\rangle_a$  and the output state  $|\phi'\rangle_c$ .

Since our resource state is only approximate, we will not have perfect interference at the beamsplitters. This will have three consequences. The first will be variations in the output state depending on the number of photons detected. This leads to variations in the fidelity between the actual and desired output states, as demonstrated in Figure 3.5(a). By taking into account the different possible output states and the probability with which we expect them to occur, we can calculate the *average* fidelity. One reason for this variation in fidelities, given different photon-number measurement results, is due to  $r$  being optimised to maximise the fidelity between  $|\text{res}\rangle_b = \hat{S}_r|1\rangle$  and  $|\text{res}\rangle_b = |\beta\rangle - |-\beta\rangle$ . This will maximise the average fidelity for the teleporter, but not the individual fidelities for each different photon-number result.

The second consequence of the imperfect interference will result in different input states being teleported with different fidelities, as demonstrated in Figure 3.5(b). This is only a small effect. Notice that in both cases the fidelity drops as a function of  $\alpha$ . This is solely due to the inadequacy of the  $\hat{S}_r|1\rangle$  as an approximation to an odd cat state at high amplitudes, and not an artifact of the gate itself.

The third consequence of the imperfect interference will be an additional way in which the gate can fail. Not only will it fail if we measure zero photons in both detectors, it will also fail if we measure a non-zero number of photons in *both* detectors simultaneously, something which was not possible when we had perfect interference. This will result in a slightly decreased probability of success, which begins to manifest itself at larger amplitudes whereas the  $m = n = 0$  events are only problematic

at low amplitudes. This is shown by the dashed curves in Figure 3.2 in Section 3.1.

One might expect that the squeezed single photon will only be as good a resource as it is an approximation to an odd cat state. It is interesting to note that it is actually better. A squeezed single photon  $\hat{S}_r|1\rangle$  will have a certain fidelity when compared with an odd cat state  $|\beta\rangle - |-\beta\rangle$ , however, using that resource for teleporting  $|\phi\rangle_a = |\alpha\rangle - |-\alpha\rangle$  results in teleportation with a higher fidelity for a given  $\beta$ . For example, for  $\beta = 1$ , the squeezed single photon has a fidelity of 0.9972 with an odd cat state, however using it as a resource state, the fidelity of the teleported state with the ideal state is 0.9984.

In the next section, we will look at teleporting physically realisable input states.

### 3.4 Proposed Experiments

In the previous section, we demonstrated that a squeezed single photon could be, in theory, a resource for teleportation of arbitrary superpositions of small-amplitude coherent states, however, at present, we are unable to create such superpositions. In this section we propose two types of experiment. The first is the teleportation of three particular examples states: a squeezed single photon as an approximation to an odd cat state; a squeezed vacuum as an approximation to an even cat state; and a coherent state. The second is an entanglement swapping scheme which demonstrates the effective teleportation of an arbitrary superposition of coherent states. In our calculations, the photon-number expansion of the states in this section were truncated at  $n = 15$ , which was sufficient for accurate results up to  $\beta = 1.2$ .

#### 3.4.1 Teleportation

We demonstrate coherent-state teleportation by using the resource state  $|\text{res}\rangle = \hat{S}_r|1\rangle$  to teleport the following input states: a squeezed single photon  $\hat{S}_{r'}|1\rangle$  as an approximation to an odd cat state  $|\alpha\rangle - |-\alpha\rangle$ ; a squeezed vacuum state  $\hat{S}_{r''}|0\rangle$  as an approximation to an even cat state  $|\alpha\rangle + |-\alpha\rangle$ ; and a coherent state  $|\alpha\rangle$ .

To teleport a squeezed single photon  $\hat{S}_{r'}|1\rangle$  using another squeezed single photon  $\hat{S}_r|1\rangle$ , we need to match the optimal squeezing parameters  $r$  and  $r'$ . This can be achieved by relating the squeezed single photons to the odd cat states they are intended to approximate. This gives  $r = r_{\text{opt}}(\beta)$  and  $r' = r_{\text{opt}}(\alpha)$ , where  $\beta = \sqrt{2}\alpha$ . We have calculated the fidelity averaged over only the odd photon-number results. For even results, a  $Z$  correction is required, which would involve sending the output state through another gate, making a meaningful comparison between the input and output states of the teleporter difficult. Allowing for the  $X$  correction is easy as it simply corresponds to a  $\pi$  phase shift. All further fidelities shown in this section have also been averaged over odd photon-number results, for consistency. We also

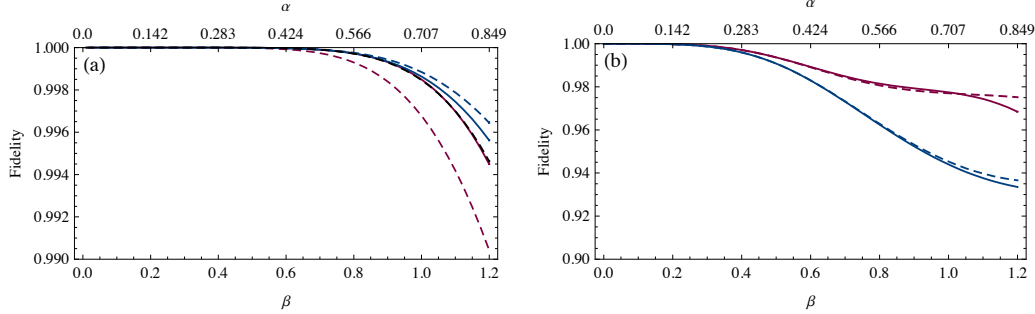


**Figure 3.6:** (a) Fidelities for teleportation using  $|\text{res}\rangle_b = \hat{S}|1\rangle_r$  and teleporting (solid, from top to bottom):  $|\phi\rangle_a = |\alpha\rangle - |-\alpha\rangle$ ; and  $|\phi\rangle_a = |\alpha\rangle + |-\alpha\rangle$  as well as: (dashed, from top to bottom)  $|\phi\rangle_a = \hat{S}_{r'}|1\rangle_a$ ;  $|\phi\rangle_a = |\alpha\rangle_a$ ; and  $|\phi\rangle_a = \hat{S}_{r''}|0\rangle_a$ . (b) Fidelities for teleportation using  $|\text{res}\rangle_b = \hat{S}_r|0\rangle_a$  and teleporting (solid, from top to bottom):  $|\phi\rangle_a = |\alpha\rangle + |-\alpha\rangle$ ; and  $|\phi\rangle_a = |\alpha\rangle - |-\alpha\rangle$  as well as: (dashed, from top to bottom)  $|\phi\rangle_a = \hat{S}_{r''}|0\rangle_a$ ; and  $|\phi\rangle_a = \hat{S}_{r'}|1\rangle_a$ . Notice different scales for the fidelity.

calculated the fidelity for teleporting  $|\phi\rangle_a = |\alpha\rangle_a - |-\alpha\rangle_a$  using  $|\text{res}\rangle_b = \hat{S}_r|1\rangle_b$ . Both results are shown in Figure 3.6 (a). For easy comparison with other figures, we have plotted the fidelity as a function of the effective  $\beta$  for the squeezed single photon, rather than the squeezing parameter  $r$ .

To teleport the squeezed vacuum state, we set  $r'' = r_{\text{opt-v}}(\alpha)$ . The fidelities for teleporting  $\hat{S}_{r''}|0\rangle$  and  $|\alpha\rangle + |-\alpha\rangle$  are also shown in Figure 3.6 (a), as is the fidelity for teleporting  $|\phi\rangle = |\alpha\rangle$ .

While there is some variation in the fidelity for the different input states, in the region where  $\beta < 1.2$ , the fidelity is always  $> 0.99$ , even when we teleport the squeezed vacuum state.

Using the squeezed vacuum state as a resource for teleportation, however, does not do as well. This is because the resource state needs to be higher in amplitude than the input state and the squeezed vacuum is not as good an approximation to an even cat state at higher amplitudes. To achieve fidelities  $> 0.99$ , we can only use  $\beta < 0.5$ . These results are shown in Figure 3.6 (b). It is interesting to note that when using the squeezed vacuum state as a resource, the fidelities for teleportation do not follow the general trends of the fidelity between the ideal and approximate resource, as is the case with using the squeezed single photon as a resource.

### 3.4.2 Entanglement Swapping

To truly demonstrate a teleportation protocol, one would like to demonstrate that the protocol is capable of teleporting an unknown arbitrary coherent-state qubit.

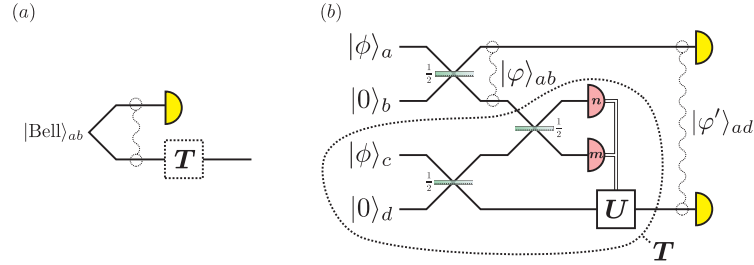


**Figure 3.7:** (a) By measuring mode  $a$  of a Bell state in an arbitrary basis, an arbitrary state can be prepared in mode  $b$ . This arbitrary state can be subsequently sent through a teleporter,  $T$ . (b) Replacing the teleporter  $T$  with the teleporter described in Figure 3.1 and delaying the measurement of mode  $a$ , until *after* the teleportation, results in an entanglement swapping scheme analogous to (a), where the Bell state is created by sending the state  $|\phi\rangle_a$  through a beam splitter and the teleporter consists of the circuit inside the dotted region. By teleporting one qubit in the Bell state before measuring the other qubit in that Bell state, we are effectively teleporting all possible states. The homodyne measurements on modes  $a$  and  $d$  can be performed at the end in the form of state tomography. The squiggly lines represent entanglement between qubits.

This is made possible by casting the teleportation of an arbitrary unknown state into an entanglement swapping scheme. Refer to the caption in Figure 3.7 for details.

To characterise how well this protocol works, we calculate the fidelity between the two-qubit entangled state in modes  $a$  and  $b$ , after the first beamsplitter, and the two-qubit entangled state in modes  $a$  and  $d$ , after the photon number measurements of modes  $b$  and  $c$ . In our calculations, as with the teleportation scheme, we have omitted the even photon-number results. The average fidelity, over the odd photon-number results, is shown in Figure 3.8. At first glance, it looks like the entanglement swapping protocol does not work as well as the teleportation scheme. This is because, in the teleportation scheme, for a given resource state of amplitude  $\beta$ , the input state to be teleported would have an amplitude  $\alpha$  and the cat state approximations are much better at lower amplitudes. For the entanglement swapping scheme, we begin with two states of amplitude  $\beta$ , which means we are already starting with lower fidelity approximations. Nevertheless, for  $\beta < 1.2$ , the fidelity is always  $> 0.99$ .

The state  $|\psi\rangle_{ab}$  will be maximally entangled in the case where  $|\phi\rangle_a$  is either an odd cat state or a squeezed-single-photon state. The maximum fidelity between a maximally entangled bipartite state and an arbitrary separable bipartite state is  $F = 0.5$ . Therefore, given a fidelity above 0.5, we can infer that the entanglement swapping scheme has preserved some amount of entanglement.

Using a squeezed vacuum state to approximate an even cat state does not perform as well. To achieve fidelities of  $> 0.99$ , we could only use  $\beta < 0.45$ .

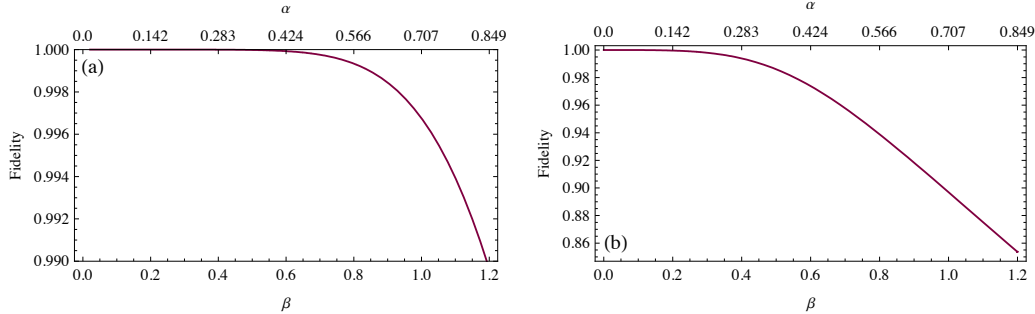


**Figure 3.8:** Fidelity for an entanglement swapping protocol using: (a)  $|\phi\rangle = \hat{S}_{r'}|1\rangle$ ; and (b)  $|\phi\rangle = \hat{S}_{r''}|0\rangle$ . Notice different scales for the fidelity.

### 3.5 Error Analysis

Until now, we have been treating the proposed experiments as lossless systems, however, propagation loss, imperfect detectors and loss in the source are likely to be issues in an experiment. In this section, we investigate the effects of loss in the proposed experiment.

Errors could occur in a number of places: the state to be teleported and the resource state could be made imperfectly; there could be photon loss at the optical elements; and of course, inefficient photon number and homodyne detection. In this chapter, we assume that imperfect creation of the state to be teleported and any inefficiencies in the homodyne detection of the output state reflect our inability to analyse how well the scheme worked and are not fundamental to the scheme itself. These errors can be compensated for in the post measurement analysis of the data. The calculations in this section were further complicated by additional loss modes, therefore, it was necessary to limit the size of  $\beta$ . The photon-number expansion of the states in this section were truncated at  $n = 6$  for the teleportation scheme and  $n = 5$  for the entanglement swapping scheme which gave accurate results up to  $\beta = 1$  and  $\beta = 0.5$  respectively.

#### 3.5.1 Teleportation

We model the imperfect creation of the resource state by placing a beamsplitter of transmittivity  $\eta_1$  just after the source and the inefficient photo-detection by placing beamsplitters of transmittivity  $\eta_2$  just before the detectors, as is shown in Figure 3.9. We assume that both detectors will have the same inefficiencies.  $\eta_i$  ranges from 0 to 1 and at  $\eta_i = 1$ , we have a lossless system. Our loss calculations have been carried out for the same scenario as in Section 3.4, however, the loss in mode  $b$  will

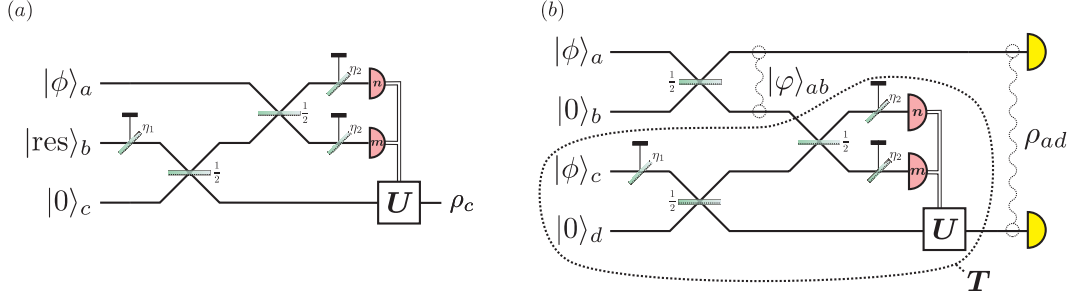


**Figure 3.9:** Teleportation scheme (a) and entanglement swapping scheme (b) with additional beam splitters of transmittivity:  $\eta_1$  to model the imperfect creation of the resource state  $|\text{res}\rangle_b = \hat{S}_r|1\rangle_b$  and;  $\eta_2$  to model the inefficiencies in the photo-detectors. The input state is  $|\phi\rangle_a = \hat{S}_{r'}|1\rangle_a$  where  $r' = r_{\text{opt}}(\sqrt{\eta_1}\alpha)$  for the teleportation scheme and  $r' = r_{\text{opt}}(\sqrt{\eta_1}\beta)$  for the entanglement swapping scheme to match the amplitude of the lossy resource state.

decrease the amplitude of the resource state  $|\text{res}\rangle_b = \hat{S}_r|1\rangle_b$  by  $\sqrt{\eta_1}$ . To match this, our states to be teleported will need to be  $|\phi\rangle_a = |\sqrt{\eta_1}\alpha\rangle_a$ ,  $\hat{S}_{r'}|1\rangle_a$  and  $\hat{S}_{r''}|0\rangle_a$  where  $r' = r_{\text{opt}}(\sqrt{\eta_1}\alpha)$  and  $r'' = r_{\text{opt-v}}(\sqrt{\eta_1}\alpha)$ . Figure 3.10 shows the fidelity as a function of  $\eta_1$  and  $\eta_2$  using  $|\text{res}\rangle_b = \hat{S}_r|1\rangle_b$  and teleporting  $|\phi\rangle_a = \hat{S}_{r'}|1\rangle_a$  (a) and  $|\sqrt{\eta_1}\alpha\rangle_a$  (b) for  $\beta = 0.5$  (solid) and  $\beta = 1.0$  (dashed). As expected, loss has less effect on the fidelity at lower  $\beta$ , unfortunately, for  $|\phi\rangle_a = \hat{S}_{r'}|1\rangle_a$ , decreasing  $\beta$  does not improve the fidelity in the high-fidelity regime where one would like to perform experiments. Teleporting  $|\phi\rangle_a = |\sqrt{\eta_1}\alpha\rangle_a$  is largely unaffected by loss. At both amplitudes, the fidelity remains extremely high.

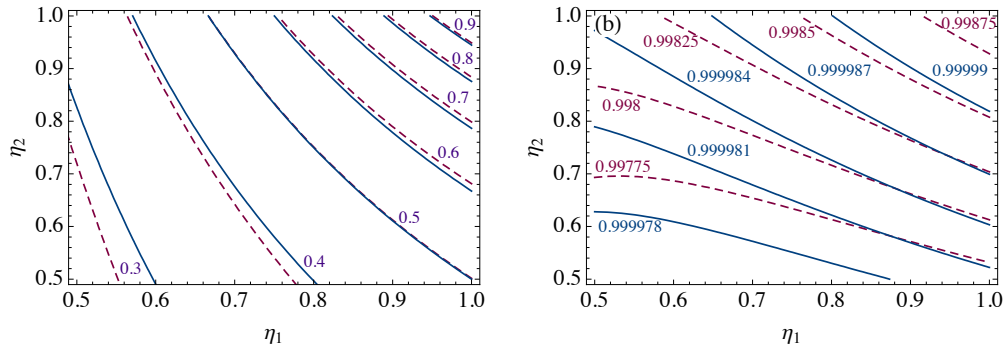


**Figure 3.10:** Contour plots of the fidelity for the teleportation scheme as a function of  $\eta_1$  and  $\eta_2$  for  $\beta = 0.5$  (solid) and  $\beta = 1.0$  (dashed): (a)  $|\text{res}\rangle = \hat{S}_r|1\rangle$  and  $|\phi\rangle = \hat{S}_{r'}|1\rangle$ ; (b)  $|\text{res}\rangle = \hat{S}_r|1\rangle$  and  $|\phi\rangle = |\sqrt{\eta_1}\alpha\rangle$ .

To compare these fidelities with those for other states, we have taken a slice through the contour plots at  $\eta_1 = \eta_2$  and plotted the fidelity as a function of the equal losses. This is shown in Figure 3.11. We have calculated the fidelity for teleporting a selection of ideal input states using both an ideal odd cat state and the squeezed single photon approximation as resources. Where possible, we have also teleported approximations to the ideal input states. This was done for  $\beta = 0.5$  and  $\beta = 1.0$ . This gives an idea of how much of the effect of loss is inherent to the scheme and how much is a result of the approximate input and resource states. At  $\beta = 0.5$ , it is difficult to distinguish between the results for any of these variations between ideal and approximate input and resource states. At this amplitude, the effects of loss are fundamental to the scheme itself. It is interesting to note that for  $|\phi\rangle_a = \hat{S}_{r'}|1\rangle_a$  (or

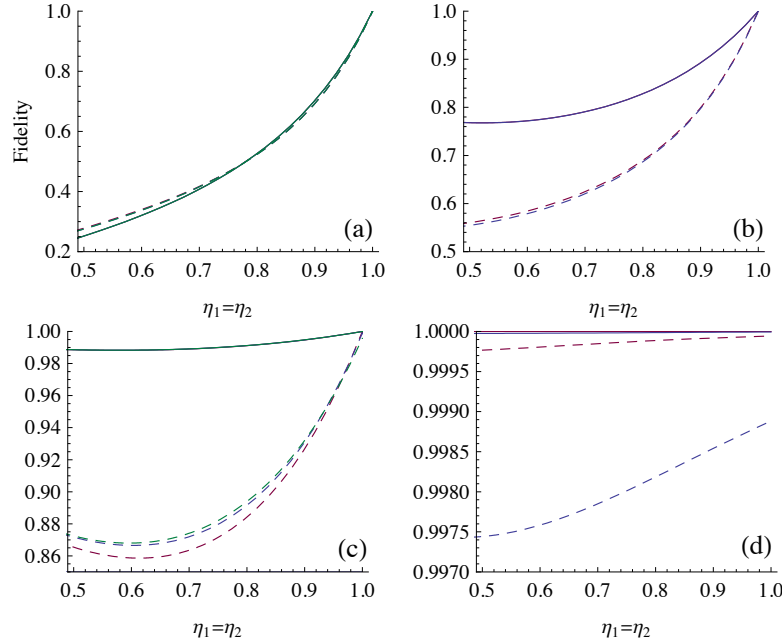


**Figure 3.11:** The fidelity for the teleportation scheme as a function of  $\eta_1$  and  $\eta_2$  where  $\eta_1 = \eta_2$  for  $\beta = 0.5$  (solid) and  $\beta = 1.0$  (dashed). (a)  $|\text{res}\rangle = |\beta\rangle - |-\beta\rangle$  and  $|\phi\rangle = |\alpha\rangle - |-\alpha\rangle$  (red),  $|\text{res}\rangle = \hat{S}_r|1\rangle$  and  $|\phi\rangle = |\alpha\rangle - |-\alpha\rangle$  (blue) and  $|\text{res}\rangle = \hat{S}_{r'}|1\rangle$  and  $|\phi\rangle = \hat{S}_{r'}|1\rangle$  (green). The fidelities for these states are so similar, they are practically indistinguishable. (b) From top to bottom,  $|\text{res}\rangle = |\beta\rangle - |-\beta\rangle$  and  $|\phi\rangle = \frac{1}{2}|\alpha\rangle - \frac{\sqrt{3}}{2}|-\alpha\rangle$  (red) and  $|\text{res}\rangle = \hat{S}_r|1\rangle$  and  $|\phi\rangle = \frac{1}{2}|\alpha\rangle - \frac{\sqrt{3}}{2}|-\alpha\rangle$  (blue). For  $\alpha = 0.5$ , the fidelities are also practically indistinguishable. (c) From top to bottom,  $|\text{res}\rangle = \hat{S}_r|1\rangle$  and  $|\phi\rangle = \hat{S}_r|0\rangle$  (green),  $|\text{res}\rangle = \hat{S}_r|1\rangle$  and  $|\phi\rangle = |\alpha\rangle + |-\alpha\rangle$  (blue) and  $|\text{res}\rangle = |\beta\rangle - |-\beta\rangle$  and  $|\phi\rangle = |\alpha\rangle + |-\alpha\rangle$  (red). Again, practically indistinguishable at  $\alpha = 0.5$ . (d) From top to bottom,  $|\text{res}\rangle = |\beta\rangle - |-\beta\rangle$  and  $|\phi\rangle = |\alpha\rangle$  (red) and  $|\text{res}\rangle = \hat{S}_r|1\rangle$  and  $|\phi\rangle = |\alpha\rangle$  (blue). Notice different scales for the fidelity.

$|\phi\rangle_a = |\alpha\rangle_a - |-\alpha\rangle_a$ , in the limit of  $\eta_1 \rightarrow 0$ , the input state amplitude is matched such that  $\alpha \rightarrow 0$ , in which case, the input state becomes  $|\phi\rangle_a \rightarrow |1\rangle_a$  and the output state will be  $|\phi'\rangle_c = |0\rangle_c$  resulting in a fidelity which goes to 0. However, for any other input state, as  $\eta_1 \rightarrow 0$ , the input state will tend to  $|\phi\rangle_a \rightarrow |0\rangle_a$ . The output state will still be  $|\phi'\rangle_c = |0\rangle_c$  resulting in a fidelity which goes to 1. This is why the loss seems to have a greater effect on the fidelity for teleporting  $|\phi\rangle_a = \hat{S}_{r'}|1\rangle_a$  and  $|\phi\rangle_a = |\alpha\rangle_a - |-\alpha\rangle_a$  than any other state.

Increasing the amplitude to  $\beta = 1.0$  does not have much effect on teleporting the odd cat state (and its approximations), but it does decrease the fidelity for the other states. In attempting high-fidelity experiments, low loss levels will be essential when teleporting states similar to  $|\phi\rangle_a = \hat{S}_{r'}|1\rangle_a$  and  $|\phi\rangle_a = |\alpha\rangle_a - |-\alpha\rangle_a$ . States closer to  $|\phi\rangle_a = |\alpha\rangle_a + |-\alpha\rangle_a$ ,  $|\phi\rangle_a = |\alpha\rangle_a$  and their approximations are more forgiving.

### 3.5.2 Entanglement Swapping

In the entanglement swapping protocol, we treat modes  $a$  and  $b$  as the input state to the teleporter and ignore loss in these modes in the analysis of the effects of loss on the teleporter, which has been modeled in much the same way as in Section 3.5.1 (see Figure 3.9 (b)). We were only able to compute reliable fidelities for  $\beta = 0.5$  as higher values of  $\beta$  would require higher truncation of the photon number which, for a 7-mode calculation, was not computationally tractable. These fidelities are shown in Figure 3.12.

At this amplitude, we can see that there is not much difference between performing the entanglement swapping with an ideal odd cat state or the squeezed single photon.

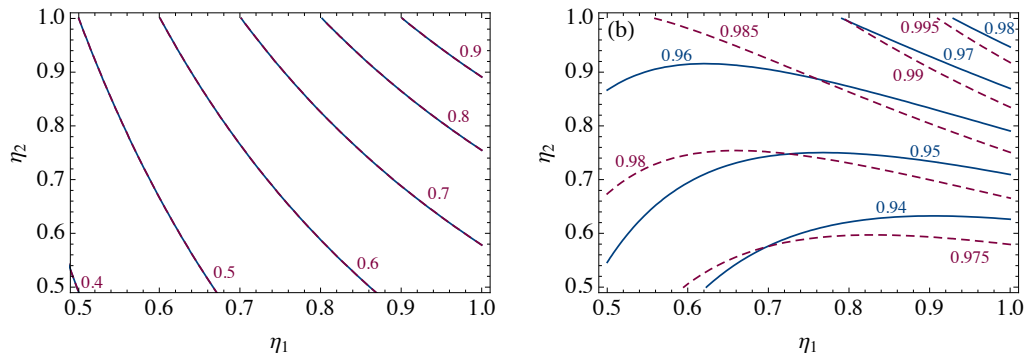


**Figure 3.12:** Contour plots of the fidelity for the entanglement swapping scheme as a function of  $\eta_1$  and  $\eta_2$  for  $\beta = 0.5$  where: (a)  $|\phi\rangle = |\alpha\rangle - |-\alpha\rangle$  (dashed) and  $|\phi\rangle = \hat{S}_{r'}|1\rangle$  (solid); and (b)  $|\phi\rangle = |\alpha\rangle + |-\alpha\rangle$  (dashed) and  $|\phi\rangle = \hat{S}_{r'}|0\rangle$  (solid).

Both are quite severely affected by loss. The ideal even cat is much more tolerant to loss whereas the squeezed vacuum is less so, however still better than the odd cat and squeezed single photon.

### 3.6 Discussion

The squeezed single photon turns out to be a great resource for high-fidelity teleportation of small-amplitude coherent state superpositions. Due to its property of always containing at least one photon, the teleportation scheme will always succeed with a probability greater than 50%. We have shown that the squeezed single photon can be used to teleport a coherent state, a squeezed single photon and a squeezed vacuum, which despite not being a very good resource for teleportation itself, is a good approximation to an even cat state at very small amplitudes. In-principle teleportation of arbitrary coherent state superpositions can be demonstrated using squeezed single photons as inputs to an entanglement swapping protocol. This also works with high fidelity at small amplitudes. Teleportation is the implementation of the identity gate and these results suggest that demonstration of more complicated non-trivial gates will be practical in the foreseeable future.

Our analysis of the effects of imperfect source preparation and inefficient detection has shown this setup to be very fragile in this regard. It would be possible to do high-fidelity teleportation of states like the coherent state and the even cat state with a lossy system, but states which are more similar to the odd cat state degrade very quickly, even with low loss. It looks like this fragility is a property of the gate, and not just the approximation of the states, however, at higher amplitudes, the fidelity is further affected by loss when using the approximate states.

In this chapter we have analysed coherent-state teleportation using small-amplitude approximations to cat states, however, there has been progress in creating larger amplitude cat state approximations via cat state amplification [47, 52] and ancilla-assisted photon-subtraction [53].

---

# Optimised Generation of Heralded Fock States Using Spontaneous Parametric Down-conversion

---

The generation of heralded pure Fock states via spontaneous parametric down-conversion (SPDC) relies on perfect photon-number correlations in the output modes. Correlations in any other degree of freedom, however, degrade the purity of the heralded state. In this chapter, we investigate spectral entanglement between the two output modes of a periodically poled waveguide. With the intent of generating heralded 1- and 2-photon Fock states, we expand the down-converted state to second order in photon number. We explore the effects of spectral filtering and inefficient detection, of the heralding mode, on the count rate,  $g^{(2)}$  and purity of the heralded state, as well as the fidelity between the resulting state and an ideal Fock state.

This chapter is structured as follows. In Section 4.2, we introduce spectral notation for photon states as well as a theoretical model of spectral effects in SPDC. In Section 4.3 we introduce spectral filtering. In Section 4.4 we present analytical results for the probability of detecting a single photon in the heralding detector, the heralded output state, its  $g^{(2)}$  and purity, as well as the maximum fidelity between the heralded output state and an ideal pure state. In Section 4.5, we present similar results for the generation of two-photon Fock states. In sections 4.6 and 4.7, we illustrate these results using realistic parameters. In Section 4.8 we discuss our results.

Finally, a note on nomenclature. In our theoretical calculations, we have a preference for using frequency (as opposed to wavelength) due to its direct relationship to energy conservation in SPDC, however, we have made an attempt to also present our results in nanometers (nm), for readers who are accustomed to “thinking in wavelengths”.

All frequencies quoted in this chapter are *angular frequencies* in units of  $\text{s}^{-1}$ . When describing Gaussian filters and beam profiles, we will specify the central frequency and Gaussian standard deviation in  $\text{s}^{-1}$  as well as the central wavelength and the FWHM<sup>1</sup> in nm.

## 4.1 Single-photon Sources

Pure photon Fock states, in particular, single-photon states, are useful for many quantum-optical applications, including quantum information, quantum computing and quantum cryptography [54, 42]. Some novel uses for photon-number states include the generation of other non-Gaussian states, such as Schrödinger kitten states [21, 48], as described in Chapter 3. A common method for creating single-photon states makes use of spontaneous parametric down-conversion (refer to section 2.4). The detection of a single photon in one spatial mode (idler) heralds the presence of another single photon in the other spatial mode (signal). In practice, however, given high enough pump power, the presence of higher order photon-number terms in the output state can lead to a photon-number mixed state in the signal mode, when inefficient detectors mistake two (or more) photons for one.

Energy conservation ensures that the frequencies of the down-converted photons always sum to the pump frequency. For CW pumped down-conversion, these correlations cannot be avoided, but pulsed pump light allows this constraint to be weakened. Strong spectral correlations are another potential source of mixedness—the signal state is projected into a spectrally mixed state when a frequency-insensitive detector heralds a single photon in the signal mode. In the context of single-mode versus multi-mode descriptions [55, 35] this property can also be interpreted as projecting the single photon onto different distinguishable broadband spectral modes [28]. In recent years, there has been a growing effort in engineering pulsed SPDC sources to produce photons uncorrelated in frequency, i.e. those with a separable joint spectral amplitude (JSA). Some examples include manipulating the crystal length, material, bandwidth and central frequency [23, 24, 25, 26, 27, 28, 29, 30, 31, 32] as well as filtering the pump field, prior to down-conversion, using an optical cavity [56]. Another promising technique produces a source of counter-propagating photons with a separable JSA [57].

In the rest of this chapter, we investigate spectral entanglement between the two output modes of a periodically poled waveguide, with the intent of generating heralded 1- and 2-photon Fock states.

---

<sup>1</sup>Full width at half maximum.

## 4.2 Spontaneous Parametric Down Conversion

Consider the output state of a spontaneous parametric down-conversion process, as introduced in Section 2.4.2.

$$|\psi_{\text{PDC}}\rangle = \mathcal{T} e^{-\frac{i}{\hbar} \int_{-\infty}^{\infty} dt \hat{H}(t)} |\psi(t_0)\rangle, \quad (4.1)$$

where  $\mathcal{T}$  is the time-ordering operator and  $\hat{H}(t)$  is defined in equation 2.65.  $\hat{U}(t_0, t)$  can be expanded into what is known as the Dyson series. In Chapter 6, we show that the Taylor and Dyson series expansions of equation 6.1 produce the same results to second order, and therefore, we can safely expand  $\hat{U}(t_0, t)$  as a Taylor series. A description of multiple pair creation in degenerate SPDC has also been analysed in the Heisenberg picture by Wasilewski *et al.* [58] and Maurerer [59].

Following Grice and Walmsley [37], we Taylor expand the phase mismatch to first order such that  $\Delta k \approx \Delta k^{(0)} + k'_s \nu_s + k'_i \nu_i - k'_p \nu_p$  where  $\nu_j = \omega_j - \mu_j$ ,  $k'_j = \partial k_j(\omega)/\partial \omega|_{\omega=\mu_j}$  and  $\mu_j$  is the center frequency of a photon in mode  $j$ . We set  $\mu_i = \mu_s = \mu$  and  $\mu_p = 2\mu$ . We can achieve perfect phase-matching by picking the poling periodicity  $\Lambda$  such that  $\Delta k^{(0)} = k_s(\mu_s) + k_i(\mu_i) - k_p(\mu_p) = 2\pi/\Lambda$  and therefore  $\Delta k \approx k'_s \nu_s + k'_i \nu_i - k'_p \nu_p$ .

To consider contributions from the 2-photon components of the down-converted state, we take the Taylor series expansion of the unitary evolution operator in equation (6.1) to second order (disregarding the time-ordering operator):

$$\hat{U}(t_0, t) \approx 1 + \frac{1}{i\hbar} \int_{-\infty}^{\infty} dt_1 \hat{H}(t_1) + \frac{1}{2(i\hbar)^2} \int_{-\infty}^{\infty} dt_2 \hat{H}(t_2) \int_{-\infty}^{\infty} dt_3 \hat{H}(t_3). \quad (4.2)$$

This gives the truncated down-converted state

$$\begin{aligned} |\psi_{\text{PDC}}\rangle = N \bigg\{ & (1 + \chi^2) |0\rangle + \chi \int \int d\omega_i d\omega_s f(\omega_i, \omega_s) \hat{a}_i^\dagger(\omega_i) \hat{a}_s^\dagger(\omega_s) |0\rangle \\ & + \frac{\chi^2}{2} \int \int d\omega_i d\omega_s f(\omega_i, \omega_s) \hat{a}_i^\dagger(\omega_i) \hat{a}_s^\dagger(\omega_s) \\ & \times \int \int d\omega'_i d\omega'_s f(\omega'_i, \omega'_s) \hat{a}_i^\dagger(\omega'_i) \hat{a}_s^\dagger(\omega'_s) |0\rangle \bigg\}, \end{aligned} \quad (4.3)$$

where  $\chi = 2\pi AL/i\hbar$  and  $N$  is defined in equation (4.7). The joint spectral amplitude (JSA) is given by

$$f(\omega_i, \omega_s) = N_f \alpha(\omega_i + \omega_s) \Phi(\omega_i, \omega_s), \quad (4.4)$$

where  $\alpha(\omega_i + \omega_s)$  is the pump envelope function and  $\Phi(\omega_i, \omega_s)$  is the phase matching function (PMF), as defined in section 2.4.2, and the normalisation parameter  $N_f$  is chosen such that  $\int d\omega_i d\omega_s |f(\omega_i, \omega_s)|^2 = 1$ .

Any well-behaved complex function can always be decomposed in terms of a discrete basis of orthonormal functions (a well known example is the basis of Hermite functions). This is known as the Schmidt decomposition.

$$f(\omega_s, \omega_i) = \sum_k b_k \xi_k(\omega_s) \zeta_k(\omega_i), \quad (4.5)$$

where the Schmidt modes  $\xi_k(\omega_s)$  and  $\zeta_k(\omega_i)$  are normalised and may be complex and the Schmidt coefficients  $b_k$  are real and  $\sum_k |b_k|^2 = 1$ , if  $f(\omega_s, \omega_i)$  is normalised. It is useful to write the down-converted state in terms of the Schmidt decomposition (refer to Table 4.1 for creation operator definitions).

$$\begin{aligned} |\psi_{\text{PDC}}\rangle = N \left\{ (1 + \chi^2) |0\rangle + \chi \sum_k b_k \hat{A}_{s\xi_k}^\dagger \hat{A}_{i\zeta_k}^\dagger |0\rangle \right. \\ \left. + \frac{\chi^2}{2} \sum_{k,k'} b_k b_{k'} \hat{A}_{s\xi_k}^\dagger \hat{A}_{s\xi_{k'}}^\dagger \hat{A}_{i\zeta_k}^\dagger \hat{A}_{i\zeta_{k'}}^\dagger |0\rangle \right\}, \end{aligned} \quad (4.6)$$

where  $\xi_k(\omega_i)$  are the Schmidt modes for the idler state and  $\zeta_k(\omega_s)$  are the Schmidt modes for the signal state and

$$N = \left\{ |1 + \chi^2|^2 + |\chi|^2 + |\chi|^4 \left( \sum_{\substack{k,k' \\ k < k'}} |b_k b_{k'}|^2 + \sum_k |b_k|^4 \right) \right\}^{-1/2}. \quad (4.7)$$

Notice, in the four-photon term of equation (4.6), when two photons are created in the same spectral mode (i.e.  $k = k'$ ) there will be a factor of  $\sqrt{2}$  in front of each two-photon Fock state, increasing the probability of down-conversion into such a state. This can be understood due to stimulation effects in the PDC process itself. To take account of this, equation (4.6) can also be written as

$$\begin{aligned} |\psi_{\text{PDC}}\rangle = N \left\{ (1 + \chi^2) |0\rangle + \chi \sum_k b_k |1; \xi_k\rangle_s |1; \zeta_k\rangle_i \right. \\ \left. + \chi^2 \left( \sum_k b_k^2 |2; \xi_k\rangle_s |2; \zeta_k\rangle_i + \sum_{\substack{k,k' \\ k < k'}} b_k b_{k'} |1; \xi_k\rangle_s |1; \xi_{k'}\rangle_s |1; \zeta_k\rangle_i |1; \zeta_{k'}\rangle_i \right) \right\}. \end{aligned} \quad (4.8)$$

We can characterise the spectral entanglement of the JSA by using the entropy of entanglement [60]. The entropy of entanglement can be defined, for the bi-partite state

$$|\Psi\rangle = \sum_k b_k |1; \xi_k\rangle |1; \zeta_k\rangle, \quad (4.9)$$

Creation Operator	Spectral Mode	State	Description
$\hat{A}_{i\zeta_k}^\dagger$	$\zeta_k(\omega_i)$	$ 1; \zeta_k\rangle_i$	initial idler Schmidt modes
$\hat{A}_{s\xi_k}^\dagger$	$\xi_k(\omega_s)$	$ 1; \xi_k\rangle_s$	initial signal Schmidt modes
$\hat{C}_{T\zeta_k}^\dagger$	$T(\omega_i)\zeta_k(\omega_i)$	$ 1; T\zeta_k\rangle_i$	filtered idler modes
$\hat{D}_{R\zeta_k}^\dagger$	$R(\omega_i)\zeta_k(\omega_i)$	$ 1; R\zeta_k\rangle_i$	reflected filtered idler modes
$\hat{C}_{\phi_j}^\dagger$	$\phi_j(\omega_i)$	$ 1; \phi_j\rangle_i$	orthog. filtered idler modes
$\hat{D}_{\varphi_j}^\dagger$	$\varphi_j(\omega_i)$	$ 1; \varphi_j\rangle_i$	orthog. reflected filtered idler modes
$\hat{A}_{i\tau_k}^\dagger$	$\tau_m(\omega_s)$	$ 1; \tau_m\rangle_s$	diag. single-photon signal modes

**Table 4.1:** Summary of multi-mode creation operators, spectral modes and states, some of which will be introduced in subsequent sections.

in terms of the Schmidt values:

$$E(|\Psi\rangle) = - \sum_k b_k^2 \log_2(b_k^2). \quad (4.10)$$

The entropy of entanglement is valid only for pure bipartite states and, when defined in terms of the Schmidt decomposition, can not be applied to the entire output state in equation (4.8). However, we can apply it to the two-photon term to get some information about the spectral entanglement arising only from the JSA. The entropy of entanglement ranges from zero for a product state to  $\log_2 N$  for a maximally entangled state of two  $N$ -state particles, which in our case corresponds to a state containing  $N$  orthogonal spectral modes. In the limit of a maximally entangled JSA, the entropy of entanglement would approach infinity.

### 4.3 Spectral Filtering

A spectral filter can be modeled as a frequency dependent beam-splitter:

$$\hat{a}^\dagger(\omega) \rightarrow \tilde{T}(\omega)\hat{c}^\dagger(\omega) + \tilde{R}(\omega)\hat{d}^\dagger(\omega), \quad (4.11)$$

where  $|\tilde{T}(\omega)|^2$  and  $|\tilde{R}(\omega)|^2$  are the transmitted and reflected probabilities and  $|\tilde{T}(\omega)|^2 + |\tilde{R}(\omega)|^2 = 1$ . In addition to the filter, we consider an inefficient detector which we model by a beam splitter of reflectivity  $1 - \eta$ , followed by a perfect detector (refer to Figure 4.1 in Section 4.4). If the reflected mode of the filter and the reflected mode of the beamsplitter are to be traced out, the filter-beamsplitter combination can be modeled by a filter with the following transformation:

$$\hat{a}^\dagger(\omega) \rightarrow T(\omega)\hat{c}^\dagger(\omega) + R(\omega)\hat{d}^\dagger(\omega), \quad (4.12)$$

where  $T(\omega) = \tilde{T}(\omega)\sqrt{\eta}$  and  $R(\omega) = \sqrt{1 - |\tilde{T}(\omega)|^2\eta}$ . In terms of the mode functions  $\zeta_k$ , this can be written as

$$\hat{A}_{\zeta_k}^\dagger \rightarrow T_{\zeta_k} \hat{C}_{T\zeta_k}^\dagger + R_{\zeta_k} \hat{D}_{R\zeta_k}^\dagger \quad (4.13)$$

where we have defined

$$T_{\zeta_k} = \sqrt{\int d\omega |T(\omega)\zeta_k(\omega)|^2}, \quad (4.14)$$

$$R_{\zeta_k} = \sqrt{\int d\omega |R(\omega)\zeta_k(\omega)|^2}, \quad (4.15)$$

$$\hat{C}_{T\zeta_k}^\dagger = \frac{1}{T_{\zeta_k}} \int d\omega T(\omega)\zeta_k(\omega)\hat{c}^\dagger(\omega), \quad (4.16)$$

$$\hat{D}_{R\zeta_k}^\dagger = \frac{1}{R_{\zeta_k}} \int d\omega R(\omega)\zeta_k(\omega)\hat{d}^\dagger(\omega). \quad (4.17)$$

The definitions in equations (4.14)-(4.17) ensure that the creation operators for the filtered modes satisfy the commutation relations  $[\hat{C}_{T\zeta_k}, \hat{C}_{T\zeta_k}^\dagger] = 1$  and  $[\hat{D}_{R\zeta_k}, \hat{D}_{R\zeta_k}^\dagger] = 1$ . However, the filtered functions  $T\zeta_k(\omega_s)$  no longer define proper modes because the functions  $\zeta_k(\omega_s)T(\omega_s)$  are, in general, not orthogonal to the functions  $\zeta_{k'}(\omega_s)T(\omega_s)$  for  $k \neq k'$  and therefore need to be orthogonalised (eg. using the Gram-Schmidt procedure) such that

$$T_{\zeta_k} \hat{C}_{T\zeta_k}^\dagger |0\rangle = \sum_j u_{kj} \hat{C}_{\phi_j}^\dagger |0\rangle, \quad (4.18)$$

$$R_{\zeta_k} \hat{D}_{R\zeta_k}^\dagger |0\rangle = \sum_j v_{kj} \hat{D}_{\varphi_j}^\dagger |0\rangle, \quad (4.19)$$

where  $\phi_j(\omega_i)$  are now the new modes defining the idler state and  $\varphi_j(\omega_i)$  are the reflected modes that will be traced out, and

$$u_{kj} = \int d\omega \phi_j(\omega)^* \zeta_k(\omega) T(\omega) = T_{\zeta_k} \langle 1; \phi_j | 1; T\zeta_k \rangle, \quad (4.20)$$

$$v_{kj} = \int d\omega \varphi_j(\omega)^* \zeta_k(\omega) R(\omega) = R_{\zeta_k} \langle 1; \varphi_j | 1; R\zeta_k \rangle. \quad (4.21)$$

The filter relationship in equation (4.13) can also be written as follows:

$$\hat{A}_{\zeta_k}^\dagger \rightarrow \sum_j \left( u_{kj} \hat{C}_{\phi_j}^\dagger + v_{kj} \hat{D}_{\varphi_j}^\dagger \right). \quad (4.22)$$

Because the filter has been modeled as a frequency dependent beamsplitter, it will have similar properties to a beamsplitter. One such property is the possibility to

allow one photon, from an incident two-photon state, to pass through the filter while rejecting the other. Detection of a filtered two-photon state may then result in, even, a perfect detector mistaking it for a one-photon state.

## 4.4 Generating Single-photon Fock States

Detection of a single photon in the idler mode heralds the presence of a single photon in the signal mode. In this section, we consider a hypothetical perfect detector, an inefficient detector and a Gaussian spectral filter placed in front of the lossy detector. We model the generation of two-photon Fock states in section 4.5.

### 4.4.1 Case 1: Perfect Detection in the Triggering Idler Mode

The projector for a detector that perfectly distinguishes photon number, but gains no information about the frequency of the photon can be written as follows:

$$\Pi_1 = \int d\omega \hat{a}^\dagger(\omega)|0\rangle \langle 0|\hat{a}(\omega) = \sum_j |1; \zeta_j\rangle \langle 1; \zeta_j|. \quad (4.23)$$

We can interpret this as: the detection of a single photon  $\hat{a}^\dagger(\omega)|0\rangle$ , however due to the lack of spectral knowledge,  $\omega$  must be integrated over; or alternatively, the detection of a single photon in the spectral mode  $|1; \zeta_j\rangle$ , however due to the lack of knowledge about which mode it was in, it is necessary to sum over  $j$ . Since photon detection is destructive, the detected mode must be traced out. The probability of detecting a single photon in the idler mode using a perfect single-photon detector (refer to Figure 4.1(a)), is

$$p_1 = \langle \Psi_{\text{PDC}} | \Pi_1 | \Psi_{\text{PDC}} \rangle = |N|^2 |\chi|^2. \quad (4.24)$$

Given a single-photon detection in the idler mode, the heralded signal state is

$$\rho_1 = \frac{1}{p_1} \text{Tr}_i [\Pi_1 | \Psi_{\text{PDC}} \rangle \langle \Psi_{\text{PDC}} |] = \sum_k |b_k|^2 |1; \xi_k\rangle_s \langle 1; \xi_k|. \quad (4.25)$$

The  $g^{(2)}$ , defined in equation 2.25, is effectively a measure of the joint photocount probability of detecting the arrival of two photons at a particular time. Given the definition of the probability in equation 4.23, the multimode normalised second order correlation function can be defined as

$$g^{(2)} = \frac{\sum_{j,j'} \langle \hat{A}_{\xi_j}^\dagger \hat{A}_{\xi_j'}^\dagger \hat{A}_{\xi_j} \hat{A}_{\xi_j'} \rangle}{\left( \sum_j \langle \hat{A}_{\xi_j}^\dagger \hat{A}_{\xi_j} \rangle \right)^2}. \quad (4.26)$$

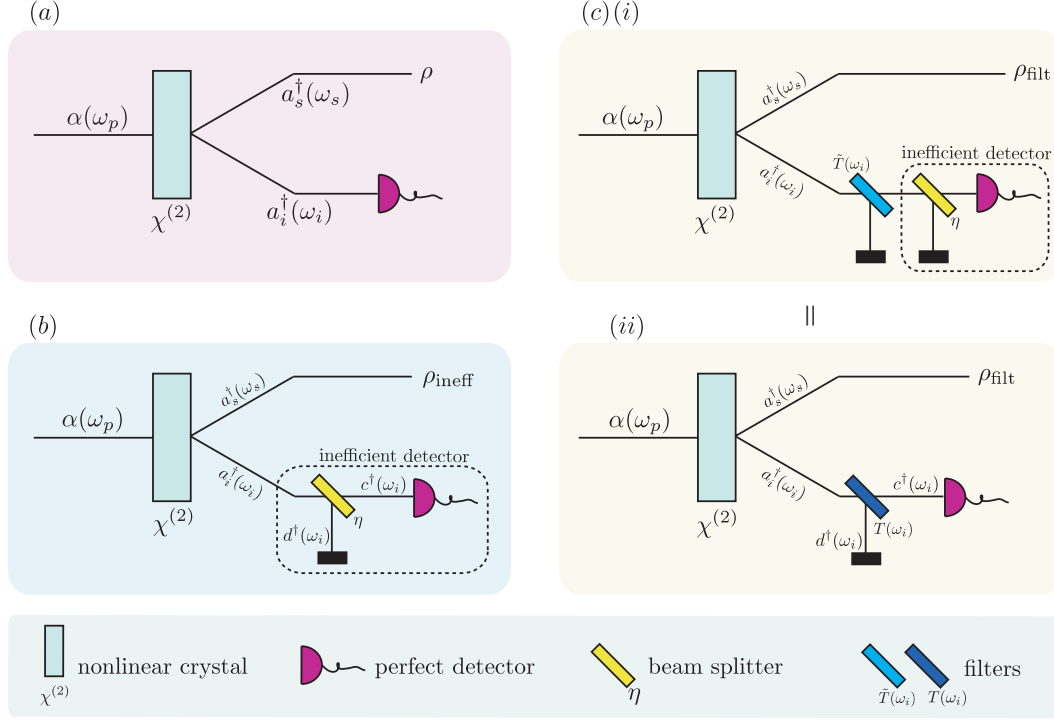


**Figure 4.1:** Schematic diagrams of SPDC setup for: (a) perfect detection in the triggering mode (see sections 4.4.1 and 4.5.1); (b) inefficient detection in the triggering mode (see sections 4.4.2 and 4.5.2); and (c)(i) filtering the triggering mode prior to detection with inefficient detector and (ii) the equivalent setup where the filter and beamsplitter have been combined into one filter (see sections 4.4.3 and 4.5.3).

The  $g^{(2)}$  of the signal state is  $g_1^{(2)} = 0$ . This reveals that there is only one photon in the signal mode, but not how pure it is. The purity of the heralded state is

$$P_1 = \text{Tr}[\rho_1^2] = |N_1|^4 \sum_k |b_k|^4. \quad (4.27)$$

For a state which only contains single photons, i.e. one that is heralded by a perfect detector, the purity is equivalent to the Hong-Ou-Mandel visibility [61].

Without loss of generality, we order the Schmidt coefficients in decreasing order from  $k = 0$ . Therefore, the pure single photon state with the highest overlap with the projected state will be the photon mode corresponding to the highest Schmidt coefficient,  $b_0$ , and hence the maximum fidelity with a single photon Fock state is

$$F_1 = \max_j F(\rho_1, |1; \xi_j\rangle) = \langle 1; \xi_0 | \rho_1 | 1; \xi_0 \rangle = |b_0|^2. \quad (4.28)$$

The fidelity does not depend on  $\chi$ . Increasing the strength of the nonlinearity only has an effect on how often the detector registers a *click*, however, once that happens, the signal mode is always projected into the same state.

#### 4.4.2 Case 2: Inefficient Detection in the Triggering Idler Mode

An inefficient detector can be modeled by the transformation in equation (4.12) where  $T(\omega) = \sqrt{\eta}$  and  $R(\omega) = \sqrt{1-\eta}$ , i.e. a beamsplitter, followed by a perfect detector (refer to Figure 4.1(b)). After the beam splitter, the joint signal-idler state is

$$\rho_{\text{ineff}} = \text{Tr}_{\hat{D}}[|\Psi_{\text{ineff}}\rangle\langle\Psi_{\text{ineff}}|], \quad (4.29)$$

where

$$\begin{aligned} |\Psi_{\text{ineff}}\rangle = N \bigg\{ & (1 + \chi^2)|0\rangle + \chi \sum_k b_k (\sqrt{\eta} \hat{A}_{s\xi_k}^\dagger \hat{C}_{\zeta_k}^\dagger + \sqrt{1-\eta} \hat{A}_{s\xi_k}^\dagger \hat{D}_{\zeta_k}^\dagger) |0\rangle \\ & + \frac{\chi^2}{2} \left( \sum_{k,k'} b_k b_{k'} \hat{A}_{s\xi_k}^\dagger \hat{A}_{s\xi_{k'}}^\dagger \left( \eta \hat{C}_{\zeta_k}^\dagger \hat{C}_{\zeta_{k'}}^\dagger + (1-\eta) \hat{D}_{\zeta_k}^\dagger \hat{D}_{\zeta_{k'}}^\dagger \right. \right. \\ & \left. \left. + \sqrt{\eta} \sqrt{1-\eta} (\hat{C}_{\zeta_{k'}}^\dagger \hat{D}_{\zeta_k}^\dagger + \hat{C}_{\zeta_k}^\dagger \hat{D}_{\zeta_{k'}}^\dagger) \right) |0\rangle \right\}. \end{aligned} \quad (4.30)$$

See table 4.1 for creation operator definitions. The probability of detecting a single photon in the idler mode, using an inefficient single-photon detector, is

$$p_{1,\text{ineff}} = \text{Tr}[\Pi_1 \rho_{\text{ineff}}] \quad (4.31)$$

$$= |N|^2 |\chi|^2 \eta \left\{ 1 + 2|\chi|^2 (1-\eta) \left( \sum_{\substack{k,k' \\ k < k'}} |b_k b_{k'}|^2 + \sum_k |b_k|^4 \right) \right\}. \quad (4.32)$$

Given a single-photon detection in the idler mode, the heralded signal state is

$$\rho_{1,\text{ineff}} = \frac{1}{p_{1,\text{ineff}}} \text{Tr}_{\hat{C}}[\Pi_1 \rho_{\text{ineff}}] \quad (4.33)$$

$$\begin{aligned} & = |N_{1,\text{ineff}}|^2 \left\{ \sum_k |b_k|^2 |1; \xi_k\rangle_s \langle 1; \xi_k| \right. \\ & \quad + 2|\chi|^2 (1-\eta) \left( \sum_k |b_k|^4 |2; \xi_k\rangle_s \langle 2; \xi_k| \right. \\ & \quad \left. \left. + \sum_{\substack{k,k' \\ k < k'}} |b_k b_{k'}|^2 |1; \xi_k\rangle_s |1; \xi_{k'}\rangle_s \langle 1; \xi_k|_s \langle 1; \xi_{k'}| \right) \right\}, \end{aligned} \quad (4.34)$$

where  $N_{1,\text{ineff}} = N \chi \sqrt{\eta} / \sqrt{p_{1,\text{ineff}}}$ .

The  $g^{(2)}$  for this state, defined in equation (4.26), is

$$g_{1,\text{ineff}}^{(2)} = \frac{\gamma_{1,\text{ineff}}}{|N_{1,\text{ineff}}|^2(1 + \gamma_{1,\text{ineff}})^2}, \quad (4.35)$$

where

$$\gamma_{1,\text{ineff}} = 4|\chi|^2(1 - \eta) \left( \sum_{\substack{k,k' \\ k < k'}} |b_k b_{k'}|^2 + \sum_{k'} |b_k|^4 \right). \quad (4.36)$$

The purity of the signal state is

$$P_{1,\text{ineff}} = \text{Tr}[\rho_{1,\text{ineff}}^2] \quad (4.37)$$

$$= |N_{1,\text{ineff}}|^4 \left\{ \sum_k |b_k|^4 + 4|\chi|^4(1 - \eta)^2 \left( \sum_{\substack{k,k' \\ k < k'}} |b_k b_{k'}|^4 + \sum_k |b_k|^8 \right) \right\}. \quad (4.38)$$

The maximum fidelity, between the heralded state and a pure Fock state  $|1; \xi_j\rangle$ , is

$$F_{1,\text{ineff}} = \max_j F(|1; \xi_j\rangle, \rho_{1,\text{ineff}}) = \langle 1; \xi_0 | \rho_{1,\text{ineff}} | 1; \xi_0 \rangle = |N_{1,\text{ineff}}|^2 |b_0|^2 \quad (4.39)$$

The fidelity is now a function of both the detector efficiency  $\eta$  and the nonlinearity strength  $\chi$ .

#### 4.4.3 Case 3: Filtering the Idler State

We now introduce a filter in the idler mode as shown in Figure 4.1(c). Applying a filter, as defined in equation (4.13), to the signal mode, gives the filtered state

$$\rho_{\text{filt}} = \text{Tr}_{\hat{D}}[|\Psi_{\text{filt}}\rangle\langle\Psi_{\text{filt}}|], \quad (4.40)$$

where

$$\begin{aligned} |\Psi_{\text{filt}}\rangle = N \Big\{ & (1 + \chi^2)|0\rangle + \chi \sum_{k,j} b_k \hat{A}_{s_{\xi_k}}^\dagger \left( u_{kj} \hat{C}_{\phi_j}^\dagger + v_{kj} \hat{D}_{\varphi_j}^\dagger \right) |0\rangle \\ & + \frac{\chi^2}{2} \sum_{k,k',j,j'} b_k b_{k'} \hat{A}_{s_{\xi_k}}^\dagger \hat{A}_{s_{\xi_{k'}}}^\dagger \left( u_{kj} u_{k'j'} \hat{C}_{\phi_j}^\dagger \hat{C}_{\phi_{j'}}^\dagger + v_{kj} u_{k'j'} \hat{D}_{\varphi_j}^\dagger \hat{C}_{\phi_{j'}}^\dagger \right. \\ & \left. + u_{kj} v_{k'j'} \hat{C}_{\phi_j}^\dagger \hat{D}_{\varphi_{j'}}^\dagger + v_{kj} v_{k'j'} \hat{D}_{\varphi_j}^\dagger \hat{D}_{\varphi_{j'}}^\dagger \right) |0\rangle \Big\}, \end{aligned} \quad (4.41)$$

and  $u_{kj}$  and  $v_{kj}$  are defined as per equations (4.20) and (4.21).

The probability of detecting a single photon in the filtered idler mode is

$$p_{1,\text{filt}} = \text{Tr}[\Pi_1 \rho_{\text{filt}}] \quad (4.42)$$

$$\begin{aligned} &= |N|^2 |\chi|^2 \left\{ \sum_k |b_k|^2 T_{\zeta_k}^2 + |\chi|^2 \left\{ \sum_k 2|b_k|^4 T_{\zeta_k}^2 R_{\zeta_k}^2 \right. \right. \\ &\quad \left. \left. + \sum_{\substack{k,k' \\ k < k'}} |b_k b_{k'}|^2 \left( T_{\zeta_k}^2 R_{\zeta_{k'}}^2 + T_{\zeta_{k'}}^2 R_{\zeta_k}^2 + \mathbb{T}_{kk'} \mathbb{R}_{k'k} + \mathbb{T}_{k'k} \mathbb{R}_{kk'} \right) \right\} \right\}, \end{aligned} \quad (4.43)$$

where

$$\mathbb{T}_{kk'} = T_{\zeta_k} T_{\zeta_{k'}}^* \langle 1; T_{\zeta_{k'}} | 1; T_{\zeta_k} \rangle = \sum_j u_{kj} u_{k'j}^*, \quad (4.44)$$

$$\mathbb{R}_{kk'} = R_{\zeta_k} R_{\zeta_{k'}}^* \langle 1; R_{\zeta_{k'}} | 1; R_{\zeta_k} \rangle = \sum_j v_{kj} v_{k'j}^*. \quad (4.45)$$

Given a single-photon detection in the idler mode, the heralded signal state is

$$\rho_{1,\text{filt}} = \frac{1}{p_{1,\text{filt}}} \text{Tr}_C [\Pi_1 \rho_{\text{filt}}] \quad (4.46)$$

$$\begin{aligned} &= |N_{1,\text{filt}}|^2 \left\{ \sum_{k,\bar{k}} b_k b_{\bar{k}}^* \mathbb{T}_{k\bar{k}} |1; \xi_k\rangle_i \langle 1; \xi_{\bar{k}}| \right. \\ &\quad \left. + |\chi|^2 \left( \sum_{k,k',\bar{k},\bar{k}'} b_k b_{k'} b_{\bar{k}}^* b_{\bar{k}'}^* \mathbb{T}_{k\bar{k}'} \mathbb{R}_{k'\bar{k}} \hat{A}_{i\xi_k}^\dagger \hat{A}_{i\xi_{k'}}^\dagger |0\rangle \langle 0| \hat{A}_{i\xi_{\bar{k}}} \hat{A}_{i\xi_{\bar{k}'}} \right) \right\}, \end{aligned} \quad (4.47)$$

where  $N_{1,\text{filt}} = N\chi/\sqrt{p_{1,\text{filt}}}$ . Note that filtering the idler mode also changes the mode structure of the heralded signal state. The  $g^{(2)}$  for this state, defined in equation (4.26), is

$$g_{1,\text{filt}}^{(2)} = \frac{\gamma_{1,\text{filt}}}{|N_{1,\text{filt}}|^2 (\sum_k |b_k|^2 |T_{\zeta_k}|^2 + \gamma_{1,\text{filt}})^2}, \quad (4.48)$$

where

$$\begin{aligned} \gamma_{1,\text{filt}} &= 2|\chi|^2 \left\{ 2 \sum_k |b_k|^4 \mathbb{R}_{kk} \mathbb{T}_{kk} \right. \\ &\quad \left. + \sum_{\substack{k,k' \\ k < k'}} |b_k b_{k'}|^2 (\mathbb{R}_{kk} \mathbb{T}_{k'k'} + \mathbb{R}_{k'k} \mathbb{T}_{kk'} + \mathbb{R}_{kk'} \mathbb{T}_{k'k} + \mathbb{R}_{k'k'} \mathbb{T}_{kk}) \right\}. \end{aligned} \quad (4.49)$$

The purity of the heralded state is

$$\begin{aligned}
P_{1,\text{filt}} &= \text{Tr}[\rho_{1,\text{filt}}^2] \tag{4.50} \\
&= |N_{1,\text{filt}}|^4 \left\{ \sum_{k,\tilde{k}} |b_k b_{\tilde{k}}|^2 |\mathbb{T}_{k\tilde{k}}|^2 + |\chi|^4 \left\{ \sum_{\tilde{k}} 2|b_{\tilde{k}}|^4 \right. \right. \\
&\quad \times \left( \sum_{\substack{k,k' \\ k < k'}} |b_k b_{k'}|^2 |\mathbb{R}_{k\tilde{k}} \mathbb{T}_{k'\tilde{k}} + \mathbb{R}_{k'\tilde{k}} \mathbb{T}_{k\tilde{k}}|^2 + \sum_k 2|b_k|^4 |\mathbb{R}_{k\tilde{k}} \mathbb{T}_{k\tilde{k}}|^2 \right) \\
&\quad + \sum_{\substack{\tilde{k},\tilde{k}' \\ \tilde{k} < \tilde{k}'}} b_{\tilde{k}}^* b_{\tilde{k}'}^* \left( \sum_k 2|b_k|^4 |\mathbb{R}_{k\tilde{k}} \mathbb{T}_{k\tilde{k}'} + \mathbb{R}_{k\tilde{k}'} \mathbb{T}_{k\tilde{k}}|^2 \right. \\
&\quad \left. \left. + \sum_{\substack{k,k' \\ k < k'}} |b_k b_{k'}|^2 |\mathbb{R}_{k\tilde{k}} \mathbb{T}_{k'\tilde{k}'} + \mathbb{R}_{k'\tilde{k}} \mathbb{T}_{k\tilde{k}'} + \mathbb{R}_{k\tilde{k}'} \mathbb{T}_{k'\tilde{k}} + \mathbb{R}_{k'\tilde{k}'} \mathbb{T}_{k\tilde{k}}|^2 \right) \right\} \Big\}. \tag{4.51}
\end{aligned}$$

The density matrix in equation (4.47) is not diagonal in the  $|1; \xi_k\rangle$  basis, but this can be easily achieved, for the part of the state which is relevant for calculating the fidelity with a single-photon Fock state, giving

$$\rho_{1,\text{filt},\text{part}} = |N_{1,\text{filt}}|^2 \sum_{k,\tilde{k}} b_k b_{\tilde{k}}^* \mathbb{T}_{k\tilde{k}} |1; \xi_k\rangle \langle 1; \xi_{\tilde{k}}| = \sum_m d_m |1; \tau_m\rangle \langle 1; \tau_m|, \tag{4.52}$$

where

$$|1; \tau_m\rangle = \sum_k c_{mk} |1; \xi_k\rangle. \tag{4.53}$$

and  $\tau_m(\omega_s)$  are the new orthogonal modes defining the signal state. The maximum fidelity, between the heralded state and a pure single-photon state  $|1; \tau_l\rangle$ , is

$$F_{1,\text{filt}} = \max_l F(|1; \tau_l\rangle, \rho_{1,\text{filt}}) = \max_l \langle 1; \tau_l | \rho_{1,\text{filt},\text{part}} | 1; \tau_l \rangle = \max_m d_m. \tag{4.54}$$

The spectral distribution  $\tau_m$  should be chosen in any interferometric experiment to optimise for the best performance of the heralded single photons.

In the extreme case where  $\tilde{T}(\omega) = \delta(\omega - \mu)$ , i.e. the filter picks out a single frequency  $\mu$ , the fidelity tends to unity and the signal state tends to the pure state

$$|\Psi_{1,\text{filt},\delta}\rangle = N_{1,\text{filt}} \sum_k b_k \zeta_k(\mu) |1; \xi_k\rangle = \sqrt{d_m} |1; \tau_m\rangle, \tag{4.55}$$

as  $\chi \rightarrow 0$ . This implies that it is possible to obtain arbitrarily pure single photon states, with the use of strong spectral filtering and by ensuring the nonlinearity strength is low, to minimise the photon-number mixedness which results from strong filtering. This is the technique that has been used in most experiments.

## 4.5 Generating 2-photon Fock States

In addition to creating single-photon states, it is becoming increasingly desirable to create higher photon-number Fock states, e.g. in the generation of Schrödinger cat states [48]. In this section we will investigate the effects of detector efficiency, and filtering of the idler mode, on the generation of two-photon Fock states in the signal mode conditional on the detection of heralded two-photon states in the idler mode.

### 4.5.1 Case 1: Perfect Detection in the Triggering Idler Mode

The projector for detecting two photons in any spectral modes  $\zeta_j$  and  $\zeta_{j'}$  will be separated into two parts: the part which detects two photons in orthogonal modes and the part which detects two photons in the same mode:

$$\Pi_2 = \sum_j |2; \zeta_j\rangle \langle 2; \zeta_j| + \sum_{\substack{j, j' \\ j < j'}} |1; \zeta_j\rangle \langle 1; \zeta_j| |1; \zeta_{j'}\rangle \langle 1; \zeta_{j'}|. \quad (4.56)$$

Refer to the schematic in Figure 4.1(a). The probability of detecting two photons in the idler mode, with a frequency insensitive detector, is

$$p_2 = \langle \Psi_{\text{PDC}} | \Pi_2 | \Psi_{\text{PDC}} \rangle = |N|^2 |\chi|^4 \left( \sum_{\substack{k, k' \\ k < k'}} |b_k b_{k'}|^2 + \sum_k |b_k|^4 \right). \quad (4.57)$$

Given a two-photon detection in the idler mode, the heralded state in the signal mode is

$$\rho_2 = \frac{1}{p_2} \text{Tr}_i [\Pi_2 | \Psi_{\text{PDC}} \rangle \langle \Psi_{\text{PDC}} |] \quad (4.58)$$

$$= |N_2|^2 \left\{ \sum_k |b_k|^4 |2; \xi_k\rangle_s \langle 2; \xi_k| + \sum_{\substack{k, k' \\ k < k'}} |b_k b_{k'}|^2 |1; \xi_k\rangle_s \langle 1; \xi_k| |1; \xi_{k'}\rangle_s \langle 1; \xi_{k'}| \right\} \quad (4.59)$$

$$= \frac{|N_2|^2}{2} \sum_k |b_k|^2 \hat{A}_{s\xi_k}^\dagger |0\rangle \langle 0| \hat{A}_{s\xi_k} \otimes \sum_{k'} |b_{k'}|^2 \hat{A}_{s\xi_{k'}}^\dagger |0\rangle \langle 0| \hat{A}_{s\xi_{k'}} , \quad (4.60)$$

where  $N_2 = N\chi^2/\sqrt{p_2}$ . The purity is

$$P_2 = \text{Tr}[\rho_2^2] = |N_2|^4 \left\{ \sum_{\substack{k, k' \\ k < k'}} |b_k b_{k'}|^4 + \sum_k |b_k|^8 \right\}. \quad (4.61)$$

The  $g^{(2)}$  for this state is  $g_2^{(2)} = 1/2$ . It is interesting to note that the  $g^{(2)}$  does not depend on the purity of the two-photon state. It will always remain at the value of 1/2 regardless of whether the two-photon state is in a Fock state or in some other

form. This reflects the fact that  $g^{(2)}$  is only sensitive to the photon number, but not the modal properties of the state.

The maximum fidelity between the heralded state and an ideal two-photon Fock state  $|2; \xi_j\rangle$  is

$$F_2 = \max_j F(\rho_2, |2; \xi_j\rangle) = \langle 2; \xi_0 | \rho_2 | 2; \xi_0 \rangle = |N_2|^2 |b_0|^4. \quad (4.62)$$

The fidelity does not depend on  $\chi$ . Increasing the strength of the nonlinearity has an effect only on how often the detector registers two photons; however, once that happens, the signal mode is always projected into the same state.

#### 4.5.2 Case 2: Inefficient Detection in the Triggering Idler Mode

The probability of detecting two photons in the idler mode, with an inefficient frequency insensitive detector (refer to Figure 4.1(b)), is

$$p_{2,\text{ineff}} = \text{Tr}[\Pi_2 \rho_{\text{ineff}}] = |N|^2 |\chi|^4 \eta^2 \left( \sum_{\substack{k,k' \\ k < k'}} |b_k b_{k'}|^2 + \sum_k |b_k|^4 \right), \quad (4.63)$$

where  $\rho_{\text{ineff}}$  is defined in equation (4.33). Because our analysis only extends to second order in photon-number, the expressions for the fidelity and purity will be the same as they were in Section 4.5.1, where a perfect detector was used. If we included higher order terms, we would expect the fidelity and purity to vary as a function of  $\chi$  and  $\eta$  in a similar fashion to the single-photon case in Section 4.4.

#### 4.5.3 Case 3: Filtering of the Idler State

We now introduce a filter in the idler mode as shown in Figure 4.1(c). After filtering the state, the probability of detecting two photons in the idler mode, with an inefficient frequency insensitive detector, is

$$p_{2,\text{filt}} = \text{Tr}[\Pi_2 \rho_{\text{filt}}] \quad (4.64)$$

$$= |N|^2 |\chi|^4 \left( \sum_{k'} |b_k|^4 |T_{\zeta_k}|^4 + \sum_{\substack{k,k' \\ k < k'}} |b_k b_{k'}|^2 (|T_{\zeta_k}|^2 |T_{\zeta_{k'}}|^2 + \Gamma_{kk'} \Gamma_{k'k}) \right), \quad (4.65)$$

where  $\rho_{\text{filt}}$  is defined in equation (4.40).

Given a two-photon detection in the idler mode, the heralded state in the signal mode is

$$\rho_{2,\text{filt}} = \frac{1}{p_2} \text{Tr}_C [\Pi_2 \rho_{\text{filt}}] \quad (4.66)$$

$$\begin{aligned} &= |N_{2,\text{filt}}|^2 \left\{ \sum_{k,\bar{k}} b_k^2 b_{\bar{k}}^{*2} \mathbb{T}_{k\bar{k}}^2 |2; \xi_k\rangle \langle 2; \xi_{\bar{k}}| \right. \\ &\quad + \sum_{\substack{k,k',\bar{k} \\ k < k'}} \sqrt{2} b_k b_{k'} b_{\bar{k}}^{*2} \mathbb{T}_{k\bar{k}} \mathbb{T}_{k'\bar{k}} |1; \xi_k\rangle \langle 1; \xi_{k'}| \langle 2; \xi_{\bar{k}}| \\ &\quad + \sum_{\substack{k,\bar{k},\bar{k}' \\ \bar{k} < \bar{k}'} \sqrt{2} b_{\bar{k}}^2 b_{\bar{k}'}^* b_{k\bar{k}} \mathbb{T}_{k\bar{k}} \mathbb{T}_{k\bar{k}'} |2; \xi_k\rangle \langle 1; \xi_{\bar{k}}| \langle 1; \xi_{\bar{k}'}| \\ &\quad \left. + \sum_{\substack{k,k',\bar{k},\bar{k}' \\ k < k', \bar{k} < \bar{k}'} b_k b_{k'} b_{\bar{k}}^* b_{\bar{k}'}^* (\mathbb{T}_{k\bar{k}} \mathbb{T}_{k'\bar{k}'} + \mathbb{T}_{k'\bar{k}} \mathbb{T}_{k\bar{k}}) |1; \xi_k\rangle \langle 1; \xi_{k'}| \langle 1; \xi_{\bar{k}}| \langle 1; \xi_{\bar{k}'}| \right\} \\ &= \frac{|N_{2,\text{filt}}|^2}{2} \sum_{k,\bar{k}} b_k b_{\bar{k}}^* \mathbb{T}_{k,\bar{k}} \hat{A}_{s_{\xi_k}}^\dagger |0\rangle \langle 0| \hat{A}_{s_{\xi_{\bar{k}}}} \otimes \sum_{k',\bar{k}'} b_{k'} b_{\bar{k}'}^* \mathbb{T}_{k',\bar{k}'} \hat{A}_{s_{\xi_{k'}}}^\dagger |0\rangle \langle 0| \hat{A}_{s_{\xi_{\bar{k}'}}} , \end{aligned} \quad (4.67)$$

$$\quad (4.68)$$

where  $N_{2,\text{filt}} = N\chi^2/\sqrt{p_{2,\text{filt}}}$ . Again  $g_{2,\text{filt}}^{(2)} = 1/2$  as there are always two photons in the state. The purity of the heralded state is

$$\begin{aligned} P_{2,\text{filt}} &= \text{Tr}[\rho_{2,\text{filt}}^2] = |N_{2,\text{filt}}|^4 \left\{ \sum_{\substack{k,k' \\ k < k'}} |b_k b_{k'}|^2 \left( \sum_{\bar{k}} 2|b_{\bar{k}}|^4 |\mathbb{T}_{k,\bar{k}} \mathbb{T}_{k',\bar{k}}|^2 \right. \right. \\ &\quad \left. \left. + \sum_{\substack{\bar{k},\bar{k}' \\ \bar{k} < \bar{k}'}} |b_{\bar{k}} b_{\bar{k}'}|^2 |\mathbb{T}_{k,\bar{k}} \mathbb{T}_{k',\bar{k}'} + \mathbb{T}_{k',\bar{k}} \mathbb{T}_{k,\bar{k}'}|^2 \right) \right. \\ &\quad \left. + \sum_k |b_k|^4 \left( \sum_{\bar{k}} |b_{\bar{k}}|^4 |\mathbb{T}_{k,\bar{k}}|^4 + \sum_{\substack{\bar{k},\bar{k}' \\ \bar{k} < \bar{k}'}} 2|b_{\bar{k}} b_{\bar{k}'}|^2 |\mathbb{T}_{k,\bar{k}} \mathbb{T}_{k,\bar{k}'}|^2 \right) \right\}. \end{aligned} \quad (4.69)$$

The density matrix in equation (4.67) is not diagonal in the  $|1; \xi_k\rangle$  basis. This can be easily achieved, giving

$$\rho_{2,\text{filt}} = \frac{1}{2} \sum_{m,m'} d_m d_{m'} \hat{A}_{s_{\tau_m}}^\dagger \hat{A}_{s_{\tau_{m'}}}^\dagger |0\rangle \langle 0| \hat{A}_{s_{\tau_m}} \hat{A}_{s_{\tau_{m'}}} \quad (4.70)$$

$$= \sum_m d_m^2 |2; \tau_m\rangle \langle 2; \tau_m| + \sum_{\substack{m,m' \\ m < m'}} d_m d_{m'} |1; \tau_m\rangle \langle 1; \tau_{m'}| \langle 1; \tau_m| \langle 1; \tau_{m'}|, \quad (4.71)$$

where  $|1; \tau_m\rangle$  is defined in equation (4.53). The maximum fidelity, between the heralded state and a pure two-photon state with an optimised spectral distribution function  $|2; \tau_l\rangle$ , is

$$F_{2,\text{filt}} = \max_l F(|2; \tau_l\rangle, \rho_{2,\text{filt}}) = \max_l \langle 2; \tau_l | \rho_{2,\text{filt}} | 2; \tau_l \rangle = \max_m d_m^2. \quad (4.72)$$

In the extreme case where  $\tilde{T}(\omega) = \delta(\omega - \mu)$ , i.e. the filter picks out a single frequency  $\mu$ , the fidelity tends to unity and the signal state tends to the pure state

$$|\Psi_{2,\text{filt},\delta}\rangle = \frac{N_{2,\text{filt}}}{2} \sum_k b_k \zeta_k(\mu) \hat{A}_{s\xi_k}^\dagger |0\rangle \otimes \sum_{k'} b_{k'} \zeta_{k'}(\mu) \hat{A}_{s\xi_{k'}}^\dagger |0\rangle \quad (4.73)$$

$$= d_m |2; \tau_m\rangle, \quad (4.74)$$

as  $\chi \rightarrow 0$ . This implies that it is possible to obtain arbitrarily pure two-photon states, with the use of spectral filtering and by ensuring the nonlinearity strength is low.

## 4.6 Physical Example I - Correlated JSA

As a physical example, we model a type II ppKTP waveguide of length  $L = 3.6$  mm and a periodicity of  $\Lambda = 8.8$   $\mu\text{m}$ , pumped with a 400 nm laser with a 1nm FWHM ( $\sigma_p = 5.00 \times 10^{12}$   $\text{s}^{-1}$ ) which down-converts to 800 nm in the signal and idler modes. In Figure 4.2(a)-(c), we have plotted the pump function, the PMF and the JSA for the given parameters. Figure 4.2(d) shows the corresponding Schmidt modes: *initial signal modes* and *initial idler modes*. In addition, it can be seen that after filtering the idler state, the idler Schmidt modes take on different spectral shapes. These *filtered idler modes* are no longer orthogonal to each other and therefore need to be orthogonalised giving the *orthogonalised idler modes*. When the idler mode is detected, the signal state gets projected into a mixture of orthogonal modes, as shown by the *diagonalised signal modes*. Filtering and detection of the idler state changes the spectral shape of the signal state even though there is no physical interaction. This is a typical effect of entanglement.

In general, the Schmidt decomposition can not be found analytically, but can be calculated numerically by computing the singular value decomposition of a discretised JSA. Unless stated otherwise, the results in this section were obtained using an  $800 \times 800$  grid, ranging over  $0.2 \times 10^{15}$   $\text{s}^{-1}$ , centered around  $\omega_i = \omega_s = \mu$ . We note that an insufficiently fine grid, or insufficiently large region, will result in inflated values for the purity. The entropy of entanglement for this particular JSA is  $E = 4.6$ , which ranges from zero for a product state to  $\log_2 N$  for a maximally entangled state of two  $N$ -state particles

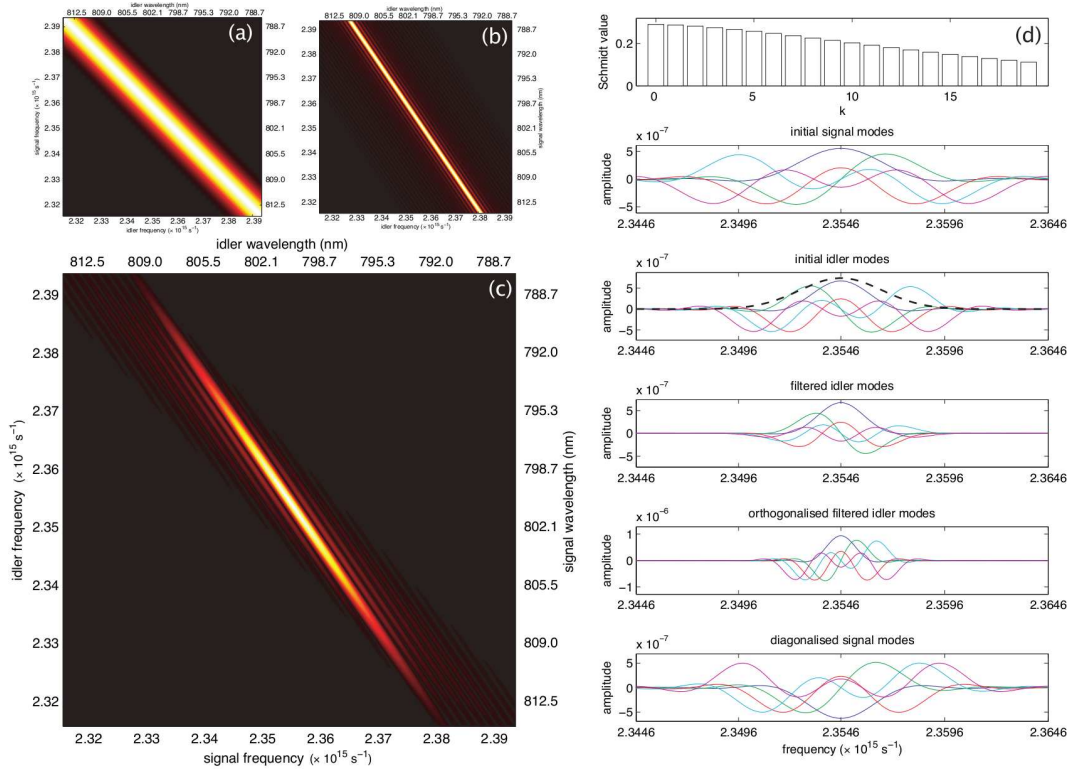


**Figure 4.2:** (a) Gaussian pump function  $\alpha(\omega_i + \omega_s)$  with a 1nm FWHM at  $\mu_p = 400$  nm. (b) Phase matching function  $\Phi(\omega_i, \omega_s)$  for waveguide of length  $L = 3.6$  mm and a periodicity of  $\Lambda = 8.8 \mu\text{m}$ . (c) The resulting JSA  $f(\omega_i, \omega_s) = \alpha(\omega_i + \omega_s)\Phi(\omega_i, \omega_s)$ . The JSA has been plotted as a function of the frequency, however corresponding values for the wavelength have been included. (d) Schmidt numbers and modes for the JSA (top to bottom): the first 20 Schmidt numbers  $b_k$ ; the first 5 Schmidt modes  $\xi_k(\omega_s)$  for the signal state; the first 5 Schmidt modes  $\zeta_k(\omega_i)$  for the idler state, as well as a Gaussian filter function of width  $\sigma_f = 2 \times 10^{12} \text{ s}^{-1}$  (dashed line); the filtered Schmidt modes  $T(\omega_i)\zeta_k(\omega_i)$  for the idler state; the orthogonalised idler modes  $\phi_j(\omega_i)$ ; the diagonalised signal modes  $\tau_m(\omega_s)$

In this section we present results for: the probability of detecting a single photon in the idler mode; the  $g^{(2)}$  and purity of the heralded state in the signal mode; and the fidelity between the signal state and the desired ideal Fock state. We compare results for: an unfiltered idler state; an idler state filtered with a Gaussian filter  $T(\omega_i) = \exp(-(\mu_f - \omega_i)^2/2\sigma_f^2)$ , of various widths  $\sigma_f$  and centered at the central idler frequency, where the filter function has been scaled such that the maximum value is always 1; as well as the limiting case where  $T(\omega_i) = \delta(\omega_i - \mu_f)$ . We also present similar results for heralding a two-photon state conditional on the detection of two photons in the idler mode.

### Generating Single-photon Fock States

Due to the second-order truncation of the down-converted state, we are not considering 6- (or higher) photon contributions. At  $\chi = 0.5$ , the fraction of 6-photon states, to 2-photon states, is roughly  $\chi^6/\chi^2 = 1/16$ . We will not plot results beyond  $\chi = 0.5$ .

In Figure 4.3(a), we have plotted the probability of detecting a single photon in the idler mode as a function of the nonlinearity  $\chi$  and the efficiency of the detector  $\eta$ . Notice that the probability of detecting a single photon in the idler mode increases with higher detector efficiency and higher nonlinearity strength, as expected.

The fidelity has been plotted in Figure 4.3(b). The inclusion of a filter has a drastic effect on the fidelity. It has a greater dependence on the strength of the nonlinearity, than in the unfiltered case, however the overall fidelity is much higher. Notice as well that there is a trade-off between the fidelity and the probability of detection.

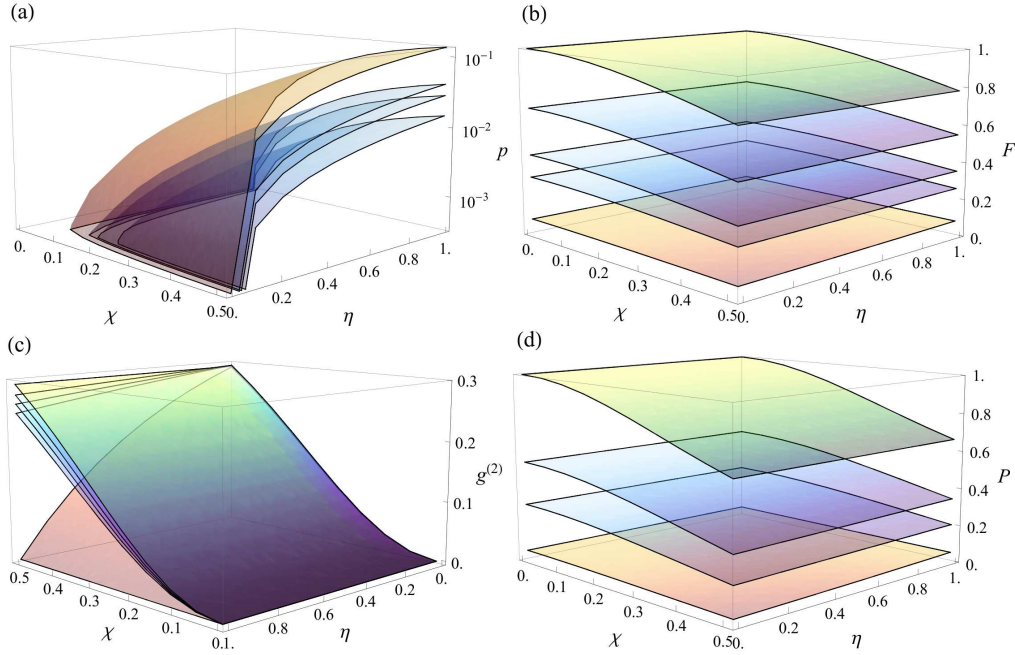


**Figure 4.3:** (a) The probability of detecting a single photon in the idler mode for (top to bottom): no filter;  $\sigma_f = 3 \times 10^{12} \text{ s}^{-1}$ ;  $\sigma_f = 2 \times 10^{12} \text{ s}^{-1}$ ;  $\sigma_f = 1 \times 10^{12} \text{ s}^{-1}$ . *Note that the probability is plotted on a log scale.* (b) The fidelity of the signal state with an ideal Fock state for (top to bottom):  $\sigma_f = 0$ ;  $\sigma_f = 1 \times 10^{12} \text{ s}^{-1}$ ;  $\sigma_f = 2 \times 10^{12} \text{ s}^{-1}$ ;  $\sigma_f = 3 \times 10^{12} \text{ s}^{-1}$ ; no filter. (c) The  $g^{(2)}$  of the signal state for (top to bottom):  $\sigma_f = 0$ ;  $\sigma_f = 1 \times 10^{12} \text{ s}^{-1}$ ;  $\sigma_f = 2 \times 10^{12} \text{ s}^{-1}$ ;  $\sigma_f = 3 \times 10^{12} \text{ s}^{-1}$ ; no filter. *Note the change in axis orientation.* (d) The purity of the signal state for (top to bottom):  $\sigma_f = 0$ ;  $\sigma_f = 1 \times 10^{12} \text{ s}^{-1}$ ;  $\sigma_f = 2 \times 10^{12} \text{ s}^{-1}$ ; no filter.

In Figure 4.3(c), we have plotted the  $g^{(2)}$  for the heralded state in the signal mode. Note that, for visual clarity, the figure orientation has been rotated by  $\pi$  around the  $z$ -axis, with respect to the other plots. It is useful to know that  $g^{(2)} = 0$  for a single-photon state and  $1/2$  for a two-photon state. A curious thing is that decreasing the filter width results in higher fidelities, despite the higher proportion of two-photon states, as shown by the  $g^{(2)}$ . This suggests that for this particular JSA, the dominant cause of impurity is the spectral entanglement, rather than the resulting photon-number mixture due to the presence of higher-order terms.

In Figure 4.3(d), we have plotted the purity of the state in the signal mode. Due to the 4-fold summation, the purity for the filtered case is very demanding computationally, therefore, we have only included examples of two filter widths. Results for the filtered case were computed using a  $600 \times 600$  grid, ranging over  $0.16 \times 10^{15} \text{ s}^{-1}$ , centered around  $\omega_i = \omega_s = \mu$ , and truncating  $b_k$  with values below  $10^{-2}$ . To achieve a fidelity of  $F = 0.95$ , using a heralding detector with efficiency  $\eta = 0.5$ , we could choose from a range of filter widths at different nonlinearity strengths. Different combinations, however, result in slightly different probabilities of success. Figure 4.4 (a) shows the probability of success, and required nonlinearity, for a number of filter widths.

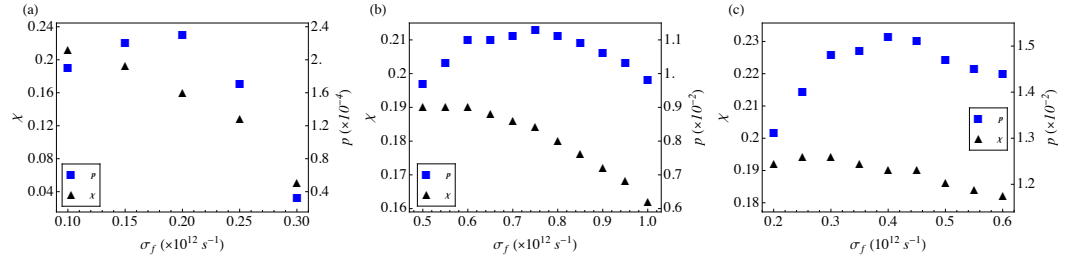


**Figure 4.4:** Probability of detecting a single photon in the idler mode, and required nonlinearity, for a number of filter widths, in order to achieve a fidelity of  $F = 0.95$ , using a heralding detector with efficiency  $\eta = 0.5$ , for: (a) correlated JSA (see Section 4.6); (b) symmetric JSA (see Section 4.7.1); (c) asymmetric JSA (see Section 4.7.2).

## Generating Two-photon Fock States

We can also analyse the probabilities and fidelities for generating two-photon Fock states. The results are summarised in Figure 4.5. At  $\chi = 0.25$ , the fraction of 6-photon states, to 4-photon states, is roughly  $\chi^6/\chi^4 = 1/16$ . We will not plot results beyond  $\chi = 0.25$ . Figure 4.5(a) shows the probability for an inefficient detector to detect two photons in the idler mode. The corresponding fidelities and purities have been shown in Figure 4.5(b) and do not vary as a function of  $\chi$  and  $\eta$ .

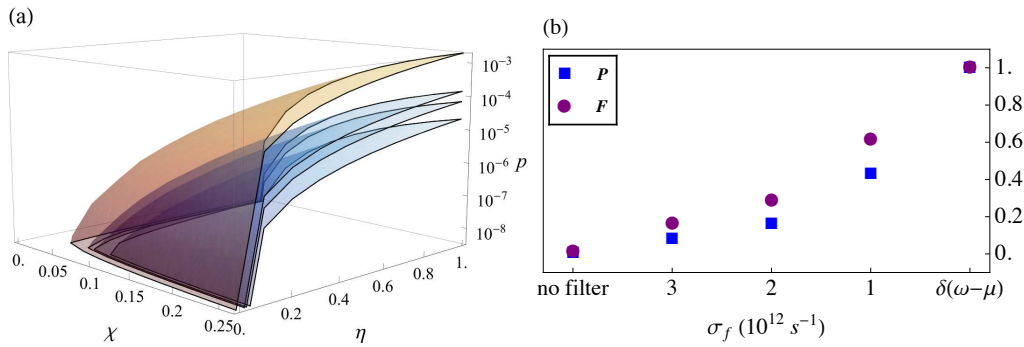


**Figure 4.5:** (a) The probability of detecting two photons in the idler mode for (top to bottom): no filter;  $\sigma_f = 3 \times 10^{12} \text{ s}^{-1}$ ;  $\sigma_f = 2 \times 10^{12} \text{ s}^{-1}$ ;  $\sigma_f = 1 \times 10^{12} \text{ s}^{-1}$ . Note that the probability is plotted on a log scale. (b) The purity and fidelity of the signal state with an ideal Fock state.

## 4.7 Physical Example II - Group Velocity Matching

In this section, we examine particular phase matching conditions which result in a less entangled JSA, and therefore a more pure heralded Fock state. It is common to approximate the phase matching function as  $\Phi(\omega_i, \omega_s) = \exp(-\gamma(\Delta k L/2)^2)$  where  $\gamma \approx 0.193$ . By making this approximation, we can write the JSA as

$$f(\omega_i, \omega_s) \propto \exp\left(-\frac{(\omega_i + \omega_s - 2\mu)^2}{2\sigma_p^2}\right) \exp\left(-\gamma\left(\frac{\Delta k L}{2}\right)^2\right). \quad (4.75)$$

In order to make equation (4.75) separable, we require all “cross-terms”, i.e. terms which contain products of  $\omega_i$  and  $\omega_s$  to vanish. This occurs when the condition

$$\frac{2}{\sigma_p^2} + \gamma L^2 (k'_s - k'_p)(k'_i - k'_p) = 0 \quad (4.76)$$

is met, yielding a JSA of the form  $f(\omega_i, \omega_s) \propto f_i(\omega_i) f_s(\omega_s)$  [28]. One way to satisfy the condition in equation (4.76) is to set  $k'_p = (k'_s + k'_i)/2$ , which results in the

following condition for the length of the waveguide, as a function of the pump width:

$$L = \sqrt{\frac{8}{\gamma\sigma_p^2(k'_s - k'_i)^2}}. \quad (4.77)$$

These conditions generate a symmetric JSA, where both signal and idler modes have equal widths. Alternatively, rearranging equation (4.76) as follows

$$\frac{4}{\sigma_p L(k'_i - k'_p)} + \gamma\sigma_p L(k'_s - k'_p) = 0, \quad (4.78)$$

we can see that by making  $L \ll \sigma^{-1}$ , i.e.  $L \rightarrow \infty$  and setting  $k'_p = k'_s$ , we can also obtain a separable JSA. These conditions generate an asymmetric JSA [28].

We have made use of the Gaussian approximation for  $\Phi(\omega_i, \omega_s)$  to obtain the conditions for separability, however we will now input these conditions into the original sinc form of the function. This analysis will not result in completely pure states being generated, however it should correspond more closely to experimental observations. The phase-matching conditions derived here may not necessarily be the optimal solutions. Numerical simulation may reveal phase-matching conditions more suited to the sinc form of the phase-matching function; however, we do not expect this to be a large effect.

### 4.7.1 Symmetric JSA

In order to meet the extended phase matching conditions for a symmetric, separable JSA, we again model a type II ppKTP waveguide, now of length  $L = 24.2$  mm and a periodicity of  $\Lambda = 68.4$   $\mu\text{m}$ , pumped with a 788 nm laser with a 0.7nm FWHM ( $\sigma_p = 0.9 \times 10^{12}$   $\text{s}^{-1}$ ) which down-converts to 1576 nm in the signal and idler modes. Unless stated otherwise, the results in this section were obtained using an  $800 \times 800$  grid, ranging over  $0.06 \times 10^{15}$   $\text{s}^{-1}$ , centered around  $\omega_i = \omega_s = \mu$ .

Figure 4.6 shows the JSA and the corresponding Schmidt values and modes. Notice in the Schmidt decomposition that the first mode is much more dominant than it was in Section 4.6. The entropy of entanglement for this JSA is  $E = 0.88$ . If we had used the Gaussian approximation for  $\Phi$ , the JSA would decompose into one pair of Schmidt modes and the entropy of entanglement would be  $E = 0$ . In such a case, the four-photon term would consist only of two-photon Fock states.

As an intuitive guide to why the above conditions generate the given JSA, notice that varying the parameter  $\Delta k$  has the effect of changing the gradient of the phase matching function  $\Phi(\omega_i, \omega_s)$  (see figure 4.6(b)), rotating it around  $\omega_i = \omega_s = \mu$  while changing the parameter  $L$ , alters the width of the phase matching function. The goal is to pick  $\Delta k$ , and therefore  $k'_p$ , and  $L$  such that the phase matching function is perpendicular, and of equal width, to the pump function.

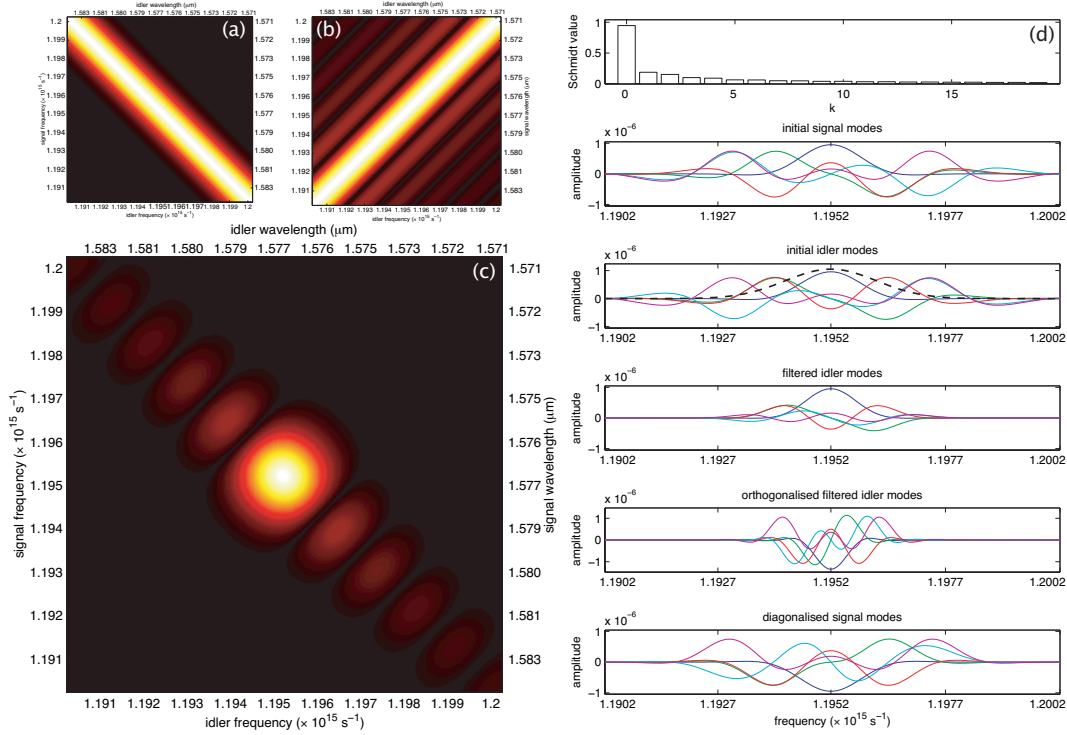


**Figure 4.6:** (a) Gaussian pump function  $\alpha(\omega_i + \omega_s)$  with a 0.7nm FWHM at  $\mu_p = 788$  nm. (b) Phase matching function  $\Phi(\omega_i, \omega_s)$  for waveguide of length  $L = 24.2$  mm and a periodicity of  $\Lambda = 68.4 \mu\text{m}$ . (c) The resulting JSA  $f(\omega_i, \omega_s) = \alpha(\omega_i + \omega_s)\Phi(\omega_i, \omega_s)$ . The JSA has been plotted as a function of the frequency, however corresponding values for the wavelength have been included. (d) Schmidt numbers and modes for the JSA (top to bottom): the first 20 Schmidt numbers  $b_k$ ; the first 5 Schmidt modes  $\xi_k(\omega_s)$  for the signal state; the first 5 Schmidt modes  $\zeta_k(\omega_i)$  for the idler state, as well as a Gaussian filter function of width  $\sigma_f = 1 \times 10^{12} \text{ s}^{-1}$  (dashed line); the filtered Schmidt modes  $T(\omega_i)\zeta_k(\omega_i)$  for the idler state; the orthogonalised idler modes  $\phi_j(\omega_i)$ ; the diagonalised signal modes  $\tau_m(\omega_s)$

As in the previous section, we present results for the probability, purity,  $g^{(2)}$  and fidelity, for the heralding of one- and two-photon Fock states. For a realistic JSA, manipulating the phase-matching conditions can result in high purity of the heralded state, however, it doesn't reach unity. From Figure 4.6(c), it can be seen that the outer lobes contribute to the spectral correlations and perhaps it is possible to increase the purity of the heralded state by filtering them out. Therefore, we will again compare results for: an unfiltered idler state; an idler state filtered with a Gaussian filter  $T(\omega_i) = \exp(-(\mu_f - \omega_i)/2\sigma_f^2)$ , of various widths  $\sigma_f$  and centered at the central idler frequency; as well as the limiting case where  $T(\omega_i) = \delta(\omega_i - \mu_f)$ .

In Chapter 5, we discuss a technique for reducing the side lobes without filtering.

### Generating Single-photon Fock States

Figure 4.7(a) shows the probability of detecting a single photon in the signal mode. Since most of the photons will have spectral distributions within the filter width, we do not see a very big drop in the probability, when filtering.

Figure 4.7(b) shows the fidelity. We distinguish between these surfaces by referring to their values at the point  $\chi = 0$  and  $\eta = 0$ . Immediately we can see that the fidelity is much higher than in section 4.6. In the region of interest, filtering the idler mode increases the fidelity of the signal state with a single photon. Decreasing the filter width can be detrimental to the fidelity when the nonlinearity and the detector efficiency are high.

Figure 4.7(c) shows the  $g^{(2)}$  and figure 4.7(d) shows the purity of the state in the signal mode. Again, will distinguish between these surfaces by referring to their values at the point  $\chi = 0$  and  $\eta = 0$ .

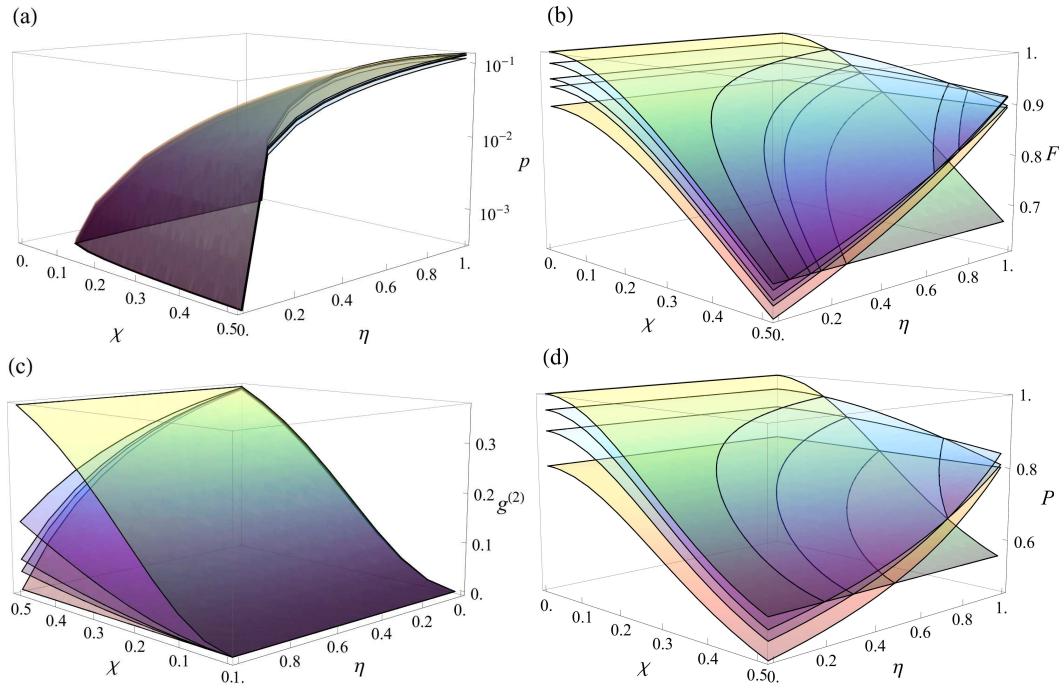


**Figure 4.7:** (a) The probability of detecting a single photon in the idler mode for (top to bottom): no filter;  $\sigma_f = 3 \times 10^{12} \text{ s}^{-1}$ ;  $\sigma_f = 2 \times 10^{12} \text{ s}^{-1}$ ;  $\sigma_f = 1 \times 10^{12} \text{ s}^{-1}$ . Note that the probability is plotted on a log scale. (b) The fidelity of the signal state with an ideal Fock state for (top to bottom at  $\chi = 0$  and  $\eta = 0$ ):  $\sigma_f = 0$ ;  $\sigma_f = 1 \times 10^{12} \text{ s}^{-1}$ ;  $\sigma_f = 2 \times 10^{12} \text{ s}^{-1}$ ;  $\sigma_f = 3 \times 10^{12} \text{ s}^{-1}$ ; no filter. (c) The  $g^{(2)}$  of the signal state for (top to bottom):  $\sigma_f = 0$ ;  $\sigma_f = 1 \times 10^{12} \text{ s}^{-1}$ ;  $\sigma_f = 2 \times 10^{12} \text{ s}^{-1}$ ;  $\sigma_f = 3 \times 10^{12} \text{ s}^{-1}$ ; no filter. Note the change in axis orientation. (d) The purity of the signal state for (top to bottom at  $\chi = 0$  and  $\eta = 0$ ):  $\sigma_f = 0$ ;  $\sigma_f = 1 \times 10^{12} \text{ s}^{-1}$ ;  $\sigma_f = 2 \times 10^{12} \text{ s}^{-1}$ ; no filter.

values at the point  $\chi = 0$  and  $\eta = 0$ . Results for the filtered case were computed using a  $600 \times 600$  grid, ranging over  $0.06 \times 10^{15} \text{ s}^{-1}$ , centered around  $\omega_i = \omega_s = \mu$ , and truncating  $b_k$  with values below  $10^{-2}$ .

Figure 4.4 (b) shows the probability of success, and required nonlinearity, for a number of filter widths, in order to achieve a fidelity of  $F = 0.95$ , using a detector with efficiency  $\eta = 0.5$ . Note that while the probability of success is greatly enhanced by using a source-engineered state, the required pump powers are nearly the same. Also notice the “flat” region, where the probability does not change much, between  $\sigma_f = 0.6 \times 10^{12} \text{ s}^{-1}$  and  $0.7 \times 10^{12} \text{ s}^{-1}$ . This corresponds to the “dark” region between the lobes on the JSA. Over this region, we do not expect much change in the flux.

### Generating Two-photon Fock States

We can also analyse the probabilities and fidelities for generating two-photon Fock states. The results are summarised in Figure 4.8. Figure 4.8(a), shows the probability for an inefficient detector to detect two photons in the idler mode. The corresponding fidelities and purities have been shown in Figure 4.8(b). The fidelity and purity do not vary as a function of  $\chi$  and  $\eta$ .

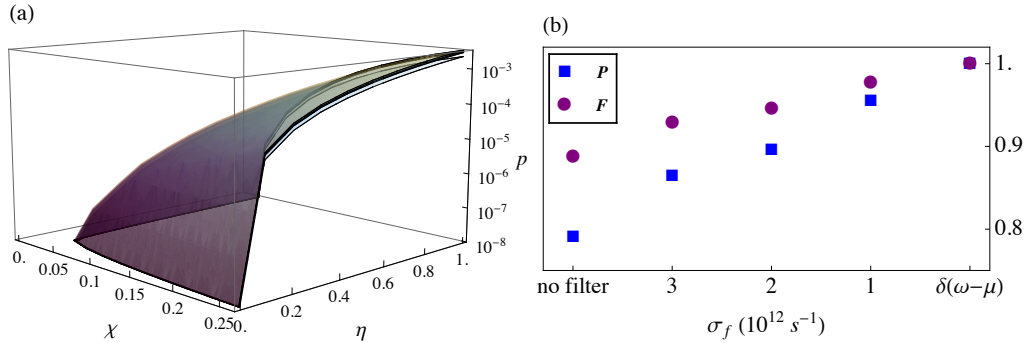


**Figure 4.8:** (a) The probability of detecting two photons in the idler mode for (top to bottom): no filter;  $\sigma_f = 3 \times 10^{12} \text{ s}^{-1}$ ;  $\sigma_f = 2 \times 10^{12} \text{ s}^{-1}$ ;  $\sigma_f = 1 \times 10^{12} \text{ s}^{-1}$ . Note that the probability is plotted on a log scale. (b) The purity and fidelity of the signal state with an ideal Fock state.

#### 4.7.2 Asymmetric JSA

In order to meet the extended phase matching conditions for an asymmetric separable JSA, we again analyse a type II ppKTP waveguide, of length  $L = 80 \text{ mm}$  and a periodicity of  $\Lambda = 232 \text{ }\mu\text{m}$ , pumped with a  $1.93 \text{ }\mu\text{m}$  laser with a  $3 \text{ nm}$  FWHM ( $\sigma_p = 0.64 \times 10^{12} \text{ s}^{-1}$ ) which down-converts to  $3.85 \text{ }\mu\text{m}$  in the signal and idler modes.

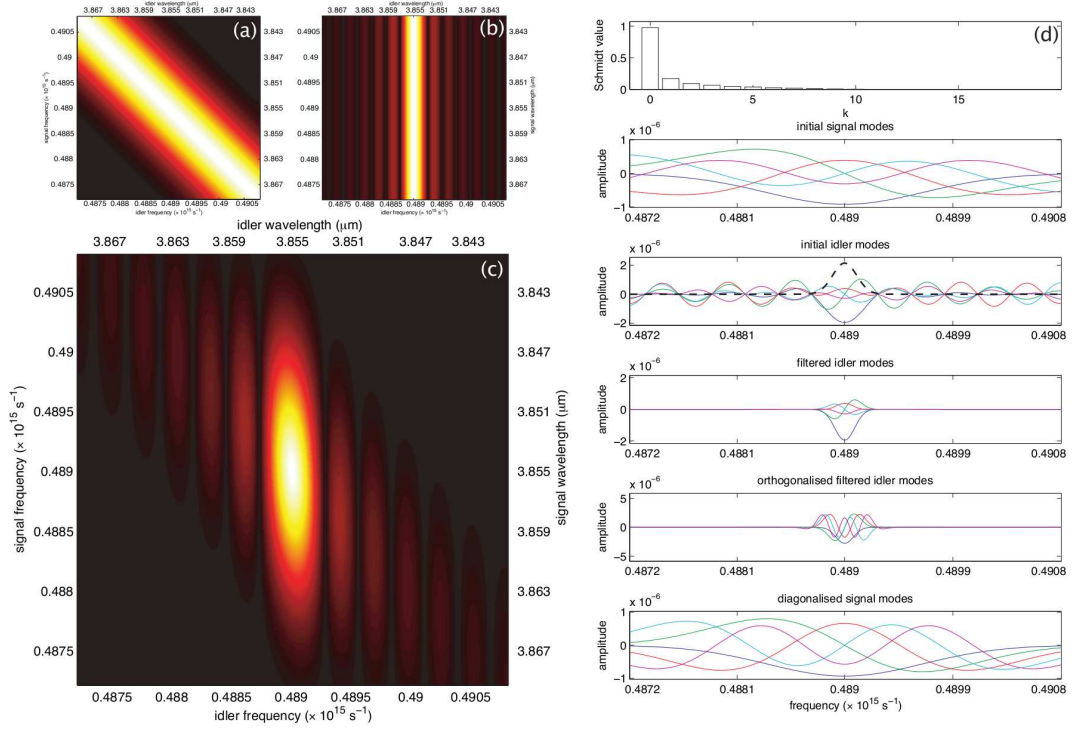


**Figure 4.9:** (a) Gaussian pump function  $\alpha(\omega_i + \omega_s)$  with a 3nm FWHM at  $\mu_p = 1.93 \mu\text{m}$ . (b) Phase matching function  $\Phi(\omega_i, \omega_s)$  for waveguide of length  $L = 80 \text{ mm}$  and a periodicity of  $\Lambda = 232 \mu\text{m}$ . (c) The resulting JSA  $f(\omega_i, \omega_s) = \alpha(\omega_i + \omega_s)\Phi(\omega_i, \omega_s)$ . The JSA has been plotted as a function of the frequency, however corresponding values for the wavelength have been included. (d) Schmidt numbers and modes for the JSA (top to bottom): the first 20 Schmidt numbers  $b_k$ ; the first 5 Schmidt modes  $\xi_k(\omega_s)$  for the signal state; the first 5 Schmidt modes  $\zeta_k(\omega_i)$  for the idler state, as well as a Gaussian filter function of width  $\sigma_f = 100 \times 10^9 \text{ s}^{-1}$  (dashed line); the filtered Schmidt modes  $T(\omega_i)\zeta_k(\omega_i)$  for the idler state; the orthogonalised idler modes  $\phi_j(\omega_i)$ ; the diagonalised signal modes  $\tau_m(\omega_s)$

We note that single-photon detection is not particularly practical at this wavelength, however for consistency, we have chosen to use a ppKTP waveguide throughout this chapter. The same JSA can be achieved in different systems, at more practical wavelengths. See, for example, Mosley *et al.* [31]. Unless stated otherwise, the results in this section were obtained using an  $800 \times 800$  grid, ranging over  $8 \times 10^{12} \text{ s}^{-1}$ , centered around  $\omega_i = \omega_s = \mu$ .

Figure 4.9 shows the JSA and the corresponding Schmidt values and modes. Notice in the Schmidt decomposition that the first mode is even more dominant than in the symmetric case. The entropy of entanglement for this JSA is  $E = 0.37$ .

Setting  $k'_p = k'_s$  generates a vertical phase matching function. As long as the waveguide is sufficiently long, and therefore, the width of the phase matching function

sufficiently thin, and the pump is sufficiently wide, the result will be a vertical, almost elliptical and very thin JSA.

As in the previous section, we present results for the probability, purity,  $g^{(2)}$  and fidelity, for the heralding of one and two photon Fock states. Although it is possible to achieve purities arbitrarily close to unity by increasing the length of the waveguide, the vertical orientation of the JSA places it in a unique position to take advantage of spectral filtering. We will once again compare results for: an unfiltered idler state; an idler state filtered with a Gaussian filter  $T(\omega_i) = \exp(-(\mu_f - \omega_i)/2\sigma_f^2)$ , of various widths  $\sigma_f$  and centered at the central idler frequency; as well as the limiting case where  $T(\omega_i) = \delta(\omega_i - \mu_f)$ .

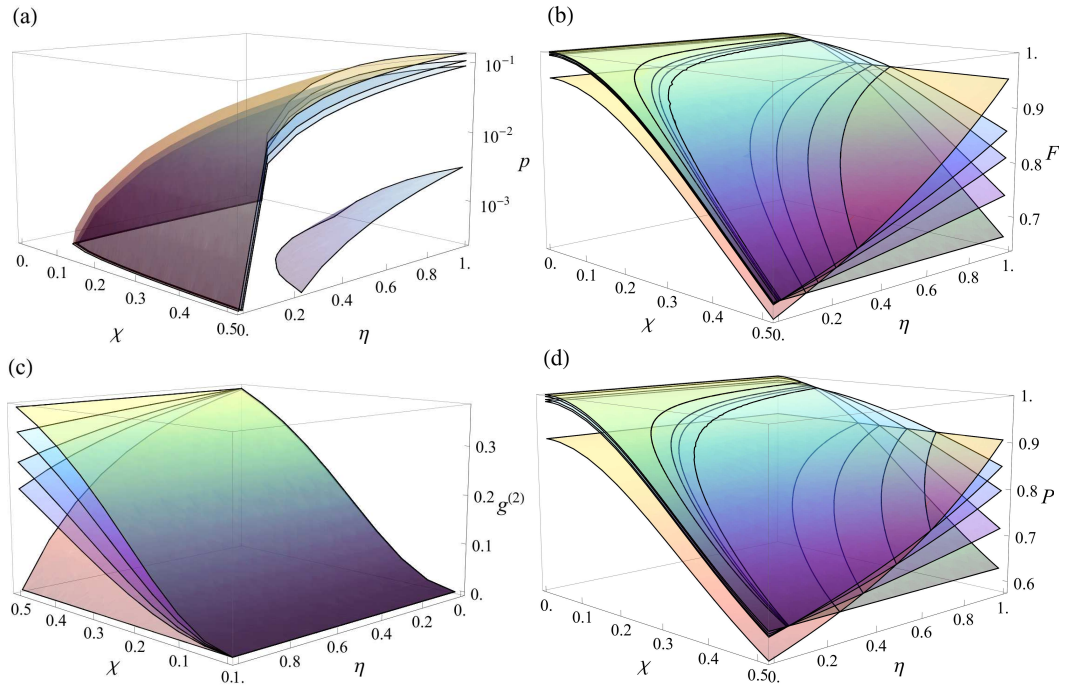
### Generating Single-photon Fock States

Figure 4.10(a) shows the probability of detecting a single photon in the signal mode. Since most of the photons will have spectral distributions within the filter width, we do not see a very big drop in the probability with filtering, until the filter is so narrow that it cuts into the central lobe.

Figure 4.10(b) shows the fidelity. We will distinguish between these surfaces by referring to their values at  $\chi = 0.5$  and  $\eta = 1$ . Again, filtering the idler mode increases the fidelity of the signal state with a single photon in the low- $\chi$  and low- $\eta$  regimes.

Figure 4.10(c) shows the  $g^{(2)}$  and Figure 4.10(d) shows the purity of the state in the signal mode. Again, we will distinguish between these surfaces by referring to their values at the point  $\chi = 0.5$  and  $\eta = 1$ . Results for the filtered case were computed using a  $600 \times 600$  grid, ranging over  $8 \times 10^{12} \text{ s}^{-1}$ , centered around  $\omega_i = \omega_s = \mu$ , and truncating  $b_k$  with values below  $10^{-2}$ .

Figure 4.4 (c) shows the probability of success, and required nonlinearity, for a number of filter widths, in order to achieve a fidelity of  $F = 0.95$ , using a heralding detector with efficiency  $\eta = 0.5$ . Note that, as with the symmetric case, while the probability of success is greatly enhanced by using a source engineered state, the required pump powers are nearly the same. Also notice the ‘‘flat’’ region, where the probability does not change much, between  $\sigma_f = 0.3 \times 10^{12} \text{ s}^{-1}$  and  $0.35 \times 10^{12} \text{ s}^{-1}$ . This corresponds to the ‘‘dark’’ region between the lobes on the JSA. Over this region, we do not expect much change in the flux.



**Figure 4.10:** (a) The probability of detecting a single photon in the idler mode for (top to bottom): no filter;  $\sigma_f = 150 \times 10^9 \text{ s}^{-1}$ ;  $\sigma_f = 100 \times 10^9 \text{ s}^{-1}$ ;  $\sigma_f = 50 \times 10^9 \text{ s}^{-1}$ . Note that the probability is plotted on a log scale. (b) The fidelity of the signal state with an ideal Fock state for (top to bottom at  $\chi = 0.5$  and  $\eta = 1$ ): no filter;  $\sigma_f = 150 \times 10^9 \text{ s}^{-1}$ ;  $\sigma_f = 100 \times 10^9 \text{ s}^{-1}$ ;  $\sigma_f = 50 \times 10^9 \text{ s}^{-1}$ ;  $\sigma_f = 0$ . (c) The  $g^{(2)}$  of the signal state for (top to bottom):  $\sigma_f = 0$ ;  $\sigma_f = 50 \times 10^9 \text{ s}^{-1}$ ;  $\sigma_f = 100 \times 10^9 \text{ s}^{-1}$ ;  $\sigma_f = 150 \times 10^9 \text{ s}^{-1}$ ; no filter. Note the change in axis orientation. (d) The purity of the signal state for (top to bottom at  $\chi = 0.5$  and  $\eta = 1$ ): no filter;  $\sigma_f = 150 \times 10^9 \text{ s}^{-1}$ ;  $\sigma_f = 100 \times 10^9 \text{ s}^{-1}$ ;  $\sigma_f = 50 \times 10^9 \text{ s}^{-1}$ ;  $\sigma_f = 0$ .

### 4.7.3 Generating Two-photon Fock States

We can also analyse the probabilities and fidelities for generating two-photon Fock states. The results are summarised in Figure 4.11. Figure 4.11(a), represents the probability of detecting two photons in the idler mode. The corresponding fidelities and purities have been shown in Figure 4.8(b). They do not vary as a function of  $\chi$  and  $\eta$ .

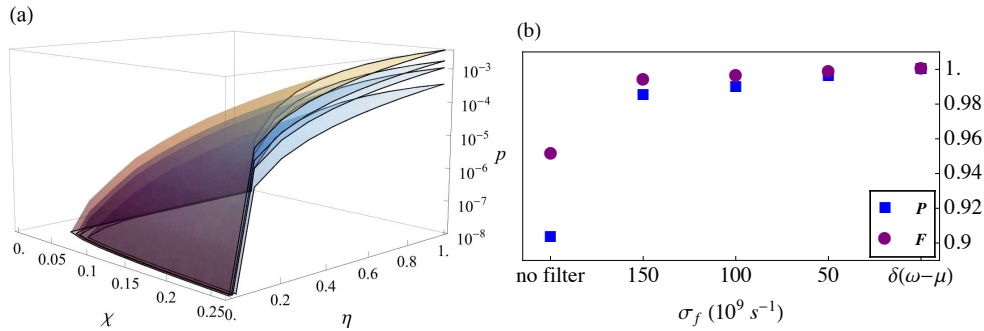


**Figure 4.11:** (a) The probability of detecting two photons in the idler mode for (top to bottom): no filter;  $\sigma_f = 150 \times 10^9$  s $^{-1}$ ;  $\sigma_f = 100 \times 10^9$  s $^{-1}$ ;  $\sigma_f = 50 \times 10^9$  s $^{-1}$ . Note that the probability is plotted on a log scale. (b) The purity and fidelity of the signal state with an ideal Fock state.

## 4.8 Discussion

We have calculated the spectrally entangled output state of a parametric down-converter to second order in photon number, with the goal of generating heralded one- and two-photon Fock states in one spatial mode (signal), conditional on the detection of one or two photons in the other spatial mode (idler). We have presented analytical expressions for the heralded state after the idler mode is spectrally filtered using a Gaussian filter and detected with an inefficient detector. The heralded signal state was then characterised by its  $g^{(2)}$  and purity. In addition, we calculated the fidelity of the heralded state with the desired ideal Fock state.

As a physical example, we modeled a type II ppKTP waveguide, pumped by lasers at wavelengths of 400 nm, 788 nm and 1.93  $\mu$ m. We found that in the first example, where no effort was made to perform any group velocity matching, the results were states with very low purity. After strong spectral filtering, Fock states with arbitrarily high purity could be achieved, however at very low probabilities of success. To achieve a fidelity of  $F = 0.95$  for a single-photon state, using a heralding detector with efficiency  $\eta = 0.5$ , the probability of success would be on the order of  $10^{-4}$ .

---

The latter two examples, which employ group velocity matching, resulted in much higher purity states, however, some additional filtering was still required to achieve very high purity states. Both the symmetric and asymmetric examples were able to achieve a fidelity, with a single-photon Fock state, of  $F = 0.95$ , using a heralding detector with efficiency  $\eta = 0.5$ , with probabilities of success on the order of  $10^{-2}$ . High-purity two-photon Fock states were also possible. While results were comparable for the symmetric and asymmetric examples, this was due to our choice of physical parameters. The asymmetric case would be able to achieve higher fidelities, with no filtering, by choosing a longer waveguide.

In a waveguide, the output modes are collinear with the pump field, resulting in no transverse momentum components. In bulk crystal, where one needs to consider the broad range of momentum vectors in the pump field, a more general treatment (see e.g. [62]) would reveal entanglement between the down-converted modes in the transverse momentum degree of freedom. The consequences of entanglement in this degree of freedom will be similar to those of spectral entanglement: the heralded state will become mixed in the transverse momentum degree of freedom; filtering this degree of freedom will introduce photon-number mixedness in the heralded state.

In this chapter, we modeled spectral filters with Gaussian profiles. Other filter profiles are possible and may be more effective. However, in the scenario considered in this chapter, the dominant effects are strong spectral correlations and subsequent photon-number mixing. Therefore, we do not expect optimisation of the filter shape to provide drastic improvements.



---

# Tailoring the Nonlinearity of a Nonlinear Crystal

---

Photon sources based on spontaneous parametric down-conversion are an ubiquitous tool for quantum computation [42], quantum communication [63] and quantum metrology [64, 65]. They are also becoming increasingly important in more specialised applications such as quantum imaging [66], quantum lithography [67] or optical coherence tomography [68]. As these experiments evolve, more stringent requirements are placed on the characteristics of the created quantum light states. In particular, to produce high-purity heralded, or even near deterministic single photons, the spectral shape and correlations of the created photon pairs must be carefully engineered.

In this chapter, we consider type-II down-conversion in a quasi-phasematched crystal with a longitudinally non-uniform grating. We can synthesise photon pairs with arbitrary spectral amplitudes by modulating the nonlinearity profile  $\chi(z)$  of a crystal through different-order poling *without* changing the phase-matching conditions. We tailor a spectral photon-pair amplitude with a Gaussian profile, which is generally optimal for optical mode matching [36]—a critical consideration in any experiment involving single photons. Although this can be achieved by filtering, this inevitably leads to loss and mixing.

This chapter is organised as follows. In Section 5.1, we introduce the relationship between the nonlinear profile of a crystal and the spectral amplitude of the down-converted photons. In Section 5.2, we design a crystal with a discrete approximation to a Gaussian nonlinearity profile and characterise the custom poled crystal in Section 5.3. We confirm the spectral amplitude of the down-converted photons using two-photon interference experiments in Sections 5.4 and 5.5. In Section 5.6, we numerically show how our method can be applied for attaining one of the currently most important goals of single-photon quantum optics, the creation of pure single photons without spectral correlations. We demonstrate that this technique may be used to generate other spectral profiles, in Section 5.7, before discussing our results

in Section 5.8.

The work in this chapter was done in collaboration with Alessandro Fedrizzi, an experimental physicist in the Quantum Technology Lab at The University of Queensland. Dr Fedrizzi performed the two-photon interference experiments and was involved in writing, and creating figures for, the journal article from which this chapter has been adapted [69]. We both contributed to the journal article in an equal capacity.

## 5.1 Spectral Amplitude of Down-converted Photons

Theoretically, the two-photon state created by down-conversion is described by [70]

$$|\psi\rangle = \int \int d\omega_i d\omega_s f(\omega_i, \omega_s) \hat{a}_i^\dagger(\omega_i) \hat{a}_s^\dagger(\omega_s) |0\rangle \quad (5.1)$$

where  $f(\omega_i, \omega_s) = \alpha(\omega_i + \omega_s) \Phi(\omega_i, \omega_s)$  is the joint spectral amplitude of the created photons in the *idler* and *signal* modes respectively (for details, refer to the Section 2.4). The spectral properties of down-converted photons can be manipulated via the pump envelope function  $\alpha(\omega_i + \omega_s)$  [71], or as we show here, the phase matching function (PMF)  $\Phi(\omega_i, \omega_s)$ . We use a monochromatic pump  $\alpha(\omega_i + \omega_s) = \delta(\omega_i + \omega_s - \mu_p)$  where  $\mu_p$  is the pump frequency, and directly tailor  $\Phi(\omega_i, \omega_s)$ , which is related to the nonlinearity profile of the crystal via the Fourier transform

$$\Phi(\omega_i, \omega_s) = \sqrt{2\pi} \int_{-\infty}^{\infty} \chi(z) e^{-i\Delta k(\omega_i, \omega_s)z} dz \quad (5.2)$$

where  $\chi$  represents the nonlinear coupling which is dominated by the material nonlinearity, and  $\Delta k$  is the phase mismatch, defined in Section 2.4.2. It is sometimes useful to Taylor expand the phase mismatch to first order around the mean idler and signal frequencies,  $\mu_i$  and  $\mu_s$ , such that  $\Delta k(\omega_i, \omega_s) = k'_i(\omega_i - \mu_i) + k'_s(\omega_i - \mu_i) - k'_p(\omega_i + \omega_s - \mu_i - \mu_s)$ .

There are several methods to control the joint spectral amplitudes of photons created in down-conversion in a QPM crystal [38, 72]. For example, imposing a linear chirp on the poling period  $\Lambda$  has been used for the generation of ultra-broad, top-hat shaped photons [68] for optical coherence tomography. However, the currently known methods involve changing  $\Lambda$ , and thus, the often carefully-tailored phase-matching conditions.

According to equation 5.2, the phase matching function of a standard crystal with a uniform nonlinearity profile is  $\Phi(\omega_i, \omega_s) = \text{sinc}(\Delta k L / 2)$ . However, to generate a Gaussian phase matching function, we require a crystal with a Gaussian nonlinearity profile.

## 5.2 Tailoring the Nonlinearity

While it is non-trivial to directly change the material properties, we can make use of higher-order poling to realise a variety of nonlinearity strengths (refer to Section 2.4.3). We exploited this feature to design a crystal consisting of a number of discrete sections, each with a different  $\chi_{\text{eff}}$ , discretely approximating the desired Gaussian shape.

We treat each crystal section  $s$  as a rectangular function with a nonlinearity inversely proportional to the poling order  $m_s$ . The nonlinearity profile for the custom-poled crystal is then given by

$$\chi_{\text{T}}(z) = \sum_{s=1}^N \frac{1}{m_s} u\left(\frac{1}{2} \sum_{r=1}^s m_r n_r \Lambda - z\right) u\left(z - \frac{1}{2} \sum_{r=1}^{s-1} m_r n_r \Lambda\right), \quad (5.3)$$

where  $u$  is the Heaviside step function,  $m_r$  is the poling order of the  $r$ th section,  $n_r$  is the number of domains within the  $r$ th section,  $N$  is the total number of sections and  $\Lambda$  is the poling order. For type-II, first-order QPM of 410 nm→820 nm+820 nm, the poling order is  $\Lambda = 10.85\mu\text{m}$ . Table 5.1 lists the values for  $m$  and  $n$  used for the tailored Gaussian crystal.

$s$	$m$	$n$	$D$ (%)	$s$	$m$	$n$	$D$ (%)
1, 21	32	2	50	7, 15	5	3	50
2, 20	15	2	25	8, 14	4	8	50
3, 19	11	2	50	9, 13	3	12	50
4, 18	9	2	37.5	10, 12	2	45	50
5, 17	7	2	50	11	1	257	48.4
6, 16	6	2	41.6				

**Table 5.1:** Values for poling order  $m$ , domain number  $n$  and Duty cycle  $D$  used to generate a discrete approximation to a Gaussian nonlinearity profile.

According to equation 5.2, the joint spectral amplitude of the down-converted photons from the tailored crystal will be

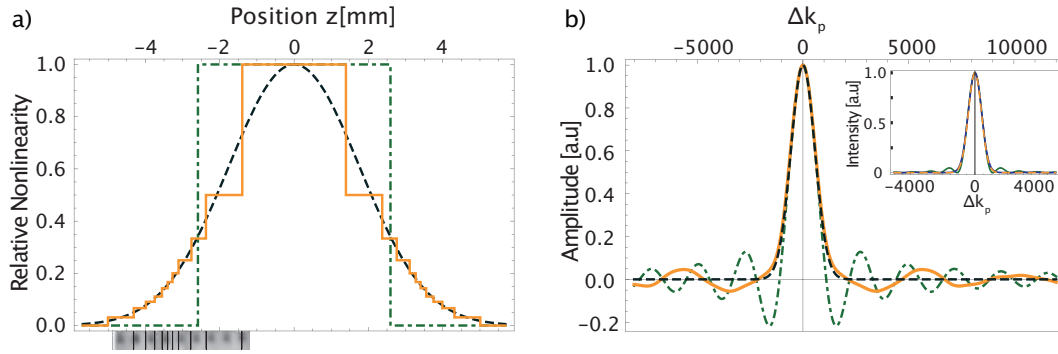
$$\Phi_{\text{T}}(\Delta k) = \sum_{s=1}^N \frac{1}{m_s} \left( \exp\left(-i\Delta k \frac{1}{2} \sum_{r=1}^s m_r n_r \Lambda\right) - \exp\left(i\Delta k \frac{1}{2} \sum_{r=1}^{s-1} m_r n_r \Lambda\right) \right). \quad (5.4)$$

Figure 5.1a) shows the tailored nonlinearity profile  $\chi_{\text{T}}(z)$ , defined in equation (5.3), superimposed with the target Gaussian profile  $\chi_{\text{G}}(z)$ . The corresponding PMF

$\Phi_T(\Delta k)$  is very similar to a Gaussian function, as shown in Figure 5.1b). Compared to the sinc-shaped phase matching function of a ppKTP of the same *effective* length as the cpKTP (5.67 mm), the side lobes on either side of the central peak are significantly suppressed. This becomes even more evident when considering the spectral intensity (see inset).

The design of the nonlinearity profile is subject to a number of constraints. First of all, the nonlinearity of each section is limited to discrete values proportional to  $1/m$ . Larger values of  $m$  provide smoother transitions between successive nonlinearites, however this leads to a greatly reduced photon creation rate. Second, the width of each section must be an integer number of  $m\Lambda/2$  and a minimum of  $2m\Lambda$ , therefore, larger values of  $m$  may demand prohibitively long sections. The ratio between positively and negatively poled regions—known as the duty cycle  $D = l/m\Lambda$  where  $l$  is the length over which the sign of the nonlinear coefficient remains constant—was chosen to be 50% for odd values of  $m$  and as close as possible to 50% for even values, as is shown in Table 5.1.

While the basic model presented here is strictly not valid due to the small number of domains within each section of  $\chi_T(z)$ , detailed modeling (refer to Appendix A.2) reveals a strong agreement with the basic model, in the region of interest, i.e. around  $\Delta k_p = 0$ . The detectors used in the above experiment are mainly sensitive to the frequency range over which the two models are in agreement and therefore the basic model is sufficient for comparison with experiment. The broad spectral filtering



**Figure 5.1:** a) Nonlinearity profile for the cpKTP crystal  $\chi_T(z)$  (solid yellow line) and target Gaussian profile  $\chi_G(z) = \exp(-(z/L_{\text{eff}})^2/\gamma)$  (black dashed line) with effective length  $L_{\text{eff}} = 5.67$  mm (green dot-dashed line) and  $\gamma \approx 0.193$  (see Appendix A.1). b) Phase-matching function amplitudes and intensities (inset) for the cpKTP (yellow solid line) compared to a ppKTP of the same *effective* length  $L_{\text{eff}}$  (green dot-dashed line) and target Gaussian profile  $\Phi_G(\omega_i, \omega_s) = \exp(-\gamma(\Delta k L/2)^2)$  (black dashed line). An image of part of the actual cpKTP crystal (see Figure 5.2) is shown below figure a).

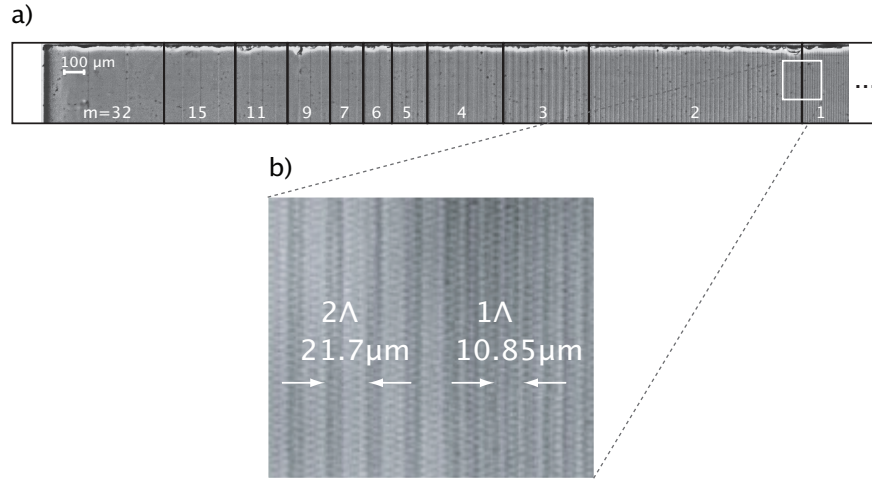


**Figure 5.2:** a) Magnified image of part of the custom-poled KTP crystal. Vertical lines separate sections with constant nonlinearity, with their poling order  $m$ , length  $L$  and poling duty cycle  $D$ . b) Zoom into the transition from poling order  $m = 1$  to  $m = 2$ . The crystal was custom-ordered from *Raicol Crystals Ltd.*, [www.raicol.com](http://www.raicol.com). Due to a slight mismatch between design and actual domain lengths, the crystal was shortened by a few tens of  $\mu\text{m}$  on one side.

which, in effect, is imposed by the spectral response of the detector will not give rise to the photon-number mixing described in Chapter 4, as this is brought on by edge effects of the filter. The edges of the spectral response function of the detectors used in this experiment lie in the region of negligible amplitude.

### 5.3 The Custom-poled Crystal

A 10 mm long Potassium Titanyl Phosphate (cpKTP) crystal was custom-poled according to the design put forward in the previous section. A microscopic image of part of the cpKTP crystal is shown in Figure 5.2a). One can clearly see the individual sections with different poling orders, which line up with the theoretical design almost perfectly. Figure 5.2b) shows a magnified view of a transition between poling-order sections  $m=1$  and  $m=2$ .

The custom-poled crystal was tested in a typical down-conversion setup, see Figure 5.3, and compared to a 10 mm long ppKTP crystal ( $\Lambda=10.95 \mu\text{m}$ ). The custom-poling technique decreases the overall nonlinearity and reduces the *effective* length of the structure (see Appendix A.1). Therefore, a lower photon-pair yield and broader bandwidths when compared to a standard periodically poled KTP (ppKTP) with the same length and phase-matching, are expected. For the two crystals, we expected a relative photon pair rate of 34.4%. The measured detection rate (detected

without a beam-splitter) was  $\sim 10$  kpairs/s for the tailored and  $\sim 33$  kpairs/s for the standard crystal, respectively. This corresponds to a relative yield of  $\sim 30.4\%$ ; we attribute the small reduction in efficiency to the fact that the custom-poled crystal, in contrast to our standard crystal, was not anti-reflection coated.

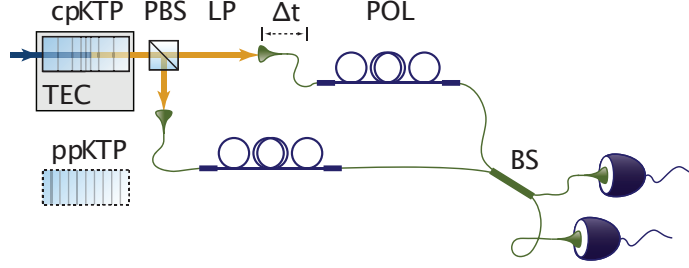


**Figure 5.3:** a) Experimental scheme. The nonlinear crystals (cpKTP, ppKTP) were temperature-stabilised with a thermoelectric element (TEC) and pumped by a 410 nm, grating-stabilised diode laser. The emitted orthogonally polarised photon pairs were split at a polarising beamsplitter (PBS) and coupled into single-mode fibres. They passed two fibre polarisation-controllers (POL) before they were superposed at a 50/50 fiber beamsplitter (BS). The photons were then detected by two avalanche single-photon detectors within a coincidence time window of 4.4 ns. We obtained two-photon interference patterns by changing the relative delay  $\Delta t$  between the photons with a motorised translation stage. The only filters in use were two RG715 long-pass filters (LP).

## 5.4 Two-photon Interference

The joint spectral amplitude of photons created in the cpKTP was verified in a two-photon interference experiment. When two indistinguishable photons hit a symmetric beamsplitter, they will always be found in the same output port. This phenomenon was first reported in the landmark experiment by Hong, Ou and Mandel [61], who observed a drop of the coincidence photon count probability behind a beam splitter as a function of the temporal delay between the photons. A beam-splitter of transmittivity  $\eta = 1/2$ , followed by a time delay  $\Delta t$  can be modeled via the transformation

$$\hat{a}_i^\dagger(\omega_i) \rightarrow \frac{1}{\sqrt{2}} (e^{it_1\omega_i} \hat{b}_1^\dagger(\omega_i) - ie^{i(t_2+\Delta t)\omega_i} \hat{b}_2^\dagger(\omega_i)), \quad (5.5)$$

$$\hat{a}_s^\dagger(\omega_s) \rightarrow \frac{1}{\sqrt{2}} (-ie^{i(t_1-\Delta t)\omega_s} \hat{b}_1^\dagger(\omega_s) + e^{it_2\omega_s} \hat{b}_2^\dagger(\omega_s)). \quad (5.6)$$

Applying this to the state in equation 5.1, gives

$$|\psi\rangle = \frac{1}{2} \int \int d\omega_i d\omega_s f(\omega_i, \omega_s) \times \left( e^{it_1\omega_i} e^{it_2\omega_s} \hat{b}_1^\dagger(\omega_i) \hat{b}_2^\dagger(\omega_s) - e^{i(t_2+\Delta t)\omega_s} e^{i(t_1-\Delta t)\omega_i} \hat{b}_2^\dagger(\omega_i) \hat{b}_1^\dagger(\omega_s) \right) |0\rangle \quad (5.7)$$

where only terms corresponding to a single photon in each mode have been retained and  $f(\omega_i, \omega_s) = \alpha(\omega_i + \omega_s) \Phi(\omega_i, \omega_s)$ .

For a monochromatic pump, we make the substitution  $\alpha(\omega_i + \omega_s) \rightarrow \delta(\omega_i + \omega_s - \mu_p)$ . We also define  $\omega_s = (\mu_p - \nu)/2$  to give

$$\begin{aligned} |\psi\rangle &= \frac{1}{2} \int d\nu \Phi\left(\frac{\mu_p + \nu}{2}, \frac{\mu_p - \nu}{2}\right) \left( e^{it_1(\frac{\mu_p + \nu}{2})} e^{it_2(\frac{\mu_p - \nu}{2})} \hat{b}_1^\dagger\left(\frac{\mu_p + \nu}{2}\right) \hat{b}_2^\dagger\left(\frac{\mu_p - \nu}{2}\right) \right. \\ &\quad \left. - e^{i(t_2 + \Delta t)(\frac{\mu_p + \nu}{2})} e^{i(t_1 - \Delta t)(\frac{\mu_p - \nu}{2})} \hat{b}_2^\dagger\left(\frac{\mu_p + \nu}{2}\right) \hat{b}_1^\dagger\left(\frac{\mu_p - \nu}{2}\right) \right) |0\rangle \quad (5.8) \\ &= \frac{e^{i(\frac{t_1 + t_2}{2})}}{2} \int d\nu \Phi\left(\frac{\mu_p + \nu}{2}, \frac{\mu_p - \nu}{2}\right) \\ &\quad \times \left( e^{it\nu} \hat{b}_1^\dagger\left(\frac{\mu_p + \nu}{2}\right) \hat{b}_2^\dagger\left(\frac{\mu_p - \nu}{2}\right) - e^{-i(t - \Delta t)\nu} \hat{b}_2^\dagger\left(\frac{\mu_p + \nu}{2}\right) \hat{b}_1^\dagger\left(\frac{\mu_p - \nu}{2}\right) \right) |0\rangle \quad (5.9) \end{aligned}$$

where  $t = (t_1 - t_2)/2$ . The probability amplitude for detecting one photon in each down-conversion mode is

$$a(t, \Delta t) = \frac{e^{i(\frac{t_1 + t_2}{2})}}{2} \int d\nu \Phi\left(\frac{\mu_p + \nu}{2}, \frac{\mu_p - \nu}{2}\right) \left( e^{it\nu} - e^{-i(t - \Delta t)\nu} \right) \quad (5.10)$$

$$= \frac{e^{i(\frac{t_1 + t_2}{2})}}{2} \left( \hat{\mathcal{F}}\left(\frac{t}{2\pi}\right) - \mathcal{F}\left(\frac{t - \Delta t}{2\pi}\right) \right), \quad (5.11)$$

where  $\mathcal{F}(x) = \int_{-\infty}^{\infty} d\xi f(\xi) e^{-i2\pi x\xi}$  is the Fourier transform and  $\hat{\mathcal{F}}$  is the inverse Fourier transform. The coincidence detection probability is therefore

$$pc(\Delta t) = \frac{a_0}{2} \int dt \left| \hat{\mathcal{F}}\left(\frac{t}{2\pi}\right) - \mathcal{F}\left(\frac{t - \Delta t}{2\pi}\right) \right|^2, \quad (5.12)$$

where  $a_0 = 1/(\int dt |\hat{\mathcal{F}}(t/2\pi)|^2 + \int dt |\mathcal{F}((t - \Delta t)/2\pi)|^2)$  is the normalisation constant.

To calculate the coincidence probability from the phase matching function (PMF) of a standard crystal, we make the substitution  $\Phi(\omega_i, \omega_s) = \text{sinc}(\Delta k L/2) \rightarrow \text{sinc}((\nu - \mu(T))/\xi)$  where  $\nu = \omega_i - \omega_s$ ,  $\mu = \mu_i - \mu_s$  and  $\xi = 4/(L(k'_i - k'_s))$  is directly connected to the spectral single-photon bandwidth  $\Delta\omega$  via  $\xi = 2\Delta\omega/\pi$  [73]. Substituting this into equation 5.12 and evaluating the time integral, we get the coincidence probability for a standard crystal

$$p_{c_{pp}}(\Delta t, \mu) = \begin{cases} \frac{1}{2} \left( 1 - \frac{\zeta}{2\mu} \sin\left(\frac{\mu}{\zeta}(2 - \zeta|\Delta t|)\right) \right) & \text{for } |\Delta t| < \frac{2}{\zeta} \\ \frac{1}{2} & \text{otherwise} \end{cases} \quad (5.13)$$

The coincidence probability for the custom poled crystal can be similarly calculated from equation 5.12 using the phase matching function in equation 5.4.

The recorded interference patterns for the cpKTP, and the standard ppKTP are shown in Figure 5.4, along with the theoretical interference patterns calculated straight from the PMFs in Figure 5.1b). The differing bandwidths result from the different *effective* lengths of the two crystals. The interference pattern for the standard crystal is triangular, just as expected for the sinc-shaped PMF [73]. The pattern for the tailored crystal departs from the triangular shape and indeed approximates a Gaussian. The interference visibility was  $\sim 95\%$  for both crystals, confirming that the modulation of the nonlinearity did not have negative effects on the distinguishability of the photons.

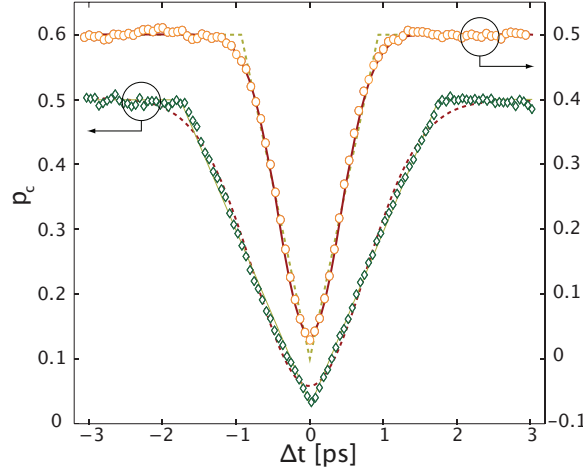


**Figure 5.4:** Two-photon interference patterns for the cpKTP crystal (yellow circles, top curve) compared to a standard ppKTP (green diamonds, bottom curve). The red lines show the theoretical values, calculated directly from the respective PMF for each crystal, with the interference visibility as the single free parameter. The reduced chi-square values of these fits are 3.07 and 5.51, respectively. The grey lines show least-square fits of a triangular pattern to the tailored crystal data and a Gaussian fitted to the normal crystal, with reduced chi-square values of 50.59 and 23.10, respectively, underlining the strong divergence from these shapes. Coincidence probabilities  $p_c$  were obtained by normalising detected pairs to twice the averaged counts outside the coherence length. All error bars are smaller than symbol size.

## 5.5 Quantum Beating

To further explore the underlying spectral correlations in the PMF, we measured spatial quantum beating patterns. We detuned the center frequencies of the down-conversion photons via a change in crystal temperature [73] away from its optimal value for collinear, degenerate quasi-phase-matching and again observed two-photon interference. The results in Figure 5.5 show that the tailored crystal shows less distinct beating, in particular, less anti-bunching, i.e. coincidence probability values above the random level of 0.5. The maximum value for the cpKTP was  $0.546 \pm 0.005$  compared to  $0.586 \pm 0.003$  for the standard crystal, a significant reduction relative to the base-line of 0.5. The theory values for a) were obtained directly from [73], while for b), we followed the calculation in [73] using the PMF for our tailored crystal, Figure 5.1b).

The observed anti-bunching occurs when the frequency-detuned spectral wavefunction, essentially the joint spectral amplitude, of the two-photon state is partially anti-symmetric, which in turn reveals the frequency entanglement intrinsic to down-conversion [74, 73, 75]. A Gaussian spectral amplitude is always positive and therefore does not have anti-symmetric components, which explains the reduced beating in the interference patterns of the custom-poled crystal.

From these measurements, we conclude that the actual PMF agrees exceedingly well with the theory prediction. It is not truly Gaussian, but a very good approximation.

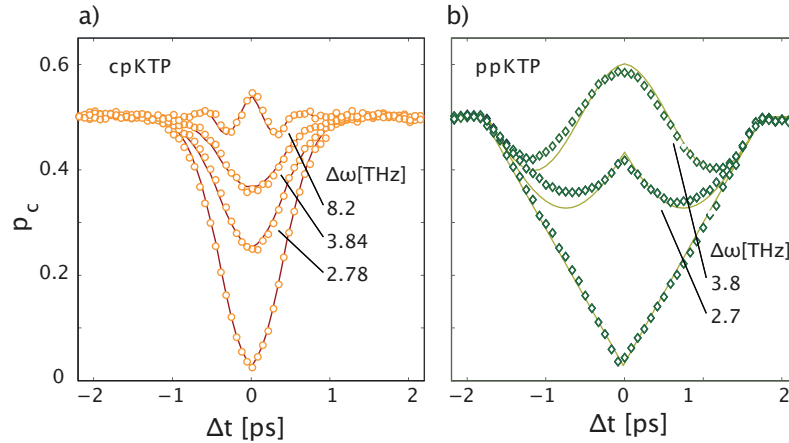


**Figure 5.5:** Spatial quantum beating for the cpKTP (a) and the ppKTP (b) crystals, for various center-frequency detunings  $\Delta\omega = \omega_i - \omega_s$ . The lines show the ideal values, calculated from the respective PMF, with the interference visibility ( $\sim 0.95$ ) as the single free parameter. Coincidence probabilities  $p_c$  were obtained by normalising detected pairs to twice the averaged counts outside the coherence length. All error bars are smaller than symbol size.

## 5.6 Separable Joint Spectral Amplitude

One situation in which we expect this method to be quite useful is the generation of pure heralded single photons. In Chapter 4, we saw that down-converted single-photons have strong spectral correlations which result in the degraded purity of a heralded state. These correlations can be reduced by filtering the heralded mode, however, spectral filtering is undesirable because it lowers the overall single-photon production rate as well as introducing photon-number mixedness which limits the allowable pump intensity.

We show that, in combination with our method of modulating the crystal nonlinearity, group velocity matching can be used to create high-purity single photon states without the use of spectral filtering. We consider the group velocity matched scenario introduced in Section 4.7.1. For type-II, first-order QPM in KTP, these group velocity conditions are met for a poling order  $\Lambda = 68.4\mu\text{m}$  pumped at  $788\text{ nm} \rightarrow 1.58\mu\text{m} + 1.58\mu\text{m}$ . Recall that these conditions generated an almost symmetric JSA with side lobes which degraded the purity of the heralded photons.

To eliminate the side lobes, we want to generate a Gaussian PMF,  $\Phi_G(\omega_i, \omega_s) = \exp(-\gamma(\Delta k L/2)^2)$ , whose FWHM matches that of the PMF generated by a standard crystal,  $\Phi(\omega_i, \omega_s) = \text{sinc}(\Delta k L/2)$ . We designed two discrete approximations to the desired Gaussian profile—the first with a minimum poling order  $m_{\min} = 1$ , and the second with a minimum poling order  $m_{\min} = 2$ . The later crystal has a lower overall nonlinearity, but offers a finer discretisation. Figure 5.6 shows the nonlinearity profiles for both crystals and the corresponding phase matching functions, generated using equations 5.3 and 5.4 respectively, using the values for the poling order  $m$  and domain number  $n$  given in Table 5.2.

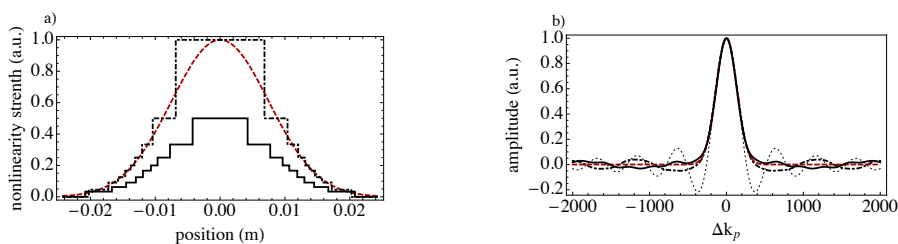


**Figure 5.6:** a) Nonlinearity profiles and b) corresponding PMFs for:  $m_{\min} = 1$  tailored crystal (solid black line);  $m_{\min} = 2$  tailored crystal (dot-dashed black line); and an ideal crystal with a Gaussian profile (dashed red line). The corresponding sinc PMF (thin dotted line) has been included for comparison.

As we saw in Section 4.7.1, for a typical group-velocity-matched configuration with a symmetric joint spectral amplitude, the maximum purity a heralded single photon state can achieve is 0.81 (assuming no spectral filtering), due to the typical sinc

$m_{\min} = 1$			$m_{\min} = 2$		
s	m	n	s	m	n
1, 17	22	2	1, 17	30	2
2, 16	11	2	2, 16	16	2
3, 15	8	2	3, 15	11	2
4, 14	6	2	4, 14	8	2
5, 13	5	2	5, 13	6	3
6, 12	4	4	6, 12	5	3
7, 11	3	8	7, 11	4	7
8, 10	2	26	8, 10	3	17
9	1	100	9	2	21

**Table 5.2:** Values for poling order  $m$ , domain number  $n$  used to generate a discrete approximation to a Gaussian nonlinearity profile

profile of the PMF. Using equation 4.27 to calculate the purity of the heralded photon, we numerically compare two designs for cpKTP crystals (see Figure 5.6), with a standard ppKTP crystal following the method in Chapter 4. Table 5.3 shows the calculated purities for our two designs compared with a standard periodically poled crystal.

Crystal	$L$ (mm)	$p$
ppKTP	24.2	0.81
cpKTP $m_{\min} = 1$	40.5	0.97
cpKTP $m_{\min} = 2$	41.6	0.99

**Table 5.3:** Numerical comparison of the purity  $p$  of heralded single-photons of a standard crystal and two cpKTP crystals of length  $L$ . Note that the effective length of both cpKTP crystals is  $L_{\text{eff}} = 24.2\text{mm}$

## 5.7 Arbitrary Phasematching Functions

The method introduced in this chapter can be applied to the generation of arbitrarily shaped phase matching functions. As described above, the nonlinearity profile of the crystal should be tailored to the Fourier transform of the desired PMF. Figure 5.7a) shows an example of a discrete approximation to a sinc function nonlinearity profile, which can be generated from the expression in equation 5.2 using the values for the poling order  $m$  and domain number  $n$  in Table 5.4. The resulting approximate triangular nonlinearity profile, generated from equation 5.3, is shown in figure 5.7b).

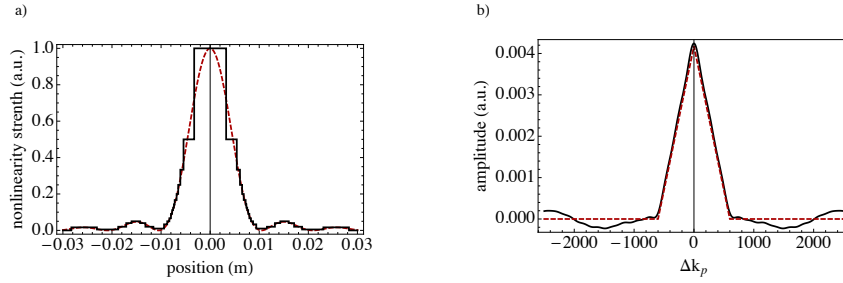


**Figure 5.7:** a) Nonlinearity profile for a tailored crystal (solid black line) and target  $\text{sinc}^2(z)$  function (dashed red line). b) Phase matching functions for a tailored crystal (solid black line) and target triangular shaped function (dashed red line).

Figure 5.8a) shows an example of a discrete approximation to a  $\text{sinc}^2$  function nonlinearity profile. Notice that the  $\text{sinc}^2$  function contains negative values of the nonlinearity. Negative values can be implemented by inverting the relevant domain [38]. Effectively, this consists of picking the poling order required for the equivalent positive nonlinearity and then flipping the direction. The resulting approximate square nonlinearity profile, generated from equation 5.3, is shown in figure 5.7b).

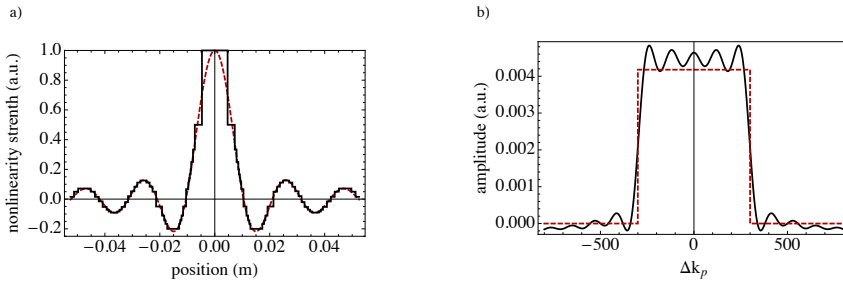


**Figure 5.8:** a) Nonlinearity profile for a tailored crystal (solid black line) and target  $\text{sinc}(z)$  function (dashed red line). b) Phase matching functions for a tailored crystal (solid black line) and target top-hat function (dashed red line).

triangle			square					
s	m	n	s	m	n	s	m	n
1, 41	60	8	1, 81	65	2	22, 60	20	6
2, 40	200	2	2, 80	20	7	23, 59	20*	10
3, 39	50	3	3, 79	14	30	24, 58	9*	8
4, 38	25	4	4, 78	20	7	25, 57	7*	6
5, 37	20	8	5, 77	65	2	26, 56	6*	10
6, 36	25	4	6, 76	65*	2	27, 55	5*	80
7, 35	50	3	7, 75	19*	7	28, 54	6*	6
8, 34	100	2	8, 74	14*	5	29, 53	7*	6
9, 33	30	2	9, 73	12*	6	30, 52	9*	6
10, 32	20	2	10, 72	11*	20	31, 51	20*	5
11, 31	15	2	11, 71	12*	6	32, 50	15	5
12, 30	11	2	12, 70	14*	5	33, 49	9	2
13, 29	9	2	13, 69	19*	6	34, 48	8	2
14, 28	8	2	14, 68	50*	2	35, 47	7	2
15, 27	7	2	15, 67	50	2	36, 46	6	5
16, 26	6	6	16, 66	19	6	37, 45	5	4
17, 25	5	6	17, 65	12	8	38, 44	4	15
18, 24	4	10	18, 64	9	12	39, 43	3	20
19, 23	3	20	19, 63	8	25	40, 42	2	120
20, 22	2	100	20, 62	9	12	41	1	430
21	1	300	21, 61	12	8			

**Table 5.4:** Values for poling order  $m$  and domain number  $n$  used to generate discrete approximations to triangular and top-hat nonlinearity profiles. \* denotes that the domain should be flipped to generate a negative effective nonlinearity.

## 5.8 Discussion

We demonstrated Gaussian shaping of single-photon wave-packets via indirect modulation of the nonlinearity of a crystal. Our method can be used to generate other phase-match profiles of interest, such as a triangle or a top-hat. The observed two-photon interference patterns agree perfectly—within error—with theoretical predictions.

The most important application of this technique is related to the creation of heralded single photons—we have shown numerically that the Gaussian shape we tailor leads to a drastic improvement in the purity of heralded single photons. The reduction in the effective nonlinearity, and thus pair yield, is an acceptable tradeoff given that modern crystals have drastically reduced the pump power requirements in recent experiments. In return, compared to the simpler alternative of just filtering out the lobes, one can pump at a higher power without introducing photon number mixedness, and therefore create purer higher-photon-number Fock states. We expect this technique to be applicable in any scenario where periodic poling is already in use, however, there may be certain materials for which the refractive index and pumping wavelength result in a large poling period. This would either have an effect on the quality of the approximation to the nonlinearity profile, and therefore, the purity of the heralded photon or result in prohibitively long crystals.

It would be interesting to apply our idea of an engineered material nonlinearity to four-wave-mixing photon-pair sources in photonic-crystal fibres, where the sinc-shaped phase-matching function is a major problem. In [76], for example, the authors observe a two-photon interference visibility reduction of 20%, which they attribute to this phenomenon. However, it is already non-trivial to achieve group-velocity matching in photonic-crystal fibres in the first place and modulating the non-linearity will inevitably come at the expense of a change of phase-matching conditions.

---

# Time Ordering in Spontaneous Parametric Down-conversion

---

In order to study the spectral properties of the down-conversion process, one needs to examine the evolution within the crystal. The time dependent Hamiltonian, which governs this evolution, does not commute with itself at all times, as is shown in Appendix B.1. Recall from Section 2.1.2, that this implies that the expansion of the evolution operator, and therefore the output state, should take the form of the time-ordered *Dyson* series.

The spectral properties of the down-converted state have been extensively analysed to first order in the output state, see e.g. [37]. To first order, a simple Taylor expansion gives the same results as the Dyson series—when only one pair is created, time ordering is not relevant. In this chapter, however, we consider the output state to higher orders, truncating the output state beyond the 6-photon term.

As prescribed, we take the Dyson series expansion, however, it would be considerably easier for future calculations to use the Taylor series. We therefore aim to identify if there are any conditions under which the Taylor series is a good approximation.

As expected, the Taylor series predicts higher-order states that consist of uncorrelated pairs of photons—the two photons in each pair are entangled in frequency, but the pairs are independent from each other. The Dyson series, however, predicts four-photon frequency-entangled states at second order and six-photon frequency-entangled states at third order. Interference between the fields within the crystal leads to some cancellation of the amplitudes. At second order, this leaves a two-photon state identical to that predicted by the Taylor series. At third order, there is a difference between the two series, as will be discussed within this chapter.

This chapter is organised as follows. In Section 6.1, we introduce the Taylor and Dyson series expansions of the down-converted state. In Section 6.2, we evaluate the state according to the Dyson series. In Section 6.3, we compare these results with those predicted by the Taylor series expansion. In Section 6.4, we conclude.

## 6.1 Type II SPDC Hamiltonian

Recall from equation 2.67 that the down-converted state is given by

$$|\psi_{\text{PDC}}\rangle = \mathcal{T} e^{-\frac{i}{\hbar} \int_{-\infty}^{\infty} dt \hat{H}(t)} |\psi(t_0)\rangle. \quad (6.1)$$

where  $\mathcal{T}$  is the time-ordering operator and the Hamiltonian is

$$\hat{H}(t) = AL \iiint d\omega_i d\omega_s d\omega_p f(\omega_i, \omega_s, \omega_p) e^{i\Delta\omega t} \hat{a}_i^\dagger(\omega_i) \hat{a}_s^\dagger(\omega_s) + \text{H.c.}, \quad (6.2)$$

where

$$f(\omega_i, \omega_s, \omega_p) = \alpha(\omega_p) \Phi(\Delta k(\omega_i, \omega_s, \omega_p)), \quad (6.3)$$

is the joint spectral amplitude,  $\alpha(\omega_p)$  is the pump function and

$$\Phi(\Delta k(\omega_i, \omega_s, \omega_p)) = \text{sinc}\left(\frac{1}{2} \Delta k(\omega_i, \omega_s, \omega_p) L\right) \quad (6.4)$$

is the phase-matching function.  $\Delta k(\omega_i, \omega_s, \omega_p) = k_i(\omega_i) + k_s(\omega_s) - k_p(\omega_p)$  is the phase mismatch and  $\Delta\omega = \omega_i + \omega_s - \omega_p$ .

The Taylor and Dyson series expansions give the state in equation 2.63 to third order, as follows.

$$\begin{aligned} |\Psi_{\text{PDC}}\rangle_{\text{T}} &\approx \frac{1}{\sqrt{\mathcal{N}_{\text{T}}}} \left( |0\rangle + \frac{1}{i\hbar} \int_{-\infty}^{\infty} dt_1 \hat{H}(t_1) |0\rangle \right. \\ &\quad + \frac{1}{2} \left( \frac{1}{i\hbar} \right)^2 \int_{-\infty}^{\infty} dt_1 \hat{H}(t_1) \int_{-\infty}^{\infty} dt_2 \hat{H}(t_2) |0\rangle \\ &\quad \left. + \frac{1}{3!} \left( \frac{1}{i\hbar} \right)^3 \int_{-\infty}^{\infty} dt_1 \hat{H}(t_1) \int_{-\infty}^{\infty} dt_2 \hat{H}(t_2) \int_{-\infty}^{\infty} dt_3 \hat{H}(t_3) |0\rangle \right). \end{aligned} \quad (6.5)$$

$$\begin{aligned} |\Psi_{\text{PDC}}\rangle_{\text{D}} &\approx \frac{1}{\sqrt{\mathcal{N}_{\text{D}}}} \left( |0\rangle + \frac{1}{i\hbar} \int_{-\infty}^{\infty} dt_1 \hat{H}(t_1) |0\rangle \right. \\ &\quad + \left( \frac{1}{i\hbar} \right)^2 \int_{-\infty}^{\infty} dt_1 \hat{H}(t_1) \int_{-\infty}^{t_1} dt_2 \hat{H}(t_2) |0\rangle \\ &\quad \left. + \left( \frac{1}{i\hbar} \right)^3 \int_{-\infty}^{\infty} dt_1 \hat{H}(t_1) \int_{-\infty}^{t_1} dt_2 \hat{H}(t_2) \int_{-\infty}^{t_2} dt_3 \hat{H}(t_3) |0\rangle \right). \end{aligned} \quad (6.6)$$

where  $|\Psi_{\text{PDC}}\rangle_{\text{T}}$  and  $|\Psi_{\text{PDC}}\rangle_{\text{D}}$  are the truncated states according to the Taylor and Dyson series respectively.  $\mathcal{N}_{\text{T}}$  and  $\mathcal{N}_{\text{D}}$  are normalisation constants which ensure that the probabilities sum to unity. Notice that the first and second terms are the same

for both states, while the third and fourth terms differ by a scaling factor and the integration limits. The Dyson series correctly orders events, while the Taylor series considers all ordering equivalent and then rescales.

Consider the second order term of the Dyson series (the third term in equation 6.6). The limits of integration represent an ordering of the time variables  $t_1$  and  $t_2$ , such that  $t_1 > t_2$ , as shown by the shaded integration region in Figure 6.1 a).

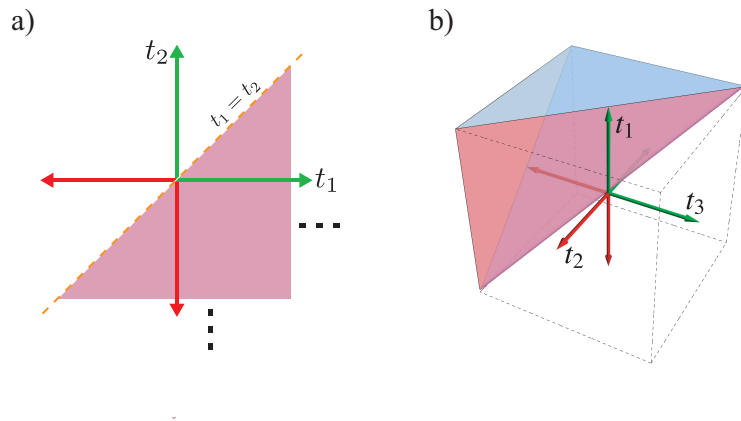


**Figure 6.1:** Integration region for a) second order term and b) third order term. The integration regions continue to infinity beyond the limits of the plotting region.

This specifies the particular time order in which the two pairs are created. This scenario is represented by the cartoon in figure 6.2 a).

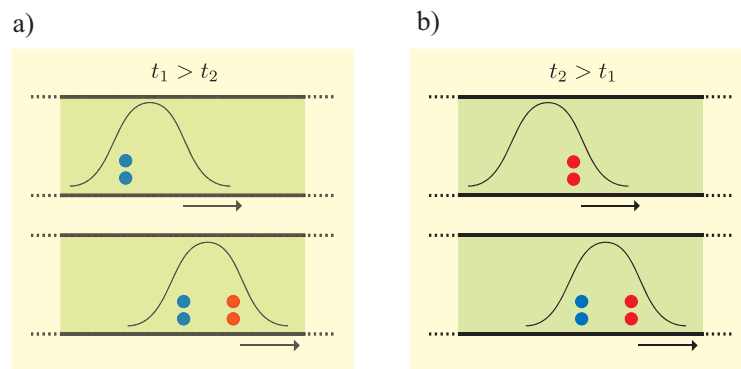


**Figure 6.2:** Cartoon depicting the different permutations of the order in which two pairs of photons are created, as the pump field propagates along the length of the crystal. Unlike the Dyson series, the Taylor series does not distinguish between the events in a) and b)

If it were the case that the Hamiltonian *did* commute with itself at all times then  $\hat{H}(t_1)\hat{H}(t_2)$  would equal  $\hat{H}(t_2)\hat{H}(t_1)$ . It wouldn't matter which pair was created first and therefore the two scenarios presented in figure 6.2 a) and b) would be indistinguishable. Considering one permutation would be equivalent to taking the sum of all permutations and dividing by that number—in this case, two. The advantage of doing so is that the time integration can be taken to be over all time, rendering the integrals much simpler. This is effectively what is done when using the Taylor series.

Similarly, at third order, there are six possible permutations of the three Hamiltonians. The Dyson series expansion considers only one particular permutation, where  $t_1 > t_2 > t_3$ , as shown by the shaded integration region in Figure 6.3 b), while the Taylor series doesn't distinguish between them and therefore considers the average of all six of the permutations shown in figure 6.3. As a sanity check, we confirm that the sum of all six permutations yields the same results for both series. This can be found in Appendix B.2.

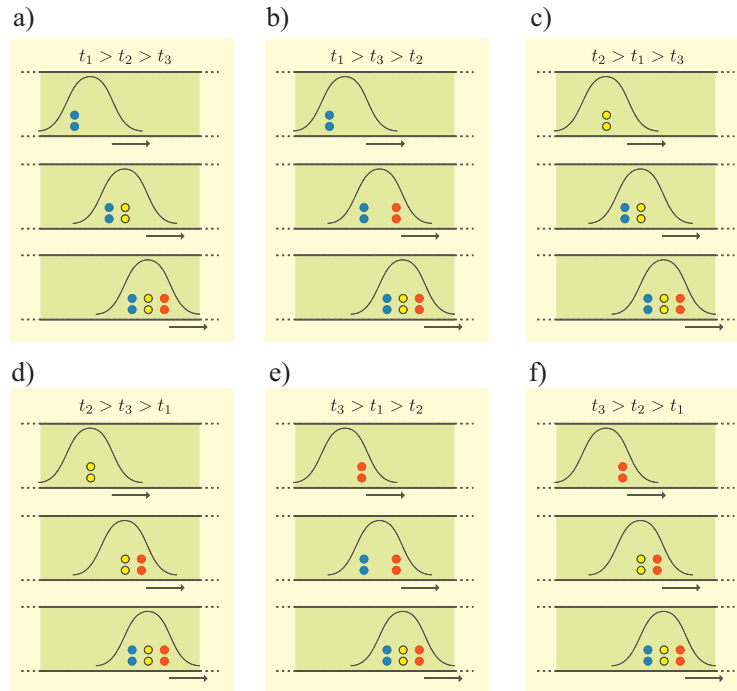


**Figure 6.3:** Cartoon depicting the different permutations of the order in which three pairs of photons are created, as the pump field propagates along the length of the crystal. Unlike the Dyson series, the Taylor series does not distinguish between the events in a)-f)

## 6.2 Evaluating the Dyson series expansion

The down-converted state in equation 6.6 can be written as follows

$$|\Psi_{\text{PDC}}\rangle_{\text{D}} = \frac{1}{\sqrt{\mathcal{N}_{\text{D}}}} \left( |\Psi_{\text{PDC}}^{(0)}\rangle_{\text{D}} + |\Psi_{\text{PDC}}^{(1)}\rangle_{\text{D}} + |\Psi_{\text{PDC}}^{(2)}\rangle_{\text{D}} + |\Psi_{\text{PDC}}^{(3)}\rangle_{\text{D}} \right), \quad (6.7)$$

where  $|\Psi_{\text{PDC}}^{(n)}\rangle_{\text{D}}$  represents the  $n$ th expansion of  $|\Psi_{\text{PDC}}\rangle_{\text{D}}$  and

$$|\Psi_{\text{PDC}}^{(0)}\rangle_{\text{D}} = |0\rangle, \quad (6.8)$$

$$|\Psi_{\text{PDC}}^{(1)}\rangle_{\text{D}} = \frac{1}{i\hbar} \int_{-\infty}^{\infty} dt_1 \hat{H}(t_1) |0\rangle, \quad (6.9)$$

$$|\Psi_{\text{PDC}}^{(2)}\rangle_{\text{D}} = \left( \frac{1}{i\hbar} \right)^2 \int_{-\infty}^{\infty} dt_1 \hat{H}(t_1) \int_{-\infty}^{t_1} dt_2 \hat{H}(t_2) |0\rangle, \quad (6.10)$$

$$|\Psi_{\text{PDC}}^{(3)}\rangle_{\text{D}} = \left( \frac{1}{i\hbar} \right)^3 \int_{-\infty}^{\infty} dt_1 \hat{H}(t_1) \int_{-\infty}^{t_1} dt_2 \hat{H}(t_2) \int_{-\infty}^{t_2} dt_3 \hat{H}(t_3) |0\rangle. \quad (6.11)$$

### 6.2.1 First Order Term

The first order terms can be calculated by substituting the Hamiltonian in Equation 6.2 into Equation 6.9

$$|\Psi_{\text{PDC}}^{(1)}\rangle_{\text{D}} = \frac{1}{i\hbar} \int_{-\infty}^{\infty} dt_1 \hat{H}(t_1) |0\rangle \quad (6.12)$$

$$= \frac{AL}{i\hbar} \int_{-\infty}^{\infty} dt_1 \iiint d\omega_i d\omega_s d\omega_p (f(\omega_i, \omega_s, \omega_p) e^{i\Delta\omega t_1} \hat{a}_i^\dagger(\omega_i) \hat{a}_s^\dagger(\omega_s) + f^*(\omega_i, \omega_s, \omega_p) e^{-i\Delta\omega t_1} \hat{a}_i(\omega_i) \hat{a}_s(\omega_s)) |0\rangle \quad (6.13)$$

$$= \frac{AL}{i\hbar} \int_{-\infty}^{\infty} dt_1 \iiint d\omega_i d\omega_s d\omega_p f(\omega_i, \omega_s, \omega_p) e^{i\Delta\omega t_1} \hat{a}_i^\dagger(\omega_i) \hat{a}_s^\dagger(\omega_s) |0\rangle \quad (6.14)$$

$$= \mathcal{A} \iiint d\omega_i d\omega_s d\omega_p f(\omega_i, \omega_s, \omega_p) \delta(\Delta\omega) \hat{a}_i^\dagger(\omega_i) \hat{a}_s^\dagger(\omega_s) |0\rangle \quad (6.15)$$

$$= \mathcal{A} \iint d\omega_i d\omega_s f(\omega_i, \omega_s, \omega_i + \omega_s) \hat{a}_i^\dagger(\omega_i) \hat{a}_s^\dagger(\omega_s) |0\rangle, \quad (6.16)$$

where  $\mathcal{A} = 2\pi AL/i\hbar$  and  $f(\omega_i, \omega_s, \omega_p)$  is defined in equation 6.3. This corresponds to a state consisting of two photons, of frequencies  $\omega_i$  and  $\omega_s$ , with a joint spectral amplitude  $f(\omega_i, \omega_s, \omega_i + \omega_s)$ . The frequencies of the down-converted photons are constrained by energy conservation according to  $\omega_i + \omega_s = \omega_p$ , where  $\omega_p$  is the frequency of the pump photon. A schematic of this process is shown in figure 6.4 a).

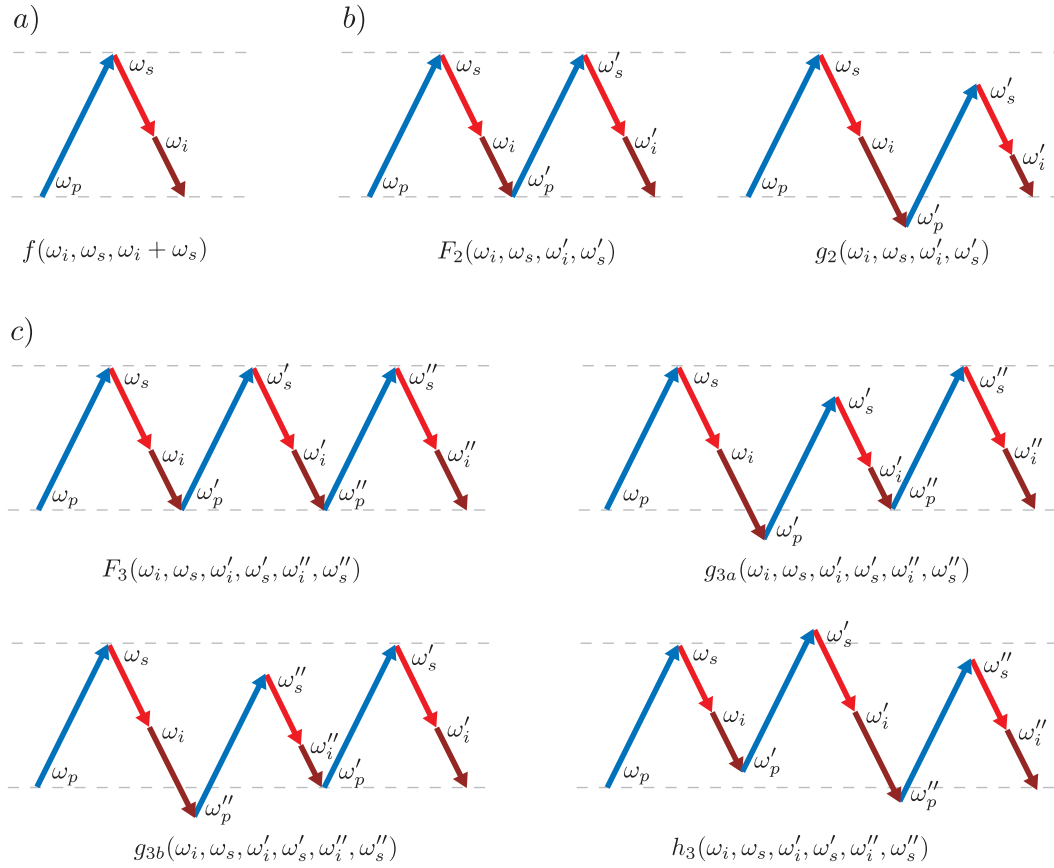


**Figure 6.4:** Schematic diagrams demonstrating the energy conservation relationships between the pump, idler and signal photons for the creation of a) two photons b) four photons and c) six photons, via down-conversion. The amplitudes below each diagram are the corresponding amplitudes for the given down-conversion event.

### 6.2.2 Second Order Term

To calculate the second order term, substitute the Hamiltonian in Equation 6.2 into Equation 6.10

$$\begin{aligned}
|\Psi_{\text{PDC}}^{(2)}\rangle_{\text{D}} &= \left(\frac{1}{i\hbar}\right)^2 \int_{-\infty}^{\infty} dt_1 \hat{H}(t_1) \int_{-\infty}^{t_1} dt_2 \hat{H}(t_2) |0\rangle \\
&= \left(\frac{AL}{i\hbar}\right)^2 \int_{-\infty}^{\infty} dt_1 \int_{-\infty}^{t_1} dt_2 \iiint d\omega_i d\omega_s d\omega_p \iiint d\omega'_i d\omega'_s d\omega'_p \\
&\quad \times \left( f(\omega_i, \omega_s, \omega_p) e^{i\Delta\omega t_1} \hat{a}_i^\dagger(\omega_i) \hat{a}_s^\dagger(\omega_s) + f^*(\omega_i, \omega_s, \omega_p) e^{-i\Delta\omega t_1} \hat{a}_i(\omega_i) \hat{a}_s(\omega_s) \right) \\
&\quad \times \left( f(\omega'_i, \omega'_s, \omega'_p) e^{i\Delta\omega' t_2} \hat{a}_i^\dagger(\omega'_i) \hat{a}_s^\dagger(\omega'_s) + f^*(\omega'_i, \omega'_s, \omega'_p) e^{-i\Delta\omega' t_2} \hat{a}_i(\omega'_i) \hat{a}_s(\omega'_s) \right) |0\rangle,
\end{aligned} \tag{6.17}$$

Some of the terms in the above equation will go to zero due to the annihilation of the vacuum state. Omitting these terms and expanding the brackets, gives

$$\begin{aligned}
|\Psi_{\text{PDC}}^{(2)}\rangle_{\text{D}} &= \left(\frac{AL}{i\hbar}\right)^2 \int_{-\infty}^{\infty} dt_1 \int_{-\infty}^{t_1} dt_2 \iiint d\omega_i d\omega_s d\omega_p \iiint d\omega'_i d\omega'_s d\omega'_p \\
&\quad \times \left( f(\omega_i, \omega_s, \omega_p) f^*(\omega_i, \omega_s, \omega_p) e^{i\Delta\omega t_1} e^{i\Delta\omega' t_2} \hat{a}_i^\dagger(\omega_i) \hat{a}_s^\dagger(\omega_s) \hat{a}_i^\dagger(\omega'_i) \hat{a}_s^\dagger(\omega'_s) \right. \\
&\quad \left. + f^*(\omega'_i, \omega'_s, \omega'_p) f(\omega'_i, \omega'_s, \omega'_p) e^{-i\Delta\omega t_1} e^{i\Delta\omega' t_2} \hat{a}_i(\omega_i) \hat{a}_s(\omega_s) \hat{a}_i^\dagger(\omega'_i) \hat{a}_s^\dagger(\omega'_s) \right) |0\rangle.
\end{aligned} \tag{6.18}$$

We can write the state in terms of the joint spectral amplitudes of the down-converted photons, such that

$$\begin{aligned}
|\Psi_{\text{PDC}}^{(2)}\rangle_{\text{D}} &= \frac{\mathcal{A}^2}{2} \left( G_0 + \iint d\omega_i d\omega_s \iint d\omega'_i d\omega'_s \right. \\
&\quad \left. \times G_2(\omega_i, \omega_s, \omega'_i, \omega'_s) \hat{a}_i^\dagger(\omega_i) \hat{a}_s^\dagger(\omega_s) \hat{a}_i^\dagger(\omega'_i) \hat{a}_s^\dagger(\omega'_s) \right) |0\rangle,
\end{aligned} \tag{6.19}$$

where  $\mathcal{A} = 2\pi AL/i\hbar$ . The first term corresponds to the vacuum state while the second term corresponds to the creation of four photons. By inspection of the state in equation 6.18, we can see that the joint spectral amplitude for the four-photon term must be

$$\begin{aligned}
G_2(\omega_i, \omega_s, \omega'_i, \omega'_s) &= \frac{1}{2\pi^2} \iint d\omega_p d\omega'_p f(\omega_i, \omega_s, \omega_p) f(\omega'_i, \omega'_s, \omega'_p) \\
&\quad \times \int_{-\infty}^{\infty} dt_1 \int_{-\infty}^{t_1} dt_2 e^{i\Delta\omega t_1} e^{i\Delta\omega' t_2}.
\end{aligned} \tag{6.20}$$

To evaluate the integrals over time, we first perform a change of variables, as detailed

in Appendix B.7.1, giving

$$G_2(\omega_i, \omega_s, \omega'_i, \omega'_s) = \frac{1}{\pi^2} \iint d\omega_p d\omega'_p f(\omega_i, \omega_s, \omega_p) f(\omega'_i, \omega'_s, \omega'_p) \times \int_{-\infty}^{\infty} dr \int_0^{\infty} ds e^{i(\Delta\omega + \Delta\omega')r} e^{i(\Delta\omega - \Delta\omega')s}. \quad (6.21)$$

where  $r = t_1 + t_2$  and  $s = t_1 - t_2$ . Now we can evaluate the time integrals, as detailed in Appendix B.8, to give

$$\begin{aligned} G_2(\omega_i, \omega_s, \omega'_i, \omega'_s) &= 2 \iint d\omega_p d\omega'_p f(\omega_i, \omega_s, \omega_p) f(\omega'_i, \omega'_s, \omega'_p) \\ &\quad \times \delta(\Delta\omega + \Delta\omega') \left( \delta(\Delta\omega - \Delta\omega') + \frac{i}{\pi} \frac{1}{\Delta\omega - \Delta\omega'} \right) \\ &= f(\omega_i, \omega_s, \omega_i + \omega_s) f(\omega'_i, \omega'_s, \omega'_i + \omega'_s) \\ &\quad + \frac{2i}{\pi} \iint d\omega_p d\omega'_p f(\omega_i, \omega_s, \omega_p) f(\omega'_i, \omega'_s, \omega'_p) \frac{\delta(\Delta\omega + \Delta\omega')}{\Delta\omega - \Delta\omega'}, \end{aligned} \quad (6.22)$$

We can therefore write

$$G_2(\omega_i, \omega_s, \omega'_i, \omega'_s) = F_2(\omega_i, \omega_s, \omega'_i, \omega'_s) + ig(\omega_i, \omega_s, \omega'_i, \omega'_s), \quad (6.24)$$

where

$$F_2(\omega_i, \omega_s, \omega'_i, \omega'_s) = f(\omega_i, \omega_s, \omega_i + \omega_s) f(\omega'_i, \omega'_s, \omega'_i + \omega'_s), \quad (6.25)$$

is the amplitude for the creation of two independent pairs of photons, each with joint spectral amplitude  $f(\omega_i, \omega_s, \omega_p)$  as defined in equation 6.3. The frequencies of each of the down-converted pairs are independently constrained by energy conservation according to  $\omega_i + \omega_s = \omega_p$  and  $\omega'_i + \omega'_s = \omega'_p$ , where  $\omega_p$  and  $\omega'_p$  are the frequencies of the pump photons. A schematic of this process is shown in figure 6.4 b). Furthermore,

$$\begin{aligned} g(\omega_i, \omega_s, \omega'_i, \omega'_s) &= \frac{2}{\pi} \iint d\omega_p d\omega'_p f(\omega_i, \omega_s, \omega_p) f(\omega'_i, \omega'_s, \omega'_p) \frac{\delta(\Delta\omega + \Delta\omega')}{\Delta\omega - \Delta\omega'} \\ &= \frac{1}{\pi} \int \frac{d\omega_p}{\Delta\omega} f(\omega_i, \omega_s, \omega_p) f(\omega'_i, \omega'_s, \omega'_i + \omega'_s + \Delta\omega). \end{aligned} \quad (6.26)$$

can be interpreted as the amplitude for the creation of a four-photon entangled state. The frequencies of these photons are constrained by a combined energy conservation condition  $\omega_i + \omega_s + \omega'_i + \omega'_s = \omega_p + \omega'_p$ . A schematic of this process is shown in figure 6.4 b). However, we find that due to destructive interference inside the crystal, this

term goes to zero. To see this, consider the state

$$\begin{aligned}
|\psi\rangle &= g(\omega_i, \omega_s, \omega'_i, \omega'_s) \hat{a}_i^\dagger(\omega_i) \hat{a}_s^\dagger(\omega_s) \hat{a}_i^\dagger(\omega'_i) \hat{a}_s^\dagger(\omega'_s) |0\rangle \\
&= \frac{1}{\pi} \iint d\omega_p d\omega'_p f(\omega_i, \omega_s, \omega_p) f(\omega'_i, \omega'_s, \omega'_p) \delta(\Delta\omega + \Delta\omega') \\
&\quad \times \left( \frac{1}{\Delta\omega - \Delta\omega'} + \frac{1}{\Delta\omega + \Delta\omega'} \right) \hat{a}_i^\dagger(\omega_i) \hat{a}_s^\dagger(\omega_s) \hat{a}_i^\dagger(\omega'_i) \hat{a}_s^\dagger(\omega'_s) |0\rangle.
\end{aligned} \tag{6.27}$$

Where we have written equation 6.26 as a sum of two terms. If we make the substitution  $\omega_j \rightarrow \omega'_j$  and vice-versa, in the second term, where  $j = i, s, p$ , we get

$$\begin{aligned}
|\psi\rangle &= \frac{1}{\pi} \iint d\omega_p d\omega'_p f(\omega_i, \omega_s, \omega_p) f(\omega'_i, \omega'_s, \omega'_p) \delta(\Delta\omega + \Delta\omega') \\
&\quad \times \left( \frac{1}{\Delta\omega - \Delta\omega'} - \frac{1}{\Delta\omega + \Delta\omega'} \right) \hat{a}_i^\dagger(\omega_i) \hat{a}_s^\dagger(\omega_s) \hat{a}_i^\dagger(\omega'_i) \hat{a}_s^\dagger(\omega'_s) |0\rangle \\
&= 0
\end{aligned} \tag{6.28}$$

$$= 0 \tag{6.29}$$

Therefore, the amplitude for the four-photon state simplifies to

$$G_2(\omega_i, \omega_s, \omega'_i, \omega'_s) = F_2(\omega_i, \omega_s, \omega'_i, \omega'_s), \tag{6.30}$$

The amplitude for the correction to the vacuum state also simplifies to

$$G_0 = F_0 = \iint d\omega_i d\omega_s |f(\omega_i, \omega_s, \omega_i + \omega_s)|^2, \tag{6.31}$$

as is detailed in Appendix B.4.

### 6.2.3 Third Order Term

For the third order term, we substitute the Hamiltonian in Equation 6.2 into Equation 6.11

$$\begin{aligned}
|\Psi_{\text{PDC}}^{(3)}\rangle_{\text{D}} &= \left( \frac{AL}{i\hbar} \right)^3 \int_{-\infty}^{\infty} dt_1 \int_{-\infty}^{t_1} dt_2 \int_{-\infty}^{t_2} dt_3 \\
&\quad \times \iiint d\omega_i d\omega_s \omega_p \iiint d\omega'_i d\omega'_s \omega'_p \iiint d\omega''_i d\omega''_s \omega''_p \\
&\quad \times \left( f(\omega_i, \omega_s, \omega_p) e^{i\Delta\omega t_1} \hat{a}_i^\dagger(\omega_i) \hat{a}_s^\dagger(\omega_s) + f^*(\omega_i, \omega_s, \omega_p) e^{-i\Delta\omega t_1} \hat{a}_i(\omega_i) \hat{a}_s(\omega_s) \right) \\
&\quad \times \left( f(\omega'_i, \omega'_s, \omega'_p) e^{i\Delta\omega' t_2} \hat{a}_i^\dagger(\omega'_i) \hat{a}_s^\dagger(\omega'_s) + f^*(\omega'_i, \omega'_s, \omega'_p) e^{-i\Delta\omega' t_2} \hat{a}_i(\omega'_i) \hat{a}_s(\omega'_s) \right) \\
&\quad \times \left( f(\omega''_i, \omega''_s, \omega''_p) e^{i\Delta\omega'' t_3} \hat{a}_i^\dagger(\omega''_i) \hat{a}_s^\dagger(\omega''_s) + f^*(\omega''_i, \omega''_s, \omega''_p) e^{-i\Delta\omega'' t_3} \hat{a}_i(\omega''_i) \hat{a}_s(\omega''_s) \right) |0\rangle
\end{aligned} \tag{6.32}$$

Expanding the brackets and omitting terms that go to zero, due to the annihilation of the vacuum, gives

$$\begin{aligned}
|\Psi_{\text{PDC}}^{(3)}\rangle_{\text{D}} &= \left(\frac{AL}{i\hbar}\right)^3 \int_{-\infty}^{\infty} dt_1 \int_{-\infty}^{t_1} dt_2 \int_{-\infty}^{t_2} dt_3 \\
&\times \iiint d\omega_i d\omega_s d\omega_p \iiint d\omega'_i d\omega'_s d\omega'_p \iiint d\omega''_i d\omega''_s d\omega''_p \\
&\times \left( f(\omega_i, \omega_s, \omega_p) f(\omega'_i, \omega'_s, \omega'_p) f(\omega''_i, \omega''_s, \omega''_p) e^{i\Delta\omega t_1} e^{i\Delta\omega' t_2} e^{i\Delta\omega'' t_3} \right. \\
&\times \hat{a}_i^\dagger(\omega_i) \hat{a}_s^\dagger(\omega_s) \hat{a}_i^\dagger(\omega'_i) \hat{a}_s^\dagger(\omega'_s) \hat{a}_i^\dagger(\omega''_i) \hat{a}_s^\dagger(\omega''_s) \\
&+ f^*(\omega_i, \omega_s, \omega_p) f(\omega'_i, \omega'_s, \omega'_p) f(\omega''_i, \omega''_s, \omega''_p) e^{-i\Delta\omega t_1} e^{i\Delta\omega' t_2} e^{i\Delta\omega'' t_3} \\
&\times (\delta(\omega_i - \omega''_i) \delta(\omega_s - \omega''_s) \hat{a}_i^\dagger(\omega'_i) \hat{a}_s^\dagger(\omega'_s) + \delta(\omega_i - \omega'_i) \delta(\omega_s - \omega''_s) \hat{a}_i^\dagger(\omega''_i) \hat{a}_s^\dagger(\omega'_s) \\
&+ \delta(\omega_i - \omega''_i) \delta(\omega_s - \omega'_s) \hat{a}_i^\dagger(\omega'_i) \hat{a}_s^\dagger(\omega''_s) + \delta(\omega_i - \omega'_i) \delta(\omega_s - \omega'_s) \hat{a}_i^\dagger(\omega''_i) \hat{a}_s^\dagger(\omega''_s)) \\
&+ f(\omega_i, \omega_s, \omega_p) f^*(\omega'_i, \omega'_s, \omega'_p) f(\omega''_i, \omega''_s, \omega''_p) e^{i\Delta\omega t_1} e^{-i\Delta\omega' t_2} e^{i\Delta\omega'' t_3} \\
&\left. \times \delta(\omega''_i - \omega'_i) \delta(\omega''_s - \omega'_s) \hat{a}_i^\dagger(\omega_i) \hat{a}_s^\dagger(\omega_s) \right) |0\rangle. \tag{6.33}
\end{aligned}$$

We can write the state in terms of the joint spectral amplitudes of the down-converted photons, such that

$$\begin{aligned}
|\Psi_{\text{PDC}}^{(3)}\rangle_{\text{D}} &= \frac{\mathcal{A}^3}{3!} \left( \iint d\omega_i d\omega_s G_1(\omega_i, \omega_s) \hat{a}_i^\dagger(\omega_i) \hat{a}_s^\dagger(\omega_s) \right. \\
&+ \iint d\omega_i d\omega_s \iint d\omega'_i d\omega'_s \iint d\omega''_i d\omega''_s G_3(\omega_i, \omega_s, \omega'_i, \omega'_s, \omega''_i, \omega''_s) \\
&\left. \times \hat{a}_i^\dagger(\omega_i) \hat{a}_s^\dagger(\omega_s) \hat{a}_i^\dagger(\omega'_i) \hat{a}_s^\dagger(\omega'_s) \hat{a}_i^\dagger(\omega''_i) \hat{a}_s^\dagger(\omega''_s) \right) |0\rangle, \tag{6.34}
\end{aligned}$$

where  $\mathcal{A} = 2\pi AL/i\hbar$ . The first term corresponds to the creation of two photons while the second term corresponds to the creation of six photons. By inspection of the state in equation 6.33, we can see that the joint spectral amplitude for the six-photon term must be

$$G_3 = G_3(\omega_i, \omega_s, \omega'_i, \omega'_s, \omega''_i, \omega''_s) \tag{6.35}$$

$$\begin{aligned}
&= \frac{3!}{(2\pi)^3} \iiint d\omega_p d\omega'_p d\omega''_p f(\omega_i, \omega_s, \omega_p) f(\omega'_i, \omega'_s, \omega'_p) f(\omega''_i, \omega''_s, \omega''_p) \\
&\times \int_{-\infty}^{\infty} dt_1 \int_{-\infty}^{t_1} dt_2 \int_{-\infty}^{t_2} dt_3 e^{i\Delta\omega t_1} e^{i\Delta\omega' t_2} e^{i\Delta\omega'' t_3}. \tag{6.36}
\end{aligned}$$

To evaluate the integrals over time, we first perform a change of variables, as detailed in Appendix B.7.2, giving

$$G_3 = \frac{3!}{3 \times (2\pi)^3} \iiint d\omega_p d\omega'_p d\omega''_p f(\omega_i, \omega_s, \omega_p) f(\omega'_i, \omega'_s, \omega'_p) f(\omega''_i, \omega''_s, \omega''_p) \times \int_{-\infty}^{\infty} dq \int_0^{\infty} dr \int_0^{\infty} ds e^{\frac{i}{3}(\Delta\omega + \Delta\omega' + \Delta\omega'')q} e^{\frac{i}{3}(2\Delta\omega - \Delta\omega' - \Delta\omega'')r} e^{\frac{i}{3}(\Delta\omega + \Delta\omega' - 2\Delta\omega'')s}. \quad (6.37)$$

where  $q = t_1 + t_2 + t_3$ ,  $r = t_1 - t_2$  and  $s = t_2 - t_3$ . Now we can evaluate the time integrals, as detailed in Appendix B.8, to give

$$G_3 = \frac{3! \times 2\pi^3}{3 \times (2\pi)^3} \iiint d\omega_p d\omega'_p d\omega''_p f(\omega_i, \omega_s, \omega_p) f(\omega'_i, \omega'_s, \omega'_p) f(\omega''_i, \omega''_s, \omega''_p) \times \delta\left(\frac{1}{3}(\Delta\omega + \Delta\omega' + \Delta\omega'')\right) \times \left(\delta\left(\frac{1}{3}(2\Delta\omega - \Delta\omega' - \Delta\omega'')\right) + \frac{i}{\pi} \frac{1}{\frac{1}{3}(2\Delta\omega - \Delta\omega' - \Delta\omega'')}\right) \times \left(\delta\left(\frac{1}{3}(\Delta\omega + \Delta\omega' - 2\Delta\omega'')\right) + \frac{i}{\pi} \frac{1}{\frac{1}{3}(\Delta\omega + \Delta\omega' - 2\Delta\omega'')}\right) = \frac{3^3 \times 3! \times 2\pi^3}{3 \times (2\pi)^3} \iiint d\omega_p d\omega'_p d\omega''_p f(\omega_i, \omega_s, \omega_p) f(\omega'_i, \omega'_s, \omega'_p) f(\omega''_i, \omega''_s, \omega''_p) \times \delta(\Delta\omega + \Delta\omega' + \Delta\omega'') \left(\delta(2\Delta\omega - \Delta\omega' - \Delta\omega'') + \frac{i}{\pi} \frac{1}{2\Delta\omega - \Delta\omega' - \Delta\omega''}\right) \times \left(\delta(\Delta\omega + \Delta\omega' - 2\Delta\omega'') + \frac{i}{\pi} \frac{1}{\Delta\omega + \Delta\omega' - 2\Delta\omega''}\right) \quad (6.39)$$

$$= \frac{3}{2} \left( f(\omega_i, \omega_s, \omega_i + \omega_s) f(\omega'_i, \omega'_s, \omega'_i + \omega'_s) f(\omega''_i, \omega''_s, \omega''_i + \omega''_s) - \frac{i}{\pi} \int \frac{d\omega'_p}{\Delta\omega'} f(\omega_i, \omega_s, \omega_i + \omega_s + \Delta\omega') f(\omega'_i, \omega'_s, \omega'_p) f(\omega''_i, \omega''_s, \omega''_i + \omega''_s) + \frac{i}{\pi} \int \frac{d\omega'_p}{\Delta\omega'} f(\omega''_i, \omega''_s, \omega''_i + \omega''_s + \Delta\omega') f(\omega'_i, \omega'_s, \omega'_p) f(\omega_i, \omega_s, \omega_i + \omega_s) + \frac{1}{\pi} \iint \frac{d\omega_p d\omega''_p}{\Delta\omega \Delta\omega''} f(\omega_i, \omega_s, \omega_p) f(\omega'_i, \omega'_s, \omega'_i + \omega'_s + \Delta\omega + \Delta\omega'') f(\omega''_i, \omega''_s, \omega''_p) \right). \quad (6.40)$$

(6.41)

We can therefore write

$$G_3 = \frac{3}{2} \left( F_3(\omega_i, \omega_s, \omega'_i, \omega'_s, \omega''_i, \omega''_s) - ig_{3a}(\omega_i, \omega_s, \omega'_i, \omega'_s, \omega''_i, \omega''_s) + ig_{3b}(\omega_i, \omega_s, \omega'_i, \omega'_s, \omega''_i, \omega''_s) + h_3(\omega_i, \omega_s, \omega'_i, \omega'_s, \omega''_i, \omega''_s) \right), \quad (6.42)$$

where

$$F_3(\omega_i, \omega_s, \omega'_i, \omega'_s, \omega''_i, \omega''_s) = f(\omega_i, \omega_s, \omega_i + \omega_s) f(\omega'_i, \omega'_s, \omega'_i + \omega'_s) f(\omega''_i, \omega''_s, \omega''_i + \omega''_s), \quad (6.43)$$

is the amplitude for the creation of three independent pairs of photons, each with joint spectral amplitude  $f(\omega_i, \omega_s, \omega_p)$  as defined in equation 6.3. The frequencies of each of the down-converted pairs are independently constrained by energy conservation according to  $\omega_i + \omega_s = \omega_p$ ,  $\omega'_i + \omega'_s = \omega'_p$  and  $\omega''_i + \omega''_s = \omega''_p$ , where  $\omega_p$ ,  $\omega'_p$  and  $\omega''_p$  are the frequencies of the pump photons. A schematic of this process is shown in figure 6.4 c). Furthermore,

$$h_3 = h_3(\omega_i, \omega_s, \omega'_i, \omega'_s, \omega''_i, \omega''_s) \quad (6.44)$$

$$= \frac{1}{\pi^2} \iint \frac{d\omega_p d\omega''_p}{\Delta\omega \Delta\omega''} f(\omega_i, \omega_s, \omega_p) f(\omega'_i, \omega'_s, \omega'_i + \omega'_s + \Delta\omega + \Delta\omega'') f(\omega''_i, \omega''_s, \omega''_p). \quad (6.45)$$

can be interpreted as the amplitude for the creation of a six-photon entangled state. The frequencies of these photons are constrained by a combined energy conservation condition  $\omega_i + \omega_s + \omega'_i + \omega'_s + \omega''_i + \omega''_s = \omega_p + \omega'_p + \omega''_p$ . A schematic of this process is shown in figure 6.4 c). In addition,

$$g_{3a} = g_{3a}(\omega_i, \omega_s, \omega'_i, \omega'_s, \omega''_i, \omega''_s) = \frac{1}{\pi} f(\omega''_i, \omega''_s, \omega''_i + \omega''_s) \int \frac{d\omega'_p}{\Delta\omega'} f(\omega_i, \omega_s, \omega_i + \omega_s + \Delta\omega') f(\omega'_i, \omega'_s, \omega'_p), \quad (6.46)$$

and

$$g_{3b} = g_{3b}(\omega_i, \omega_s, \omega'_i, \omega'_s, \omega''_i, \omega''_s) = \frac{1}{\pi} f(\omega_i, \omega_s, \omega_i + \omega_s) \int \frac{d\omega'_p}{\Delta\omega'} f(\omega''_i, \omega''_s, \omega''_i + \omega''_s + \Delta\omega') f(\omega'_i, \omega'_s, \omega'_p) \quad (6.47)$$

can be interpreted as the amplitude for the creation of a four-photon entangled state along with an independent photon-pair. The frequencies of these photons are constrained by a combined energy conservation condition  $\omega_i + \omega_s + \omega'_i + \omega'_s = \omega_p + \omega'_p$

as well as an independent condition  $\omega_i'' + \omega_s'' = \omega_p''^1$ . A schematic of these processes is shown in figure 6.4 c). However, we find that due to destructive interference inside the crystal, these terms go to zero. Motivated by equation 6.42, we write the state

$$\begin{aligned}
|\psi\rangle &= (g_{3b} - g_{3a})\hat{a}_i^\dagger(\omega_i)\hat{a}_s^\dagger(\omega_s)\hat{a}_i^\dagger(\omega_i'')\hat{a}_s^\dagger(\omega_s'')\hat{a}_i^\dagger(\omega_i'')\hat{a}_s^\dagger(\omega_s'')|0\rangle \\
&= \frac{1}{\pi} \int \frac{d\omega'_p f(\omega_i', \omega_s', \omega_p')}{\Delta\omega'} (f(\omega_i'', \omega_s'', \omega_i'' + \omega_s'' + \Delta\omega') f(\omega_i, \omega_s, \omega_i + \omega_s) \\
&\quad - f(\omega_i, \omega_s, \omega_i + \omega_s + \Delta\omega') f(\omega_i'', \omega_s'', \omega_i'' + \omega_s'')) \\
&\quad \times \hat{a}_i^\dagger(\omega_i)\hat{a}_s^\dagger(\omega_s)\hat{a}_i^\dagger(\omega_i'')\hat{a}_s^\dagger(\omega_s'')\hat{a}_i^\dagger(\omega_i'')\hat{a}_s^\dagger(\omega_s'')|0\rangle
\end{aligned} \tag{6.48}$$

If we make the substitution  $\omega_j \rightarrow \omega_j''$  and vice-versa, in the second term, where  $j = i, s$ , we get

$$\begin{aligned}
|\psi\rangle &= \frac{1}{\pi} \int \frac{d\omega'_p f(\omega_i', \omega_s', \omega_p')}{\Delta\omega'} (f(\omega_i'', \omega_s'', \omega_i'' + \omega_s'' + \Delta\omega') f(\omega_i, \omega_s, \omega_i + \omega_s) \\
&\quad - f(\omega_i'', \omega_s'', \omega_i'' + \omega_s'' + \Delta\omega') f(\omega_i, \omega_s, \omega_i + \omega_s)) \\
&\quad \times \hat{a}_i^\dagger(\omega_i)\hat{a}_s^\dagger(\omega_s)\hat{a}_i^\dagger(\omega_i'')\hat{a}_s^\dagger(\omega_s'')\hat{a}_i^\dagger(\omega_i'')\hat{a}_s^\dagger(\omega_s'')|0\rangle
\end{aligned} \tag{6.49}$$

$$= 0. \tag{6.50}$$

Therefore, the amplitude for the six-photon state simplifies to

$$G_3 = \frac{3}{2} \left( F_3(\omega_i, \omega_s, \omega_i', \omega_s', \omega_i'', \omega_s'') + h_3(\omega_i, \omega_s, \omega_i', \omega_s', \omega_i'', \omega_s'') \right), \tag{6.51}$$

The amplitude for the correction to the two-photon state also simplifies to

$$G_1(\omega_i, \omega_s) = \frac{3}{2} \left( F_1(\omega_i, \omega_s) - h_1(\omega_i, \omega_s) \right), \tag{6.52}$$

as is detailed in Appendix B.5, where

$$\begin{aligned}
F_1(\omega_i, \omega_s) &= \iint d\omega_i' d\omega_s' f^*(\omega_i', \omega_s', \omega_i' + \omega_s') (f(\omega_i, \omega_s, \omega_i + \omega_s) f(\omega_i', \omega_s', \omega_i' + \omega_s')) \\
&\quad + \sum_{\substack{[j,k]= \\ \mathcal{P}[\omega_i, \omega_i']}} \sum_{\substack{[m,n]= \\ \mathcal{P}[\omega_s, \omega_s']}} f(j, m, j + m) f(k, n, k + n),
\end{aligned} \tag{6.53}$$

<sup>1</sup>This is the case for the state described by  $g_{3a}$ . For the state described by  $g_{3b}$ , the energy conservation conditions are  $\omega_i + \omega_s + \omega_i'' + \omega_s'' = \omega_p + \omega_p''$  and  $\omega_i' + \omega_s' = \omega_p'$

and

$$\begin{aligned}
h_1(\omega_i, \omega_s) &= \frac{1}{\pi^2} \iint d\omega'_i d\omega'_s \iint d\omega_p d\omega''_p \left( f^*(\omega'_i, \omega'_s, \omega_p) \right. \\
&\times \sum_{\substack{[j,k]= \\ \mathcal{P}[\omega_i, \omega'_i]}} \sum_{\substack{[m,n]= \\ \mathcal{P}[\omega_s, \omega'_s]}} \frac{f(j, m, j+m+\omega'_i+\omega'_s-\omega_p-k-n+\omega''_p) f(k, n, \omega''_p)}{(\omega'_i+\omega'_s-\omega_p)(k+n-\omega''_p)} \\
&\left. - \frac{f(\omega_i, \omega_s, \omega_p) f^*(\omega'_i, \omega'_s, 2\omega'_i+2\omega'_s-\omega''_p-\Delta\omega) f(\omega'_i, \omega'_s, \omega''_p)}{\Delta\omega(\omega'_i+\omega'_s-\omega''_p)} \right). \tag{6.54}
\end{aligned}$$

We define

$$\sum_{[i,j]=\mathcal{P}[a,b]} f(i, j) = f(a, b) + f(b, a). \tag{6.55}$$

### 6.3 Comparing With the Taylor Series

The terms of the state in Equation 6.7 can be summarised as follows

$$|\Psi_{\text{PDC}}^{(0)}\rangle_{\text{D}} = |0\rangle, \tag{6.56}$$

$$|\Psi_{\text{PDC}}^{(1)}\rangle_{\text{D}} = \mathcal{A} \iint d\omega_i d\omega_s f(\omega_i, \omega_s, \omega_i + \omega_s) \hat{a}_i^\dagger(\omega_i) \hat{a}_s^\dagger(\omega_s) |0\rangle, \tag{6.57}$$

$$\begin{aligned}
|\Psi_{\text{PDC}}^{(2)}\rangle_{\text{D}} &= \frac{\mathcal{A}^2}{2} \left( F_0 + \iiint d\omega_i d\omega_s d\omega'_i d\omega'_s \right. \\
&\times F_2(\omega_i, \omega_s, \omega'_i, \omega'_s) \hat{a}_i^\dagger(\omega_i) \hat{a}_s^\dagger(\omega_s) \hat{a}_i^\dagger(\omega'_i) \hat{a}_s^\dagger(\omega'_s) \left. \right) |0\rangle, \tag{6.58}
\end{aligned}$$

$$\begin{aligned}
|\Psi_{\text{PDC}}^{(3)}\rangle_{\text{D}} &= \frac{\mathcal{A}^3}{3!} \left( \iint d\omega_i d\omega_s G_1(\omega_i, \omega_s) \hat{a}_i^\dagger(\omega_i) \hat{a}_s^\dagger(\omega_s) \right. \\
&+ \iiint d\omega_i d\omega_s d\omega'_i d\omega'_s d\omega''_i d\omega''_s G_3(\omega_i, \omega_s, \omega'_i, \omega'_s, \omega''_i, \omega''_s) \\
&\times \hat{a}_i^\dagger(\omega_i) \hat{a}_s^\dagger(\omega_s) \hat{a}_i^\dagger(\omega'_i) \hat{a}_s^\dagger(\omega'_s) \hat{a}_i^\dagger(\omega''_i) \hat{a}_s^\dagger(\omega''_s) \left. \right) |0\rangle, \tag{6.59}
\end{aligned}$$

where we have made use of the result that  $G_0 = F_0$  and  $G_2(\omega_i, \omega_s, \omega'_i, \omega'_s) = F_2(\omega_i, \omega_s, \omega'_i, \omega'_s)$  as calculated in the previous section.

Following a similar procedure (detailed in Appendix B.3), we find that the corresponding terms from the Taylor expansion are

$$|\Psi_{\text{PDC}}^{(0)}\rangle_{\text{T}} = |0\rangle, \quad (6.60)$$

$$|\Psi_{\text{PDC}}^{(1)}\rangle_{\text{T}} = \mathcal{A} \iint d\omega_i d\omega_s f(\omega_i, \omega_s, \omega_i + \omega_s) \hat{a}_i^\dagger(\omega_i) \hat{a}_s^\dagger(\omega_s) |0\rangle \quad (6.61)$$

$$\begin{aligned} |\Psi_{\text{PDC}}^{(2)}\rangle_{\text{T}} = & \frac{\mathcal{A}^2}{2} \left( F_0 + \iiint d\omega_i d\omega_s d\omega'_i d\omega'_s \right. \\ & \left. \times F_2(\omega_i, \omega_s, \omega'_i, \omega'_s) \hat{a}_i^\dagger(\omega_i) \hat{a}_s^\dagger(\omega_s) \hat{a}_i^\dagger(\omega'_i) \hat{a}_s^\dagger(\omega'_s) \right) |0\rangle, \end{aligned} \quad (6.62)$$

$$\begin{aligned} |\Psi_{\text{PDC}}^{(3)}\rangle_{\text{T}} = & \frac{\mathcal{A}^3}{3!} \left( \iint d\omega_i d\omega_s F_1(\omega_i, \omega_s) \hat{a}_i^\dagger(\omega_i) \hat{a}_s^\dagger(\omega_s) \right. \\ & + \iiint d\omega_i d\omega_s d\omega'_i d\omega'_s d\omega''_i d\omega''_s F_3(\omega_i, \omega_s, \omega'_i, \omega'_s, \omega''_i, \omega''_s) \\ & \left. \times \hat{a}_i^\dagger(\omega_i) \hat{a}_s^\dagger(\omega_s) \hat{a}_i^\dagger(\omega'_i) \hat{a}_s^\dagger(\omega'_s) \hat{a}_i^\dagger(\omega''_i) \hat{a}_s^\dagger(\omega''_s) \right) |0\rangle, \end{aligned} \quad (6.63)$$

Comparing equations 6.56-6.58 with equations 6.60-6.62, we notice that up to second order, the two series give identical results. The difference reveals itself when comparing the third order terms, in equations 6.59 and 6.63, at the level of the joint spectral amplitudes, which are

Taylor Series

Dyson Series

$$F_3(\omega_i, \omega_s, \omega'_i, \omega'_s, \omega''_i, \omega''_s) \quad \frac{3}{2} \left( F_3(\omega_i, \omega_s, \omega'_i, \omega'_s, \omega''_i, \omega''_s) + h_3(\omega_i, \omega_s, \omega'_i, \omega'_s, \omega''_i, \omega''_s) \right)$$

The key differences are an overall increase in the amplitude by a factor of 3/2 as well as an additional amplitude for a six-photon entangled state that is not predicted by the Taylor series. Notice that the  $n$ th order term doesn't directly correspond to an  $n$  photon state. We can however, group the state in terms of the photon numbers.

$$|\Psi_{\text{PDC}}\rangle_{\text{D}} = \frac{1}{\sqrt{\mathcal{N}_{\text{D}}}} \left( |\Psi_{0,0}\rangle_{\text{D}} + |\Psi_{1,1}\rangle_{\text{D}} + |\Psi_{2,2}\rangle_{\text{D}} + |\Psi_{3,3}\rangle_{\text{D}} \right) \quad (6.64)$$

where  $|\Psi_{n,n}\rangle_{\text{D}}$  represents the  $2n$ -photon component of the state and

$$|\Psi_{0,0}\rangle_{\text{D}} = \left( 1 + \frac{\mathcal{A}^2}{2} F_0 \right) |0\rangle, \quad (6.65)$$

$$|\Psi_{1,1}\rangle_{\text{D}} = \mathcal{A} \iint d\omega_i d\omega_s \left( f(\omega_i, \omega_s, \omega_i + \omega_s) + \frac{\mathcal{A}^2}{3!} G_1(\omega_i, \omega_s) \right) \hat{a}_i^\dagger(\omega_i) \hat{a}_s^\dagger(\omega_s) |0\rangle, \quad (6.66)$$

$$\begin{aligned}
|\Psi_{3,3}\rangle_D = & \frac{\mathcal{A}^3}{3!} \iiint \iiint \iiint d\omega_i d\omega_s d\omega'_i d\omega'_s d\omega''_i d\omega''_s G_3(\omega_i, \omega_s, \omega'_i, \omega'_s, \omega''_i, \omega''_s) \\
& \times \hat{a}_i^\dagger(\omega_i) \hat{a}_s^\dagger(\omega_s) \hat{a}_i^\dagger(\omega'_i) \hat{a}_s^\dagger(\omega'_s) \hat{a}_i^\dagger(\omega''_i) \hat{a}_s^\dagger(\omega''_s) |0\rangle. \tag{6.67}
\end{aligned}$$

In this form, we see that the Dyson series predicts a modification to the two- and six-photon number amplitudes in such a way that the output state is no longer Gaussian.

## 6.4 Discussion

Expanding to first order, we see no difference between the Dyson and Taylor series. At second order, there appears to be an additional phenomenon for creating four-photon states in the Dyson series, however, these events are not observable due to destructive interference of the fields within the crystal. Only at third order, do we see a real difference between the two series. There is a similar additional phenomenon for creating six-photon states, however, only some of these events destructively interfere. The Dyson series predicts the creation of three independent pairs of photons as well as a six-photon entangled state whose energies sum nontrivially to the energy of three pump photons. Additionally, there is a curious factor of 3/2 in front of the six-photon amplitude predicted by the Dyson series. There is an expectation that under some conditions, the amplitudes predicted by the series will interfere in a way that cancels this factor, however, this has not yet been explored successfully. While using a monochromatic pump will not, in general, reduce the Dyson series to the Taylor series, sufficiently narrow filtering around the frequencies which correspond to the generation of independent pairs—e.g. by placing the setup inside a cavity—may have this effect.

The implications of these conclusions are two-fold. If an experiment is performed in a regime where four-photon terms are significant, while six-photon terms are not<sup>2</sup>, then it is sufficient to use the Taylor series expansion to model this experiment. However, there also seems to be the possibility of creating 6-photon entangled states if the experiment is pumped at pump powers high enough to make the 3rd order events significant. In this regime, the Dyson series predicts a modification to the two- and six-photon number amplitudes in such a way that the output state is no longer Gaussian.

---

<sup>2</sup>This was the case in Chapter 4.

---

# Conclusion

---

This thesis focused on the investigation of non-classical states of light generated via spontaneous parametric down-conversion, in the context of quantum computing and quantum information.

Superpositions of coherent states, known as *kitten states*, can be approximated by subtracting photons from a single-mode down-converted state, i.e. a squeezed vacuum state. We found that such a state turns out to be a great resource for high-fidelity teleportation of small-amplitude kitten states. In-principle teleportation of arbitrary coherent-state superpositions can be demonstrated using photon-subtracted squeezed vacuum states as inputs to an entanglement swapping protocol. This also works with high fidelity at small amplitudes.

Our analysis of the effects of imperfect source preparation and inefficient detection has shown this setup to be fragile in this regard. It would be possible to implement high-fidelity teleportation of states like the coherent state and the even cat state with a lossy system, but states which are more similar to the odd cat state degrade very quickly, even with low loss. It looks like this fragility is a property of the gate, and not just the approximation of the states, however, at higher amplitudes, the fidelity is additionally affected by loss when using the approximate states.

As teleportation is the implementation of the identity gate, our results suggest that demonstration of more complicated non-trivial gates, as introduced by Lund *et al.* [41], will be practical in the foreseeable future. Another extension could include the analysis and experimental implementation of the teleportation of arbitrary coherent-state qubits, that were recently realised and characterised by Neergaard-Nielsen *et al.* [77].

While this work considered a simplified single-frequency-mode picture, the remainder of this thesis dealt with the spectral properties of the states generated by parametric down-conversion. In such a scenario, the down-converted photons are typically entangled in the frequency degree of freedom.

We first modeled the heralded preparation of one- and two-photon states, conditional on the detection of one or two photons, respectively, in one of the down-converted

modes. Spectral entanglement, combined with the low spectral resolution of the heralding detector, renders the heralded state mixed in frequency—an undesirable consequence. The effects of spectral filtering of the heralding state were analysed to determine an optimal method for generating pure photon-number states. We calculated the output state to second order in photon number and presented analytical expressions for the heralded one- and two-photon state after the idler mode is spectrally filtered using a Gaussian filter and detected with an inefficient detector. The heralded signal state was then characterised by its  $g^{(2)}$  and purity. In addition, we calculated the fidelity of the heralded state with the desired ideal Fock state.

As a physical example, we modeled a type II ppKTP waveguide, pumped by lasers at wavelengths of 400 nm, 788 nm and 1.93  $\mu\text{m}$ , corresponding to a highly correlated, a symmetric separable and an asymmetric separable joint spectral amplitude, respectively. We found that in the first example, where no effort was made to perform any group velocity matching, the results were states with very low purity. After strong spectral filtering, Fock states with arbitrarily high purity could be achieved, however at very low probabilities of success.

By employing group velocity matching, it is possible to generate higher purity states, however, some additional filtering is still required to achieve very high purity states. High-purity two-photon Fock states were also possible. While results were comparable for the symmetric and asymmetric examples, this was due to our choice of physical parameters. The asymmetric case would be able to achieve higher fidelities, with no filtering, by choosing a longer waveguide.

As an alternative to filtering the side lobes of the sinc-shaped joint spectral profile, we also developed a technique for controlling the spectral profile of the down-converted photons. By exploiting the dependence of the effective nonlinearity of a periodically poled crystal on its poling order, it was possible to tailor a nonlinearity profile and therefore the phasematching function of the down-converted photons.

We tailored a spectral photon-pair amplitude with a Gaussian profile, which is generally optimal for optical mode matching—a critical consideration in any experiment involving single photons. We designed a custom-poled KTP crystal accordingly and verified the joint spectral amplitude of the output photons in two-photon interference experiments.

It would be interesting to apply our idea of an engineered material nonlinearity to four-wave-mixing photon-pair sources in photonic-crystal fibres, where the sinc-shaped phase-matching function is a major problem.

Finally, we considered the validity of the simpler, yet not strictly correct, Taylor series expansion of the unitary operator which governs the evolution of the fields within the crystal. Since the multimode down-conversion Hamiltonian does not commute with itself at all times, the expansion should take the form of the time-ordered Dyson series. By expanding the evolution operator to third order, it was

---

revealed that both series expansions gave identical predictions to second order. At third order, in addition to the six-photon state predicted by the Taylor series, which consists of three independent pairs of photons, the Dyson series predicts a six-photon entangled state. Additionally, there is a curious factor of  $3/2$  in front of the six-photon amplitude predicted by the Dyson series. A future extension of this work could be to identify if there are any conditions under which the Dyson series simplifies to the Taylor series. This would occur if the third order amplitudes interfere in a way that cancels this factor of  $3/2$ . A plausible candidate for this is the limit where the length of the crystal goes to infinity.



---

# Tailoring the Nonlinearity of a Nonlinear Crystal

---

## A.1 Gaussian Approximation to Sinc Function

To determine the exact shape of the target Gaussian function for the nonlinearity profile, we match the width of the desired Gaussian PMF with the sinc PMF of the form,  $\text{sinc}(\Delta k L_{\text{eff}}/2)$ , that would be generated by a standard crystal. The appropriate function is  $\Phi_G(\omega_i, \omega_s) = \exp(-\gamma(\Delta k L_{\text{eff}}/2)^2)$  where the parameter  $\gamma \approx 0.193$  is derived from matching the FWHM of the two functions. We refer to  $L_{\text{eff}}$  as the *effective* length, as it does not correspond to the actual length of the final Gaussian shaped crystal, but rather the length of the hypothetical standard crystal.

## A.2 Detailed Model

We modeled each section of the crystal as having a nonlinearity inversely proportional to the poling order  $m$ . This approximation is only valid for a large number of domains in each section. Here we calculate the PMF by explicitly considering the contribution from each domain. The nonlinearity profile  $\chi_D(z)$  will consist of domains of nonlinear coefficients  $\pm\chi^{(2)}$ , with sign changes occurring at positions corresponding to the poling order and duty cycle (this is the case for the entire length of a typical periodically poled crystal). For example, in the section corresponding to  $m = 3$ —where the duty cycle is 50%—the sign changes every  $3\Lambda$ , while for  $m = 6$ —where the duty cycle is  $\approx 41.6\%$ —the sign changes from “+” to “−” after  $5\Lambda$  and back again after  $7\Lambda$ . The resulting PMF takes the form

$$\Phi_D(\Delta k_p) = \chi^{(2)} \sum_j s_j (e^{-i\Delta k_p z_j} - e^{-i\Delta k_p z_{j-1}}), \quad (\text{A.1})$$

where  $s_j$  is the sign of the  $j$ th domain and  $z_{j-1} - z_j$  is the width of each domain. Fig. A.1 shows that as  $\Delta k_p$  departs from 0, the two models begin to deviate. However, as we discuss in the main text, there is very good agreement between the basic and detailed models in the region of interest, i.e. around  $\Delta k_p = 0$ .

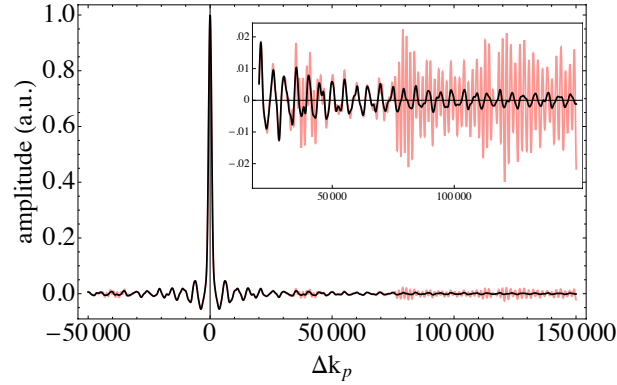


**Figure A.1:** Comparison between basic and domain-by-domain models. Phase matching functions generated from the basic model (black solid line) and the detailed model (light red line). The inset shows a magnified portion of the PMFs, detailing the deviation between the models.

---

# Time-ordering in Spontaneous Parametric Down-conversion

---

## B.1 Commutativity of the SPDC Hamiltonian

We would like to show that the SPDC Hamiltonian doesn't commute with itself at all times, i.e. that the commutator is zero. The commutator is

$$\begin{aligned}
[\hat{H}(t_1), \hat{H}(t_2)] &= \hat{H}(t_1)\hat{H}(t_2) - \hat{H}(t_2)\hat{H}(t_1) & (B.1) \\
&= A^2 \int_{-L/2}^{L/2} dz \int_{-L/2}^{L/2} dz' \iiint d\omega_i d\omega_s d\omega_p \iiint d\omega'_i d\omega'_s d\omega'_p \\
&\quad \times \left( \left( e^{-i\Delta k(\omega_i, \omega_s, \omega_p)z} e^{i\Delta\omega t_1} \alpha(\omega_p) \hat{a}_i^\dagger(\omega_i) \hat{a}_s^\dagger(\omega_s) \right. \right. \\
&\quad + e^{i\Delta k(\omega_i, \omega_s, \omega_p)z} e^{-i\Delta\omega t_1} \alpha^*(\omega_p) \hat{a}_i(\omega_i) \hat{a}_s(\omega_s) \left. \right) \\
&\quad \times \left( e^{-i\Delta k(\omega'_i, \omega'_s, \omega'_p)z'} e^{i\Delta\omega' t_2} \alpha(\omega'_p) \hat{a}_i^\dagger(\omega'_i) \hat{a}_s^\dagger(\omega'_s) \right. \\
&\quad + e^{i\Delta k(\omega'_i, \omega'_s, \omega'_p)z'} e^{-i\Delta\omega' t_2} \alpha^*(\omega'_p) \hat{a}_i(\omega'_i) \hat{a}_s(\omega'_s) \left. \right) & (B.2) \\
&\quad - \left( e^{-i\Delta k(\omega'_i, \omega'_s, \omega'_p)z'} e^{i\Delta\omega' t_2} \alpha(\omega'_p) \hat{a}_i^\dagger(\omega'_i) \hat{a}_s^\dagger(\omega'_s) \right. \\
&\quad + e^{i\Delta k(\omega'_i, \omega'_s, \omega'_p)z'} e^{-i\Delta\omega' t_2} \alpha^*(\omega'_p) \hat{a}_i(\omega'_i) \hat{a}_s(\omega'_s) \left. \right) \\
&\quad \times \left( e^{-i\Delta k(\omega_i, \omega_s, \omega_p)z} e^{i\Delta\omega t_1} \alpha(\omega_p) \hat{a}_i^\dagger(\omega_i) \hat{a}_s^\dagger(\omega_s) \right. \\
&\quad \left. \left. + e^{i\Delta k(\omega_i, \omega_s, \omega_p)z} e^{-i\Delta\omega t_1} \alpha^*(\omega_p) \hat{a}_i(\omega_i) \hat{a}_s(\omega_s) \right) \right)
\end{aligned}$$

Make the substitution that  $z \rightarrow -z$  and  $z' \rightarrow -z'$  and invert the limits of integration in the terms containing  $e^{-i\Delta k(\omega_i, \omega_s, \omega_p)z}$  and  $e^{-i\Delta k(\omega_i, \omega_s, \omega_p)z'}$ .

$$\begin{aligned}
 [\hat{H}(t_1), \hat{H}(t_2)] &= A^2 \int_{-L/2}^{L/2} dz \int_{-L/2}^{L/2} dz' \iiint d\omega_i d\omega_s d\omega_p \iiint d\omega'_i d\omega'_s d\omega'_p \\
 &\quad \times e^{i\Delta k(\omega_i, \omega_s, \omega_p)z} e^{i\Delta k(\omega'_i, \omega'_s, \omega'_p)z'} \\
 &\quad \times \left( (e^{i\Delta\omega t_1} \alpha(\omega_p) \hat{a}_i^\dagger(\omega_i) \hat{a}_s^\dagger(\omega_s) + e^{-i\Delta\omega t_1} \alpha^*(\omega_p) \hat{a}_i(\omega_i) \hat{a}_s(\omega_s)) \right. \\
 &\quad \times (e^{i\Delta\omega' t_2} \alpha(\omega'_p) \hat{a}_i^\dagger(\omega'_i) \hat{a}_s^\dagger(\omega'_s) + e^{-i\Delta\omega' t_2} \alpha^*(\omega'_p) \hat{a}_i(\omega'_i) \hat{a}_s(\omega'_s)) \\
 &\quad - (e^{i\Delta\omega' t_2} \alpha(\omega'_p) \hat{a}_i^\dagger(\omega'_i) \hat{a}_s^\dagger(\omega'_s) + e^{-i\Delta\omega' t_2} \alpha^*(\omega'_p) \hat{a}_i(\omega'_i) \hat{a}_s(\omega'_s)) \\
 &\quad \left. \times (e^{i\Delta\omega t_1} \alpha(\omega_p) \hat{a}_i^\dagger(\omega_i) \hat{a}_s^\dagger(\omega_s) + e^{-i\Delta\omega t_1} \alpha^*(\omega_p) \hat{a}_i(\omega_i) \hat{a}_s(\omega_s)) \right) \quad (\text{B.3})
 \end{aligned}$$

Expand the brackets.

$$\begin{aligned}
 [\hat{H}(t_1), \hat{H}(t_2)] &= A^2 \int_{-L/2}^{L/2} dz \int_{-L/2}^{L/2} dz' \iiint d\omega_i d\omega_s d\omega_p \iiint d\omega'_i d\omega'_s d\omega'_p \\
 &\quad \times e^{i\Delta k(\omega_i, \omega_s, \omega_p)z} e^{i\Delta k(\omega'_i, \omega'_s, \omega'_p)z'} \\
 &\quad \times \left( e^{i\Delta\omega t_1} e^{i\Delta\omega' t_2} \alpha(\omega_p) \alpha(\omega'_p) \right. \\
 &\quad \times (\hat{a}_i^\dagger(\omega_i) \hat{a}_i^\dagger(\omega'_i) \hat{a}_s^\dagger(\omega_s) \hat{a}_s^\dagger(\omega'_s) - \hat{a}_i^\dagger(\omega'_i) \hat{a}_i^\dagger(\omega_i) \hat{a}_s^\dagger(\omega_s) \hat{a}_s^\dagger(\omega'_s)) \\
 &\quad + e^{-i\Delta\omega t_1} e^{i\Delta\omega' t_2} \alpha^*(\omega_p) \alpha(\omega'_p) \\
 &\quad \times (\hat{a}_i(\omega_i) \hat{a}_i^\dagger(\omega'_i) \hat{a}_s(\omega_s) \hat{a}_s^\dagger(\omega'_s) - \hat{a}_i^\dagger(\omega'_i) \hat{a}_i(\omega_i) \hat{a}_s^\dagger(\omega'_s) \hat{a}_s(\omega_s)) \\
 &\quad + e^{i\Delta\omega t_1} e^{-i\Delta\omega' t_2} \alpha(\omega_p) \alpha^*(\omega'_p) \\
 &\quad \times (\hat{a}_i^\dagger(\omega_i) \hat{a}_i(\omega'_i) \hat{a}_s^\dagger(\omega_s) \hat{a}_s(\omega'_s) - \hat{a}_i(\omega'_i) \hat{a}_i^\dagger(\omega_i) \hat{a}_s(\omega'_s) \hat{a}_s^\dagger(\omega_s)) \\
 &\quad + e^{-i\Delta\omega t_1} e^{-i\Delta\omega' t_2} \alpha^*(\omega_p) \alpha^*(\omega'_p) \\
 &\quad \left. \times (\hat{a}_i(\omega_i) \hat{a}_i(\omega'_i) \hat{a}_s(\omega_s) \hat{a}_s(\omega'_s) - \hat{a}_i(\omega'_i) \hat{a}_i(\omega_i) \hat{a}_s(\omega'_s) \hat{a}_s(\omega_s)) \right) \quad (\text{B.4})
 \end{aligned}$$

The first and last terms go to zero.

$$\begin{aligned}
 [\hat{H}(t_1), \hat{H}(t_2)] &= A^2 \int_{-L/2}^{L/2} dz \int_{-L/2}^{L/2} dz' \iiint d\omega_i d\omega_s d\omega_p \iiint d\omega'_i d\omega'_s d\omega'_p \\
 &\quad \times e^{i\Delta k(\omega_i, \omega_s, \omega_p)z} e^{i\Delta k(\omega'_i, \omega'_s, \omega'_p)z'} \\
 &\quad \times \left( e^{-i\Delta\omega t_1} e^{i\Delta\omega' t_2} \alpha^*(\omega_p) \alpha(\omega'_p) \right. \\
 &\quad \times (\hat{a}_i(\omega_i) \hat{a}_i^\dagger(\omega'_i) \hat{a}_s(\omega_s) \hat{a}_s^\dagger(\omega'_s) - \hat{a}_i^\dagger(\omega'_i) \hat{a}_i(\omega_i) \hat{a}_s^\dagger(\omega'_s) \hat{a}_s(\omega_s)) \\
 &\quad + e^{i\Delta\omega t_1} e^{-i\Delta\omega' t_2} \alpha(\omega_p) \alpha^*(\omega'_p) \\
 &\quad \left. \times (\hat{a}_i^\dagger(\omega_i) \hat{a}_i(\omega'_i) \hat{a}_s^\dagger(\omega_s) \hat{a}_s(\omega'_s) - \hat{a}_i(\omega_i) \hat{a}_i^\dagger(\omega'_i) \hat{a}_s(\omega_s) \hat{a}_s^\dagger(\omega'_s)) \right)
 \end{aligned} \tag{B.5}$$

Substitute  $\omega_j \rightarrow \omega'_j$  and  $z \rightarrow z'$  and vice-versa in the second term.

$$\begin{aligned}
 [\hat{H}(t_1), \hat{H}(t_2)] &= A^2 \int_{-L/2}^{L/2} dz \int_{-L/2}^{L/2} dz' \iiint d\omega_i d\omega_s d\omega_p \iiint d\omega'_i d\omega'_s d\omega'_p \\
 &\quad \times e^{i\Delta k(\omega_i, \omega_s, \omega_p)z} e^{i\Delta k(\omega'_i, \omega'_s, \omega'_p)z'} \\
 &\quad \times \left( e^{-i\Delta\omega t_1} e^{i\Delta\omega' t_2} \alpha^*(\omega_p) \alpha(\omega'_p) \right. \\
 &\quad \times (\hat{a}_i(\omega_i) \hat{a}_i^\dagger(\omega'_i) \hat{a}_s(\omega_s) \hat{a}_s^\dagger(\omega'_s) - \hat{a}_i^\dagger(\omega'_i) \hat{a}_i(\omega_i) \hat{a}_s^\dagger(\omega'_s) \hat{a}_s(\omega_s)) \\
 &\quad + e^{i\Delta\omega' t_1} e^{-i\Delta\omega t_2} \alpha(\omega'_p) \alpha^*(\omega_p) \\
 &\quad \left. \times (\hat{a}_i^\dagger(\omega'_i) \hat{a}_i(\omega_i) \hat{a}_s^\dagger(\omega'_s) \hat{a}_s(\omega_s) - \hat{a}_i(\omega_i) \hat{a}_i^\dagger(\omega'_i) \hat{a}_s(\omega_s) \hat{a}_s^\dagger(\omega'_s)) \right) \\
 &= A^2 \int_{-L/2}^{L/2} dz \int_{-L/2}^{L/2} dz' \iiint d\omega_i d\omega_s d\omega_p \iiint d\omega'_i d\omega'_s d\omega'_p \\
 &\quad \times \alpha(\omega'_p) \alpha^*(\omega_p) e^{i\Delta k(\omega_i, \omega_s, \omega_p)z} e^{i\Delta k(\omega'_i, \omega'_s, \omega'_p)z'} \\
 &\quad \times \left( e^{-i\Delta\omega t_1} e^{i\Delta\omega' t_2} - e^{i\Delta\omega' t_1} e^{-i\Delta\omega t_2} \right) \\
 &\quad \times \left( \hat{a}_i(\omega_i) \hat{a}_i^\dagger(\omega'_i) \hat{a}_s(\omega_s) \hat{a}_s^\dagger(\omega'_s) - \hat{a}_i^\dagger(\omega'_i) \hat{a}_i(\omega_i) \hat{a}_s^\dagger(\omega'_s) \hat{a}_s(\omega_s) \right)
 \end{aligned} \tag{B.6}$$

Since the integrals are only over positive frequencies, this expression is nonzero.

## B.2 Sanity Check

As a sanity check, we compare the sum of all six permutations within the third order term of both the Taylor and Dyson series. They should give the same answer. For the Taylor series, we can write

$$\begin{aligned}
 P_{6T} = & \frac{1}{3!} \int_{-\infty}^{\infty} dt_1 \int_{-\infty}^{\infty} dt_2 \int_{-\infty}^{\infty} dt_3 \\
 & \times (\hat{H}(t_1)\hat{H}(t_2)\hat{H}(t_3) + \hat{H}(t_1)\hat{H}(t_3)\hat{H}(t_2) + \hat{H}(t_2)\hat{H}(t_1)\hat{H}(t_3) \\
 & + \hat{H}(t_2)\hat{H}(t_3)\hat{H}(t_1) + \hat{H}(t_3)\hat{H}(t_1)\hat{H}(t_2) + \hat{H}(t_3)\hat{H}(t_2)\hat{H}(t_1)). \quad (B.8)
 \end{aligned}$$

More specifically, looking at just the six-photon state, we can write

$$\begin{aligned}
 |P_{6T}\rangle = & \frac{1}{3!} \left( \frac{AL}{i\hbar} \right)^3 \iiint d\omega_i d\omega_s \omega_p \iiint d\omega'_i d\omega'_s \omega'_p \iiint d\omega''_i d\omega''_s \omega''_p \\
 & \times f(\omega_i, \omega_s, \omega_p) f(\omega'_i, \omega'_s, \omega'_p) f(\omega''_i, \omega''_s, \omega''_p) \int_{-\infty}^{\infty} dt_1 \int_{-\infty}^{\infty} dt_2 \int_{-\infty}^{\infty} dt_3 \\
 & \times \left( e^{i\Delta\omega t_1} e^{i\Delta\omega' t_2} e^{i\Delta\omega'' t_3} + e^{i\Delta\omega t_1} e^{i\Delta\omega' t_3} e^{i\Delta\omega'' t_2} + e^{i\Delta\omega t_2} e^{i\Delta\omega' t_1} e^{i\Delta\omega'' t_3} \right. \\
 & \left. + e^{i\Delta\omega t_2} e^{i\Delta\omega' t_3} e^{i\Delta\omega'' t_1} + e^{i\Delta\omega t_3} e^{i\Delta\omega' t_1} e^{i\Delta\omega'' t_2} + e^{i\Delta\omega t_3} e^{i\Delta\omega' t_2} e^{i\Delta\omega'' t_1} \right) \\
 & \times \hat{a}_i^\dagger(\omega_i) \hat{a}_s^\dagger(\omega_s) \hat{a}_i^\dagger(\omega'_i) \hat{a}_s^\dagger(\omega'_s) \hat{a}_i^\dagger(\omega''_i) \hat{a}_s^\dagger(\omega''_s) |0\rangle. \quad (B.9)
 \end{aligned}$$

Relabeling the time variables, and then performing the time integrals, yields

$$\begin{aligned}
 |P_{6T}\rangle = & \left( \frac{AL}{i\hbar} \right)^3 \iiint d\omega_i d\omega_s \omega_p \iiint d\omega'_i d\omega'_s \omega'_p \iiint d\omega''_i d\omega''_s \omega''_p \\
 & \times f(\omega_i, \omega_s, \omega_p) f(\omega'_i, \omega'_s, \omega'_p) f(\omega''_i, \omega''_s, \omega''_p) \\
 & \times \int_{-\infty}^{\infty} dt_1 \int_{-\infty}^{\infty} dt_2 \int_{-\infty}^{\infty} dt_3 e^{i\Delta\omega t_1} e^{i\Delta\omega' t_2} e^{i\Delta\omega'' t_3} \\
 & \times \hat{a}_i^\dagger(\omega_i) \hat{a}_s^\dagger(\omega_s) \hat{a}_i^\dagger(\omega'_i) \hat{a}_s^\dagger(\omega'_s) \hat{a}_i^\dagger(\omega''_i) \hat{a}_s^\dagger(\omega''_s) |0\rangle \quad (B.10)
 \end{aligned}$$

$$\begin{aligned}
 = & \left( \frac{2\pi AL}{i\hbar} \right)^3 \iiint d\omega_i d\omega_s \omega_p \iiint d\omega'_i d\omega'_s \omega'_p \iiint d\omega''_i d\omega''_s \omega''_p \\
 & \times f(\omega_i, \omega_s, \omega_p) f(\omega'_i, \omega'_s, \omega'_p) f(\omega''_i, \omega''_s, \omega''_p) \delta(\Delta\omega) \delta(\Delta\omega') \delta(\Delta\omega'') \\
 & \times \hat{a}_i^\dagger(\omega_i) \hat{a}_s^\dagger(\omega_s) \hat{a}_i^\dagger(\omega'_i) \hat{a}_s^\dagger(\omega'_s) \hat{a}_i^\dagger(\omega''_i) \hat{a}_s^\dagger(\omega''_s) |0\rangle. \quad (B.11)
 \end{aligned}$$

For the Dyson series, we can write the sum of all permutations as

$$\begin{aligned}
P_{6\text{D}} &= \int_{-\infty}^{\infty} dt_1 \int_{-\infty}^{t_1} dt_2 \int_{-\infty}^{t_2} dt_3 \\
&\times \left( \hat{H}(t_1)\hat{H}(t_2)\hat{H}(t_3) + \hat{H}(t_1)\hat{H}(t_3)\hat{H}(t_2) + \hat{H}(t_2)\hat{H}(t_1)\hat{H}(t_3) \right. \\
&\quad \left. + \hat{H}(t_2)\hat{H}(t_3)\hat{H}(t_1) + \hat{H}(t_3)\hat{H}(t_1)\hat{H}(t_2) + \hat{H}(t_3)\hat{H}(t_2)\hat{H}(t_1) \right). \tag{B.12}
\end{aligned}$$

More specifically, looking at just the six-photon state

$$\begin{aligned}
|P_{6\text{D}}\rangle &= \left(\frac{AL}{i\hbar}\right)^3 \iiint d\omega_i d\omega_s \omega_p \iiint d\omega'_i d\omega'_s \omega'_p \iiint d\omega''_i d\omega''_s \omega''_p \\
&\times f(\omega_i, \omega_s, \omega_p) f(\omega'_i, \omega'_s, \omega'_p) f(\omega''_i, \omega''_s, \omega''_p) \int_{-\infty}^{\infty} dt_1 \int_{-\infty}^{t_1} dt_2 \int_{-\infty}^{t_2} dt_3 \\
&\times \left( e^{i\Delta\omega t_1} e^{i\Delta\omega' t_2} e^{i\Delta\omega'' t_3} + e^{i\Delta\omega t_1} e^{i\Delta\omega' t_3} e^{i\Delta\omega'' t_2} + e^{i\Delta\omega t_2} e^{i\Delta\omega' t_1} e^{i\Delta\omega'' t_3} \right. \\
&\quad \left. + e^{i\Delta\omega t_2} e^{i\Delta\omega' t_3} e^{i\Delta\omega'' t_1} + e^{i\Delta\omega t_3} e^{i\Delta\omega' t_1} e^{i\Delta\omega'' t_2} + e^{i\Delta\omega t_3} e^{i\Delta\omega' t_2} e^{i\Delta\omega'' t_1} \right) \\
&\times \hat{a}_i^\dagger(\omega_i) \hat{a}_s^\dagger(\omega_s) \hat{a}_i^\dagger(\omega'_i) \hat{a}_s^\dagger(\omega'_s) \hat{a}_i^\dagger(\omega''_i) \hat{a}_s^\dagger(\omega''_s) |0\rangle. \tag{B.13}
\end{aligned}$$

Relabeling the time variables yields

$$\begin{aligned}
|P_{6\text{D}}\rangle &= \left(\frac{AL}{i\hbar}\right)^3 \iiint d\omega_i d\omega_s \omega_p \iiint d\omega'_i d\omega'_s \omega'_p \iiint d\omega''_i d\omega''_s \omega''_p \\
&\times f(\omega_i, \omega_s, \omega_p) f(\omega'_i, \omega'_s, \omega'_p) f(\omega''_i, \omega''_s, \omega''_p) \\
&\times \left( \int_{-\infty}^{\infty} dt_1 \int_{-\infty}^{t_1} dt_2 \int_{-\infty}^{t_2} dt_3 + \int_{-\infty}^{\infty} dt_1 \int_{-\infty}^{t_1} dt_3 \int_{-\infty}^{t_3} dt_2 \right. \\
&\quad \left. + \int_{-\infty}^{\infty} dt_2 \int_{-\infty}^{t_2} dt_1 \int_{-\infty}^{t_1} dt_3 + \int_{-\infty}^{\infty} dt_2 \int_{-\infty}^{t_2} dt_3 \int_{-\infty}^{t_3} dt_1 \right. \\
&\quad \left. + \int_{-\infty}^{\infty} dt_3 \int_{-\infty}^{t_3} dt_1 \int_{-\infty}^{t_1} dt_2 + \int_{-\infty}^{\infty} dt_3 \int_{-\infty}^{t_3} dt_2 \int_{-\infty}^{t_2} dt_1 \right) e^{i\Delta\omega t_1} e^{i\Delta\omega' t_2} e^{i\Delta\omega'' t_3} \\
&\times \hat{a}_i^\dagger(\omega_i) \hat{a}_s^\dagger(\omega_s) \hat{a}_i^\dagger(\omega'_i) \hat{a}_s^\dagger(\omega'_s) \hat{a}_i^\dagger(\omega''_i) \hat{a}_s^\dagger(\omega''_s) |0\rangle. \tag{B.14}
\end{aligned}$$

We can make use of the following identities<sup>1</sup>

$$\int_{-\infty}^{\infty} dt_2 \int_{-\infty}^{t_2} dt_1 \int_{-\infty}^{t_1} dt_3 + \int_{-\infty}^{\infty} dt_2 \int_{-\infty}^{t_2} dt_3 \int_{-\infty}^{t_3} dt_1 = \int_{-\infty}^{\infty} dt_1 \int_{t_1}^{\infty} dt_2 \int_{-\infty}^{t_2} dt_3, \quad (\text{B.15})$$

$$\int_{-\infty}^{\infty} dt_1 \int_{-\infty}^{t_1} dt_3 \int_{-\infty}^{t_3} dt_2 + \int_{-\infty}^{\infty} dt_3 \int_{-\infty}^{t_3} dt_1 \int_{-\infty}^{t_1} dt_2 = \int_{-\infty}^{\infty} dt_1 \int_{-\infty}^{t_1} dt_1 \int_{t_1}^{\infty} dt_3, \quad (\text{B.16})$$

$$\int_{-\infty}^{\infty} dt_3 \int_{-\infty}^{t_3} dt_2 \int_{-\infty}^{t_2} dt_1 = \int_{-\infty}^{\infty} dt_1 \int_{t_1}^{\infty} dt_2 \int_{t_2}^{\infty} dt_3, \quad (\text{B.17})$$

to write

$$\begin{aligned} |P_{6D}\rangle &= \left(\frac{AL}{i\hbar}\right)^3 \iiint d\omega_i d\omega_s \omega_p \iiint d\omega'_i d\omega'_s \omega'_p \iiint d\omega''_i d\omega''_s \omega''_p \\ &\quad \times f(\omega_i, \omega_s, \omega_p) f(\omega'_i, \omega'_s, \omega'_p) f(\omega''_i, \omega''_s, \omega''_p) \\ &\quad \times \left( \int_{-\infty}^{\infty} dt_1 \int_{-\infty}^{t_1} dt_2 \int_{-\infty}^{t_2} dt_3 + \int_{-\infty}^{\infty} dt_1 \int_{t_1}^{\infty} dt_2 \int_{-\infty}^{t_2} dt_3 \right. \\ &\quad \left. + \int_{-\infty}^{\infty} dt_1 \int_{-\infty}^{t_1} dt_1 \int_{t_1}^{\infty} dt_3 + \int_{-\infty}^{\infty} dt_1 \int_{t_1}^{\infty} dt_2 \int_{t_2}^{\infty} dt_3 \right) \\ &\quad \times e^{i\Delta\omega t_1} e^{i\Delta\omega' t_2} e^{i\Delta\omega'' t_3} \\ &\quad \times \hat{a}_i^\dagger(\omega_i) \hat{a}_s^\dagger(\omega_s) \hat{a}_i^\dagger(\omega'_i) \hat{a}_s^\dagger(\omega'_s) \hat{a}_i^\dagger(\omega''_i) \hat{a}_s^\dagger(\omega''_s) |0\rangle. \end{aligned} \quad (\text{B.18})$$

Now perform a change of variables with respect to the time integrals according to B.7.1

$$\begin{aligned} |P_{6D}\rangle &= \frac{1}{3} \left(\frac{AL}{i\hbar}\right)^3 \iiint d\omega_i d\omega_s \omega_p \iiint d\omega'_i d\omega'_s \omega'_p \iiint d\omega''_i d\omega''_s \omega''_p \\ &\quad \times f(\omega_i, \omega_s, \omega_p) f(\omega'_i, \omega'_s, \omega'_p) f(\omega''_i, \omega''_s, \omega''_p) \\ &\quad \times \left( \int_{-\infty}^{\infty} dq \int_0^{\infty} dr \int_0^{\infty} ds + \int_{-\infty}^{\infty} dq \int_0^{\infty} dr \int_{-\infty}^0 ds \right. \\ &\quad \left. + \int_{-\infty}^{\infty} dq \int_{-\infty}^0 dr \int_0^{\infty} ds + \int_{-\infty}^{\infty} dq \int_{-\infty}^0 dr \int_{-\infty}^0 ds \right) \\ &\quad e^{\frac{i}{3}(\Delta\omega + \Delta\omega' + \Delta\omega'')q} e^{\frac{i}{3}(2\Delta\omega - \Delta\omega' - \Delta\omega'')r} e^{\frac{i}{3}(\Delta\omega + \Delta\omega' - 2\Delta\omega'')s} \\ &\quad \times \hat{a}_i^\dagger(\omega_i) \hat{a}_s^\dagger(\omega_s) \hat{a}_i^\dagger(\omega'_i) \hat{a}_s^\dagger(\omega'_s) \hat{a}_i^\dagger(\omega''_i) \hat{a}_s^\dagger(\omega''_s) |0\rangle. \end{aligned} \quad (\text{B.19})$$

<sup>1</sup>It is easy to convince oneself of these identities by plotting the 3-dimensional integration regions in, e.g., Mathematica.

Performing the integral over the new time variables, according to Appendix B.8, yields

$$\begin{aligned}
|P_{6D}\rangle &= \frac{2 \times 3^3}{3} \left( \frac{\pi AL}{i\hbar} \right)^3 \iiint d\omega_i d\omega_s \omega_p \iiint d\omega'_i d\omega'_s \omega'_p \iiint d\omega''_i d\omega''_s \omega''_p \\
&\quad \times f(\omega_i, \omega_s, \omega_p) f(\omega'_i, \omega'_s, \omega'_p) f(\omega''_i, \omega''_s, \omega''_p) \delta(\Delta\omega + \Delta\omega' + \Delta\omega'') \\
&\quad \left( \left( \delta(2\Delta\omega - \Delta\omega' - \Delta\omega'') + \frac{i}{\pi} \frac{1}{2\Delta\omega - \Delta\omega' - \Delta\omega''} \right) \right. \\
&\quad \times \left( \delta(\Delta\omega + \Delta\omega' - 2\Delta\omega'') + \frac{i}{\pi} \frac{1}{\Delta\omega + \Delta\omega' - 2\Delta\omega''} \right) \\
&\quad + \left( \delta(2\Delta\omega - \Delta\omega' - \Delta\omega'') + \frac{i}{\pi} \frac{1}{2\Delta\omega - \Delta\omega' - \Delta\omega''} \right) \\
&\quad \times \left( \delta(\Delta\omega + \Delta\omega' - 2\Delta\omega'') - \frac{i}{\pi} \frac{1}{\Delta\omega + \Delta\omega' - 2\Delta\omega''} \right) \\
&\quad + \left( \delta(2\Delta\omega - \Delta\omega' - \Delta\omega'') - \frac{i}{\pi} \frac{1}{2\Delta\omega - \Delta\omega' - \Delta\omega''} \right) \\
&\quad \times \left( \delta(\Delta\omega + \Delta\omega' - 2\Delta\omega'') + \frac{i}{\pi} \frac{1}{\Delta\omega + \Delta\omega' - 2\Delta\omega''} \right) \\
&\quad + \left( \delta(2\Delta\omega - \Delta\omega' - \Delta\omega'') - \frac{i}{\pi} \frac{1}{2\Delta\omega - \Delta\omega' - \Delta\omega''} \right) \\
&\quad \times \left. \left( \delta(\Delta\omega + \Delta\omega' - 2\Delta\omega'') - \frac{i}{\pi} \frac{1}{\Delta\omega + \Delta\omega' - 2\Delta\omega''} \right) \right) \\
&\quad \times \hat{a}_i^\dagger(\omega_i) \hat{a}_s^\dagger(\omega_s) \hat{a}_i^\dagger(\omega'_i) \hat{a}_s^\dagger(\omega'_s) \hat{a}_i^\dagger(\omega''_i) \hat{a}_s^\dagger(\omega''_s) |0\rangle.
\end{aligned} \tag{B.20}$$

After cancellation of all the imaginary terms, we get

$$\begin{aligned}
|P_{6D}\rangle &= \frac{4 \times 2 \times 3^3}{3} \left( \frac{\pi AL}{i\hbar} \right)^3 \iiint d\omega_i d\omega_s \omega_p \iiint d\omega'_i d\omega'_s \omega'_p \iiint d\omega''_i d\omega''_s \omega''_p \\
&\quad \times f(\omega_i, \omega_s, \omega_p) f(\omega'_i, \omega'_s, \omega'_p) f(\omega''_i, \omega''_s, \omega''_p) \delta(\Delta\omega + \Delta\omega' + \Delta\omega'') \\
&\quad \delta(2\Delta\omega - \Delta\omega' - \Delta\omega'') \delta(\Delta\omega + \Delta\omega' - 2\Delta\omega'') \\
&\quad \times \hat{a}_i^\dagger(\omega_i) \hat{a}_s^\dagger(\omega_s) \hat{a}_i^\dagger(\omega'_i) \hat{a}_s^\dagger(\omega'_s) \hat{a}_i^\dagger(\omega''_i) \hat{a}_s^\dagger(\omega''_s) |0\rangle
\end{aligned} \tag{B.21}$$

$$\begin{aligned}
&= \left( \frac{2\pi AL}{i\hbar} \right)^3 \iiint d\omega_i d\omega_s \omega_p \iiint d\omega'_i d\omega'_s \omega'_p \iiint d\omega''_i d\omega''_s \omega''_p \\
&\quad \times f(\omega_i, \omega_s, \omega_p) f(\omega'_i, \omega'_s, \omega'_p) f(\omega''_i, \omega''_s, \omega''_p) \delta(\Delta\omega) \delta(\Delta\omega') \delta(\Delta\omega'') \\
&\quad \times \hat{a}_i^\dagger(\omega_i) \hat{a}_s^\dagger(\omega_s) \hat{a}_i^\dagger(\omega'_i) \hat{a}_s^\dagger(\omega'_s) \hat{a}_i^\dagger(\omega''_i) \hat{a}_s^\dagger(\omega''_s) |0\rangle
\end{aligned} \tag{B.22}$$

$$= |P_{6T}\rangle, \tag{B.23}$$

where  $|P_{6T}\rangle$  is defined in equation B.11.

### B.3 Evaluating the Taylor series expansion

The down-converted state in equation 6.6 can be written as follows

$$|\Psi_{\text{PDC}}\rangle_{\text{T}} = \frac{1}{\sqrt{\mathcal{N}_{\text{T}}}} \left( |\Psi_{\text{PDC}}^{(0)}\rangle_{\text{T}} + |\Psi_{\text{PDC}}^{(1)}\rangle_{\text{T}} + |\Psi_{\text{PDC}}^{(2)}\rangle_{\text{T}} + |\Psi_{\text{PDC}}^{(3)}\rangle_{\text{T}} \right), \quad (\text{B.24})$$

where  $|\Psi_{\text{PDC}}^{(n)}\rangle_{\text{T}}$  represents the  $n$ th expansion of  $|\Psi_{\text{PDC}}\rangle_{\text{T}}$  and

$$|\Psi_{\text{PDC}}^{(0)}\rangle_{\text{T}} = |0\rangle, \quad (\text{B.25})$$

$$|\Psi_{\text{PDC}}^{(1)}\rangle_{\text{T}} = \frac{1}{i\hbar} \int_{-\infty}^{\infty} dt_1 \hat{H}(t_1) |0\rangle, \quad (\text{B.26})$$

$$|\Psi_{\text{PDC}}^{(2)}\rangle_{\text{T}} = \left( \frac{1}{i\hbar} \right)^2 \int_{-\infty}^{\infty} dt_1 \hat{H}(t_1) \int_{-\infty}^{\infty} dt_2 \hat{H}(t_2) |0\rangle, \quad (\text{B.27})$$

$$|\Psi_{\text{PDC}}^{(3)}\rangle_{\text{T}} = \left( \frac{1}{i\hbar} \right)^3 \int_{-\infty}^{\infty} dt_1 \hat{H}(t_1) \int_{-\infty}^{\infty} dt_2 \hat{H}(t_2) \int_{-\infty}^{\infty} dt_3 \hat{H}(t_3) |0\rangle. \quad (\text{B.28})$$

#### B.3.1 First Order Term

The first order state can be calculated by substituting the Hamiltonian in Equation 6.2 into Equation B.26

$$|\Psi_{\text{PDC}}^{(1)}\rangle_{\text{T}} = \frac{1}{i\hbar} \int_{-\infty}^{\infty} dt_1 \hat{H}(t_1) |0\rangle \quad (\text{B.29})$$

$$= \frac{AL}{i\hbar} \int_{-\infty}^{\infty} dt_1 \iiint d\omega_i d\omega_s d\omega_p (f(\omega_i, \omega_s, \omega_p) e^{i\Delta\omega t_1} \hat{a}_i^\dagger(\omega_i) \hat{a}_s^\dagger(\omega_s) + f^*(\omega_i, \omega_s, \omega_p) e^{-i\Delta\omega t_1} \hat{a}_i(\omega_i) \hat{a}_s(\omega_s)) |0\rangle \quad (\text{B.30})$$

$$= \frac{AL}{i\hbar} \int_{-\infty}^{\infty} dt_1 \iiint d\omega_i d\omega_s d\omega_p f(\omega_i, \omega_s, \omega_p) e^{i\Delta\omega t_1} \hat{a}_i^\dagger(\omega_i) \hat{a}_s^\dagger(\omega_s) |0\rangle \quad (\text{B.31})$$

$$= \mathcal{A} \iiint d\omega_i d\omega_s d\omega_p f(\omega_i, \omega_s, \omega_p) \delta(\Delta\omega) \hat{a}_i^\dagger(\omega_i) \hat{a}_s^\dagger(\omega_s) |0\rangle \quad (\text{B.32})$$

$$= \mathcal{A} \iint d\omega_i d\omega_s f(\omega_i, \omega_s, \omega_i + \omega_s) \hat{a}_i^\dagger(\omega_i) \hat{a}_s^\dagger(\omega_s) |0\rangle, \quad (\text{B.33})$$

where  $\mathcal{A} = 2\pi AL/i\hbar$  and  $f(\omega_i, \omega_s, \omega_p)$  is defined in equation 6.3. This corresponds to a state consisting of two photons, of frequencies  $\omega_i$  and  $\omega_s$ , with a joint spectral amplitude  $f(\omega_i, \omega_s, \omega_i + \omega_s)$ . The frequencies of the down-converted photons are constrained by energy conservation according to  $\omega_i + \omega_s = \omega_p$ , where  $\omega_p$  is the frequency of the pump photon. A schematic of this process is shown in figure 6.4 a).

### B.3.2 Second Order Term

To calculate the second order term, substitute the Hamiltonian in Equation 6.2 into Equation B.27

$$\begin{aligned}
|\Psi_{\text{PDC}}^{(2)}\rangle_{\text{T}} &= \left(\frac{1}{i\hbar}\right)^2 \int_{-\infty}^{\infty} dt_1 \hat{H}(t_1) \int_{-\infty}^{\infty} dt_2 \hat{H}(t_2) |0\rangle \\
&= \left(\frac{AL}{i\hbar}\right)^2 \int_{-\infty}^{\infty} dt_1 \int_{-\infty}^{\infty} dt_2 \iiint d\omega_i d\omega_s d\omega_p \iiint d\omega'_i d\omega'_s d\omega'_p \\
&\quad \times \left( f(\omega_i, \omega_s, \omega_p) e^{i\Delta\omega t_1} \hat{a}_i^\dagger(\omega_i) \hat{a}_s^\dagger(\omega_s) + f^*(\omega_i, \omega_s, \omega_p) e^{-i\Delta\omega t_1} \hat{a}_i(\omega_i) \hat{a}_s(\omega_s) \right) \\
&\quad \times \left( f(\omega'_i, \omega'_s, \omega'_p) e^{i\Delta\omega' t_2} \hat{a}_i^\dagger(\omega'_i) \hat{a}_s^\dagger(\omega'_s) + f^*(\omega'_i, \omega'_s, \omega'_p) e^{-i\Delta\omega' t_2} \hat{a}_i(\omega'_i) \hat{a}_s(\omega'_s) \right) |0\rangle,
\end{aligned} \tag{B.34}$$

Some of the terms in the above equation will go to zero due to the annihilation of the vacuum state. Omitting these terms and expanding the brackets, gives

$$\begin{aligned}
|\Psi_{\text{PDC}}^{(2)}\rangle_{\text{T}} &= \left(\frac{AL}{i\hbar}\right)^2 \int_{-\infty}^{\infty} dt_1 \int_{-\infty}^{\infty} dt_2 \iiint d\omega_i d\omega_s d\omega_p \iiint d\omega'_i d\omega'_s d\omega'_p \\
&\quad \times \left( f(\omega_i, \omega_s, \omega_p) e^{i\Delta\omega t_1} \hat{a}_i^\dagger(\omega_i) \hat{a}_s^\dagger(\omega_s) f^*(\omega_i, \omega_s, \omega_p) e^{i\Delta\omega' t_2} \hat{a}_i^\dagger(\omega'_i) \hat{a}_s^\dagger(\omega'_s) \right. \\
&\quad \left. + f^*(\omega'_i, \omega'_s, \omega'_p) e^{-i\Delta\omega t_1} \hat{a}_i(\omega_i) \hat{a}_s(\omega_s) f(\omega'_i, \omega'_s, \omega'_p) e^{i\Delta\omega' t_2} \hat{a}_i^\dagger(\omega'_i) \hat{a}_s^\dagger(\omega'_s) \right) |0\rangle.
\end{aligned} \tag{B.35}$$

We can write the state in terms of the joint spectral amplitudes of the down-converted photons, such that

$$\begin{aligned}
|\Psi_{\text{PDC}}^{(2)}\rangle_{\text{D}} &= \frac{\mathcal{A}^2}{2} \left( F_0 + \iint d\omega_i d\omega_s \iint d\omega'_i d\omega'_s \right. \\
&\quad \left. \times F_2(\omega_i, \omega_s, \omega'_i, \omega'_s) \hat{a}_i^\dagger(\omega_i) \hat{a}_s^\dagger(\omega_s) \hat{a}_i^\dagger(\omega'_i) \hat{a}_s^\dagger(\omega'_s) \right) |0\rangle,
\end{aligned} \tag{B.36}$$

where  $\mathcal{A} = 2\pi AL/i\hbar$ . The first term corresponds to the vacuum state while the second term corresponds to the creation of four photons. By inspection of the state in equation B.35, we can see that the joint spectral amplitude for the four-photon term must be

$$\begin{aligned}
F_2(\omega_i, \omega_s, \omega'_i, \omega'_s) &= \frac{1}{(2\pi)^2} \iint d\omega_p d\omega'_p f(\omega_i, \omega_s, \omega_p) f(\omega'_i, \omega'_s, \omega'_p) \\
&\quad \times \int_{-\infty}^{\infty} dt_1 \int_{-\infty}^{\infty} dt_2 e^{i\Delta\omega t_1} e^{i\Delta\omega' t_2}.
\end{aligned} \tag{B.37}$$

Evaluating the time integrals yields

$$F_2(\omega_i, \omega_s, \omega'_i, \omega'_s) = \iint d\omega_p d\omega'_p f(\omega_i, \omega_s, \omega_p) f(\omega'_i, \omega'_s, \omega'_p) \delta(\Delta\omega) \delta(\Delta\omega') \quad (\text{B.38})$$

$$= f(\omega_i, \omega_s, \omega_i + \omega_s) f(\omega'_i, \omega'_s, \omega'_i + \omega'_s) \quad (\text{B.39})$$

which is the amplitude for the creation of two independent pairs of photons, each with joint spectral amplitude  $f(\omega_i, \omega_s, \omega_p)$  as defined in equation 6.3. The frequencies of each of the down-converted pairs are independently constrained by energy conservation according to  $\omega_i + \omega_s = \omega_p$  and  $\omega'_i + \omega'_s = \omega'_p$ , where  $\omega_p$  and  $\omega'_p$  are the frequencies of the pump photons. A schematic of this process is shown in figure 6.4 b).

The amplitude for the correction to the vacuum state is

$$F_0 = \left(\frac{1}{2\pi}\right)^2 \iint d\omega_i d\omega_s \iint d\omega'_i d\omega'_s \iint d\omega_p d\omega'_p f^*(\omega_i, \omega_s, \omega_p) f(\omega'_i, \omega'_s, \omega'_p) \quad (\text{B.40})$$

$$\times \int_{-\infty}^{\infty} dt_1 \int_{-\infty}^{\infty} dt_2 e^{-i\Delta\omega t_1} e^{i\Delta\omega' t_2} \delta(\omega_i - \omega'_i) \delta(\omega_s - \omega'_s)$$

$$= \iint d\omega_i d\omega_s \iint d\omega'_i d\omega'_s \iint d\omega_p d\omega'_p f^*(\omega_i, \omega_s, \omega_p) f(\omega'_i, \omega'_s, \omega'_p) \quad (\text{B.41})$$

$$\times \delta(\Delta\omega) \delta(\Delta\omega') \delta(\omega_i - \omega'_i) \delta(\omega_s - \omega'_s)$$

$$= \iint d\omega_i d\omega_s \iint d\omega'_i d\omega'_s f^*(\omega_i, \omega_s, \omega_i + \omega_s) f(\omega'_i, \omega'_s, \omega'_i + \omega'_s) \quad (\text{B.42})$$

$$\times \delta(\omega_i - \omega'_i) \delta(\omega_s - \omega'_s)$$

$$= \iint d\omega_i d\omega_s |f(\omega_i, \omega_s, \omega_i + \omega_s)|^2, \quad (\text{B.43})$$

### B.3.3 Third Order Term

For the third order term, we substitute the Hamiltonian in Equation 6.2 into Equation B.28

$$\begin{aligned}
|\Psi_{\text{PDC}}^{(3)}\rangle_{\text{T}} &= \left(\frac{AL}{i\hbar}\right)^3 \int_{-\infty}^{\infty} dt_1 \int_{-\infty}^{\infty} dt_2 \int_{-\infty}^{\infty} dt_3 \\
&\times \iiint d\omega_i d\omega_s d\omega_p \iiint d\omega'_i d\omega'_s d\omega'_p \iiint d\omega''_i d\omega''_s d\omega''_p \\
&\times \left( f(\omega_i, \omega_s, \omega_p) e^{i\Delta\omega t_1} \hat{a}_i^\dagger(\omega_i) \hat{a}_s^\dagger(\omega_s) + f^*(\omega_i, \omega_s, \omega_p) e^{-i\Delta\omega t_1} \hat{a}_i(\omega_i) \hat{a}_s(\omega_s) \right) \\
&\times \left( f(\omega'_i, \omega'_s, \omega'_p) e^{i\Delta\omega' t_2} \hat{a}_i^\dagger(\omega'_i) \hat{a}_s^\dagger(\omega'_s) + f^*(\omega'_i, \omega'_s, \omega'_p) e^{-i\Delta\omega' t_2} \hat{a}_i(\omega'_i) \hat{a}_s(\omega'_s) \right) \\
&\times \left( f(\omega''_i, \omega''_s, \omega''_p) e^{i\Delta\omega'' t_3} \hat{a}_i^\dagger(\omega''_i) \hat{a}_s^\dagger(\omega''_s) + f^*(\omega''_i, \omega''_s, \omega''_p) e^{-i\Delta\omega'' t_3} \hat{a}_i(\omega''_i) \hat{a}_s(\omega''_s) \right) |0\rangle
\end{aligned} \tag{B.44}$$

Expanding the brackets and omitting terms that go to zero, due to the annihilation of the vacuum, gives

$$\begin{aligned}
|\Psi_{\text{PDC}}^{(3)}\rangle_{\text{T}} &= \left(\frac{AL}{i\hbar}\right)^3 \int_{-\infty}^{\infty} dt_1 \int_{-\infty}^{\infty} dt_2 \int_{-\infty}^{\infty} dt_3 \\
&\times \iiint d\omega_i d\omega_s d\omega_p \iiint d\omega'_i d\omega'_s d\omega'_p \iiint d\omega''_i d\omega''_s d\omega''_p \\
&\times \left( f(\omega_i, \omega_s, \omega_p) e^{i\Delta\omega t_1} f(\omega'_i, \omega'_s, \omega'_p) e^{i\Delta\omega' t_2} f(\omega''_i, \omega''_s, \omega''_p) e^{i\Delta\omega'' t_3} \right. \\
&\times \hat{a}_i^\dagger(\omega_i) \hat{a}_s^\dagger(\omega_s) \hat{a}_i^\dagger(\omega'_i) \hat{a}_s^\dagger(\omega'_s) \hat{a}_i^\dagger(\omega''_i) \hat{a}_s^\dagger(\omega''_s) \\
&+ f^*(\omega_i, \omega_s, \omega_p) e^{-i\Delta\omega t_1} f(\omega'_i, \omega'_s, \omega'_p) e^{i\Delta\omega' t_2} f(\omega''_i, \omega''_s, \omega''_p) e^{i\Delta\omega'' t_3} \\
&\times (\delta(\omega_i - \omega''_i) \delta(\omega_s - \omega''_s) \hat{a}_i^\dagger(\omega'_i) \hat{a}_s^\dagger(\omega'_s) + \delta(\omega_i - \omega'_i) \delta(\omega_s - \omega''_s) \hat{a}_i^\dagger(\omega''_i) \hat{a}_s^\dagger(\omega'_s) \\
&+ \delta(\omega_i - \omega''_i) \delta(\omega_s - \omega'_s) \hat{a}_i^\dagger(\omega'_i) \hat{a}_s^\dagger(\omega''_s) + \delta(\omega_i - \omega'_i) \delta(\omega_s - \omega'_s) \hat{a}_i^\dagger(\omega''_i) \hat{a}_s^\dagger(\omega''_s)) \\
&+ f(\omega_i, \omega_s, \omega_p) e^{i\Delta\omega t_1} f^*(\omega'_i, \omega'_s, \omega'_p) e^{-i\Delta\omega' t_2} f(\omega''_i, \omega''_s, \omega''_p) e^{i\Delta\omega'' t_3} \\
&\times \delta(\omega''_i - \omega'_i) \delta(\omega''_s - \omega'_s) \hat{a}_i^\dagger(\omega_i) \hat{a}_s^\dagger(\omega_s) \left. \right) |0\rangle.
\end{aligned} \tag{B.45}$$

We can write the state in terms of the joint spectral amplitudes of the down-converted photons, such that

$$\begin{aligned}
 |\Psi_{\text{PDC}}^{(3)}\rangle_{\text{T}} = & \frac{\mathcal{A}}{3!} \left( \iint d\omega_i d\omega_s F_1(\omega_i, \omega_s) \hat{a}_i^\dagger(\omega_i) \hat{a}_s^\dagger(\omega_s) \right. \\
 & + \iint d\omega_i d\omega_s \iint d\omega'_i d\omega'_s \iint d\omega''_i d\omega''_s F_3(\omega_i, \omega_s, \omega'_i, \omega'_s, \omega''_i, \omega''_s) \\
 & \left. \times \hat{a}_i^\dagger(\omega_i) \hat{a}_s^\dagger(\omega_s) \hat{a}_i^\dagger(\omega'_i) \hat{a}_s^\dagger(\omega'_s) \hat{a}_i^\dagger(\omega''_i) \hat{a}_s^\dagger(\omega''_s) \right) |0\rangle, \quad (\text{B.46})
 \end{aligned}$$

where the first term corresponds to the creation of two photons while the second term corresponds to the creation of six photons. By inspection of the state in equation B.45, we can see that the joint spectral amplitude for the six-photon term must be

$$F_3 = F_3(\omega_i, \omega_s, \omega'_i, \omega'_s, \omega''_i, \omega''_s) \quad (\text{B.47})$$

$$\begin{aligned}
 & = \frac{1}{(2\pi)^3} \iiint d\omega_p d\omega'_p d\omega''_p f(\omega_i, \omega_s, \omega_p) f(\omega'_i, \omega'_s, \omega'_p) f(\omega''_i, \omega''_s, \omega''_p) \\
 & \times \int_{-\infty}^{\infty} dt_1 \int_{-\infty}^{\infty} dt_2 \int_{-\infty}^{\infty} dt_3 e^{i\Delta\omega t_1} e^{i\Delta\omega' t_2} e^{i\Delta\omega'' t_3}. \quad (\text{B.48})
 \end{aligned}$$

Evaluating the time integrals yields

$$F_3 = \iiint d\omega_p d\omega'_p d\omega''_p f(\omega_i, \omega_s, \omega_p) f(\omega'_i, \omega'_s, \omega'_p) f(\omega''_i, \omega''_s, \omega''_p) \delta\Delta\omega \delta\Delta\omega' \delta\Delta\omega'' \quad (\text{B.49})$$

$$= f(\omega_i, \omega_s, \omega_i + \omega_s) f(\omega'_i, \omega'_s, \omega'_i + \omega'_s) f(\omega''_i, \omega''_s, \omega''_i + \omega''_s) \quad (\text{B.50})$$

which is the amplitude for the creation of three independent pairs of photons, each with joint spectral amplitude  $f(\omega_i, \omega_s, \omega_p)$  as defined in equation 6.3. The frequencies of each of the down-converted pairs are independently constrained by energy conservation according to  $\omega_i + \omega_s = \omega_p$ ,  $\omega'_i + \omega'_s = \omega'_p$  and  $\omega''_i + \omega''_s = \omega''_p$ , where  $\omega_p$ ,  $\omega'_p$  and  $\omega''_p$  are the frequencies of the pump photons. A schematic of this process is shown in figure 6.4 c).

The amplitude for the correction to the two-photon state is

$$\begin{aligned}
F_1(\omega_i, \omega_s) &= \iint d\omega'_i d\omega'_s \iint d\omega''_i d\omega''_s \delta(\omega''_i - \omega'_i) \delta(\omega''_s - \omega'_s) \\
&\quad \times (F_1^{(a)}(\omega'_i, \omega'_s, \omega_i, \omega_s, \omega''_i, \omega''_s) + F_1^{(a)}(\omega''_i, \omega'_s, \omega'_i, \omega_s, \omega_i, \omega''_s)) \\
&\quad + F_1^{(a)}(\omega'_i, \omega''_s, \omega_i, \omega'_s, \omega''_i, \omega_s) + F_1^{(a)}(\omega''_i, \omega''_s, \omega'_i, \omega'_s, \omega_i, \omega_s) \\
&\quad + F_1^{(b)}(\omega_i, \omega_s, \omega'_i, \omega'_s, \omega''_i, \omega''_s)) \\
&= \iint d\omega'_i d\omega'_s (F_1^{(a)}(\omega'_i, \omega'_s, \omega_i, \omega_s, \omega'_i, \omega'_s) + F_1^{(a)}(\omega'_i, \omega'_s, \omega'_i, \omega_s, \omega_i, \omega'_s) \\
&\quad + F_1^{(a)}(\omega'_i, \omega'_s, \omega_i, \omega'_s, \omega'_i, \omega_s) + F_1^{(a)}(\omega'_i, \omega'_s, \omega'_i, \omega'_s, \omega_i, \omega_s) \\
&\quad + F_1^{(b)}(\omega_i, \omega_s, \omega'_i, \omega'_s, \omega'_i, \omega'_s)),
\end{aligned} \tag{B.51}$$

(B.52)

where

$$\begin{aligned}
F_1^{(a)}(\omega_i, \omega_s, \omega'_i, \omega'_s, \omega''_i, \omega''_s) &= \left(\frac{1}{2\pi}\right)^3 \iiint d\omega_p d\omega'_p d\omega''_p \\
&\quad \times f^*(\omega_i, \omega_s, \omega_p) f(\omega'_i, \omega'_s, \omega'_p) f(\omega''_i, \omega''_s, \omega''_p) \\
&\quad \times \int_{-\infty}^{\infty} dt_1 \int_{-\infty}^{\infty} dt_2 \int_{-\infty}^{\infty} dt_3 e^{-i\Delta\omega t_1} e^{i\Delta\omega' t_2} e^{i\Delta\omega'' t_3}
\end{aligned} \tag{B.53}$$

$$\begin{aligned}
&= \iiint d\omega_p d\omega'_p d\omega''_p f^*(\omega_i, \omega_s, \omega_p) f(\omega'_i, \omega'_s, \omega'_p) \\
&\quad \times f(\omega''_i, \omega''_s, \omega''_p) \delta(\Delta\omega) \delta(\Delta\omega') \delta(\Delta\omega'')
\end{aligned} \tag{B.54}$$

$$= f^*(\omega_i, \omega_s, \omega_i + \omega_s) f(\omega'_i, \omega'_s, \omega'_i + \omega'_s) f(\omega''_i, \omega''_s, \omega''_i + \omega''_s), \tag{B.55}$$

and

$$\begin{aligned}
 F_1^{(b)}(\omega_i, \omega_s, \omega'_i, \omega'_s, \omega''_i, \omega''_s) &= \left(\frac{1}{2\pi}\right)^3 \iiint d\omega_p d\omega'_p d\omega''_p \\
 &\quad \times f(\omega_i, \omega_s, \omega_p) f^*(\omega'_i, \omega'_s, \omega'_p) f(\omega''_i, \omega''_s, \omega''_p) \\
 &\quad \times \int_{-\infty}^{\infty} dt_1 \int_{-\infty}^{\infty} dt_2 \int_{-\infty}^{\infty} dt_3 e^{i\Delta\omega t_1} e^{-i\Delta\omega' t_2} e^{i\Delta\omega'' t_3}
 \end{aligned} \tag{B.56}$$

$$\begin{aligned}
 &= \iiint d\omega_p d\omega'_p d\omega''_p f(\omega_i, \omega_s, \omega_p) f^*(\omega'_i, \omega'_s, \omega'_p) f(\omega''_i, \omega''_s, \omega''_p) \\
 &\quad \times \delta(\Delta\omega) \delta(\Delta\omega') \delta(\Delta\omega'')
 \end{aligned} \tag{B.57}$$

$$= f(\omega_i, \omega_s, \omega_i + \omega_s) f^*(\omega'_i, \omega'_s, \omega'_i + \omega'_s) f(\omega''_i, \omega''_s, \omega''_i + \omega''_s). \tag{B.58}$$

Inserting equations B.55 and B.58 into equation B.52 gives

$$\begin{aligned}
 F_1(\omega_i, \omega_s) &= \iint d\omega'_i d\omega'_s (f^*(\omega'_i, \omega'_s, \omega'_i + \omega'_s) f(\omega_i, \omega_s, \omega_i + \omega_s) f(\omega'_i, \omega'_s, \omega'_i + \omega'_s) \\
 &\quad + f^*(\omega'_i, \omega'_s, \omega'_i + \omega'_s) f(\omega'_i, \omega_s, \omega'_i + \omega_s) f(\omega_i, \omega'_s, \omega_i + \omega'_s) \\
 &\quad + f^*(\omega'_i, \omega'_s, \omega'_i + \omega'_s) f(\omega_i, \omega'_s, \omega_i + \omega'_s) f(\omega'_i, \omega_s, \omega'_i + \omega_s) \\
 &\quad + f^*(\omega'_i, \omega'_s, \omega'_i + \omega'_s) f(\omega'_i, \omega'_s, \omega'_i + \omega'_s) f(\omega_i, \omega_s, \omega_i + \omega_s) \\
 &\quad + f(\omega_i, \omega_s, \omega_i + \omega_s) f^*(\omega'_i, \omega'_s, \omega'_i + \omega'_s) f(\omega'_i, \omega'_s, \omega'_i + \omega'_s)) \\
 &= \iint d\omega'_i d\omega'_s (f^*(\omega'_i, \omega'_s, \omega'_i + \omega'_s) f(\omega_i, \omega_s, \omega_i + \omega_s) f(\omega'_i, \omega'_s, \omega'_i + \omega'_s) \\
 &\quad + f^*(\omega'_i, \omega'_s, \omega'_i + \omega'_s) \sum_{\substack{[j,k]= \\ \mathcal{P}[\omega_i, \omega'_i]}} \sum_{\substack{[m,n]= \\ \mathcal{P}[\omega_s, \omega'_s]}} f(j, m, j + m) f(k, n, k + n)).
 \end{aligned} \tag{B.59}$$

## B.4 Correction to the vacuum state amplitude using the Dyson series

The amplitude for the vacuum term correction is

$$G_0 = \frac{1}{2\pi^2} \iint d\omega_i d\omega_s \iint d\omega'_i d\omega'_s \iint d\omega_p d\omega'_p f^*(\omega_i, \omega_s, \omega_p) f(\omega'_i, \omega'_s, \omega'_p) \times \int_{-\infty}^{\infty} dt_1 \int_{-\infty}^{t_1} dt_2 e^{-i\Delta\omega t_1} e^{i\Delta\omega' t_2} \delta(\omega_i - \omega'_i) \delta(\omega_s - \omega'_s) \quad (\text{B.60})$$

$$= \frac{1}{\pi^2} \iint d\omega_i d\omega_s \iint d\omega'_i d\omega'_s \iint d\omega_p d\omega'_p f^*(\omega_i, \omega_s, \omega_p) f(\omega'_i, \omega'_s, \omega'_p) \times \int_{-\infty}^{\infty} dr \int_0^{\infty} ds e^{i(\Delta\omega - \Delta\omega')r} e^{i(\Delta\omega + \Delta\omega')s} \delta(\omega_i - \omega'_i) \delta(\omega_s - \omega'_s) \quad (\text{B.61})$$

$$= 2 \iint d\omega_i d\omega_s \iint d\omega'_i d\omega'_s \iint d\omega_p d\omega'_p f^*(\omega_i, \omega_s, \omega_p) f(\omega'_i, \omega'_s, \omega'_p) \times \delta(\Delta\omega - \Delta\omega') \left( \delta(\Delta\omega + \Delta\omega') + \frac{i}{\pi} \frac{1}{\Delta\omega + \Delta\omega'} \right) \delta(\omega_i - \omega'_i) \delta(\omega_s - \omega'_s) \quad (\text{B.62})$$

$$= \iint d\omega_i d\omega_s \int d\omega_p |f(\omega_i, \omega_s, \omega_p)|^2 \left( \delta(\Delta\omega) + \frac{i}{\pi} \frac{1}{\Delta\omega} \right) \quad (\text{B.63})$$

$$= \iint d\omega_i d\omega_s \left( |f(\omega_i, \omega_s, \omega_i + \omega_s)|^2 + \frac{i}{\pi} \int d\omega_p |f(\omega_i, \omega_s, \omega_p)|^2 \frac{1}{\Delta\omega} \right). \quad (\text{B.64})$$

Details on the change of variables performed between equation B.60 and B.61 can be found in Appendix B.7.1. Details on the evaluation of the integral in equation B.61 can be found in Appendix B.8. Since the function  $f(\omega_i, \omega_s, \omega_p)$  is typically even, the second term in the integrand will be an odd function, and therefore, that part of the integral will go to zero. This gives

$$G_0 = F_0, \quad (\text{B.65})$$

where  $F_0$  is defined in Equation B.43.

## B.5 Correction to the two-photon state amplitude using the Dyson series

Consider the two-photon part of the state in equation 6.34.

$$\begin{aligned}
|\Psi_{\text{PDC},2}^{(3)}\rangle_{\text{D}} &= \left(\frac{AL}{i\hbar}\right)^3 \int_{-\infty}^{\infty} dt_1 \int_{-\infty}^{t_1} dt_2 \int_{-\infty}^{t_2} dt_3 \\
&\times \iiint d\omega_i d\omega_s d\omega_p \iiint d\omega'_i d\omega'_s d\omega'_p \iiint d\omega''_i d\omega''_s d\omega''_p \\
&\times \left( f^*(\omega_i, \omega_s, \omega_p) e^{-i\Delta\omega t_1} f(\omega'_i, \omega'_s, \omega'_p) e^{i\Delta\omega' t_2} f(\omega''_i, \omega''_s, \omega''_p) e^{i\Delta\omega'' t_3} \right. \\
&\times \left( \delta(\omega_i - \omega'_i) \delta(\omega_s - \omega''_s) \hat{a}_i^\dagger(\omega'_i) \hat{a}_s^\dagger(\omega''_s) + \delta(\omega_i - \omega'_i) \delta(\omega_s - \omega''_s) \hat{a}_i^\dagger(\omega''_i) \hat{a}_s^\dagger(\omega'_s) \right. \\
&+ \delta(\omega_i - \omega''_i) \delta(\omega_s - \omega'_s) \hat{a}_i^\dagger(\omega'_i) \hat{a}_s^\dagger(\omega''_s) + \delta(\omega_i - \omega'_i) \delta(\omega_s - \omega'_s) \hat{a}_i^\dagger(\omega''_i) \hat{a}_s^\dagger(\omega''_s) \left. \right) \\
&+ f(\omega_i, \omega_s, \omega_p) e^{i\Delta\omega t_1} f^*(\omega'_i, \omega'_s, \omega'_p) e^{-i\Delta\omega' t_2} f(\omega''_i, \omega''_s, \omega''_p) e^{i\Delta\omega'' t_3} \\
&\times \left. \delta(\omega''_i - \omega'_i) \delta(\omega''_s - \omega'_s) \hat{a}_i^\dagger(\omega_i) \hat{a}_s^\dagger(\omega_s) \right) |0\rangle
\end{aligned} \tag{B.66}$$

Perform a change of variables for the time integrals (refer to Appendix B.7.2 for details)

$$\begin{aligned}
|\Psi_{\text{PDC},2}^{(3)}\rangle_{\text{D}} &= \frac{1}{3} \left(\frac{AL}{i\hbar}\right)^3 \iiint d\omega_i d\omega_s d\omega_p \iiint d\omega'_i d\omega'_s d\omega'_p \iiint d\omega''_i d\omega''_s d\omega''_p \\
&\times \left( f^*(\omega_i, \omega_s, \omega_p) f(\omega'_i, \omega'_s, \omega'_p) f(\omega''_i, \omega''_s, \omega''_p) \int_{-\infty}^{\infty} dq \int_0^{\infty} dr \int_0^{\infty} ds \right. \\
&\times e^{\frac{i}{3}(-\Delta\omega + \Delta\omega' + \Delta\omega'')q} e^{\frac{i}{3}(-2\Delta\omega - \Delta\omega' - \Delta\omega'')r} e^{\frac{i}{3}(-\Delta\omega + \Delta\omega' - 2\Delta\omega'')s} \\
&\times \left( \delta(\omega_i - \omega''_i) \delta(\omega_s - \omega''_s) \hat{a}_i^\dagger(\omega'_i) \hat{a}_s^\dagger(\omega''_s) + \delta(\omega_i - \omega'_i) \delta(\omega_s - \omega''_s) \hat{a}_i^\dagger(\omega''_i) \hat{a}_s^\dagger(\omega'_s) \right. \\
&+ \delta(\omega_i - \omega''_i) \delta(\omega_s - \omega'_s) \hat{a}_i^\dagger(\omega'_i) \hat{a}_s^\dagger(\omega''_s) + \delta(\omega_i - \omega'_i) \delta(\omega_s - \omega'_s) \hat{a}_i^\dagger(\omega''_i) \hat{a}_s^\dagger(\omega''_s) \left. \right) \\
&+ f(\omega_i, \omega_s, \omega_p) f^*(\omega'_i, \omega'_s, \omega'_p) f(\omega''_i, \omega''_s, \omega''_p) \int_{-\infty}^{\infty} dq \int_0^{\infty} dr \int_0^{\infty} ds \\
&\times e^{i\frac{1}{3}(\Delta\omega - \Delta\omega' + \Delta\omega'')q} e^{i\frac{1}{3}(2\Delta\omega + \Delta\omega' - \Delta\omega'')r} e^{i\frac{1}{3}(\Delta\omega - \Delta\omega' - 2\Delta\omega'')s} \\
&\times \left. \delta(\omega''_i - \omega'_i) \delta(\omega''_s - \omega'_s) \hat{a}_i^\dagger(\omega_i) \hat{a}_s^\dagger(\omega_s) \right) |0\rangle
\end{aligned} \tag{B.67}$$

Evaluate the time integrals (refer to Appendix B.8 for details)

$$\begin{aligned}
 |\Psi_{\text{PDC},2}^{(3)}\rangle_{\text{D}} = & \frac{9\mathcal{A}^3}{4} \iiint d\omega_i d\omega_s d\omega_p \iiint d\omega'_i d\omega'_s d\omega'_p \iiint d\omega''_i d\omega''_s d\omega''_p \\
 & \times \left( f^*(\omega_i, \omega_s, \omega_p) f(\omega'_i, \omega'_s, \omega'_p) f(\omega''_i, \omega''_s, \omega''_p) \delta(-\Delta\omega + \Delta\omega' + \Delta\omega'') \right. \\
 & \times \left( \delta(-2\Delta\omega - \Delta\omega' - \Delta\omega'') + \frac{i}{\pi} \frac{1}{-2\Delta\omega - \Delta\omega' - \Delta\omega''} \right) \\
 & \times \left( \delta(-\Delta\omega + \Delta\omega' - 2\Delta\omega'') + \frac{i}{\pi} \frac{1}{-\Delta\omega + \Delta\omega' - 2\Delta\omega''} \right) \\
 & \times \left( \delta(\omega_i - \omega''_i) \delta(\omega_s - \omega''_s) \hat{a}_i^\dagger(\omega'_i) \hat{a}_s^\dagger(\omega'_s) + \delta(\omega_i - \omega'_i) \delta(\omega_s - \omega''_s) \hat{a}_i^\dagger(\omega''_i) \hat{a}_s^\dagger(\omega'_s) \right. \\
 & \left. + \delta(\omega_i - \omega''_i) \delta(\omega_s - \omega'_s) \hat{a}_i^\dagger(\omega'_i) \hat{a}_s^\dagger(\omega''_s) + \delta(\omega_i - \omega'_i) \delta(\omega_s - \omega'_s) \hat{a}_i^\dagger(\omega''_i) \hat{a}_s^\dagger(\omega''_s) \right) \\
 & + f(\omega_i, \omega_s, \omega_p) f^*(\omega'_i, \omega'_s, \omega'_p) f(\omega''_i, \omega''_s, \omega''_p) \delta(\Delta\omega - \Delta\omega' + \Delta\omega'') \\
 & \times \left( \delta(2\Delta\omega + \Delta\omega' - \Delta\omega'') + \frac{i}{\pi} \frac{1}{2\Delta\omega + \Delta\omega' - \Delta\omega''} \right) \\
 & \times \left( \delta(\Delta\omega - \Delta\omega' - 2\Delta\omega'') + \frac{i}{\pi} \frac{1}{\Delta\omega - \Delta\omega' - 2\Delta\omega''} \right) \\
 & \times \delta(\omega''_i - \omega'_i) \delta(\omega''_s - \omega'_s) \hat{a}_i^\dagger(\omega_i) \hat{a}_s^\dagger(\omega_s) \Big| 0 \rangle
 \end{aligned} \tag{B.68}$$

where  $\mathcal{A} = 2\pi AL/i\hbar$ . Expand some brackets

$$\begin{aligned}
 |\Psi_{\text{PDC},2}^{(3)}\rangle_{\text{D}} &= \frac{9\mathcal{A}^3}{4} \left( \frac{2\pi AL}{i\hbar} \right)^3 \iint d\omega_i d\omega_s \iint d\omega'_i d\omega'_s \iint d\omega''_i d\omega''_s \\
 &\times \left( \iiint d\omega_p d\omega'_p d\omega''_p f^*(\omega_i, \omega_s, \omega_p) f(\omega'_i, \omega'_s, \omega'_p) f(\omega''_i, \omega''_s, \omega''_p) \right. \\
 &\times \delta(-\Delta\omega + \Delta\omega' + \Delta\omega'') \delta(-2\Delta\omega - \Delta\omega' - \Delta\omega'') \delta(-\Delta\omega + \Delta\omega' - 2\Delta\omega'') \\
 &+ \iiint d\omega_p d\omega'_p d\omega''_p f^*(\omega_i, \omega_s, \omega_p) f(\omega'_i, \omega'_s, \omega'_p) f(\omega''_i, \omega''_s, \omega''_p) \\
 &\times \frac{i}{\pi} \frac{\delta(-\Delta\omega + \Delta\omega' + \Delta\omega'') \delta(-\Delta\omega + \Delta\omega' - 2\Delta\omega'')}{-2\Delta\omega - \Delta\omega' - \Delta\omega''} \\
 &+ \iiint d\omega_p d\omega'_p d\omega''_p f^*(\omega_i, \omega_s, \omega_p) f(\omega'_i, \omega'_s, \omega'_p) f(\omega''_i, \omega''_s, \omega''_p) \\
 &\times \frac{i}{\pi} \frac{\delta(-\Delta\omega + \Delta\omega' + \Delta\omega'') \delta(-2\Delta\omega - \Delta\omega' - \Delta\omega'')}{-\Delta\omega + \Delta\omega' - 2\Delta\omega''} \\
 &+ \iiint d\omega_p d\omega'_p d\omega''_p f^*(\omega_i, \omega_s, \omega_p) f(\omega'_i, \omega'_s, \omega'_p) f(\omega''_i, \omega''_s, \omega''_p) \\
 &\times \left. \frac{i}{\pi} \frac{i}{\pi} \frac{\delta(-\Delta\omega + \Delta\omega' + \Delta\omega'')}{(-2\Delta\omega - \Delta\omega' - \Delta\omega'')(-\Delta\omega + \Delta\omega' - 2\Delta\omega'')} \right) \\
 &\times \left( \delta(\omega_i - \omega'_i) \delta(\omega_s - \omega'_s) \hat{a}_i^\dagger(\omega'_i) \hat{a}_s^\dagger(\omega'_s) + \delta(\omega_i - \omega'_i) \delta(\omega_s - \omega''_s) \hat{a}_i^\dagger(\omega'_i) \hat{a}_s^\dagger(\omega''_s) \right. \\
 &+ \delta(\omega_i - \omega''_i) \delta(\omega_s - \omega'_s) \hat{a}_i^\dagger(\omega'_i) \hat{a}_s^\dagger(\omega'_s) + \delta(\omega_i - \omega'_i) \delta(\omega_s - \omega''_s) \hat{a}_i^\dagger(\omega'_i) \hat{a}_s^\dagger(\omega''_s) \left. \right) \\
 &\times \left( \iiint d\omega_p d\omega'_p d\omega''_p f(\omega_i, \omega_s, \omega_p) f^*(\omega'_i, \omega'_s, \omega'_p) f(\omega''_i, \omega''_s, \omega''_p) \right. \\
 &\times \delta(\Delta\omega - \Delta\omega' + \Delta\omega'') \delta(2\Delta\omega + \Delta\omega' - \Delta\omega'') \delta(\Delta\omega - \Delta\omega' - 2\Delta\omega'') \\
 &+ \iiint d\omega_p d\omega'_p d\omega''_p f(\omega_i, \omega_s, \omega_p) f^*(\omega'_i, \omega'_s, \omega'_p) f(\omega''_i, \omega''_s, \omega''_p) \\
 &\times \frac{i}{\pi} \frac{\delta(\Delta\omega - \Delta\omega' + \Delta\omega'') \delta(\Delta\omega - \Delta\omega' - 2\Delta\omega'')}{2\Delta\omega + \Delta\omega' - \Delta\omega''} \\
 &+ \iiint d\omega_p d\omega'_p d\omega''_p f(\omega_i, \omega_s, \omega_p) f^*(\omega'_i, \omega'_s, \omega'_p) f(\omega''_i, \omega''_s, \omega''_p) \\
 &\times \frac{i}{\pi} \frac{\delta(\Delta\omega - \Delta\omega' + \Delta\omega'') \delta(2\Delta\omega + \Delta\omega' - \Delta\omega'')}{\Delta\omega - \Delta\omega' - 2\Delta\omega''} \\
 &+ \iiint d\omega_p d\omega'_p d\omega''_p f(\omega_i, \omega_s, \omega_p) f^*(\omega'_i, \omega'_s, \omega'_p) f(\omega''_i, \omega''_s, \omega''_p) \\
 &\times \left. \frac{i}{\pi} \frac{i}{\pi} \frac{\delta(\Delta\omega - \Delta\omega' + \Delta\omega'')}{(2\Delta\omega + \Delta\omega' - \Delta\omega'')(\Delta\omega - \Delta\omega' - 2\Delta\omega'')} \right) \\
 &\times \delta(\omega''_i - \omega'_i) \delta(\omega''_s - \omega'_s) \hat{a}_i^\dagger(\omega_i) \hat{a}_s^\dagger(\omega_s) |0\rangle
 \end{aligned}
 \tag{B.69}$$

Evaluate the pump integrals, where possible, using the delta functions.

$$\begin{aligned}
 |\Psi_{\text{PDC},2}^{(3)}\rangle_{\text{D}} &= \frac{\mathcal{A}^3}{4} \iint d\omega_i d\omega_s \iint d\omega'_i d\omega'_s \iint d\omega''_i d\omega''_s \\
 &\times \left( f^*(\omega_i, \omega_s, \omega_i + \omega_s) f(\omega'_i, \omega'_s, \omega'_i + \omega'_s) f(\omega''_i, \omega''_s, \omega''_i + \omega''_s) \right. \\
 &- \frac{i}{\pi} \int \frac{d\omega_p}{\Delta\omega} f^*(\omega_i, \omega_s, \omega_p) f(\omega'_i, \omega'_s, \omega'_i + \omega'_s - \Delta\omega) f(\omega''_i, \omega''_s, \omega''_i + \omega''_s) \\
 &+ \frac{i}{\pi} \int \frac{d\omega_p}{\Delta\omega} f^*(\omega_i, \omega_s, \omega_p) f(\omega'_i, \omega'_s, \omega'_i + \omega'_s) f(\omega''_i, \omega''_s, \omega''_i + \omega''_s - \Delta\omega) \\
 &- \frac{1}{\pi^2} \iint \frac{d\omega_p d\omega''_p}{\Delta\omega \Delta\omega''} f^*(\omega_i, \omega_s, \omega_p) f(\omega'_i, \omega'_s, \omega'_i + \omega'_s + \Delta\omega - \Delta\omega'') f(\omega''_i, \omega''_s, \omega''_p) \left. \right) \\
 &\times \left( \delta(\omega_i - \omega''_i) \delta(\omega_s - \omega''_s) \hat{a}_i^\dagger(\omega'_i) \hat{a}_s^\dagger(\omega'_s) + \delta(\omega_i - \omega'_i) \delta(\omega_s - \omega''_s) \hat{a}_i^\dagger(\omega''_i) \hat{a}_s^\dagger(\omega'_s) \right. \\
 &+ \delta(\omega_i - \omega''_i) \delta(\omega_s - \omega'_s) \hat{a}_i^\dagger(\omega'_i) \hat{a}_s^\dagger(\omega''_s) + \delta(\omega_i - \omega'_i) \delta(\omega_s - \omega'_s) \hat{a}_i^\dagger(\omega''_i) \hat{a}_s^\dagger(\omega''_s) \left. \right) \\
 &+ \left( f(\omega_i, \omega_s, \omega_i + \omega_s) f^*(\omega'_i, \omega'_s, \omega'_i + \omega'_s) f(\omega''_i, \omega''_s, \omega''_i + \omega''_s) \right. \\
 &+ \frac{i}{\pi} \int \frac{d\omega_p}{\Delta\omega} f(\omega_i, \omega_s, \omega_p - \Delta\omega') f^*(\omega'_i, \omega'_s, \omega'_p) f(\omega''_i, \omega''_s, \omega''_i + \omega''_s) \\
 &- \frac{i}{\pi} \int \frac{d\omega_p}{\Delta\omega} f(\omega_i, \omega_s, \omega_i + \omega'_s) f^*(\omega'_i, \omega'_s, \omega_p) f(\omega''_i, \omega''_s, \omega''_i + \omega''_s - \Delta\omega) \\
 &+ \frac{1}{\pi^2} \iint \frac{d\omega_p d\omega''_p}{\Delta\omega \Delta\omega''} f(\omega_i, \omega_s, \omega_p) f^*(\omega'_i, \omega'_s, \omega'_i + \omega'_s - \Delta\omega + \Delta\omega'') f(\omega''_i, \omega''_s, \omega''_p) \left. \right) \\
 &\times \delta(\omega''_i - \omega'_i) \delta(\omega''_s - \omega'_s) \hat{a}_i^\dagger(\omega_i) \hat{a}_s^\dagger(\omega_s) \Big| 0 \rangle
 \end{aligned} \tag{B.70}$$

Notice that it is possible to cancel the terms containing  $i/\pi$ .

Once this is done, we expand some brackets to give

$$\begin{aligned}
 |\Psi_{\text{PDC},2}^{(3)}\rangle_{\text{D}} = & \frac{\mathcal{A}^3}{4} \iint d\omega_i d\omega_s \iint d\omega'_i d\omega'_s \iint d\omega''_i d\omega''_s \\
 & \times \left( \delta(\omega_i - \omega''_i) \delta(\omega_s - \omega''_s) \hat{a}_i^\dagger(\omega'_i) \hat{a}_s^\dagger(\omega'_s) \right. \\
 & \times \left( f^*(\omega_i, \omega_s, \omega_i + \omega_s) f(\omega'_i, \omega'_s, \omega'_i + \omega'_s) f(\omega''_i, \omega''_s, \omega''_i + \omega''_s) \right. \\
 & - \frac{1}{\pi^2} \iint \frac{d\omega_p d\omega''_p}{\Delta\omega \Delta\omega''} f^*(\omega_i, \omega_s, \omega_p) f(\omega'_i, \omega'_s, \omega'_i + \omega'_s + \Delta\omega - \Delta\omega'') f(\omega''_i, \omega''_s, \omega''_p) \Big) \\
 & + \delta(\omega_i - \omega'_i) \delta(\omega_s - \omega''_s) \hat{a}_i^\dagger(\omega''_i) \hat{a}_s^\dagger(\omega'_s) \\
 & \times \left( f^*(\omega_i, \omega_s, \omega_i + \omega_s) f(\omega'_i, \omega'_s, \omega'_i + \omega'_s) f(\omega''_i, \omega''_s, \omega''_i + \omega''_s) \right. \\
 & - \frac{1}{\pi^2} \iint \frac{d\omega_p d\omega''_p}{\Delta\omega \Delta\omega''} f^*(\omega_i, \omega_s, \omega_p) f(\omega'_i, \omega'_s, \omega'_i + \omega'_s + \Delta\omega - \Delta\omega'') f(\omega''_i, \omega''_s, \omega''_p) \Big) \\
 & + \delta(\omega_i - \omega''_i) \delta(\omega_s - \omega'_s) \hat{a}_i^\dagger(\omega'_i) \hat{a}_s^\dagger(\omega''_s) \\
 & \times \left( f^*(\omega_i, \omega_s, \omega_i + \omega_s) f(\omega'_i, \omega'_s, \omega'_i + \omega'_s) f(\omega''_i, \omega''_s, \omega''_i + \omega''_s) \right. \\
 & - \frac{1}{\pi^2} \iint \frac{d\omega_p d\omega''_p}{\Delta\omega \Delta\omega''} f^*(\omega_i, \omega_s, \omega_p) f(\omega'_i, \omega'_s, \omega'_i + \omega'_s + \Delta\omega - \Delta\omega'') f(\omega''_i, \omega''_s, \omega''_p) \Big) \\
 & + \delta(\omega_i - \omega'_i) \delta(\omega_s - \omega''_s) \hat{a}_i^\dagger(\omega''_i) \hat{a}_s^\dagger(\omega'_s) \\
 & \times \left( f^*(\omega_i, \omega_s, \omega_i + \omega_s) f(\omega'_i, \omega'_s, \omega'_i + \omega'_s) f(\omega''_i, \omega''_s, \omega''_i + \omega''_s) \right. \\
 & - \frac{1}{\pi^2} \iint \frac{d\omega_p d\omega''_p}{\Delta\omega \Delta\omega''} f^*(\omega_i, \omega_s, \omega_p) f(\omega'_i, \omega'_s, \omega'_i + \omega'_s + \Delta\omega - \Delta\omega'') f(\omega''_i, \omega''_s, \omega''_p) \Big) \\
 & + \delta(\omega''_i - \omega'_i) \delta(\omega''_s - \omega'_s) \hat{a}_i^\dagger(\omega_i) \hat{a}_s^\dagger(\omega_s) \\
 & \times \left( f(\omega_i, \omega_s, \omega_i + \omega_s) f^*(\omega'_i, \omega'_s, \omega'_i + \omega'_s) f(\omega''_i, \omega''_s, \omega''_i + \omega''_s) \right. \\
 & \left. \left. + \frac{1}{\pi^2} \iint \frac{d\omega_p d\omega''_p}{\Delta\omega \Delta\omega''} f(\omega_i, \omega_s, \omega_p) f^*(\omega'_i, \omega'_s, \omega'_i + \omega'_s - \Delta\omega + \Delta\omega'') f(\omega''_i, \omega''_s, \omega''_p) \right) \right) |0\rangle
 \end{aligned} \tag{B.71}$$

Evaluate the idler and signal integrals, where possible, using the delta functions.

$$\begin{aligned}
 |\Psi_{\text{PDC},2}^{(3)}\rangle_{\text{D}} = & \frac{\mathcal{A}^3}{4} \left( \frac{AL}{i\hbar} \right)^3 \left( \iint d\omega_i d\omega_s \iint d\omega'_i d\omega'_s \hat{a}_i^\dagger(\omega'_i) \hat{a}_s^\dagger(\omega'_s) \right. \\
 & \times \left( f^*(\omega_i, \omega_s, \omega_i + \omega_s) f(\omega'_i, \omega'_s, \omega'_i + \omega'_s) f(\omega_i, \omega_s, \omega_i + \omega_s) \right. \\
 & - \frac{1}{\pi^2} \iiint \frac{d\omega_p d\omega''_p}{(\omega_i + \omega_s - \omega_p)(\omega_i + \omega_s - \omega''_p)} f^*(\omega_i, \omega_s, \omega_p) \\
 & \times f(\omega'_i, \omega'_s, \omega'_i + \omega'_s + (\omega_i + \omega_s - \omega_p) - (\omega_i + \omega_s - \omega''_p)) f(\omega_i, \omega_s, \omega''_p) \Big) \\
 & + \iint d\omega_i d\omega_s \iint d\omega'_i d\omega'_s \hat{a}_i^\dagger(\omega'_i) \hat{a}_s^\dagger(\omega'_s) \\
 & \times \left( f^*(\omega_i, \omega_s, \omega_i + \omega_s) f(\omega_i, \omega'_s, \omega_i + \omega'_s) f(\omega''_i, \omega_s, \omega''_i + \omega_s) \right. \\
 & - \frac{1}{\pi^2} \iiint \frac{d\omega_p d\omega''_p}{(\omega_i + \omega_s - \omega_p)(\omega''_i + \omega_s - \omega''_p)} f^*(\omega_i, \omega_s, \omega_p) \\
 & \times f(\omega_i, \omega'_s, \omega_i + \omega'_s + (\omega_i + \omega_s - \omega_p) - (\omega''_i + \omega_s - \omega''_p)) f(\omega''_i, \omega_s, \omega''_p) \Big) \\
 & + \iint d\omega_i d\omega_s \iint d\omega'_i d\omega'_s \hat{a}_i^\dagger(\omega'_i) \hat{a}_s^\dagger(\omega'_s) \\
 & \times \left( f^*(\omega_i, \omega_s, \omega_i + \omega_s) f(\omega'_i, \omega_s, \omega'_i + \omega'_s) f(\omega_i, \omega''_s, \omega_i + \omega''_s) \right. \\
 & - \frac{1}{\pi^2} \iiint \frac{d\omega_p d\omega''_p}{(\omega_i + \omega_s - \omega_p)(\omega_i + \omega''_s - \omega''_p)} f^*(\omega_i, \omega_s, \omega_p) \\
 & \times f(\omega'_i, \omega_s, \omega'_i + \omega'_s + (\omega_i + \omega_s - \omega_p) - (\omega_i + \omega''_s - \omega''_p)) f(\omega_i, \omega''_s, \omega''_p) \Big) \\
 & + \iint d\omega_i d\omega_s \iint d\omega'_i d\omega'_s \hat{a}_i^\dagger(\omega'_i) \hat{a}_s^\dagger(\omega'_s) \\
 & \times \left( f^*(\omega_i, \omega_s, \omega_i + \omega_s) f(\omega_i, \omega_s, \omega_i + \omega_s) f(\omega''_i, \omega''_s, \omega''_i + \omega''_s) \right. \\
 & - \frac{1}{\pi^2} \iiint \frac{d\omega_p d\omega''_p}{(\omega_i + \omega_s - \omega_p)(\omega''_i + \omega''_s - \omega''_p)} f^*(\omega_i, \omega_s, \omega_p) \\
 & \times f(\omega_i, \omega_s, \omega_i + \omega_s + (\omega_i + \omega_s - \omega_p) - (\omega''_i + \omega''_s - \omega''_p)) f(\omega''_i, \omega''_s, \omega''_p) \Big) \\
 & + \iint d\omega_i d\omega_s \iint d\omega'_i d\omega'_s \hat{a}_i^\dagger(\omega_i) \hat{a}_s^\dagger(\omega_s) \\
 & \times \left( f(\omega_i, \omega_s, \omega_i + \omega_s) f^*(\omega'_i, \omega'_s, \omega'_i + \omega'_s) f(\omega'_i, \omega'_s, \omega'_i + \omega'_s) \right. \\
 & + \frac{1}{\pi^2} \iiint \frac{d\omega_p d\omega''_p}{(\omega_i + \omega_s - \omega_p)(\omega'_i + \omega'_s - \omega''_p)} f(\omega_i, \omega_s, \omega_p) \\
 & \times f^*(\omega'_i, \omega'_s, \omega'_i + \omega'_s - (\omega_i + \omega_s - \omega_p) + (\omega'_i + \omega'_s - \omega''_p)) f(\omega'_i, \omega'_s, \omega''_p) \Big) \Big) |0\rangle
 \end{aligned} \tag{B.72}$$

Finally, perform a change of variables among the signal and idler frequencies, in order to collect like terms in the creation operators.

$$\begin{aligned}
 |\Psi_{\text{PDC},2}^{(3)}\rangle_{\text{D}} &= \frac{\mathcal{A}^3}{4} \left( \iint d\omega_i d\omega_s \iint d\omega'_i d\omega'_s \hat{a}_i^\dagger(\omega_i) \hat{a}_s^\dagger(\omega_s) |0\rangle \right. \\
 &\quad \times \left( f^*(\omega'_i, \omega'_s, \omega'_i + \omega'_s) \sum_{\substack{[j,k]= \\ \mathcal{P}[\omega_i, \omega'_i]}} \sum_{\substack{[m,n]= \\ \mathcal{P}[\omega_s, \omega'_s]}} f(j, m, j+m) f(k, n, k+n) \right. \\
 &\quad + f(\omega_i, \omega_s, \omega_i + \omega_s) f^*(\omega'_i, \omega'_s, \omega'_i + \omega'_s) f(\omega'_i, \omega'_s, \omega'_i + \omega'_s) \\
 &\quad - \frac{1}{\pi^2} \iiint \frac{d\omega_p d\omega''_p}{(\omega'_i + \omega'_s - \omega_p)(\omega'_i + \omega'_s - \omega''_p)} \\
 &\quad \left. \left( f^*(\omega'_i, \omega'_s, \omega_p) \sum_{\substack{[j,k]= \\ \mathcal{P}[\omega_i, \omega'_i]}} \sum_{\substack{[m,n]= \\ \mathcal{P}[\omega_s, \omega'_s]}} f(\omega_i, \omega_s, \omega_i + \omega_s - \omega_p + \omega''_p) f(\omega'_i, \omega'_s, \omega''_p) \right. \right. \\
 &\quad \left. \left. - f(\omega_i, \omega_s, \omega''_p) f^*(\omega'_i, \omega'_s, 2\omega'_i + 2\omega'_s - \omega_i - \omega_s + \omega''_p - \omega_p) f(\omega'_i, \omega'_s, \omega_p) \right) \right). \tag{B.73}
 \end{aligned}$$

Using this form of the two-photon component of the state, we can write the state third order term in terms of the joint spectral amplitudes of the down-converted photons, such that

$$\begin{aligned}
 |\Psi_{\text{PDC}}^{(3)}\rangle_{\text{D}} &= \frac{\mathcal{A}}{3!} \left( \iint d\omega_i d\omega_s G_1(\omega_i, \omega_s) \hat{a}_i^\dagger(\omega_i) \hat{a}_s^\dagger(\omega_s) \right. \\
 &\quad + \iint d\omega_i d\omega_s \iint d\omega'_i d\omega'_s \iint d\omega''_i d\omega''_s G_3(\omega_i, \omega_s, \omega'_i, \omega'_s, \omega''_i, \omega''_s) \tag{B.74} \\
 &\quad \left. \times \hat{a}_i^\dagger(\omega_i) \hat{a}_s^\dagger(\omega_s) \hat{a}_i^\dagger(\omega'_i) \hat{a}_s^\dagger(\omega'_s) \hat{a}_i^\dagger(\omega''_i) \hat{a}_s^\dagger(\omega''_s) \right) |0\rangle.
 \end{aligned}$$

From Equation B.73, we can see that the joint spectral amplitude for the two-photon component is

$$G_1(\omega_i, \omega_s) = \frac{3}{2} (F_1(\omega_i, \omega_s) + h_1(\omega_i, \omega_s)), \tag{B.75}$$

where  $F_1$  is defined in Equation B.59,

and

$$\begin{aligned}
h_1 &= h_1(\omega_i, \omega_s) \\
&= \frac{1}{\pi^2} \iint d\omega'_i d\omega'_s \iint d\omega_p d\omega''_p \sum_{\substack{[j,k]= \\ \mathcal{P}[\omega_i, \omega'_i]}} \sum_{\substack{[m,n]= \\ \mathcal{P}[\omega_s, \omega'_s]}} \\
&\quad \times \left( \frac{f(\omega_i, \omega_s, \omega_p) f^*(\omega'_i, \omega'_s, 2\omega'_i + 2\omega'_s - \omega''_p - \Delta\omega) f(\omega'_i, \omega'_s, \omega''_p)}{\Delta\omega(\omega'_i + \omega'_s - \omega''_p)} \right. \\
&\quad \left. - \frac{f^*(\omega'_i, \omega'_s, \omega_p) f(j, m, j + m + \omega'_i + \omega'_s - \omega_p - k - n + \omega''_p) f(k, n, \omega''_p)}{(\omega'_i + \omega'_s - \omega_p)(k + n - \omega''_p)} \right). \tag{B.76}
\end{aligned}$$

## B.6 Permutations

$$\sum_{[i,j]=\mathcal{P}[a,b]} f(i, j) = f(a, b) + f(b, a) \tag{B.77}$$

$$\begin{aligned}
\sum_{[i,j,k]=\mathcal{P}[a,b,c]} f(i, j, k) &= f(a, b, c) + f(a, c, b) + f(b, a, c) \\
&\quad + f(b, c, a) + f(c, a, b) + f(c, b, a) \tag{B.78}
\end{aligned}$$

$$\sum_{[i,j,k]=\mathcal{P}[a,a,b]} f(i, j, k) = f(a, a, b) + f(a, b, a) + f(b, a, a) \tag{B.79}$$

## B.7 Change of Time Integration Variables

### B.7.1 Two Dimensional

In the following time integrals, we can see that the limits of integration over  $t_2$  depend on the integration variable  $t_1$ .

$$\int_{-\infty}^{\infty} dt_1 \int_{-\infty}^{t_1} dt_2 \quad (\text{B.80})$$

To solve these integrals, it is useful to perform a change of variables such that the two integrals become independent. Figure B.1 shows how this can be done by inspection.

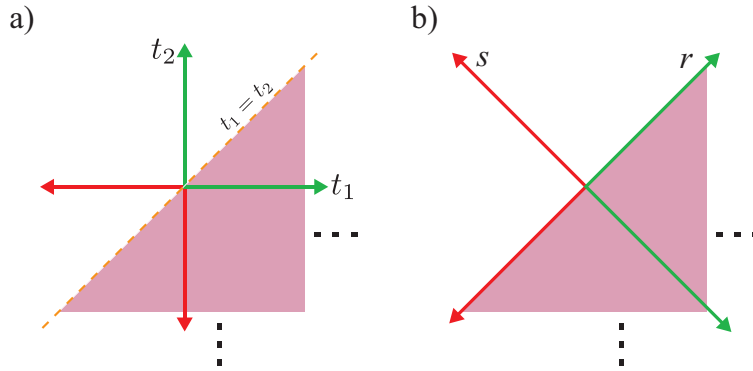


**Figure B.1:** Time integration region for second-order term. a) indicates the original integration variables, while b) indicates the new, independent, integration variables. The integration region continues to infinity beyond the limits of the plotting region.

The new integration variables are  $r = t_1 + t_2$  and  $s = t_1 - t_2$ . Since the Jacobian is 2,  $dt_1 dt_2 = 2 dr ds$  and we can write

$$\int_{-\infty}^{\infty} dt_1 \int_{-\infty}^{t_1} dt_2 = 2 \int_{-\infty}^{\infty} dr \int_0^{\infty} ds \quad (\text{B.81})$$

### B.7.2 Three Dimensional

In the third order term, we have the following dependent integrals over three time variables.

$$\int_{-\infty}^{\infty} dt_1 \int_{-\infty}^{t_1} dt_2 \int_{-\infty}^{t_2} dt_3 \quad (\text{B.82})$$

Once again, we would like to perform a change of variables in order to decouple them. We repeat the same process as above, however, we now draw a three-dimensional volume of integration. This is shown in figure B.2.

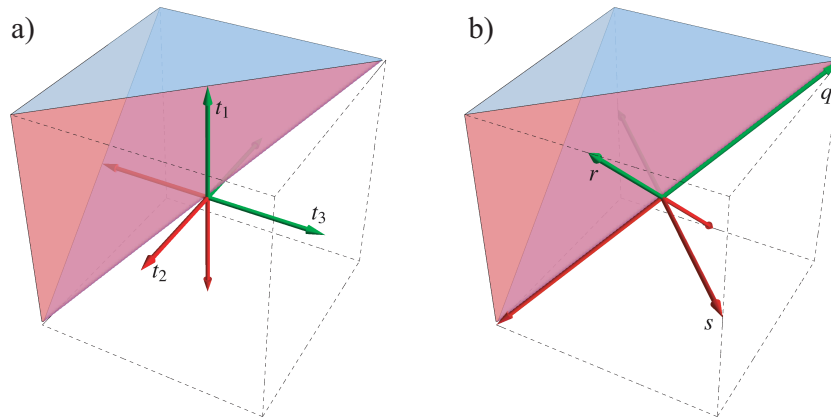


**Figure B.2:** Time integration region for third-order term. a) indicates the original integration variables, while b) indicates the new, independent, integration variables. The integration region continues to infinity beyond the limits of the plotting region.

The new integration variables are  $q = t_1 + t_2 + t_3$ ,  $r = t_1 - t_2$  and  $s = t_2 - t_3$ . This time, the change of variables was a bit more complicated and the Jacobian is  $1/3$ . This gives  $dt_1 dt_2 dt_3 = dq dr ds / 3$  and we can write

$$\int_{-\infty}^{\infty} dt_1 \int_{-\infty}^{t_1} dt_2 \int_{-\infty}^{t_2} dt_3 = \frac{1}{3} \int_{-\infty}^{\infty} ds \int_0^{\infty} dr \int_0^{\infty} ds \quad (\text{B.83})$$

**B.8 Evaluate  $\int_0^\infty ds \exp(ixs)$** 

$$\int_0^\infty ds \exp(ixs) = \int_0^\infty ds \cos(xs) + i \int_0^\infty ds \sin(xs) \quad (\text{B.84})$$

$$= \lim_{a \rightarrow 0} \int_0^\infty ds \sin(xs) e^{-as} + i \lim_{a \rightarrow 0} \int_0^\infty ds \sin(xs) e^{-as} \quad (\text{B.85})$$

$$= \lim_{a \rightarrow 0} \frac{a}{a^2 + x^2} + i \lim_{a \rightarrow 0} \frac{x}{a^2 + x^2} \quad (\text{B.86})$$

$$= \pi \delta(x) + \frac{i}{x} \quad (\text{B.87})$$

Alternatively, the solution can be found by taking the Fourier transform of a step function.

---

# References

---

- [1] I. Newton, *Hypothesis of Light* (1675).  
[Cited p. 1]
- [2] C. Huygens, *Traité de la Lumière* (1690).  
[Cited p. 1]
- [3] C. Cohen-Tannoudji, B. Diu, and F. Laloë, *Quantum Mechanics, Vol. I* (John Wiley and Sons, New York, 1977).  
[Cited p. 2]
- [4] M. A. Nielsen and I. L. Chuang, *Quantum computation and quantum information* (Cambridge University Press, Cambridge, 2000). [Cited pp. 2, 3, 7, 11, 13, and 14]
- [5] J. J. Sakurai, *Modern quantum mechanics*, revised ed. (Addison-Wesley, Reading, Mass., 1994). [Cited pp. 2, 7, and 8]
- [6] D. F. Walls and G. J. Milburn, *Quantum Optics* (1984). [Cited pp. 2, 9, 10, 11, 18, and 27]
- [7] H.-A. Bachor and T. C. Ralph, *A Guide to Experiments in Quantum Optics*, 2 ed. (Wiley-VCH, 2004). [Cited pp. 2 and 17]
- [8] A. M. Turing, “On computable numbers, with an application to the Entscheidungsproblem,” *Proc. Lond. Math. Soc.* 2 **42**, 230 (1936).  
[Cited p. 3]
- [9] C. E. Shannon, “A mathematical theory of communication,” *Bell System Tech. J.* **27**, 379 (1948).  
[Cited p. 3]
- [10] D. Deutsch, “Quantum Theory, the Church-Turing Principle and the Universal Quantum Computer,” *Proc. R. Soc. Lond. A* **400**, 97 (1985).  
[Cited p. 3]

- [11] P. W. Shor, “Algorithms for quantum computation: discrete logarithms and factoring,” in *Proceedings, 35th Annual Symposium on Fundamentals of Computer Science*, (IEEE Press, Los Alamitos, 1994).  
[Cited p. 3]
- [12] P. W. Shor, “Polynomial-Time Algorithms for Prime Factorization and Discrete Logarithms on a Quantum Computer,” *SIAM J. Comp.* **26**, 1484 (1997).  
[Cited p. 3]
- [13] L. K. Grover, “A fast quantum mechanical algorithm for database search,” in *28th ACM Symposium on Theory of Computation*, p. 212 (Association for Computing Machinery, New York, 1996).  
[Cited p. 3]
- [14] A. Einstein, B. Podolsky, and N. Rosen, “Can quantum-mechanical description of physical reality be considered complete?,” *Phys. Rev.* **47**, 777 (1935).  
[Cited p. 3]
- [15] A. Aspect, P. Grangier, and G. Roger, “Experimental Realization of Einstein-Podolsky-Rosen-Bohm Gedankenexperiment: A New Violation of Bell’s Inequalities,” *Phys. Rev. Lett.* **49**, 91 (1982).  
[Cited p. 3]
- [16] C. H. Bennett *et al.*, “Teleporting an unknown quantum state via dual classical and Einstein-Podolsky-Rosen channels,” *Phys. Rev. Lett.* **70**, 1895 (1993).  
[Cited pp. 3 and 24]
- [17] D. Bouwmeester *et al.*, “Experimental quantum teleportation,” *Nature* **390**, 575 (1997). [Cited pp. 3 and 23]
- [18] E. Knill, R. Laflamme, and G. J. Milburn, “A scheme for efficient quantum computation with linear optics,” *Nature* **409**, 46 (2001). [Cited pp. 4 and 23]
- [19] J. L. O’Brien *et al.*, “Demonstration of an all-optical quantum controlled-NOT gate,” *Nature* **426**, 264 (2003).  
[Cited p. 4]
- [20] T. B. Pittman *et al.*, “Experimental controlled-NOT logic gate for single photons in the coincidence basis,” *Phys. Rev. A* **68**, 032316 (2003).  
[Cited p. 4]
- [21] A. Ourjoumtsev *et al.*, “Generating Optical Schrödinger Kittens for Quantum Information Processing,” *Science* **312**, 83 (2006). [Cited pp. 4, 24, 28, and 40]

- 
- [22] J. S. Neergaard-Nielsen *et al.*, “Generation of a Superposition of Odd Photon Number States for Quantum Information Networks,” *Phys. Rev. Lett.* **97**, 083604 (2006). [Cited pp. 4, 24, and 28]
- [23] Y.-H. Kim and W. P. Grice, “Generation of pulsed polarization-entangled two-photon state via temporal and spectral engineering,” *Journal of Modern Optics* **49**, 2309 (2002). [Cited pp. 5 and 40]
- [24] W. P. Grice, A. B. U’Ren, and I. A. Walmsley, “Eliminating frequency and space-time correlations in multiphoton states,” *Phys. Rev. A* **64**, 063815 (2001). [Cited pp. 5 and 40]
- [25] Z. D. Walton *et al.*, “Generation of polarization-entangled photon pairs with arbitrary joint spectrum,” *Phys. Rev. A* **70**, 052317 (2004). [Cited pp. 5 and 40]
- [26] A. B. U’Ren *et al.*, “Generation of Two-Photon States with an Arbitrary Degree of Entanglement Via Nonlinear Crystal Superlattices,” *Phys. Rev. Lett.* **97**, 223602 (2006). [Cited pp. 5 and 40]
- [27] M. Corona and A. B. U’Ren, “Parametric down-conversion with optimized spectral properties in nonlinear photonic crystals,” *Phys. Rev. A* **76**, 043829 (2007). [Cited pp. 5 and 40]
- [28] A. B. U’Ren *et al.*, “Generation of Pure-State Single-Photon Wavepackets by Conditional Preparation Based on Spontaneous Parametric Downconversion,” *Laser Physics* **15**, 146 (2005). [Cited pp. 5, 40, 58, and 59]
- [29] A. B. U’Ren, Y. Jeronimo-Moreno, and H. Garcia-Gracia, “Generation of Fourier-transform-limited heralded single photons,” *Phys. Rev. A* **75**, 023810 (2007). [Cited pp. 5 and 40]
- [30] O. Kuzucu *et al.*, “Joint Temporal Density Measurements for Two-Photon State Characterization,” *Phys. Rev. Lett.* **101**, 153602 (2008). [Cited pp. 5 and 40]
- [31] P. J. Mosley *et al.*, “Heralded Generation of Ultrafast Single Photons in Pure Quantum States,” *Phys. Rev. Lett.* **100**, 133601 (2008). [Cited pp. 5, 40, and 63]
- [32] K. Garay-Palmett *et al.*, “Photon pair-state preparation with tailored spectral properties by spontaneous four-wave mixing in photonic-crystal fiber,” *Opt. Express* **15**, 14870 (2007). [Cited pp. 5 and 40]
- [33] Z. Ficek and M. R. Wahiddin, *Quantum Optics: Fundamentals and Applications*, 1st ed. (IIUM, Kuala Lumpur, 2004). [Cited p. 9]

- 
- [34] H. Jeong and T. C. Ralph, “Schrödinger Cat States for Quantum Information Processing,” in *Quantum Information with Continuous Variables of Atoms and Light*, N. J. Cerf, G. Leuchs, and E. S. Polzik, eds., (Imperial College Press, 2007), Vol. 1, Chap. 9, pp. 159–177. [Cited pp. 16 and 25]
- [35] P. P. Rohde, W. Mauerer, and C. Silberhorn, “Spectral structure and decompositions of optical states, and their applications,” *New J. Phys.* **9**, 91 (2007). [Cited pp. 16 and 40]
- [36] P. P. Rohde, T. C. Ralph, and M. A. Nielsen, “Optimal photons for quantum-information processing,” *Phys. Rev. A* **72**, 052332 (2005). [Cited pp. 16 and 69]
- [37] W. P. Grice and I. A. Walmsley, “Spectral information and distinguishability in type-II down-conversion with a broadband pump,” *Phys. Rev. A* **56**, 1627 (1997). [Cited pp. 18, 41, and 83]
- [38] M. M. Fejer *et al.*, “Quasi-Phase-Matched Second Harmonic Generation: Tuning and Tolerances,” *IEEE J. Quantum. Electron.* **QE-28**, 2631 (1992). [Cited pp. 19, 21, 70, and 80]
- [39] S. Boyd and L. Vandenberghe, *Convex optimization* (Cambridge University Press, Cambridge, 2003), online at <http://www.stanford.edu/boyd/>. [Cited p. 19]
- [40] T. C. Ralph *et al.*, “Quantum computation with optical coherent states,” *Phys. Rev. A* **68**, 042319 (2003). [Cited p. 23]
- [41] A. P. Lund, T. C. Ralph, and H. L. Haselgrove, “Fault-Tolerant Linear Optical Quantum Computing with Small-Amplitude Coherent States,” *Phys. Rev. Lett.* **100**, 030503 (2008). [Cited pp. 23, 24, 28, and 99]
- [42] P. Kok *et al.*, “Linear optical quantum computing with photonic qubits,” *Rev. Mod. Phys.* **79**, 135 (2007). [Cited pp. 23, 40, and 69]
- [43] D. Gottesman and I. L. Chuang, “Demonstrating the viability of universal quantum computation using teleportation and single-qubit operations,” *Nature* **402**, 390 (1999). [Cited p. 23]
- [44] S. J. van Enk and O. Hirota, “Entangled coherent states: Teleportation and decoherence,” *Phys. Rev. A* **64**, 022313 (2001). [Cited pp. 23 and 24]
- [45] H. Jeong, M. S. Kim, and J. Lee, “Quantum-information processing for a coherent superposition state via a mixedentangled coherent channel,” *Phys. Rev. A* **64**, 052308 (2001). [Cited pp. 23 and 24]

- 
- [46] A. P. Lund and T. C. Ralph, “Coherent-state linear optical quantum computing gates using simplified diagonal superposition resource states,” *Phys. Rev. A* **71**, 032305 (2005).  
[Cited p. 23]
- [47] A. P. Lund *et al.*, “Conditional production of superpositions of coherent states with inefficient photon detection,” *Phys. Rev. A* **70**, 020101 (2004). [Cited pp. 24, 28, and 38]
- [48] A. Ourjoumtsev *et al.*, “Generation of optical ‘Schrödinger cats’ from photon number states,” *Nature* **448**, 784 (2007). [Cited pp. 24, 40, and 51]
- [49] M. A. Nielsen, “Cluster-state quantum computation,” quant-ph/0504097v2 (2005).  
[Cited p. 26]
- [50] M. Dakna *et al.*, “Generating Schrödinger-cat-like states by means of conditional measurements on a beam splitter,” *Phys. Rev. A* **55**, 3184 (1997). [Cited pp. 27 and 28]
- [51] A. E. B. Nielsen and K. Mølmer, “Transforming squeezed light into a large-amplitude coherent-state superposition,” *Phys. Rev. A* **76**, 043840 (2007).  
[Cited p. 28]
- [52] H. Jeong, A. P. Lund, and T. C. Ralph, “Production of superpositions of coherent states in traveling optical fields with inefficient photon detection,” *Phys. Rev. A* **72**, 013801 (2005). [Cited pp. 28 and 38]
- [53] H. Takahashi *et al.*, “Generation of large-amplitude coherent-state superposition via ancilla-assisted photon-subtraction,” arXiv:0806.2965v1 [quant-ph] (2008).  
[Cited p. 38]
- [54] T. C. Ralph, “Quantum optical systems for the implementation of quantum information processing,” *Reports on Progress in Physics* **69**, 853 (2006).  
[Cited p. 40]
- [55] R. Tualle-Brouri *et al.*, “Multimode model for projective photon-counting measurements,” *Phys. Rev. A* **80**, 013806 (2009).  
[Cited p. 40]
- [56] M. G. Raymer *et al.*, “Pure-state single-photon wave-packet generation by parametric down-conversion in a distributed microcavity,” *Phys. Rev. A* **72**, 023825 (2005).  
[Cited p. 40]

- [57] A. Christ *et al.*, “Pure single photon generation by type-IPDC with backward-wave amplification,” *Opt. Express* **17**, 3441 (2009).  
[Cited p. 40]
- [58] W. Wasilewski *et al.*, “Pulsed squeezed light: Simultaneous squeezing of multiple modes,” *Phys. Rev. A* **73**, 063819 (2006).  
[Cited p. 41]
- [59] W. Mauerer, *On Colours, Keys, and Correlations: Multimode Parametric Downconversion in the Photon Number Basis*, Ph.D. thesis, Friedrich-Alexander-Universität Erlangen-Nürnberg, 2009.  
[Cited p. 41]
- [60] C. H. Bennett *et al.*, “Mixed state entanglement and quantum error correction,” *Phys. Rev. A* **54**, 3824 (1996).  
[Cited p. 42]
- [61] C. K. Hong, Z. Y. Ou, and L. Mandel, “Measurement of subpicosecond time intervals between two photons by interference,” *Phys. Rev. Lett.* **59**, 2044 (1987).  
[Cited pp. 46 and 74]
- [62] L. E. Vicent *et al.*, “Design of bright, fiber-coupled and fully factorable photon pair sources,” *New Journal of Physics* **12**, 093027 (2010).  
[Cited p. 67]
- [63] N. Gisin and R. Thew, “Quantum communication,” *Nat Photon* **1**, 165 (2007).  
[Cited p. 69]
- [64] B. L. Higgins *et al.*, “Entanglement-free Heisenberg-limited phase estimation,” *Nature* **450**, 393 (2007).  
[Cited p. 69]
- [65] T. Nagata *et al.*, “Beating the Standard Quantum Limit with Four-Entangled Photons,” *Science* **316**, 726 (2007).  
[Cited p. 69]
- [66] G. Brida, M. Genovese, and R. Berchera, “Experimental realization of sub-shot-noise quantum imaging,” *Nat Photon* **4**, 227 (2010).  
[Cited p. 69]
- [67] A. N. Boto *et al.*, “Quantum Interferometric Optical Lithography: Exploiting Entanglement to Beat the Diffraction Limit,” *Phys. Rev. Lett.* **85**, 2733 (2000).  
[Cited p. 69]

- 
- [68] M. Nasr *et al.*, “Ultrabroadband biphotons generated via chirped quasi-phase-matched optical parametric down-conversion,” *Physical review letters* **100**, 183601 (2008). [Cited pp. 69 and 70]
- [69] A. M. Brańczyk *et al.*, “Optimized generation of heralded Fock states using parametric down-conversion,” *New Journal of Physics* **12**, 063001 (2010). [Cited p. 70]
- [70] M. H. Rubin *et al.*, “Theory of two-photon entanglement in type-II optical parametric down-conversion,” *Phys. Rev. A* **50**, 5122 (1994). [Cited p. 70]
- [71] A. Valencia *et al.*, “Shaping the Waveform of Entangled Photons,” *Phys. Rev. Lett.* **99**, 243601 (2007). [Cited p. 70]
- [72] G. Imeshev *et al.*, “Pulse shaping by difference-frequency mixing with quasi-phase-matching gratings,” *Journal of the Optical Society of America B* **18**, 534 (2001). [Cited p. 70]
- [73] A. Fedrizzi *et al.*, “Anti-symmetrization reveals hidden entanglement,” *New J. Phys.* **11**, 103052 (2009). [Cited pp. 75, 76, and 77]
- [74] K. Wang, “Quantum theory of two-photon wavepacket interference in a beam-splitter,” *Journal of Physics B: Atomic, Molecular and Optical Physics* **39**, R293 (2006). [Cited p. 77]
- [75] A. Eckstein and C. Silberhorn, “Broadband frequency mode entanglement in waveguided parametric downconversion,” *Optics Letters* **33**, 1825 (2008). [Cited p. 77]
- [76] M. Halder *et al.*, “Nonclassical 2-photon interference with separate intrinsically narrowband fibre sources,” *Opt. Express* **17**, 4670 (2009). [Cited p. 82]
- [77] J. S. Neergaard-Nielsen *et al.*, “Optical Continuous-Variable Qubit,” *Phys. Rev. Lett.* **105**, 053602 (2010). [Cited p. 99]